Kyushu Institute of Technology

Effects of Solid–liquid Interfacial Resistance on Thermal Elastohydrodynamic Lubrication

Submitted to Department of Mechanical Engineering

In Partial Fulfilment of the Requirements

for the Degree of Doctor of Philosophy Engineering

by

Xianghua MENG

February 2022

Contents

Nomenclature

a	Half Hertzian contact width [m]
c, c_a, c_b	Specific heat of lubricant and solids [J/kg·K]
d	Thickness of solids in z direction [m]
E'	Reduced elastic modulus [Pa]
G	Dimensionless material parameter, $\alpha E'$
h	Film thickness [m]
h_{00}	Rigid central film thickness [m]
H	Dimensionless film thickness, hR/a^2
k, k_a, k_b	Thermal conductivity of lubricant and solids [W/m·K]
l_k	Thermal slip length [m]
$\bar{l}_\mathrm{k}$	Dimensionless thermal slip length, $l_\mathrm{k}R/a^2$
l_s	Slip length [m]
$\bar{l}_\mathrm{s}$	Dimensionless slip length, $l_\mathrm{s}R/a^2$
p	Film pressure [Pa]
p_H	Maximum Hertzian pressure [Pa]
P	Dimensionless pressure, p/p_H
R	Equivalent radius for point contact [m]
SRR	Slide-roll ratio [–]
S_0	Roelands viscosity-temperature coefficient [–]

T	Temperature [K]
T_0	Ambient temperature [K]
ΔT	Temperature jump at solid–lubricant interface [K]
$\overline{T}$	Dimensionless temperature, T/T_0
u	Lubricant velocity [m/s]
u_0	Reference velocity parameter [m/s]
u_a, u_b	Velocity of two surfaces [m/s]
u_e	Entrainment velocity, $(u_a+ u_b)/2$
U	Dimensionless lubricant velocity [–]
U_0	Dimensionless reference velocity parameter, $\eta_0 u_0/RE'$
U_a, U_b	Dimensionless velocity of two surfaces, u_a/u_e, u_b/u_e
U_e	Dimensionless entrainment velocity, $\eta_0 u_e/RE'$
v	Lubricant velocity in y direction [m/s]
V	Dimensionless lubricant velocity in y direction [–]
w	Load [N]
W	Dimensionless Load, w/R^2E'
x, y	Horizontal coordinates [m]
x_{in}, x_{out}	Positions of start and end of domain [m]
X, Y	Dimensionless horizontal coordinates, x/a, y/a
X_{in}, X_{out}	Dimensionless positions of start and end of domain, x_{in}/a, x_{out}/a
ΔX, ΔY	Dimensionless mesh size [–]
y_{in}, y_{out}	Positions of start and end of domain [m]

Y_{in}, Y_{out}	Dimensionless positions of start and end of domain, y_{in}/a, y_{out}/a
z, z_a, z_b	Vertical coordinates of film and solids [m]
Z	Dimensionless vertical coordinates of film, z/h
Z_a, Z_b	Dimensionless vertical coordinates of solids, z_a/a, z_b/a
ΔZ	Dimensionless mesh size [–]
Z_0	Roelands viscosity-pressure coefficient [–]
α	Baur's viscosity-pressure coefficient [–]
β	Reynolds viscosity-temperature coefficient [K^{-1}]
η	Lubricant viscosity [Pa·s]
η_0	Lubricant viscosity at $p = p_0$, $T = T_0$ [Pa·s]
$\bar{\eta}$	Dimensionless lubricant viscosity, η/η_0
ρ, ρ_a, ρ_b	Density of lubricant and solids [kg/m^3]
ρ_0	Lubricant density at $p = p_0$, $T = T_0$ [kg/m^3]
$\bar{\rho}$	Dimensionless lubricant density, ρ/ρ_0
τ	Shear stress [Pa]

Chapter 1

1. Introduction

Tribology is the technology and science of interacting objects in relative motion. It is highly interdisciplinary, drawing on chemistry, mathematics, biology, materials science, physics, and engineering etc. The word of *Tribology* is the literal translation of "the study of rubbing" from Greek word, and becomes widespread following the Jost Report [1] in 1966. It includes the study and application of wear, friction, and lubrication, which are closely related to our daily life. Today, the exploration of tribology is not only limited in the context of mechanical engineering, but also expands to micro and nanotechnology as well as other qualitatively new fields [2].

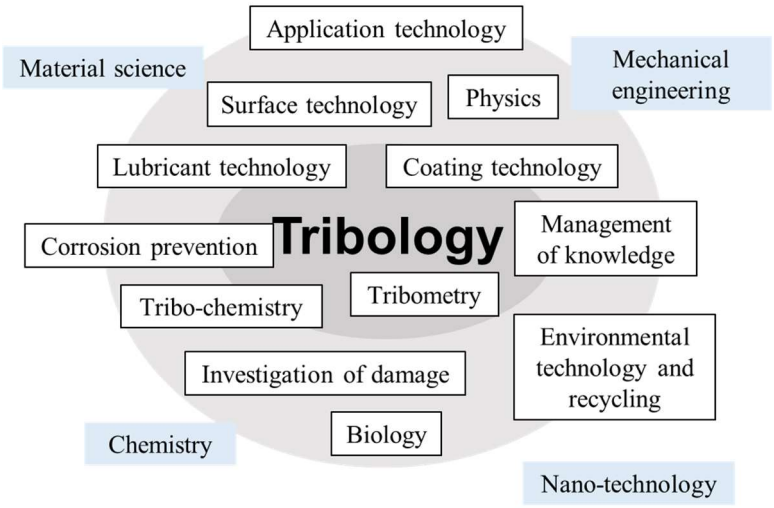

Figure 1-1 Graphic description of tribology interacting with other science [2].

In tribology, lubrication is an indispensable technique to reduce friction and wear between two contact surfaces by using lubricant. In terms of lubrication mechanism, it can be divided into following regimes: hydrodynamic lubrication, elastohydrodynamic

lubrication, mixed lubrication and boundary lubrication, as shown in Fig. 1-2 [3]. Good lubrication could prevent the destructive and damage, extend the operation life of machine elements.

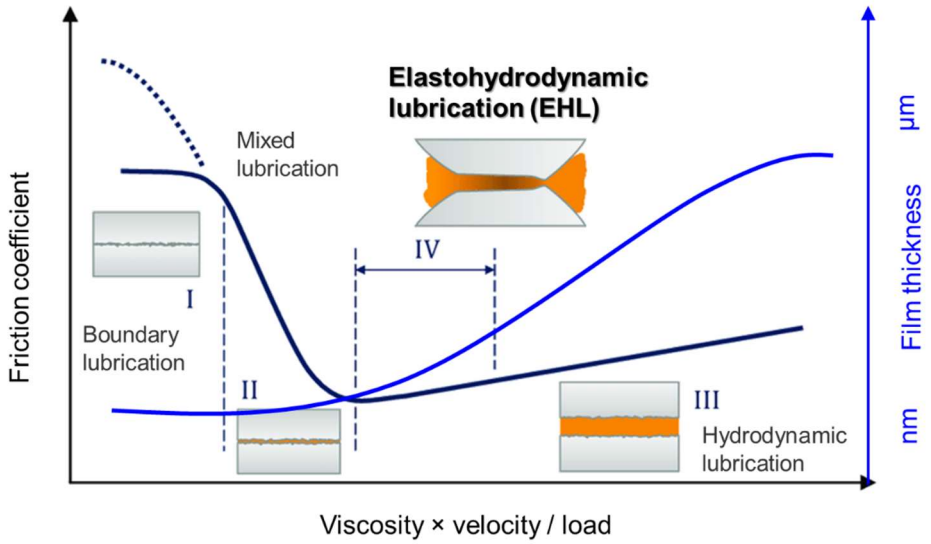

Figure 1-2 Schematic of Stribeck curve [3].

Due to the low friction and long-life operation, the working elements are commonly designed in the elastohydrodynamic lubrication (EHL) regime. EHL theory describes the mechanism of non-conformal lubricated contacts, where the pressure magnitude can be up to the order of gigapascals. This high pressure results in the elastic deformation of surfaces and the great increase in lubricant viscosity. Owing to the extreme conditions (pressures of gigapascal), small contact areas (around 300 μm in diameter), and the thermal effect (temperature rise affects the lubricant viscosity), the continuum boundary condition in EHL may breakdown, results in slip boundary condition. Therefore, the thermal EHL theory with boundary slips continues receive attentions in researchers to improve the working performance and durability of non-conformal lubricated machine elements.

1.1 Elastohydrodynamic lubrication

Elastohydrodynamic lubrication (EHL) has been extensively studied during the last decades to understand the lubrication mechanism in tribological components. The

research on EHL can be divided into the aspects of experimentally and theoretically, which are both mutual promotion and common development.

1.1.1 Experimental study

Experimental study plays a vital role in determining the lubrication performance of EHL filed, which has been widely investigated. In these studies, the parameters of friction, film thickness and temperature rise are general used to assess the performances of lubrication.

In EHL, the generation of friction inside lubricated contact is usually connected with the properties of lubricant and surface. Through the earlier experimental friction measurement on journal bearings by Tower [4], the lubricant property, such as limiting shear stress, could affect the friction value. At high pressure, the friction coefficient of different lubricant rheology no longer increases with the increases of shear rate after reaches the limiting value [5–7]. Thermal property of lubricant is another factor in the measurement of friction. The lubricant rheological properties modulate the temperature rise in EHL contacts, affecting the lubricant viscosity and hence friction. Because of its key role, Lu rt al. [8] combined the experimental tests and theoretical calculations to gain the temperature and friction information of lubricant rheological, which can be used to control friction in practical applications. Zhang and Spikes [9] measured friction curves up to very high pressures using ball on disc friction machine. At high pressure condition, thermal effects on friction value become substantial in terms of underlying rheological properties of the lubricants.

To reduce friction and improve the tribological performance of lubricated systems, surface coating has been widely used. Chhowalla and Ameratunga [10] utilized the Molybdenum disulfide (MoS2) coating in dry machine contacts, and the ultra-low friction was observed. Fabricating MoS2 coating on contact surfaces prevent oxidation and preserve the layered structure in circumstances where liquid lubricants are impractical [11–13]. Diamond Like Carbon (DLC) coating is very resistant to abrasive and adhesive wear, making it suitable for extreme contact pressure conditions. Björling and Shi [14] investigated the performance of DLC coating at pressure up to 1.95 GPa under various operation conditions. Evans et al. [15] and Kalin et al. [16,17] reported the friction

reduction in DLC coated EHL contacts through experiments. Compared to uncoated surfaces, DLC coatings have significantly lower conductivity, which results in higher lubricant temperature, therefrom leads to the viscosity and friction reductions in contacts. The heat dissipation mitigated by DLC coating are examined by Beilicke et al. [18] and Habchi et al. [19,20]. Other important contributions studying the friction problem includes the plastic coating [21], graphene coating [22–24], absorbed mucin layer [25], and glycerol [26] etc.

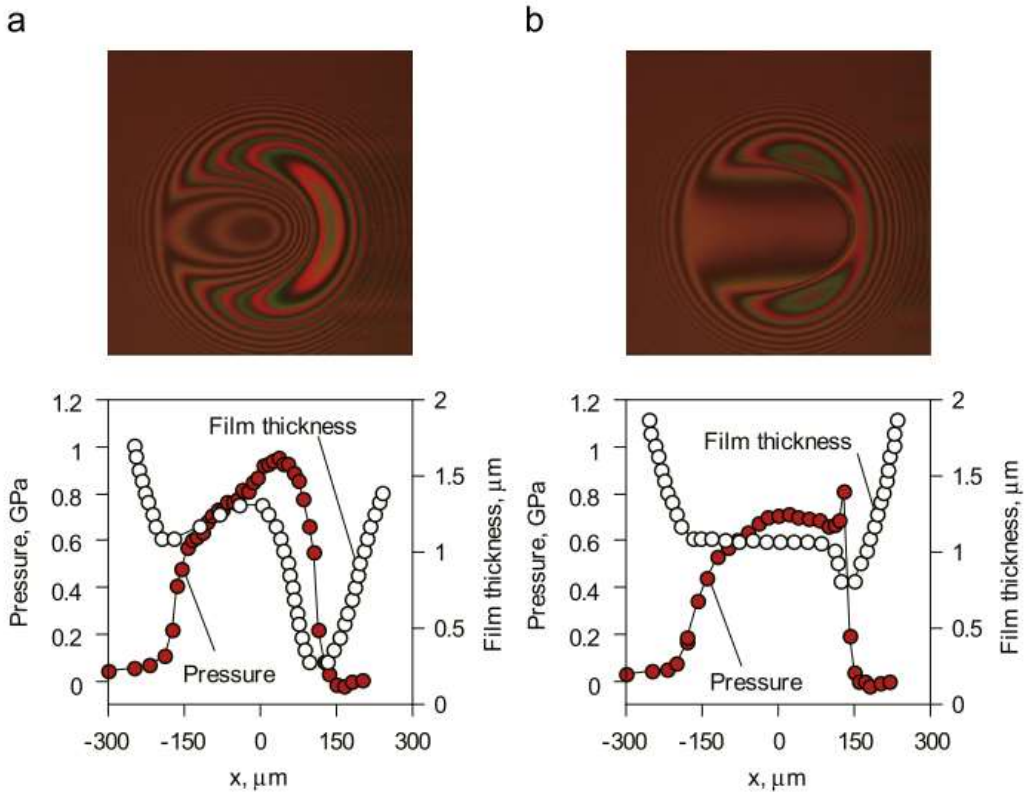

Figure 1-3 Typical film thickness and pressure distributions in EHL contact (p_{hmax} = 0.57 GPa, u_m = 0.2 m/s and T = 32 °C): (a) SRR = -1.8, (b) SRR = 0. [34]

Film thickness and shape have been a major concern in experimental studies, which represent the separation of contact surfaces. According to the reports of Crook [27], a flat plateau exists in the central zone and a constriction appears around the exit region. In the point case, Cameron's group [28] observed a horseshoe shape constriction in the exit zone by using optical interferometry. Kaneta et al. [29,30] reported a large and deep dimple in glass–steel point contacts, quite different from the conventional shape. Following the

results of Yagi et al. [31], the occurrence of the dimple phenomenon can be explained by viscosity wedge effect [32,33]. Yagi et al. [34] conducted the experiments using a ball on disc type apparatus in which a circular contact is formed between a rotating glass disc and a rotating steel ball. A high resolution Raman spectrometer is used to measure the pressure profiles in sliding glass–steel point contacts, while the film thickness was determined by optical interferometry [35–40] prior to pressure measurements. Results showed the typical film thickness and pressure profiles under the horseshoe shape and dimple shape film in EHL contact, as shown in Fig. 1-3.

Thermal effects have been a major detection index for satisfactory and reliable operation of machine components. These machine elements working in EHL regime are often under high pressure and heavy load, where significant temperature rise occurs. In these circumstances, the lubrication may breakdown, results in surface failures. Therefore, measurement of temperature has attached much attention in decades. However, obtain the temperature distributions in EHL contact becomes far more difficult due to its microscale. Turchina et al. [41] firstly introduced the infrared radiation technique for the measurement of temperature distributions in EHL conjunction. This technique was then improved by Ausherman et al. [42] with band pass filter. Yagi et al. [43,44] investigated the impact of lubricant temperature on film thickness by using infrared technique. As in Spikes work [45], the temperature rise maps of solid surfaces and maps of shear stress in rolling/sliding contacts were described. Lu et al. [46] measured the film temperature in three dimensions. The temperature profile measured through film is largely determined by heat conduction in the z direction. Nishikawa et al. [47] concentrated their focus on temperature distributions on surfaces with longitudinal or transverse ridges, which bring about higher lubricant temperature than that with smooth surface. Omasta et al. [48] determined the temperature distributions of both contacting surfaces and oil film by infrared microscopy. Two band filters referred to as L and S filter, and disc with and without a chromium layer were used to separate individual components of radiation.

1.1.2 Theoretical analysis

Elastohydrodynamic lubrication theory has been well established to predict the performance of lubrication in machine elements during last decades. Petrusevich [49]

firstly presented an numerical solution for the EHL problem. They showed lubricated contact pressure and film thickness distributions as the characteristic of EHL. Later, Dowson and Higginson [50] developed an empirical formula for minimum film thickness based on inverse solution method in line EHL contact. This method initial assumed a pressure distribution. Then calculated the film thickness based on the elastic equation and Reynolds equation, respectively. Compared the two film results and adjusted the pressure until the two film shapes agrees well. Gohar [51] presented a forward iterative method to initial pressure distribution for solving Reynolds equation and calculate film thickness. The obtained results are used to update the pressure until convergence is received. In the solution of pressure, Newton-Raphson method are employed for solving discretized Reynolds equation, film thickness equation and force balance equation in line contact [52,53]. Multigrid (MG) and multilevel multi-integration (MLMI) methods [54,55] was developed to fast calculation of elastic deformation in the solution of point EHL contact. In the theoretical studies of EHL theory, the temperature rise, lubricant rheology, film thickness and shapes are important influential factors to assess the lubrication performances. Therefore, these aspects are elaborated further in the following reference reviews.

For the EHL problem, the lubricant in contact area, where the applied load lead high pressure and sliding velocity is considerable, can generate very large and rapid temperature rise. In the history of EHL theory, there has been numerous studies trying to understand the played role of temperature variation. The full numerical solution of EHL with thermal effects was firstly obtained by the Cheng et al. [56,57]. In the pointing work done by Sadeghi et al. [58], the lubricant shear heating, convection in lubricant film and conduction across the film are the major mechanisms of heat generation and removal, respectively. The generated heat leads high lubricant temperature, affecting the film thickness, friction, and pressure distributions [59,60]. Effects of solid and lubricant thermal conductivity [61–63] and solid body temperature on lubrication [64] were also adopted in thermal EHL solution. Kim and Sadeghi [65] employed the multigrid technique to obtain temperature distributions. Later, Guo and Yang [66] developed the sequential line sweeping scheme for the solution of energy equations. The results presented by Zhu et al. [67] indicated that the lubricant temperature increases as surface velocity and slide-roll ratios. Hsiao et al. [68] revealed the strong effects of sliding

conditions includes pure rolling, simple sliding and opposite sliding, on the temperature distributions. Wang and Yang [69] confirmed the influence of temperature rise not only on friction, but also on the minimum film thickness. Wang et al. [70] investigated the lubrication film thickness and temperature rise variation from full film status to boundary lubrication with three dimensional (3D) surface roughness involved. Ebner et al. [71] simulated the temperature rise inside the lubricant and solids. The lower thermal conductivity of solids, the higher lubricant temperature, shown in Fig. 1-4.

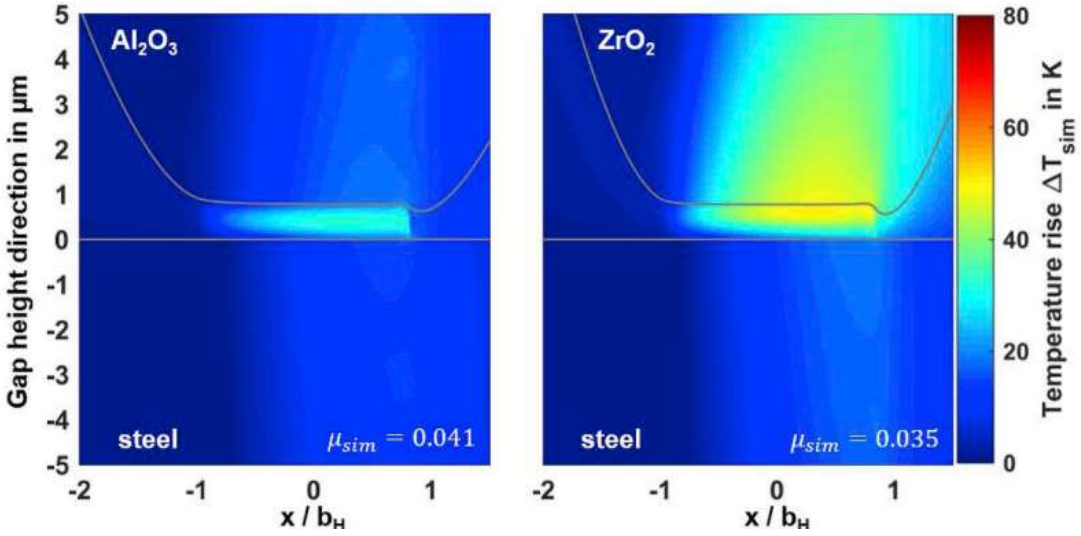

Figure 1-4 Simulated temperature distributions inside lubricant and solids. λ_{steel} = 44 W/(m·K), λ_{Al2O3} = 28 W/(m·K) and λ_{ZrO2} = 2.5 W/(m·K) [71].

Lubricant rheology is one of the fundamental parameters considered in numerical analysis, which is related to the types of lubricant. Under EHL conditions, the lubricant usually suffers high pressure, in conjunction with microscale film thickness and meter scale sliding velocity. This results lubricant rheology in several special phenomenon such as shear thinning [72], phase transitions [73,74]. For employed rheology model, Newtonian lubricant is mostly widely accepted in EHL theory [75–77], however, non-Newtonian EHL models has been developed over the years. Yang et al. [78] investigated behavior of the thermal elastohydrodynamic lubrication as the lubricant is assumed to be an Eyring fluid, which includes nonlinear stress-strain behaviors. The Eyring rheology model has been proved useful for the description of shear thinning behavior of the lubricant [79–81]. Ochoa et al. [82] presented thermal line EHL calculations for lubricants

whose rheological behavior follows a modified Carreau model. Zhang et al. [83] compared the film thickness variation in point ZEV contact by employing both Newtonian and Ree-Eyring fluid models. Results showed that the convergence using Ree–Eyring model is better than that of the Newtonian model.

Good lubrication performance has been justified by the magnitude of film thickness and shape in EHL contact, that has led to the development of numerical studies on film thickness calculation. Hamrock and Dowson [84] proposed a curve fitting formula of center and center minimum film thickness for lubrication consideration. The lubricating film thickness is related to the working conditions and properties of materials, which are reviewed previously [27–31]. Following the studies on film thickness, extensive investigations on shapes of EHL film have been conducted by numerous researchers. Classical EHL film shape resembles like a horseshoe: flat central plateau, side lobes, outer constriction with an outlet pressure spike. However, an abnormal thick of film instead of flat central plateau was observed in contact area, which is known as dimple phenomenon [85]. This is attributed to the thermal viscosity wedge effect, according to the analysis by Yang et al. [86]. The viscosity wedge, which originated from the temperature difference in the contact surfaces, has a contribution to the film formation and related to temperature rise in contact area. Yagi et al. [87] measured the temperature distribution in the dimple zone, showed that the maximum temperature sometimes reached 400K, revealed the relationship between the dimple and temperature rise. Wang et al. [88] studied the thermal viscosity wedge effect on the transient grease lubricated ZEV contacts in bearings and ball screws. They reported that the thermal viscosity wedge effect was large at high speeds, on the contrary, it became weak when the thermal effect was not significant at low speeds.

Another situation creates dimple phenomenon in contact area is large SRR or ZEV conditions. When one of the contacting surfaces moves with the same velocity as the opponent surface, but in the opposite direction, the worst situation referred as zero entrainment velocity (ZEV) is produced. Applications of ZEV contact can be found in retainerless bearings, wind turbines and mining machineries etc. Dyson et al. [89] confirmed the existence of an effective lubricating film at a twin disc machine under ZEV conditions. Guo et al. [90,91] conducted a thermal EHL analysis of point ZEV contact, and attributed the dimple formation to thermal viscosity wedge. Under ZEV condition, the lubricant at ambient temperature is dragged into the contact by one surface and is also

ejected out after being heated by the other one. As a result, a viscosity gradient is created across the film thickness which, in turn, modifies the pressure profile. That is responsible for the film formation in the central area of the contact. Zhang et al. [92] focused on the variation of dimple with surface velocity under ZEV contact. From high to modest surface velocity, a large classical surface dimple is predicted, and the depth of the surface dimple increases with decrease of the surface velocity. However, if the surface velocity is further decreased, a smaller centralized dimple is obtained, as shown in Fig. 1-5.

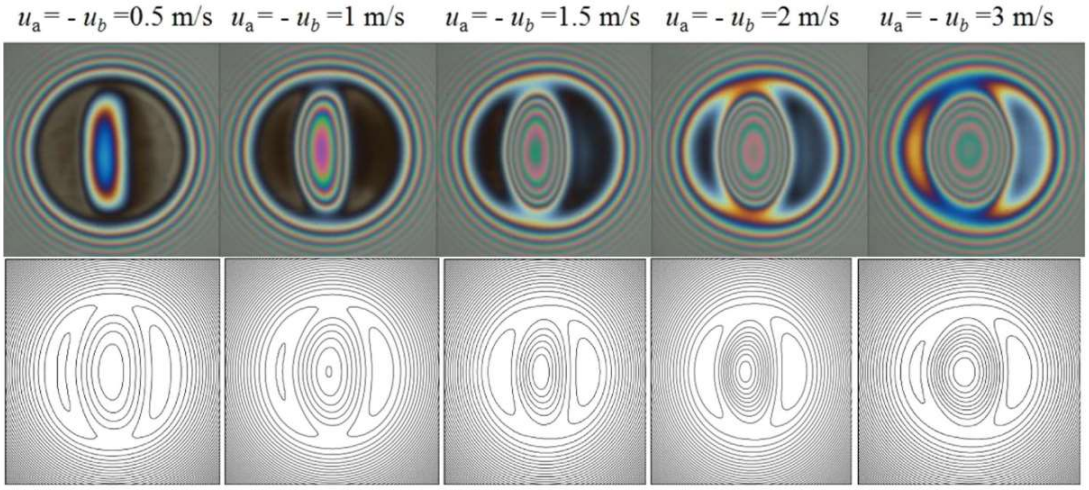

Figure 1-5 Experiment and simulation result for point contact under ZEV [92].

1.2 Solid–liquid interfacial resistance

Solid–liquid interfacial resistance is crucial to the lubrication analysis. In conventional lubrication theory, continuum boundary condition is common accepted, which states the continuity of velocity and temperature between lubricant and adjacent solid at interfaces. However, evidence of interfacial resistance has been obtained experimentally and theoretically in recent research. It depicts the relative movement between the lubricant and solid, and the temperature jump at solid–lubricant interfaces, referred as velocity slip and thermal slip respectively. The slip conditions can be encounter in practical application of many branches of industry, such as EHL, superlubricity, micro channel, heat dissipation etc. Therefore, the mechanisms and applications of interfacial resistance have

drawn considerable interest in recent years.

1.2.1 Hydrodynamic resistance at solid–liquid interface

Hydrodynamic resistance (velocity slip) occurs at solid–liquid interface when the velocity of the liquid near the surface is unequal to the velocity of solid surface [93]. Fig. 1-6 shows the well-known linear Navier model. The slip velocity u_s at solid–fluid interface is linearly proportional to the velocity gradient at the surface. The slip length b can be obtained by extrapolating the velocity profile from the position at the solid–fluid interface in the fluid to the position at which the velocity becomes zero.

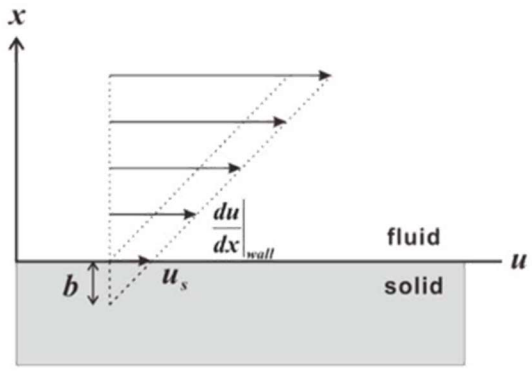

Figure 1-6 Schematic of velocity slip at solid–liquid on interface. [93]

Reviewed on the works of literatures, measurement methods have been developed to investigate the occurrence and influence of velocity slip at interfaces. In the experiments of Lee et al [94,95], the slip length was obtained through torque measurements with a rheometer, which produces a uniform shear rate over the sample. Pit et al [96,97] used the technique of fluorescence recovery after photobleaching to show the evidence of slip between hexadecane and sapphire surface. The technique of particle image velocimetry allows direct access to the velocity profile and extraction of the slip length with high accuracy. David Schäffel et al [98] also used fluorescence correlation spectroscopy to measure the flow field and slip length for water on a microstructure superhydrophobic surface. They revealed that the slip length is finite, nonconstant, anisotropic, and sensitive to the presence of surfactants. Bonaccurso et al. [99] found the degree of slip increase

with surface roughness by measurement of hydrodynamic drainage force. Maali et al [100] presented a drainage experiment of water between a borosilicate sphere and a micro structured surface, to measure the hydrodynamic drag force and slip length on microstructure surfaces. Guo et al. [101–103] focused on dimple phenomenon in an EHL conjunction to identify the boundary slip. The evidence of velocity slip was captured based on the relative movement of entrapped lubricant in contact area by using optical interferometry. The Neto group [104–107] obtained a resolution on the measurement of slip length of the order of 5 nm with colloid probe atomic force microscopy, greatly improved the reliability and reproducibility of slip results.

In recent decades, studies of velocity slip on EHL problem have become increasingly important owing to their significant influence on lubrication performance. As early in 1990, Kaneta et al. [29] reported that the lubricant in EHL contacts can slipped at the contact interface. Ehret and Bauget [108] attributed the occurrence of the dimple in contact area to the velocity slip. They proposed a slip coefficient model [109], which the degree of slip is proportional to the pressure, to reproduce the observed dimple in experiments. Spikes et al. [110] developed a mathematically model in the presence of slip at solid surface. The slip is envisaged to occur when a critical shear stress is reached. Zhang et al. [111] incorporated the limiting shear stress into isothermal line contact. Load effects on lubricant flow, friction and so on were analyzed. Ståhl and Jacobson [112] concerned the lubricant velocities variation at the surfaces with a wall slip. As long as the value of the shear stress reaches the limiting shear stress, interfacial slip appeared, and the lubricant velocity differed from the surface velocity. Zhang and Wen [113] showed that the interfacial limiting shear stress directly caused a drastic film thickness reduction. Zhao et al. [114] evaluated the film thickness and friction for isothermal EHL point contact with a critical shear stress slip model. The film thickness under slip/no slip contact is higher than that under slip/slip contact. Zhang et al.[115,116] established a layered oil slip model considering the slip and thermal effect to explore the mechanism of film thickness behaviors. The results indicated that the interfacial slip may occur at both fast or/and slow surfaces depending on the speed conditions.

Another most common slip model in EHL is the Navier slip length model, shown in Fig. 1-6. Recent example in the application of the slip length model in EHL studies can be found in the works of Chu et al. [117], they derived an extended Reynolds equation

which includes the effects of Navier slip and flow rheology. Results showed that as the slip length increases, the film thickness decreases, the central pressure increases, the maximum pressure switches from the pressure spike to the central pressure, and the film shape and pressure profiles moves gradually toward the outlet. The point contact problem under isothermal EHL conditions was also studied by Chen et al. [118] in consideration of the anisotropic boundary slip, and found that the slip in the sliding direction was the dominant factor for lubrication film formation. Wang and Reddyhoff [119] have recently observed anomalous hat shaped films in 1-dodecanol EHL contacts under large slide-roll ratios. The anomalous film shapes were attributed to velocity slip at the central region where pressure exceeded a threshold value. Zhao et al [120,121] also investigated the coupled effects of slip length model and heat transfer on EHL contacts under large slide–roll ratio conditions. The velocity slip reduces temperature rise and promotes film thickness due to the positive effect of lubricant entrainment. However, if the magnitude of the boundary slip is excessively small, the lubricating film thickness may be reduced.

Some results of coating experiments have indicated that the slip may occur at the oleophobic surface. The principle of "half-wetted bearing", that consists of a nonwetted (oleophobic) surface with a fully wetted (oleophilic) surface, was proposed by Spikes [122,123]. Boundary slips occurred at oleophobic surface led to substantial reduction in friction. Later, Choo et al. [124,125] experimentally verified the "half wetted bearing" principle, and showed that simple Newtonian liquids can slip against very smooth, lyophobic surfaces. The effect of the fluorine and nitrogen-doped DLC coatings, which modified surface properties, such as surface energy and contact angle, on the tribological performance was reported by Kalin and Polajnor [126]. The DLC/steel contacts resulted in lower friction than the original steel/steel contact due to the boundary slips on DLC surface. Wong et al. [127,128] achieved an effective lubrication with very low surface velocity under ZEV contacts by using the velocity slip, where the lubricated contacts composed of an oleophobic and an oleophilic surfaces. Based on this experiment, a new type of retainerless rolling element bearings that enables to run in a wider speed range incorporates is devised.

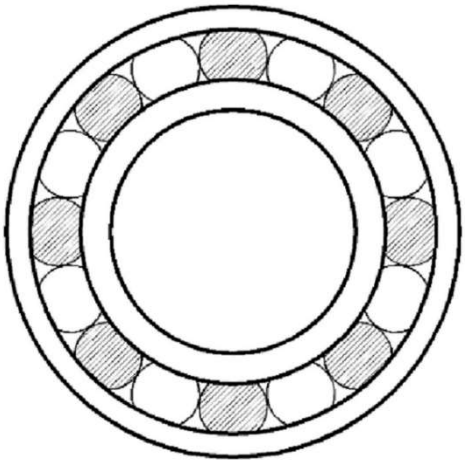

Figure 1-7 Novel design of alternate slip/nonslip retainerless rolling element bearing. [128]

Besides the applications in EHL, many studies on micro channel problems and molecular dynamic (MD) simulations have been conducted to further understand the mechanisms of velocity slips. Migler et al. [129] presented the first direct measurements of the local velocity of a sheared polymer melt. For high enough shear rates, a sharp transition between weak and strong slip in the case of weak polymer surface interactions was observed. In the experiments performed by Tretheway [130], the apparent velocity slip existed in a microchannel coated with a hydrophobic monolayer while the clean hydrophilic microchannel was under the no slip boundary condition. Jao et al. [131] studied the effect of anisotropy slip combined with roughness on the lubrication behavior of journal bearings. It was found that wall slip was easier to occur in the zones of high shear stress gradient and small film thickness. Zhu and Granick [132,133] measured the friction force in a hydrodynamic squeeze film using a surface force apparatus and found that the velocity slip depends on the flow rate and the surface wettability. Munch et al. [134] concluded that the velocity profile changed from parabolic to plug flow under very large the slip length condition. A combined surface radial sleeve bearing using the interfacial slip technique was discussed by Wang et al. [135], the velocity slip gives a large load support, but a low temperature rise in high speed and precise spindle systems. Cheng et al [136] solved the problem of slip occurring in the cavitation zone. They showed that slip effects in the cavitation region have an influence on the oil film pressure, the load capacity, the dynamic characteristics, and the stability of journal bearing.

Extensive molecular dynamics (MD) simulations have been reported for the investigation of the velocity slip problem. Thompson et al. [137,138] firstly used MD simulation for slip in a Lennard–Jones (L–J) fluid, showing that the slip length increases and begins to diverge as the shear rate approaches a critical value. Priezjev et al. [139] investigated the behavior of the slip length in thin polymer films subject to planar shear. The dynamical response of the slip length with increasing shear rate agreed well with a power law. Asproulis et al.[140] found that decreases in the surface stiffness lead to a small degree of velocity slip. Savio et al. [141], via MD simulations, showed that the occurrence of wall slip depends on the wall–fluid interactions and the chain length of the lubricant molecules. Later, they developed a novel nano to elastohydrodynamic lubrication (EHL) multiscale approach [142], to integrate lubrication performance with a ceramic–steel interface and a nanometric film thickness. They quantified the nanoscale slip variation with pressure, film thickness and sliding velocity by MD simulation, and applied it in modeling EHL for better understanding of film thickness and friction prediction.

1.2.2 Thermal resistance at solid–liquid interface

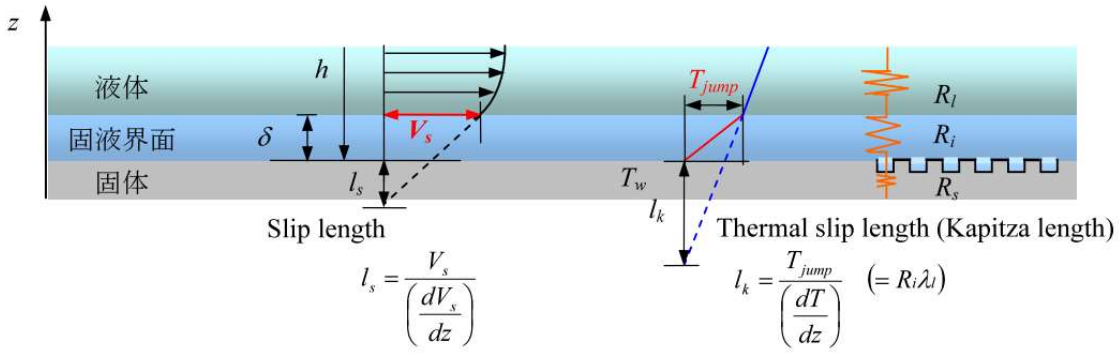

Figure 1-8 Schematic of boundary slips at solid–liquid interface. [144]

Thermal resistance (thermal slip) denotes the temperature jump phenomena at the boundary, and it occurs when the heat flows across the liquid–solid interface. Generally the thermal slip degree can be identified by thermal slip length, which is also called the Kapitza length [143,144], as shown in Fig. 1-8. The occurrence of thermal slip at interface restricts the heat dissipation between liquid and solid, altering the temperature

distributions of system. For this reason, it is of particular importance to be understand the fundamental behavior of the thermal slip. Historically, the studies of thermal slip at liquid–solid interfaces are mostly focused on molecular dynamics simulations.

Through the MD simulations, Kim et al [145,146] presented an interactive thermal wall model that can properly simulate the flow and heat transfer in nanoscale channels. As a result, temperature profiles exhibited jumps at the interface. The simulations presented by Voeltzel et al. [147] confirmed the presence of hydrodynamic and thermal slip in an ionic liquid confined between iron oxide surfaces under relatively high pressure and severe shearing of steel–steel lubricated contact. Barrat et al [143] determined the Kapitza length can reach appreciable values when the liquid does not wet the solid. Shenogina et al [148] also quantified the Kapitza conductance over a broad range of surface chemistries from hydrophobic to hydrophilic using molecular simulations. Nagayama et al [149] found that hydrodynamic boundary condition depends on both the interface wettability and the magnitude of the driving force. The wettability at interface affected the temperature and pressure profiles near the solid walls. Later. they estimated the scale effect of slip boundary at solid–liquid interface in microchannel [150]. As the hydraulic diameter D_h decreases, the effects of slip boundary on hydrodynamic resistance and convective heat transfer become great, shown in Fig. 1-9.

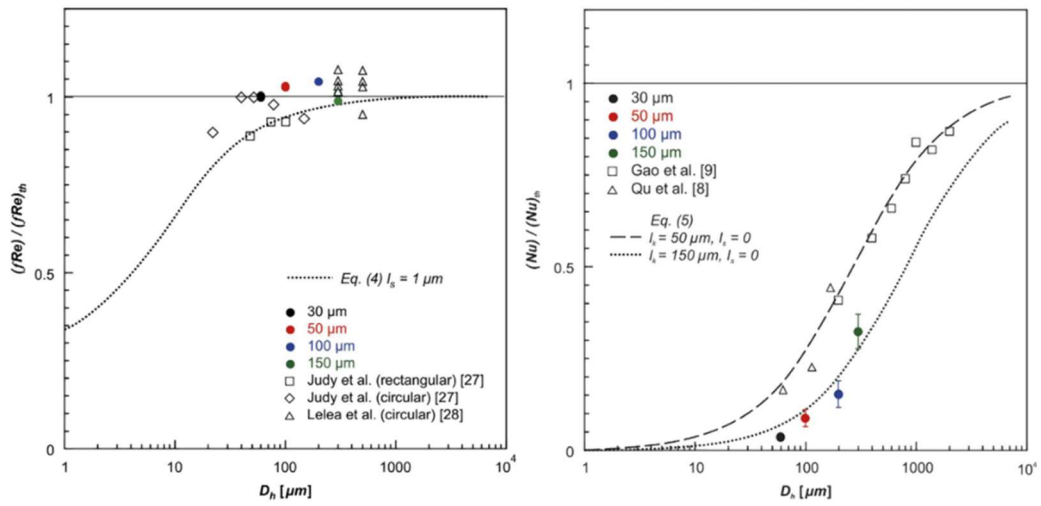

(a) (b)

Figure 1-9 Scale effect of (a) slip length on hydrodynamic resistance and (b) thermal slip length on convective heat transfer in microchannels. [150]

Table 1 Representative research results on boundary slips in EHL.

Year	Authors	Method/findings	Reference
Experimental studies			
1990	Kaneta et al.	Ball–disc under pure rolling and sliding contact / velocity slip at or near contact surfaces	[29]
2007	Fu et al.	Ball–disc under pure sliding contact with high viscosity polymeric lubricant / velocity slip induced inlet dimple in contact region	[151]
2009	Kalin et al.	DLC–DLC contacts / 20% friction reduction compared to steel-steel contact	[17]
2012	Guo et al.	Entrapped lubricant in ball–disc contact / slip length based on the dimple movement	[101–103]
2014	Ponjavic et al.	Glass–Fusso contact in PCS Instruments / central film thickness reduction of 50% due to velocity slip at Fusso coating surface	[152,153]
2017	Wang et al.	Ball–disc contact lubricated by 1-dodecanol / anomalous EHL film caused by velocity slip	[119]
2018	Wong et al.	ZEV contact with oleophobic coating / hydrodynamic lubrication film due to velocity slip at oleophobic surface	[127,128]
Theoretical analysis			
2000	Wen et al.	Isothermal line contact, viscoplastic rheological model / velocity slip occurred at the inlet zone	[154]
2003	Ståhl et al.	Line contact, limiting shear stress / central film thickness variations due to velocity slip	[112]
2012	Chu et al.	Line contact, Navier slip and flow rheology / correlation between slip length and film thickness	[117]
2016	Chen et al.	Circular contact, anisotropic slip / film thickness reduction due to slip length in sliding direction	[118]
2019	Zhao et al.	Point contact, SRR = 44, velocity slips at two surfaces / variations of temperature rise and film thickness	[120]
2020	Zhang et al.	Point contact, layered oil slip model / reduction of film thickness due to velocity slip and thermal effect	[115,116]

1.3 Outline of this thesis

In the elastohydrodynamic lubrication (EHL) regime, the no slip boundary condition is a common hypothesis, where both the velocity and temperature of the lubricant adjacent to the solid surface are the same as those of the solid surface. However, with the recent technical advances in interface sciences, the friction reduction induced by boundary slip at superlubricity surface has attracted academic interests with practical implications. Although boundary slip includes a velocity discontinuity and a temperature jump at the solid–lubricant interface, emphasis has been put on the velocity discontinuity (velocity slip) in the EHL regime.

Since less attention has been paid on the temperature jump (thermal slip) for EHL previously according to the literature review shown in Table 1, a thermal EHL theory under boundary slips in ball–disc point contact is proposed by taking both the velocity and thermal slips into consideration in this thesis. Numerical simulation based on the thermal EHL theory under boundary slips as well as the experiments have been conducted to clarify the EHL behavior at the solid–lubricant interfaces.

This thesis consists of 5 chapters and its outline is given below.

Chapter 1, Introduction describes the background of elastohydrodynamic lubrication and the literature survey of solid–liquid interfacial resistance.

Chapter 2, Theory of thermal elastohydrodynamic lubrication presents the proposed thermal EHL theory for the ball–disc point EHL contact problem. The boundary slips, i.e., velocity slip and thermal slip, were adopted to solid–lubricant interfaces. The modified Reynolds equation is derived, coupled with energy equations, to obtain the pressure, film thickness and temperature distributions in the contact area. Meanwhile, the numerical techniques for solving the pressure and temperature governing equations were explained. The proposed methodology provides an effective and convenient tool to investigate the effects of velocity and thermal slips on EHL performances under complex operating conditions.

Chapter 3, Numerical analysis of boundary slips for thermal point EHL contact described the numerical simulation results based on the thermal EHL theory. The simulation model of a ball–disc point contact is described and three kinds of motion, (1)

pure rolling motion, (2) opposite sliding motion and (3) rolling/sliding motion are analyzed. To distinguish the effects of boundary slips on EHL behaviors, three cases of boundary slips, velocity slip, thermal slip, and coupled velocity/thermal slips, were investigated. Under the pure rolling motion, the velocity slip leads to a general reduction in film thickness, while the thermal slip effect is negligible. Under the opposite sliding motion, the velocity slip causes the surface dimple shifting, while the thermal slip causes the surface dimple shifting in the opposite direction. The effect of velocity slip and that of thermal slip cancels out one another when the velocity slip length equals to thermal slip length. Under the rolling/sliding motion, velocity slip dominates the film thickness reduction when the slip length is comparable to the thermal slip length, whereas the effect of thermal slip on lubrication is more dominant than that of velocity slip while increasing entrainment velocity or slide-roll ratio. The coupled velocity/thermal slips case leads the most significant temperature rise and film thickness reduction among the three cases.

Chapter 4, Experimental study on lubrication with hydrophobic coating describes the experimental apparatus, procedures, sample preparation and the experimental results. The measured film thickness and friction coefficient at the surfaces with or without coating provide evidence of boundary slips at surface with hydrophobic coating. The friction reduction at the surface with hydrophobic coating gradually decreases while increase entrainment velocity or ambient temperature. Comparisons between numerical and experimental results has been drawn and further to be applied to estimate the velocity slip and thermal slip lengths quantitatively. The proposed method is challenging but beneficial for gaining a fundamental understanding of superlubrication.

Chapter 5 Conclusions and outlook summarizes the main findings of this thesis and the future works.

This study, for the first time, clarified the effect of thermal slip and the coupled effect of velocity/thermal slips on EHL behavior under point contact. The solid–lubricant interfacial resistance is one of the key parameters in EHL contact and thus is of particular importance for ensuring the lubrication performance to avoid lubrication breakdown or surface failure. These findings will provide useful insights into advanced surface and interface design of superlubricity, as well as promising prospects of energy saving, environmentally friendly lubrication and long-life machine operation in industrial applications.

Chapter 2

2. Theory of thermal elastohydrodynamic lubrication

2.1 Introduction

Thermal elastohydrodynamic lubrication (EHL) theory is the theory of EHL considering heat generation in the fluid film and heat transfer in the lubrication system. The main work of the establishment of a thermal EHL theory was to get numerical solutions under boundary slips conditions from a nonlinear mathematical model inclusive of the modified Reynolds equation for pressure, the energy equation of the fluid film, and the heat transfer equations of the bounding solids for temperature.

Recently, evidence of boundary slip in lubrication have been obtained experimentally [127,128] and theoretically [120,155,156], which differs from the classical no slip boundary condition. Based on the fundamental point of view, the boundary slips, i.e., velocity discontinuity [138,157] and temperature jump [144,158,159] at solid–lubricant interface, are of certain importance for ensuring the lubrication performance in EHL contact to avoid lubrication breakdown or surface failure. Although the effect of velocity slip on lubrication performance has been studied extensively, very little attentions are focus on the effect of thermal slip on temperature rise and film thickness.

In this chapter, a complete mathematical model for a point contact thermal EHL problem will be presented and discussed; meanwhile, the numerical technique for solving the pressure and temperature governing equations will be explained briefly. The boundary slip conditions are adopted at solid–lubricant interfaces. The presented theory provides an effective and convenient methodology to investigate the effects of velocity and thermal slips on performances of machine elements under complex operating conditions.

2.2 Governing equations

In this study, the elastohydrodynamic lubrication (EHL) contact is considered formed between a disc and a ball, and subject to an external applied load w. Fig. 2-1 shows the schematic of ball–disc contact, defined by the respective solids a and b with moving velocities of u_a and u_b. The origin of the EHL coordinate system is positioned at the center contact area, characterized by point o. The x axis is chosen to be in the same direction as that of the entrainment velocity, $u_e = (u_a + u_b)/2$; z axis is in the direction perpendicular to solids across the lubricant.

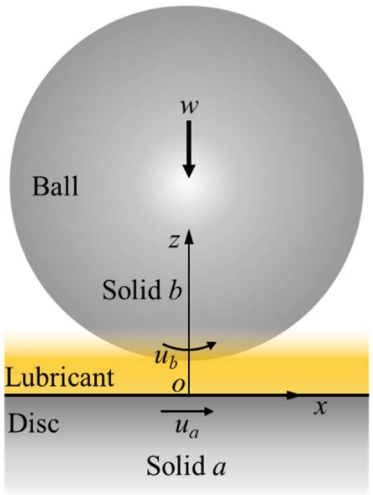

Figure 2-1 Schematics diagram of ball-disc contact.

2.2.1 Modified Reynolds equation

Interfacial resistance

Previous studies generally adopt the no slip boundary conditions [160–162], which states the continuum of velocity and temperature at solid–lubricant interfaces. However, interfacial resistances (boundary slips) have drawn considerable interest in EHL. The current study adopts the Navier slip length model [93], because its universality and agrees well with experimental results [117,118,157].

Boundary slip conditions are employed for both the solids *a* and *b*, as illustrated in Fig. 2-2. The slip length l_s is the distance beyond the solid–lubricant interface at which the lubricant velocity linearly extrapolates to zero, related to the velocity gradient and slip velocity by the expression. Analogously, the thermal slip length l_k is introduced to quantify the temperature jump, which is defined by the linear extrapolation of the lubricant temperature profile to the continuum boundary [144,150,159].

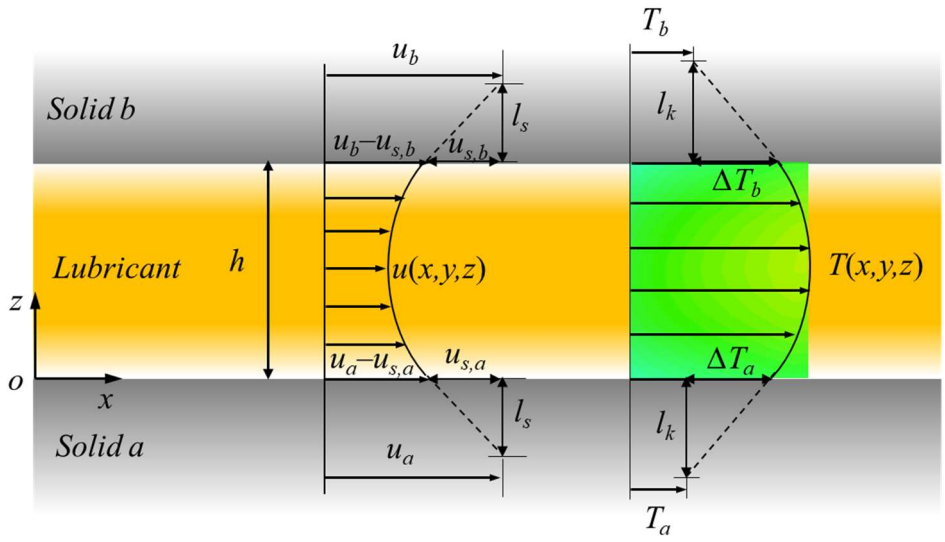

Figure 2-2 Boundary slips at surfaces of moving solids: velocity slip (left) and thermal slip (right).

With the slip boundary conditions at solid–lubricant interfaces, the lubricant velocity and temperature are expressed as

$$\begin{cases} u_{z=0} = u_a - l_s \left.\dfrac{\partial u}{\partial z}\right|_{z=0} \\ u_{z=h} = u_b + l_s \left.\dfrac{\partial u}{\partial z}\right|_{z=h} \end{cases} \tag{2-1}$$

$$\begin{cases} T_{z=0} = T_a + l_k \left.\dfrac{\partial T}{\partial z}\right|_{z=0} \\ T_{z=h} = T_b + l_k \left.\dfrac{\partial T}{\partial z}\right|_{z=h} \end{cases} \tag{2-2}$$

Reynolds equation

Reynolds equation is the foundation for most EHL simulation and follows the assumptions of laminar lubricant flow and variable density and viscosity of lubricant in x, y, z directions. Through the force equilibrium analysis of the fluid elements, we obtain:

$$\begin{cases} \dfrac{\partial p}{\partial x} = \dfrac{\partial \tau_x}{\partial z} \\ \dfrac{\partial p}{\partial y} = \dfrac{\partial \tau_y}{\partial z} \end{cases} \tag{2-3}$$

where p is the film pressure, τ_x and τ_y are the shear stress components of x and y directions in contact.

The general form of constitutive for commonly used rheological models in EHL is expressed as:

$$\begin{cases} \dfrac{\partial u}{\partial z} = f_x(\tau_x, \tau_y, \eta) \\ \dfrac{\partial v}{\partial z} = f_y(\tau_x, \tau_y, \eta) \end{cases} \tag{2-4}$$

where u and v are lubricant velocity in x and y directions, η is lubricant viscosity, $f(\tau_x, \tau_y, \eta)$ is a general rheological relationship for lubricant flow.

The equivalent viscosity in x and y directions is defined:

$$\begin{cases} \eta_x^* = \dfrac{\tau_x}{f_x(\tau_x, \tau_y, \eta)} \\ \eta_y^* = \dfrac{\tau_y}{f_y(\tau_x, \tau_y, \eta)} \end{cases} \tag{2-5}$$

Combining the Eqs. (2-3)–(2-5), the shear stress equilibrium equations in lubricant film can be written:

$$\begin{cases} \dfrac{\partial}{\partial z}(\eta_x^* \dfrac{\partial u}{\partial z}) = \dfrac{\partial p}{\partial x} \\ \dfrac{\partial}{\partial z}(\eta_y^* \dfrac{\partial v}{\partial z}) = \dfrac{\partial p}{\partial y} \end{cases} \tag{2-6}$$

Integrating the Eq. (2-6) twice with respect to z, and using the velocity slip boundary

condition in Eq. (2-1), the lubricant velocity can be obtained as follows:

$$\begin{cases} u = u_a + \dfrac{\partial p}{\partial x}\left[\displaystyle\int_0^z \frac{z}{\eta}dz - \frac{h^2\eta_{z=h}\left(\eta_e/\eta_e'\right) - hl_s\eta_e}{A\eta_{z=h} - l_s\eta_e\eta_{z=0}}\left(l_s + \eta_{z=0}\int_0^z \frac{1}{\eta}dz\right)\right] \\ \qquad + \left(u_b - u_a\right)\dfrac{\eta_e\eta_{z=h}}{A\eta_{z=h} - l_s\eta_e\eta_{z=0}}\left(l_s + \eta_{z=0}\displaystyle\int_0^z \frac{1}{\eta}dz\right) \\ v = \dfrac{\partial p}{\partial y}\left(\displaystyle\int_0^z \frac{z}{\eta}dz - h\frac{\eta_e}{\eta_e'}\int_0^z \frac{1}{\eta}dz\right) \end{cases} \tag{2-7}$$

The conservation equation of mass flow is

$$\frac{\partial(\rho u)}{\partial x} + \frac{\partial(\rho v)}{\partial y} = 0 \tag{2-8}$$

Substituting the lubricant velocity Eq. (2-7) into the conservation equation Eq. (2-8). we can obtain the modified Reynolds equation with the consideration of boundary slips:

$$\frac{\partial}{\partial x}\left[\left(\frac{\rho}{\eta}\right)_{es} h^3\frac{\partial p}{\partial x}\right] + \frac{\partial}{\partial x}\left[\left(\frac{\rho}{\eta}\right)_{e} h^3\frac{\partial p}{\partial x}\right] + \frac{\partial}{\partial y}\left[\left(\frac{\rho}{\eta}\right)_{e} h^3\frac{\partial p}{\partial y}\right] = 6\left(u_a + u_b\right)\frac{\partial \rho^* h}{\partial x} \tag{2-9}$$

where

$$\left(\frac{\rho}{\eta}\right)_{es} = 12\left[l_s\frac{\rho_e}{A}\frac{\eta_e}{\eta_e'} + \left(\frac{h}{A}\eta_{z=0} - 1\right)\frac{\eta_e}{\eta_e'}\rho_e'\right],\ \left(\frac{\rho}{\eta}\right)_{e} = 12\left(\frac{\eta_e}{\eta_e'}\rho_e' - \rho_e''\right),$$

$$A = h\eta_{z=0} + l_s\eta_e,\ \ \eta_e = h\Big/\int_0^h \frac{1}{\eta}dz,\ \ \eta_e' = h^2\Big/\int_0^h \frac{z}{\eta}dz,$$

$$\rho_e = h^{-1}\int_0^h \rho dz,\ \ \rho_e' = h^{-2}\int_0^h \rho\int_0^z \frac{1}{\eta}dz'dz,\ \ \rho_e'' = h^{-3}\int_0^h \rho\int_0^z \frac{z'}{\eta}dz'dz,$$

$$\rho^* = \frac{2}{u_a + u_b}\left[u_a\rho_e - \left(u_a - u_b\right)\eta_e\rho_e'\rho_{es}\right],\ \ \rho_{es} = \frac{1}{A}\left(l_s\frac{\rho_e}{\rho_e'} + h\eta_{z=0}\right).$$

In Eq. (2-9), $(\rho/\eta)_{es}$ and ρ_{es} are the slip parameters. Under no slip boundary condition ($l_s = 0$), the slip parameters $(\rho/\eta)_{es} = 0$, and $\rho_{es} = 1$, the Eq. (2-9) coincides with the classical Reynolds equation [164].

As film pressure boundary condition, the zero pressure at the inlet and outlet of the contact area is used:

$$\begin{cases} p = 0, \text{ at } x = x_{in} = x_{out}, y = y_{out} \\ p \geq 0, \text{ at } x_{in} \leq x \leq x_{out}, -y_{out} \leq y \leq y_{out} \end{cases} \tag{2-10}$$

where x_{in}, and x_{out}, y_{out} represent the start and end of the calculation domain, respectively.

Load

Under EHL contact, the load should be same as the film pressure generated in lubricant. The load balance equation ensures the equilibrium between the applied load and the hydrodynamic film pressure in contact area.

$$w = \iint_{\Omega} p(x, y) dx dy \tag{2-11}$$

where Ω represents the entire calculation domain.

Density and viscosity of lubricant

Density and viscosity of lubricant are very important for the predications of friction, temperature rise, and film thickness in EHL contact. Due to the high film pressure and temperature rise in contact area, the variation of the density and viscosity of lubricant is significant. Therefore, the present study applied Dowson and Higginson model [165] to estimate the lubricant density.

$$\rho = \rho_0 \left[1 + \frac{0.6 \times 10^{-9} p}{1 + 1.7 \times 10^{-9} p} - 0.00065 \left(T - T_0 \right) \right] \tag{2-12}$$

where ρ_0 is lubricant density at $p = p_0$ and $T = T_0$.

The viscosity-pressure-temperature relationship is determined using the Roelands equation [166]:

$$\eta = \eta_0 \exp \left\{ \left(\ln \left(\eta_0 \right) + 9.67 \right) \times \left[-1 + \left(1 + 5.1 \times 10^{-9} p \right)^{Z_0} \left(\frac{T - 138}{T_0 - 138} \right)^{-S_0} \right] \right\} \tag{2-13}$$

where ρ_0 is lubricant density at $p = p_0$ and $T = T_0$. Z_0 is the pressure–viscosity index, and S_0 is the temperature–viscosity index, which are calculated according to the following expressions:

$$\begin{cases} Z_0 = \dfrac{\alpha}{5.1\times10^{-9}\left[\ln\left(\eta_0\right)+9.67\right]} \\ S_0 = \dfrac{\beta(T_0-138)}{\ln\left(\eta_0\right)+9.67} \end{cases} \tag{2-14}$$

In above expressions, α and β are the index in Roeland's equation, measured as $\alpha = 2.4 \times 10^{-8}$ m^2/N, and $\beta = 4.6 \times 10^{-2}$ 1/K.

Film thickness

The lubricant film thickness is the combination of the spacing between the rigid solids h_0, geometry of contact surfaces, and the deformations of solids. It is written as:

$$h\left(x,y\right) = h_{00} + \frac{x^2}{2R} + \frac{y^2}{2R} + \frac{2}{\pi E'}\iint \frac{p\left(x',y'\right)}{\sqrt{\left(x-x'\right)^2+\left(y-y'\right)^2}}dx'dy' \tag{2-15}$$

where R is the radius of ball (solid b), E' is the equivalent elastic modulus, relating to the elastic modulus E_a, E_b, and the Poisson's ratios υ_a, υ_b of two contact solids.

$$\frac{1}{E'} = \frac{1}{2}\left(\frac{1-\upsilon_a^2}{E_a} + \frac{1-\upsilon_b^2}{E_b}\right) \tag{2-16}$$

2.2.2 Energy equation

Thermal effect is considered in this study. To resolve the local temperature, the full energy equations within the lubricant film and solids are described. The heat generated in contact from the shearing and compression of the lubricant, then is dissipated through and transported by the lubricant and contacting solids.

Within the lubricant film, the energy equation [167] is expressed as:

$$\begin{aligned} c\left(\rho u\frac{\partial T}{\partial x} + \rho v\frac{\partial T}{\partial y} - q\frac{\partial T}{\partial z}\right) - k\frac{\partial^2 T}{\partial z^2} \\ = -\frac{T}{\rho}\frac{\partial \rho}{\partial T}\left(u\frac{\partial p}{\partial x} + v\frac{\partial p}{\partial y}\right) + \eta\left[\left(\frac{\partial u}{\partial z}\right)^2 + \left(\frac{\partial v}{\partial z}\right)^2\right] \end{aligned} \tag{2-17}$$

where

$$q = \frac{\partial}{\partial x}\int_0^z \rho u dz' + \frac{\partial}{\partial y}\int_0^z \rho v dz'$$

The four terms in Eq. (2-17) from left to right represent: heat convection, heat conduction, heat generated due to compression and shearing of lubricant, respectively. The expressions of u and v are presented at Eq. (2-7). Eq. (2-17) requires the following boundary conditions:

$$\begin{cases} T\left(x = x_{in}\right) = T_0, \;\; u\left(x_{in}, y, z\right) \geq 0 \\ T\left(x = x_{out}\right) = T_0, \;\; u\left(x_{out}, y, z\right) \geq 0 \end{cases} \tag{2-18}$$

Within the solids, no compression and shearing are present, the energy equation for solids are written as:

$$\begin{cases} c_a \rho_a u_a \dfrac{\partial T}{\partial x} = k_a \left(\dfrac{\partial^2 T}{\partial z_a^2} + \dfrac{\partial^2 T}{\partial x^2} + \dfrac{\partial^2 T}{\partial y^2} \right) \\ c_b \rho_b u_b \dfrac{\partial T}{\partial x} = k_b \left(\dfrac{\partial^2 T}{\partial z_a^2} + \dfrac{\partial^2 T}{\partial x^2} + \dfrac{\partial^2 T}{\partial y^2} \right) \end{cases} \tag{2-19}$$

In Eq. (2-19), the terms in the left hand of equation describes the energy transport phenomena due to the movement of solids in x direction, which is indispensable for the heat diffusion in the solids. The terms in the right hand of equations represents the heat conduction in x, y, z directions. The boundary conditions required are as follows:

$$\begin{cases} T\left(x = x_{in}, y, z\right) = T_0 \\ T\left(x, y, z_a = -d\right) = T_0 \\ T\left(x, y, z_b = d\right) = T_0 \end{cases} \tag{2-20}$$

At the solid–lubricant interface, the following continuity equations of heat flux are applied as boundary conditions:

$$\begin{cases} k \left.\dfrac{\partial T}{\partial z}\right|_{z=h} = k_b \left.\dfrac{\partial T}{\partial z_b}\right|_{z_b=0} \\ k \left.\dfrac{\partial T}{\partial z}\right|_{z=0} = k_a \left.\dfrac{\partial T}{\partial z_a}\right|_{z_a=0} \end{cases} \tag{2-21}$$

2.3 Dimensionless equations

In the present study, all the above governing equations and their boundary conditions are transformed into dimensionless forms to facilitate programing and calculation. The following dimensionless quantities are introduced.

$$P=\frac{p}{p_H},\ W=\frac{w}{E'R^2},\ G=\alpha E',\ \bar{T}=\frac{T}{T_0},\ U_0=\frac{u_0\eta_0}{E'R},\ U_{a,b}=\frac{u_{a,b}}{u_0}$$

$$U=\frac{u}{u_0},\ X=\frac{x}{a},\ Y=\frac{y}{a},\ Z=\frac{z}{h},\ Z_{a,b}=\frac{z_{a,b}}{a},\ \bar{d}=\frac{d}{a},\ h_0=\frac{a^2}{R},$$

$$H=\frac{h}{h_0},\ \bar{\eta}=\frac{\eta}{\eta_0},\ \bar{\rho}=\frac{\rho}{\rho_0},\ l_{\mathrm{s}}^*=\frac{l_{\mathrm{s}}}{h_0},\ l_{\mathrm{k}}^*=\frac{l_{\mathrm{k}}}{h_0}.$$

where u_0 is a reference velocity for simplify of calculation. Under rolling/sliding contact, the u_0 equals to the entrainment velocity u_e, while under ZEV contact, the value of u_0 has no effect on solution.

Using the above dimensionless parameters, the non-dimensionally Reynolds equation is written as:

$$\frac{\partial}{\partial X}\left(\varepsilon_{es}\frac{\partial P}{\partial X}\right)+\frac{\partial}{\partial X}\left(\varepsilon\frac{\partial P}{\partial X}\right)+\frac{\partial}{\partial Y}\left(\varepsilon\frac{\partial P}{\partial Y}\right)=\frac{\partial}{\partial X}\left(\bar{\rho}^*H\right) \tag{2-22}$$

where

$$\varepsilon_{es}=\left(\frac{\bar{\rho}}{\bar{\eta}}\right)_{es}\bar{h}^3\Big/\lambda,\ \varepsilon=\left(\frac{\bar{\rho}}{\bar{\eta}}\right)_{e}\bar{h}^3\Big/\lambda,\ \lambda=12\pi U_e\varphi^{1/3}k_e^{4/3}\left(\frac{2}{3W}\right)^{4/3},$$

$$\left(\frac{\bar{\rho}}{\bar{\eta}}\right)_{es}=12\left[l_s^*\frac{\bar{\rho}_e}{\bar{A}}\frac{\bar{\eta}_e}{\bar{\eta}_e'}+\left(\frac{H}{\bar{A}}\bar{\eta}_{z=0}-1\right)\frac{\bar{\eta}_e}{\bar{\eta}_e'}\bar{\rho}_e'\right],\ \left(\frac{\bar{\rho}}{\bar{\eta}}\right)_{e}=12\left[\bar{\rho}_e\frac{\overline{\eta_e}}{\overline{\eta_e'}}-\bar{\rho}_e''\right],$$

$$\bar{A}=H\bar{\eta}_{z=0}+l_s^*\bar{\eta}_e,\ \bar{\eta}_e=1\Big/\int_0^1\frac{1}{\bar{\eta}}dZ,\ \bar{\eta}_e'=1\Big/\int_0^1\frac{Z}{\bar{\eta}}dZ,$$

$$\bar{\rho}_e=\int_0^1\bar{\rho}dZ,\ \bar{\rho}_e'=\int_0^1\bar{\rho}\int_0^Z\frac{1}{\bar{\eta}}dZ'dZ,\ \bar{\rho}_e''=\int_0^1\bar{\rho}\int_0^Z\frac{Z'}{\bar{\eta}}dZ'dZ,$$

$$\bar{\rho}^*=\frac{2}{U_a+U_b}\left[U_a\bar{\rho}_e-\left(U_a-U_b\right)\bar{\eta}_e\bar{\rho}_e'\bar{\rho}_{es}\right],\ \bar{\rho}_{es}=\frac{1}{\bar{A}}\left(l_s^*\frac{\bar{\rho}_e}{\bar{\rho}_e'}+H\bar{\eta}_{z=0}\right).$$

Dimensionless pressure boundary conditions are

$$\begin{cases} P = 0, \text{ at } \mathrm{X} = X_{in} = X_{out}, Y = Y_{out} \\ P \geq 0, \text{ at } \mathrm{X}_{in} \leq X \leq X_{out}, -Y_{out} \leq Y \leq Y_{out} \end{cases} \tag{2-23}$$

The non-dimensional load balance equation is

$$\frac{2\pi}{3} = \iint_{\Omega} P(X,Y)dXdY \tag{2-24}$$

The dimensionless density-pressure-temperature relationship is written as

$$\overline{\rho} = 1 + \frac{C_1 p_H P}{1 + C_2 p_H P} - C_3\left(\overline{T} - 1\right) \tag{2-25}$$

Dimensionless viscosity-pressure-temperature relationship is written as

$$\overline{\eta} = \exp\left\{A_1\left[-1 + \left(1 + A_2 P\right)^{Z_0}\left(A_3\overline{T} - A_4\right)^{-S_0}\right]\right\} \tag{2-26}$$

where

$$C_1 = 0.6\times10^{-9},\ \ C_2 = 1.7\times10^{-9},\ \ C_3 = 0.00065T_0,$$

$$A_1 = \ln\left(\eta_0\right) + 9.67,\ \ A_2 = 1 + 5.1\times10^{-9}\, p_H,$$

$$A_3 = \frac{T_0}{T_0 - 138},\ \ A_4 = \frac{138}{T_0 - 138}.$$

Dimensionless film thickness equation is expressed as:

$$H\left(X,Y\right) = H_{00} + \frac{X^2 + Y^2}{2} + \frac{2\varphi}{\pi^2}\iint \frac{P\left(X',Y'\right)}{\sqrt{\left(X - X'\right)^2 + \left(Y - Y'\right)^2}}dX'dY' \tag{2-27}$$

where φ = 1 under point contact.

The dimensionless energy equation within the lubricant film is

$$\begin{aligned} CS_1\left(\overline{\rho}U\frac{\partial\overline{T}}{\partial X} + \overline{\rho}V\frac{\partial\overline{T}}{\partial Y} - \frac{\overline{q}}{H}\frac{\partial\overline{T}}{\partial Z}\right) - \frac{1}{H^2}\frac{\partial^2\overline{T}}{\partial Z^2} \\ = CS_2\frac{\overline{T}}{\overline{\rho}}\left(U\frac{\partial P}{\partial X} + V\frac{\partial P}{\partial Y}\right) + CS_3\frac{\overline{\eta}}{H^2}\left[\left(\frac{\partial U}{\partial Z}\right)^2 + \left(\frac{\partial V}{\partial Z}\right)^2\right] \end{aligned} \tag{2-28}$$

where

$$CS_1 = \mathrm{Pr}\cdot \mathrm{Re}^*,\ \ CS_2 = C_3\cdot \mathrm{Ec}\cdot \mathrm{Yt}\left(\frac{h_0}{a}\right)^2,\ \ CS_3 = \frac{u_0^2\eta_0}{kT_0},$$

$$\mathrm{Pr} = \frac{c\eta_0}{k},\ \ \mathrm{Re} = \frac{\rho_0 u_0 a}{\eta_0},\ \ \mathrm{Re}^* = \mathrm{Re}\left(\frac{h_0}{a}\right)^2,\ \ \mathrm{Ec} = \frac{u_0^2}{cT_0},\ \ \mathrm{Yt} = \frac{cap_H}{u_0 k},$$

$$\overline{q} = \frac{\partial}{\partial X}\left(H\int_0^Z \overline{\rho}U dZ'\right) + \frac{\partial}{\partial Y}\left(H\int_0^Z \overline{\rho}V dZ'\right).$$

In Eq. (2-28), the dimensionless lubricant velocities are

$$\begin{cases} U = U_a + CV\dfrac{\partial P}{\partial X}\left[\displaystyle\int_0^1 \frac{Z}{\overline{\eta}}dZ - \frac{H^2\overline{\eta}_{z=h}\left(\overline{\eta}_e/\overline{\eta}'_e\right) - Hl_s^*\overline{\eta}_e}{\overline{A}\overline{\eta}_{z=h} - l_s^*\overline{\eta}_e\overline{\eta}_{z=0}}\left(l_s^* + \overline{\eta}_{z=0}\displaystyle\int_0^1 \frac{1}{\overline{\eta}}dZ\right)\right] \\ \qquad + \left(U_b - U_a\right)\dfrac{\overline{\eta}_e\overline{\eta}_{z=h}}{\overline{A}\overline{\eta}_{z=h} - l_s^*\overline{\eta}_e\overline{\eta}_{z=0}}\left(l_s^* + \overline{\eta}_{z=0}\displaystyle\int_0^1 \frac{1}{\overline{\eta}}dZ\right) \\ v = CV\dfrac{\partial P}{\partial Y}\left(\displaystyle\int_0^1 \frac{Z}{\overline{\eta}}dZ - H\frac{\overline{\eta}_e}{\overline{\eta}'_e}\int_0^1 \frac{1}{\overline{\eta}}dZ\right) \end{cases} \tag{2-29}$$

where

$$CV = \frac{p_H a^3}{u_0\eta_0 R^2}$$

The boundary conditions for energy equation of lubricant are dimensionalized as:

$$\begin{cases} \overline{T}\left(X = X_{in}\right) = 1,\ \ U\left(X_{in}, Y, Z\right) \ge 0 \\ \overline{T}\left(X = X_{out}\right) = 1\ ,\ \ U\left(X_{out}, Y, Z\right) \ge 0 \end{cases} \tag{2-30}$$

The energy equations for solids are dimensionalized as:

$$\begin{cases} CNA\cdot U_a\dfrac{\partial \overline{T}}{\partial X} = \dfrac{\partial^2\overline{T}}{\partial Z_a^2} + \dfrac{\partial^2\overline{T}}{\partial X^2} + \dfrac{\partial^2\overline{T}}{\partial Y^2} \\ CNB\cdot U_b\dfrac{\partial \overline{T}}{\partial X} = \dfrac{\partial^2\overline{T}}{\partial Z_b^2} + \dfrac{\partial^2\overline{T}}{\partial X^2} + \dfrac{\partial^2\overline{T}}{\partial Y^2} \end{cases} \tag{2-31}$$

where

$$CNA = \frac{c_a\rho_a u_0 a}{k_a},\ \ CNB = \frac{c_b\rho_b u_0 a}{k_b}.$$

Dimensionless boundary conditions of Eq. (2-31) are required as follows:

$$\begin{cases} \bar{T}\left(X = X_{in}, Y, Z\right) = 1 \\ \bar{T}\left(X, Y, Z_a = -\bar{d}\right) = 1 \\ T\left(X, Y, Z_b = \bar{d}\right) = 1 \end{cases} \tag{2-32}$$

The heat flux continues at the solid–lubricant interfaces are:

$$\begin{cases} CMB \cdot \dfrac{1}{H} \dfrac{\partial \bar{T}}{\partial Z}\bigg|_{Z=1} = \dfrac{\partial \bar{T}}{\partial Z_b}\bigg|_{Z_b=0} \\ CMA \cdot \dfrac{1}{H} \dfrac{\partial \bar{T}}{\partial Z}\bigg|_{Z=0} = \dfrac{\partial \bar{T}}{\partial Z_a}\bigg|_{Z_a=0} \end{cases} \tag{2-33}$$

where

$$CMA = \frac{ka}{k_a h_0}, CMB = \frac{ka}{k_b h_0}.$$

2.4 Dispersion of equations

The dimensionless equations are discretized for calculation in the computational domain, shown in Fig. 2-3. The origin of the EHL coordinate system is positioned at the center contact area, characterized by point *o*. Five grid levels with 256 nodes along the *x* and *y* directions at the finest grid level were applied in the calculation domain $-5a \le x \le 5a$, $-5a \le y \le 5a$. In the *z* direction, eleven nodes were used in the film, and six non-equidistant nodes were adopted in each solid of $d = 5a$ in thickness.

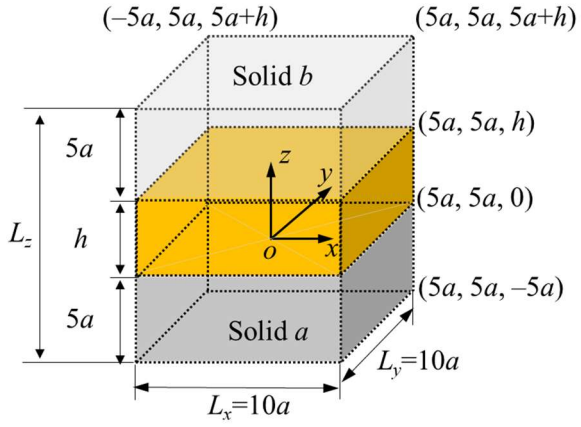

Figure 2-3 Dimensionless computational domain (not to scale).

Reynolds equations

In the process of Reynolds equations discretization, the terms $\frac{\partial}{\partial X}\left(\varepsilon_{es}\frac{\partial P}{\partial X}\right)$, $\frac{\partial}{\partial X}\left(\varepsilon\frac{\partial P}{\partial X}\right)$ and $\frac{\partial}{\partial Y}\left(\varepsilon\frac{\partial P}{\partial Y}\right)$ at the left hand of Eq. (2-22) are discretized using central difference operators, while the right term $\frac{\partial}{\partial X}\left(\overline{\rho}^{*}H\right)$ adopt the backward difference operators.

$$\begin{aligned}&\frac{1}{\left(\Delta X\right)^{2}}\left[\varepsilon_{es\ i-1/2,j}P_{i-1,j}-\left(\varepsilon_{es\ i-1/2,j}+\varepsilon_{es\ i+1/2,j}\right)P_{i,j}+\varepsilon_{es\ i+1/2,j}P_{i+1,j}\right]\\&+\frac{1}{\left(\Delta X\right)^{2}}\left[\varepsilon_{i-1/2,j}P_{i-1,j}-\left(\varepsilon_{i-1/2,j}+\varepsilon_{i+1/2,j}\right)P_{i,j}+\varepsilon_{i+1/2,j}P_{i+1,j}\right]\\&+\frac{1}{\left(\Delta Y\right)^{2}}\left[\varepsilon_{i,j-1/2}P_{i,j-1}-\left(\varepsilon_{i,j-1/2}+\varepsilon_{i,j+1/2}\right)P_{i,j}+\varepsilon_{i,j+1/2}P_{i,j+1}\right]\\&-\frac{1}{\Delta X}\left[\left(\overline{\rho}^{*}H\right)_{i,j}-\left(\overline{\rho}^{*}H\right)_{i-1,j}\right]=0\end{aligned}\tag{2-34}$$

where *i* and *j* stands for the node number in X and Y directions, respectively.

$$\varepsilon_{es\ i-1/2,j}=\frac{1}{2}\left(\varepsilon_{es\ i-1,j}+\varepsilon_{es\ i,j}\right),\quad \varepsilon_{es\ i+1/2,j}=\frac{1}{2}\left(\varepsilon_{es\ i+1,j}+\varepsilon_{es\ i,j}\right),$$

$$\varepsilon_{i-1/2,j}=\frac{1}{2}\left(\varepsilon_{i-1,j}+\varepsilon_{i,j}\right),\quad \varepsilon_{i+1/2,j}=\frac{1}{2}\left(\varepsilon_{i+1,j}+\varepsilon_{i,j}\right).$$

Load

To ensure the accuracy of solution, the load equation employed the nine-point Simpson method for discretization.

$$\begin{aligned}&\frac{1}{9}\Delta X\Delta Y\sum_{i=0}^{n_X/2-1}\sum_{j=0}^{n_Y/2-1}\left[16P_{2i+1,2j+1}+4\left(P_{2i+1,2j}+P_{2i+1,2j+2}+P_{2i,2j+1}+P_{2i+2,2j+1}\right)\right.\\&\left.+\left(P_{2i,2j}+P_{2i+2,2j}+P_{2i+2,2j+2}+P_{2i,2j+2}\right)\right]=\frac{2}{3}\pi\end{aligned}\tag{2-35}$$

Lubricant density and viscosity

The discretization of density-pressure-temperature relationship and viscosity-pressure-temperature relationship can be obtained based on the Eqs. (2-25) and (2-26).

$$\bar{\rho}_{i,j,k} = 1 + \frac{C_1 p_H P_{i,j}}{1 + C_2 p_H P_{i,j}} - C_3 \left(\bar{T}_{i,j,k} - 1 \right) \tag{2-36}$$

$$\bar{\eta}_{i,j,k} = \exp\left\{ A_1 \left[-1 + \left(1 + A_2 P_{i,j} \right)^{Z_0} \left(A_3 \bar{T}_{i,j,k} - A_4 \right)^{-S_0} \right] \right\} \tag{2-37}$$

Film thickness

For the elastic deformation term of the film thickness equation, the zero-order polynomial is used to approximate the pressure distribution. Therefore, the discretization of the film thickness equation can be obtained as follows:

$$H\left(X_i, Y_j \right) = H_{00} + \frac{X_i^{\,2} + Y_j^{\,2}}{2} + \frac{2\varphi}{\pi^2} \sum_{k=0}^{n_X} \sum_{l=0}^{n_Y} K_{ij,kl} P_{k,l} \tag{2-38}$$

where $\left(K_{ij,kl} \right)$ is four-dimensional array, named as the deformation matrix:

$$K_{ij,kl} = E_1 + E_2 + E_3 + E_4 ,$$

$$\Gamma_1 = \left(k - i + \frac{1}{2} \right) \Delta X , \quad \Gamma_2 = \left(k - i - \frac{1}{2} \right) \Delta X ,$$

$$\Psi_1 = \left(l - j + \frac{1}{2} \right) \Delta Y , \quad \Psi_2 = \left(l - j - \frac{1}{2} \right) \Delta Y ,$$

$$E_1 = \Psi_1 \ln \frac{\Gamma_1 + \sqrt{\Gamma_1^2 + \Psi_1^2}}{\Gamma_2 + \sqrt{\Gamma_2^2 + \Psi_1^2}} , \quad E_2 = \Psi_2 \ln \frac{\Gamma_2 + \sqrt{\Gamma_2^2 + \Psi_2^2}}{\Gamma_1 + \sqrt{\Gamma_1^2 + \Psi_2^2}} ,$$

$$E_3 = \Gamma_1 \ln \frac{\Psi_1 + \sqrt{\Gamma_1^2 + \Psi_1^2}}{\Psi_2 + \sqrt{\Gamma_1^2 + \Psi_2^2}} , \quad E_4 = \Gamma_2 \ln \frac{\Psi_2 + \sqrt{\Gamma_2^2 + \Psi_2^2}}{\Psi_1 + \sqrt{\Gamma_2^2 + \Psi_1^2}} .$$

Energy equations

The temperature distributions are obtained by solving discretized energy equations of lubricant and solids in the calculation domain. Fig. 2-4 shows the grid structure in the *Z* direction. Within the lubricant film, 11 equidistant nodes were adopted and 6 non-equidistant nodes in the each solid because the temperature variation in solids is less pronounced than that in lubricant. The thickness of solids is set to 5*a*, different from the common value of 3.15*a* [90,92,120]. At the nodes far form lubricant, the temperature tends to be ambient temperature.

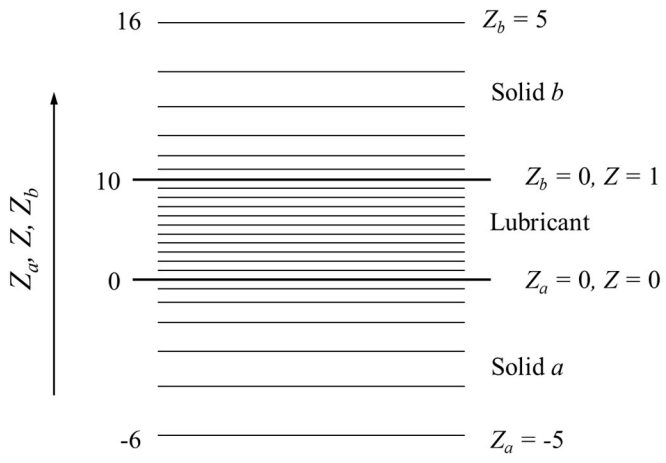

Figure 2-4 Grid structure in the Z direction.

In the process of energy equation discretization, the subscript k denotes the node number in the Z direction. The node number of k = -6 and k = 16 stand the boundaries of solids, where $T = T_0$. Note that the different node number employed different difference operators as shown follows.

$$\left(\frac{\partial^2 \overline{T}}{\partial Z_a^2}\right)_{i,j,k} = A_{k,k-1}\overline{T}_{i,j,k-1} + A_{k,k}\overline{T}_{i,j,k} + A_{k,k+1}\overline{T}_{i,j,k+1} \quad (k = -5 \sim -1) \tag{2-39}$$

$$\left(\frac{\partial^2 \overline{T}}{\partial Z_b^2}\right)_{i,j,k} = B_{k,k-1}\overline{T}_{i,j,k-1} + B_{k,k}\overline{T}_{i,j,k} + B_{k,k+1}\overline{T}_{i,j,k+1} \quad (k = 11 \sim 15) \tag{2-40}$$

$$\left(\frac{\partial^2 \overline{T}}{\partial Z^2}\right)_{i,j,k} = \left(\overline{T}_{i,j,k+1} - 2\overline{T}_{i,j,k} + \overline{T}_{i,j,k-1}\right) \Big/ \Delta Z^2 \quad (k = 1 \sim 9) \tag{2-41}$$

$$\left(\frac{\partial \overline{T}}{\partial Z}\right)_{i,j,k} = 0.5\left(\overline{T}_{i,j,k+1} - \overline{T}_{i,j,k-1}\right) \Big/ \Delta Z \quad (k = 1 \sim 9) \tag{2-42}$$

$$\left(\frac{\partial \overline{T}}{\partial Z_a}\right)_{i,j,k} = \left(\overline{T}_{i,j,k} - \overline{T}_{i,j,k-1}\right) \Big/ \Delta Z_a \quad (k = 0) \tag{2-43}$$

$$\left(\frac{\partial \overline{T}}{\partial Z}\right)_{i,j,k} = \left(\overline{T}_{i,j,k+1} - \overline{T}_{i,j,k}\right) \Big/ \Delta Z \quad (k = 0) \tag{2-44}$$

$$\left(\frac{\partial \overline{T}}{\partial Z}\right)_{i,j,k} = \left(\overline{T}_{i,j,k} - \overline{T}_{i,j,k-1}\right) \Big/ \Delta Z \quad (k = 10) \tag{2-45}$$

$$\left(\frac{\partial \overline{T}}{\partial Z_b}\right)_{i,j,k} = \left(\overline{T}_{i,j,k+1} - \overline{T}_{i,j,k}\right) \Big/ \Delta Z_b \quad (k = 10) \tag{2-46}$$

The difference coefficients shown in Eqs. (2-39) and (2-40) are expressed as

$$\begin{cases} A_{k,k-1} = 2 \Big/ \left\{ \left[(Z_a)_{k-1} - (Z_a)_k \right] \times \left[(Z_a)_{k-1} - (Z_a)_{k+1} \right] \right\} \\ A_{k,k} = 2 \Big/ \left\{ \left[(Z_a)_k - (Z_a)_{k-1} \right] \times \left[(Z_a)_k - (Z_a)_{k+1} \right] \right\} \\ A_{k,k+1} = 2 \Big/ \left\{ \left[(Z_a)_{k+1} - (Z_a)_{k-1} \right] \times \left[(Z_a)_{k+1} - (Z_a)_k \right] \right\} \end{cases} \tag{2-47}$$

$$\begin{cases} B_{k,k-1} = 2 \Big/ \left\{ \left[(Z_b)_{k-1} - (Z_b)_k \right] \times \left[(Z_b)_{k-1} - (Z_b)_{k+1} \right] \right\} \\ B_{k,k} = 2 \Big/ \left\{ \left[(Z_b)_k - (Z_b)_{k-1} \right] \times \left[(Z_b)_k - (Z_b)_{k+1} \right] \right\} \\ B_{k,k+1} = 2 \Big/ \left\{ \left[(Z_b)_{k+1} - (Z_b)_{k-1} \right] \times \left[(Z_b)_{k+1} - (Z_b)_k \right] \right\} \end{cases} \tag{2-48}$$

For the node in the X and Y directions, the difference operators are

$$\begin{cases} \left(\dfrac{\partial \overline{T}}{\partial X}\right)_{i,j,k} = \dfrac{1}{\Delta X}\left(\overline{T}_{i,j,k} - \overline{T}_{i-1,j,k}\right) & U_{i,j,k} \geq 0 \\ \left(\dfrac{\partial \overline{T}}{\partial X}\right)_{i,j,k} = \dfrac{1}{\Delta X}\left(\overline{T}_{i+1,j,k} - \overline{T}_{i,j,k}\right) & U_{i,j,k} \leq 0 \\ \left(\dfrac{\partial^2 \overline{T}}{\partial X^2}\right)_{i,j,k} = \dfrac{1}{\Delta X^2}\left(\overline{T}_{i+1,j,k} - 2\overline{T}_{i,j,k} + \overline{T}_{i-1,j,k}\right) & \end{cases} \tag{2-49}$$

$$\begin{cases} \left(\dfrac{\partial \overline{T}}{\partial Y}\right)_{i,j,k} = \dfrac{1}{\Delta Y}\left(\overline{T}_{i,j,k} - \overline{T}_{i,j-1,k}\right) & V_{i,j,k} \geq 0 \\ \left(\dfrac{\partial \overline{T}}{\partial Y}\right)_{i,j,k} = \dfrac{1}{\Delta Y}\left(\overline{T}_{i,j+1,k} - \overline{T}_{i,j,k}\right) & V_{i,j,k} \leq 0 \\ \left(\dfrac{\partial^2 \overline{T}}{\partial Y^2}\right)_{i,j,k} = \dfrac{1}{\Delta Y^2}\left(\overline{T}_{i,j+1,k} - 2\overline{T}_{i,j,k} + \overline{T}_{i,j-1,k}\right) & \end{cases} \tag{2-50}$$

Temperature discretized expressions of energy equations Eqs. (2-28), (2-31) and (2-33) can be obtained by using the above different difference operators.

The energy equation in solid *a* is discretized as

$$\begin{aligned}&-A_{k,k-1}\overline{T}_{i,j,k-1}+\left(\frac{CNA\cdot U_a}{\Delta X}-A_{k,k}+\frac{2}{\Delta X^2}+\frac{2}{\Delta Y^2}\right)\overline{T}_{i,j,k}-A_{k,k+1}\overline{T}_{i,j,k+1}\\&=\frac{CNA\cdot U_a}{\Delta X}\overline{T}_{i-1,j,k}+\frac{\overline{T}_{i-1,j,k}+\overline{T}_{i+1,j,k}}{\Delta X^2}+\frac{\overline{T}_{i,j-1,k}+\overline{T}_{i,j+1,k}}{\Delta Y^2}\quad\left(k=-5\sim-1\right)\end{aligned}\tag{2-51}$$

For the equation at lubricant–solid *a* interface

$$\frac{1}{\Delta Z_a}\overline{T}_{i,j,k-1}-\left(\frac{CMA}{H_{i,j}\Delta Z}+\frac{1}{\Delta Z_a}\right)\overline{T}_{i,j,k}+\frac{CMA}{H_{i,j}\Delta Z}\overline{T}_{i,j,k+1}=0\quad\left(k=0\right)\tag{2-52}$$

The discretized energy equation in lubricant when $U>0$, $V>0$

$$\begin{aligned}&-\left[\frac{1}{\left(H_{i,j}\Delta Z\right)^2}-\frac{1}{2}CS_1\frac{\overline{q}_{i,j,k}}{H_{i,j}\Delta Z}\right]\overline{T}_{i,j,k-1}\\&+\left[\frac{2}{\left(H_{i,j}\Delta Z\right)^2}+\frac{CS_1}{\Delta X}\left(\overline{\rho}U\right)_{i,j,k}+\frac{CS_1}{\Delta Y}\left(\overline{\rho}V\right)_{i,j,k}\right]\overline{T}_{i,j,k}\\&-\left[\frac{1}{\left(H_{i,j}\Delta Z\right)^2}+\frac{1}{2}CS_1\frac{\overline{q}_{i,j,k}}{H_{i,j}\Delta Z}\right]\overline{T}_{i,j,k+1}\\&=\frac{CS_1}{\Delta X}\left(\overline{\rho}U\right)_{i,j,k}\overline{T}_{i-1,j,k}+\frac{CS_1}{\Delta Y}\left(\overline{\rho}V\right)_{i,j,k}\overline{T}_{i,j-1,k}\\&+\frac{CS_2}{\overline{\rho}_{i,j,k}}\left[U_{i,j,k}\left(\frac{\partial P}{\partial X}\right)_{i,j}+V_{i,j,k}\left(\frac{\partial P}{\partial Y}\right)_{i,j}\right]\overline{T}_{i,j,k}\\&+CS_3\frac{\overline{\eta}_{i,j,k}}{H_{i,j}^2}\left[\left(\frac{\partial U}{\partial Z}\right)_{i,j,k}^2+\left(\frac{\partial V}{\partial Z}\right)_{i,j,k}^2\right]\quad(k=1\sim9)\end{aligned}\tag{2-53}$$

The discretized energy equation in lubricant when $U>0$, $V\le0$

$$\begin{aligned}&-\left[\frac{1}{\left(H_{i,j}\Delta Z\right)^2}-\frac{1}{2}CS_1\frac{\overline{q}_{i,j,k}}{H_{i,j}\Delta Z}\right]\overline{T}_{i,j,k-1}\\&+\left[\frac{2}{\left(H_{i,j}\Delta Z\right)^2}+\frac{CS_1}{\Delta X}\left(\overline{\rho}U\right)_{i,j,k}-\frac{CS_1}{\Delta Y}\left(\overline{\rho}V\right)_{i,j,k}\right]\overline{T}_{i,j,k}\\&-\left[\frac{1}{\left(H_{i,j}\Delta Z\right)^2}+\frac{1}{2}CS_1\frac{\overline{q}_{i,j,k}}{H_{i,j}\Delta Z}\right]\overline{T}_{i,j,k+1}\end{aligned}\tag{2-54}$$

$$
\begin{aligned}
&= \frac{CS_1}{\Delta X}\left(\overline{\rho}U\right)_{i,j,k}\overline{T}_{i-1,j,k} - \frac{CS_1}{\Delta Y}\left(\overline{\rho}V\right)_{i,j,k}\overline{T}_{i,j-1,k} \\
&+ \frac{CS_2}{\overline{\rho}_{i,j,k}}\left[U_{i,j,k}\left(\frac{\partial P}{\partial X}\right)_{i,j} + V_{i,j,k}\left(\frac{\partial P}{\partial Y}\right)_{i,j}\right]\overline{T}_{i,j,k} \\
&+ CS_3\frac{\overline{\eta}_{i,j,k}}{H_{i,j}^2}\left[\left(\frac{\partial U}{\partial Z}\right)_{i,j,k}^2 + \left(\frac{\partial V}{\partial Z}\right)_{i,j,k}^2\right] \quad (k = 1 \sim 9)
\end{aligned}
$$

The discretized energy equation in lubricant when $U \le 0$, $V > 0$

$$
\begin{aligned}
&-\left[\frac{1}{\left(H_{i,j}\Delta Z\right)^2} - \frac{1}{2}CS_1\frac{\overline{q}_{i,j,k}}{H_{i,j}\Delta Z}\right]\overline{T}_{i,j,k-1} \\
&+\left[\frac{2}{\left(H_{i,j}\Delta Z\right)^2} - \frac{CS_1}{\Delta X}\left(\overline{\rho}U\right)_{i,j,k} + \frac{CS_1}{\Delta Y}\left(\overline{\rho}V\right)_{i,j,k}\right]\overline{T}_{i,j,k} \\
&-\left[\frac{1}{\left(H_{i,j}\Delta Z\right)^2} + \frac{1}{2}CS_1\frac{\overline{q}_{i,j,k}}{H_{i,j}\Delta Z}\right]\overline{T}_{i,j,k+1} \\
&= -\frac{CS_1}{\Delta X}\left(\overline{\rho}U\right)_{i,j,k}\overline{T}_{i-1,j,k} + \frac{CS_1}{\Delta Y}\left(\overline{\rho}V\right)_{i,j,k}\overline{T}_{i,j-1,k} \\
&+ \frac{CS_2}{\overline{\rho}_{i,j,k}}\left[U_{i,j,k}\left(\frac{\partial P}{\partial X}\right)_{i,j} + V_{i,j,k}\left(\frac{\partial P}{\partial Y}\right)_{i,j}\right]\overline{T}_{i,j,k} \\
&+ CS_3\frac{\overline{\eta}_{i,j,k}}{H_{i,j}^2}\left[\left(\frac{\partial U}{\partial Z}\right)_{i,j,k}^2 + \left(\frac{\partial V}{\partial Z}\right)_{i,j,k}^2\right] \quad (k = 1 \sim 9)
\end{aligned}
\tag{2-55}
$$

The discretized energy equation in lubricant when $U \le 0$, $V \le 0$

$$
\begin{aligned}
&-\left[\frac{1}{\left(H_{i,j}\Delta Z\right)^2} - \frac{1}{2}CS_1\frac{\overline{q}_{i,j,k}}{H_{i,j}\Delta Z}\right]\overline{T}_{i,j,k-1} \\
&+\left[\frac{2}{\left(H_{i,j}\Delta Z\right)^2} - \frac{CS_1}{\Delta X}\left(\overline{\rho}U\right)_{i,j,k} - \frac{CS_1}{\Delta Y}\left(\overline{\rho}V\right)_{i,j,k}\right]\overline{T}_{i,j,k} \\
&-\left[\frac{1}{\left(H_{i,j}\Delta Z\right)^2} + \frac{1}{2}CS_1\frac{\overline{q}_{i,j,k}}{H_{i,j}\Delta Z}\right]\overline{T}_{i,j,k+1}
\end{aligned}
\tag{2-56}
$$

$$
\begin{aligned}
&= -\frac{CS_1}{\Delta X}\left(\overline{\rho}U\right)_{i,j,k}\overline{T}_{i-1,j,k} - \frac{CS_1}{\Delta Y}\left(\overline{\rho}V\right)_{i,j,k}\overline{T}_{i,j-1,k} \\
&\quad + \frac{CS_2}{\overline{\rho}_{i,j,k}}\left[U_{i,j,k}\left(\frac{\partial P}{\partial X}\right)_{i,j} + V_{i,j,k}\left(\frac{\partial P}{\partial Y}\right)_{i,j}\right]\overline{T}_{i,j,k} \\
&\quad + CS_3\frac{\overline{\eta}_{i,j,k}}{H_{i,j}^2}\left[\left(\frac{\partial U}{\partial Z}\right)_{i,j,k}^2 + \left(\frac{\partial V}{\partial Z}\right)_{i,j,k}^2\right] \quad (k = 1 \sim 9)
\end{aligned}
$$

For the equation at lubricant–solid *b* interface

$$
\frac{CMB}{H_{i,j}\Delta Z}\overline{T}_{i,j,k-1} - \left(\frac{CMB}{H_{i,j}\Delta Z} + \frac{1}{\Delta Z_b}\right)\overline{T}_{i,j,k} + \frac{1}{\Delta Z_b}\overline{T}_{i,j,k+1} = 0 \quad (k = 10) \tag{2-57}
$$

The discretized energy equation in solid *b* is written as

$$
\begin{aligned}
&-B_{k,k-1}\overline{T}_{i,j,k-1} + \left(\frac{CNB\cdot U_b}{\Delta X} - B_{k,k} + \frac{2}{\Delta X^2} + \frac{2}{\Delta Y^2}\right)\overline{T}_{i,j,k} - B_{k,k+1}\overline{T}_{i,j,k+1} \\
&= \frac{CNB\cdot U_b}{\Delta X}\overline{T}_{i-1,j,k} + \frac{\overline{T}_{i-1,j,k} + \overline{T}_{i+1,j,k}}{\Delta X^2} + \frac{\overline{T}_{i,j-1,k} + \overline{T}_{i,j+1,k}}{\Delta Y^2} \quad (k = 11 \sim 15)
\end{aligned} \tag{2-58}
$$

2.5 Numerical simulation method

The numerical solution of present EHL problems consists of two parts: the solution of pressure with fixed temperature and the solution of temperature with fixed pressure and film thickness. In the solution of pressure, the temperature filed is assumed as known. The pressure distribution is obtained by solving Reynolds equation, load equation, and then the film thickness is calculated by using the pressure filed. In the solution of temperature, the energy equations are solved using the obtained pressure and film thickness distributions to update the temperature filed. The iteration between pressure and temperature is repeated until the convergent criteria are reached. The process of numerical solution is summarized in a flow chart in Fig. 2-5.

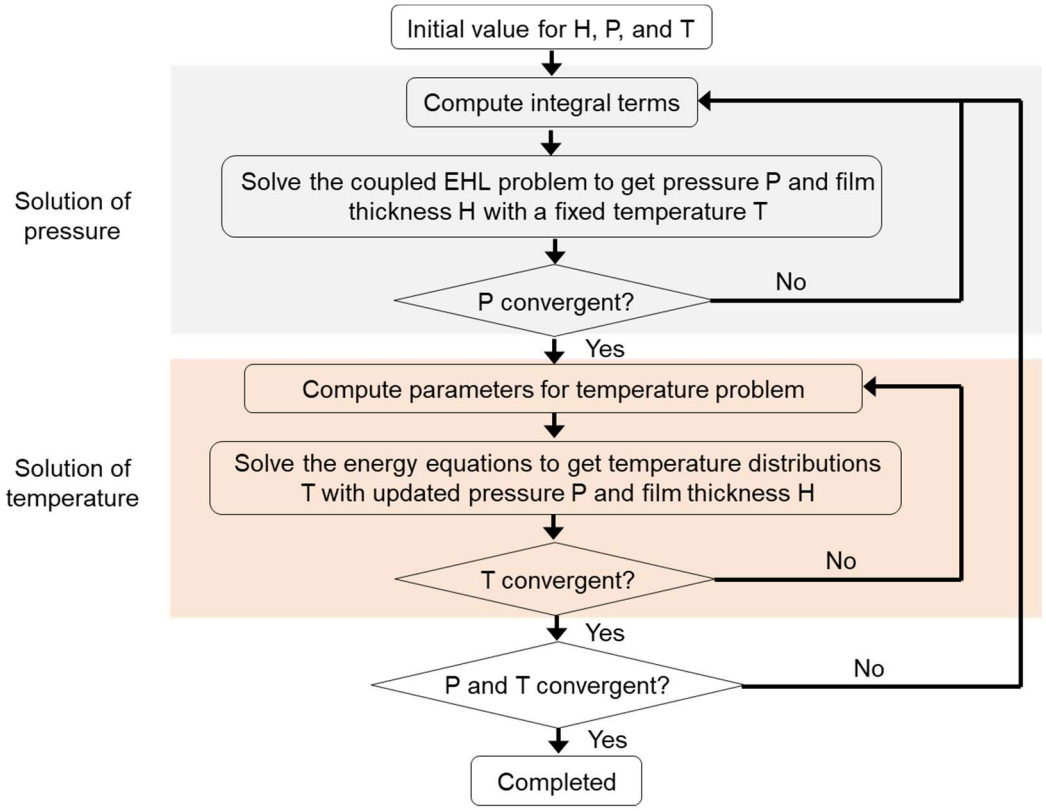

Figure 2-5 Flow diagram of the thermal EHL model solution.

2.5.1 Pressure solution

In the process of pressure solution, the Reynolds equation is solved with Multigrid Method [168], and the elastic deformation in film thickness equation is evaluated using Multilevel Multi-integration (MLMI) Method [169]. Five levels of grids are used for the calculations of pressure and film thickness.

With the Multigrid Method, the computational domain is divided into grids with different density, so that each layer of grid represents the same computational domain for the same problem. On each layer of the grid, Partial Differential Equations must be discretized in the same format. The obtained approximate solutions and deviations of the algebraic equations are transferred layer by layer and iterated on each layer of the grid. Finally, an accuracy numerical solution that meets the requirements is obtained on the finest grid.

The circulation and transfer between different grids include the circulation format and solution values transfer between different layers. The present study adopts the general W cycle due to its good numerical stability, as shown in Fig. 2-6.

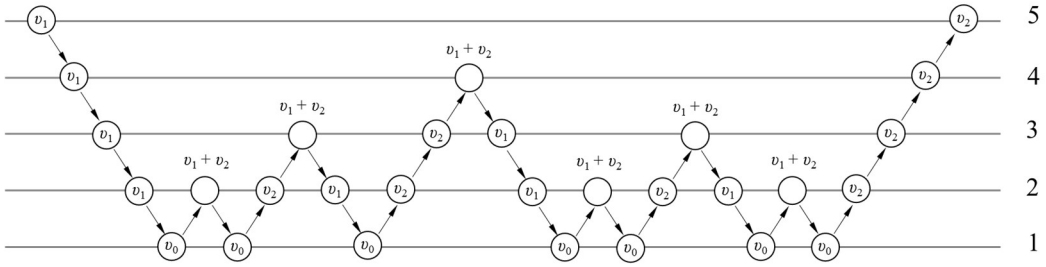

Figure 2-6 The general W cycle with five grid level. υ_0, υ_1, υ_2 are relaxation numbers.

At each layer, the pressure needs iterative relaxation. The discrete form of Reynolds equation is written as

$$L_{i,j}\left(P\right)=F_{i,j} \tag{2-59}$$

where L is discrete relation operator, F is right vector.

For the difference equation, the Newtown-Raphson method [167] is employed to construct iterative equations.

$$\begin{cases}\delta_{i,j}=r_{i,j}\Big/\left(\dfrac{\partial L_{i,j}}{\partial P_{i,j}}\right)\\ r_{i,j}=F_{i,j}-L_{i,j}(P)\end{cases} \tag{2-60}$$

For the nodes at each grid, the Gauss-Seidel method is used.

$$\tilde{P}_{i,j}=P_{i,j}+\omega_P\delta_{i,j} \tag{2-61}$$

where ω_P is pressure relaxation factor.

The Multilevel Multi-integration (MLMI) Method is used to solve the elastic deformation term in the film thickness equation.

$$E_{i,j}=\sum_{k=0}^{n_X}\sum_{l=0}^{n_Y}K_{ij,kl}P_{k,l} \tag{2-62}$$

This method is combined with the Multigrid Method of Reynolds equation. The layer of pressure iterative relaxation is target layer which named as fine grid. The layer of elastic deformation term integrated is named as coarse grid. The MLMI method is transfer

the information of elastic deformation term on the fine grid to the coarse grid, calculate the integral on the coarse grid, and then transfer the calculation result back to the fine grid, make corrections on the fine grid. Through this process, the accuracy results are obtained on the fine grid. Detailed information of pressure solution can be found in [167].

2.5.2 Temperature solution

To obtain the temperature field in lubricant and solids, the energy equations are solved by using sequential column sweeping method [170]. This technique had been proven to be an efficient solver for thermal EHL problem, and successfully obtained full numerical solutions of temperature fields by Yang and his coworkers [66,76,171,172].

In the entire computational domain, the dispersal equations of Eqs. (2-51)–(2-58) can be written as tridiagonal system with the same nodes i, j and different k.

$$\Lambda_{i,j}\overline{T}_{i,j} = B_{i,j} \tag{2-63}$$

where $\Lambda_{i,j}$ is the tridiagonal coefficient matrix, $B_{i,j}$ is the array of right hand terms.

$$\Lambda_{i,j} = \begin{bmatrix} a_{-5,-5} & a_{-5,-4} & & & & & & \\ a_{-4,-5} & a_{-4,-4} & a_{-4,-3} & & & & & \\ & \cdot & \cdot & \cdot & & & & \\ & & \cdot & \cdot & \cdot & & & \\ & & & \cdot & \cdot & \cdot & & \\ & & & & a_{14,13} & a_{14,14} & a_{14,15} & \\ & & & & & a_{15,14} & a_{15,15} & \end{bmatrix} \tag{2-64}$$

$$\overline{T}_{i,j} = \begin{Bmatrix} \overline{T}_{-5} \\ \overline{T}_{-4} \\ \cdot \\ \cdot \\ \cdot \\ \overline{T}_{14} \\ \overline{T}_{15} \end{Bmatrix} \qquad B_{i,j} = \begin{Bmatrix} b_{-5} \\ b_{-4} \\ \cdot \\ \cdot \\ \cdot \\ b_{14} \\ b_{15} \end{Bmatrix} \tag{2-65}$$

The line temperature across the lubricant and solids with different k nodes at each site i, j can be obtained by solving the Eq. (2-63). $\Lambda_{i,j}$ and $B_{i,j}$ are formed based on the latest

calculated temperature in the iteration or initial values. After the entire temperature field is solved, the results are updated for an initial value of the next cycle by the following equation.

$$\overline{T}_{i,j,k}^{s+1} = \overline{T}_{i,j,k}^{s} + \omega_T \left(\overline{\overline{T}}_{i,j,k}^{s} - \overline{T}_{i,j,k}^{s} \right) \tag{2-66}$$

where s, s+1 denote the cycle number, ω_T is the coefficient of iterative relaxation.

2.5.3 Convergence criteria

An iterative procedure was used to solve the Reynolds and energy equations for present numerical model. The results meet the accuracy requirements are collected when the convergence was achieved. In the solution of pressure, the iterative errors of pressure and load are checked on the finest grid level as follows:

$$Err_P = \frac{\sum_i \sum_j \left| P_{i,j}^{new} - P_{i,j}^{old} \right|}{\sum_i \sum_j P_{i,j}^{new}} \le 0.001 \tag{2-67}$$

$$Err_W = \frac{\left| \iint_\Omega PdXdY - W_{load} \right|}{W_{load}} \le 0.001 \tag{2-68}$$

where the superscripts *new* and *old* represents the pressure results at the beginning and end of the pressure iteration.

In the solution of temperature, convergence was achieved if the following convergent criterion for the entire temperature domain is reached.

$$Err_{\overline{T}} = \frac{\sum_i \sum_j \sum_k \left| \overline{T}_{i,j,k}^{new} - \overline{T}_{i,j,k}^{old} \right|}{\sum_i \sum_j \sum_k \overline{T}_{i,j,k}^{new}} \le 0.0001 \tag{2-69}$$

2.6 Summary

In this chapter, a thermal EHL theory was developed to better understand the lubrication performances with boundary slips for EHL contact. The modified Reynolds

equation is derived, coupled with load equation, film thickness equation and energy equations, to obtain the pressure, film thickness and temperature in contact area. Also, the solution methods of pressure and temperature were presented. The pressure solution employed the Multigrid method to solve Reynolds equation, while the Multilevel Multi-integration method was used for elastic deformation calculation in film thickness equation. The sequential column sweeping method was adopted to solve the energy equations of lubricant and solids.

The thermal EHL theory proposed in this chapter can be used to investigate the effects of velocity and thermal slips on lubrication performances, such as film thickness, pressure, and temperature rise in contact. Furthermore, the lubrication under different working conditions, entrainment velocity and slide-roll ratio etc. can be qualified by present theory. More details are presented in next Chapter.

Chapter 3

3. Numerical analysis of boundary slips for thermal point EHL contact

3.1 Introduction

Numerical simulation is an important concern for investigation and discussion of lubrication performance in tribological fields. Within simulation, it is convenient to vary the surface velocity, SRR and slip boundary condition at solid–lubricant interfaces, which possible to explore their effects on lubrication characterizes such as friction, film thickness and temperature rise. Since the lubrication in machine elements is still complex, it is necessary to conduct the numerical simulation to better predict and improve lubrication performance, efficiency, and reliability.

Based on the theory of thermal EHL presented in chapter 2, the influence of boundary slips on lubrication performances are investigated under various motion. In this chapter, the pure rolling motion, opposite sliding motion and rolling/sliding motion are estimated in order to clarify the mechanism of boundary slips at solid–lubricant interfaces. The degrees of boundary slips are represented by slip length and thermal slip length, respectively. Details of boundary slips are shown in Fig. 2-2.

Fig. 3-1 shows the schematic of EHL contact and computational domain. The contact is formed between steel ball and steel disc while are moving with u_b and u_a respectively. The applied load w is constant. For the computational domain, the length of x and y is $10a$, where a is the half contact width. In the z direction, the thickness of each solid is $5a$ in thickness. The origin of the coordinate system is positioned at the center of surface a, characterized by point o.

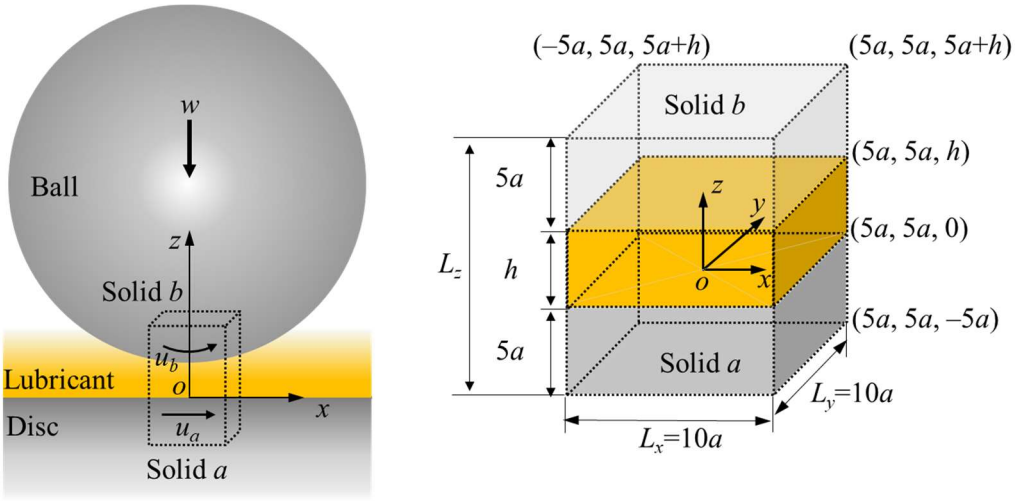

(a) (b)

Figure 3-1 Schematic of (a) EHL contact (steel–steel) and (b) computational domain (not to scale).

Table 3-1 lists the properties of materials. The current work employed a steel–steel contact and mineral oil Shell Turbo 33, which provides excellent oxidative stability, low foaming and excellent demulsibility for industry applications.

Table 3-1 Properties of lubricant and steel.

Density of steel, $\rho_{a,b}$, kg/m^3	7850
Specific heat of steel, $c_{a,b}$, J/(kg·K)	470
Thermal conductivity of steel, $k_{a,b}$, W/(m·K)	46
Ambient density of lubricant, ρ_0, kg/m^3	875
Specific heat of lubricant, c, J/(kg·K)	2000
Thermal conductivity of lubricant, k, W/(m·K)	0.14
Pressure viscosity coefficient, α, 1/Pa	2.4×10^{-8}
Ambient viscosity of lubricant, η_0, Pa·s	0.08
Thermal viscosity coefficient of lubricant, β, 1/K	0.042
Reduced elastic modules, E', Pa	2.26×10^{11}

Among these parameters in Table 3-1, the thermal conductivity plays vital role in affecting the temperature rise. Habchi et al. [63], Reddyhoff et al.[173] and Liu et al. [61]. discussed the effects of the thermal conductivity on the EHL performance. To simplify the problem, the thermal conductivity of steel in its annealed/soft state is given as 46 W/(m·K), which is commonly used in literatures [129,131,132,188].

3.2 Pure rolling motion

3.2.1 Simulation system

Under pure rolling motion, the contact surfaces have same velocity with same direction, which are widely existed in EHL lubricated components, such as gears, cams and rolling element bearings. Fig. 3-2 shows the schematic of pure rolling motion. The surfaces of the disc and ball are assumed to be smooth and moving at same surface speeds in the x direction, SRR = 0. The contact is subject to an external applied load w and a fully flooded regime is assumed. Under pure rolling motion, the influence of boundary slips on lubrication performances are investigated as the boundary slips on disc surface or both contact surfaces. The degrees of boundary slips are represented by slip length and thermal slip length, respectively.

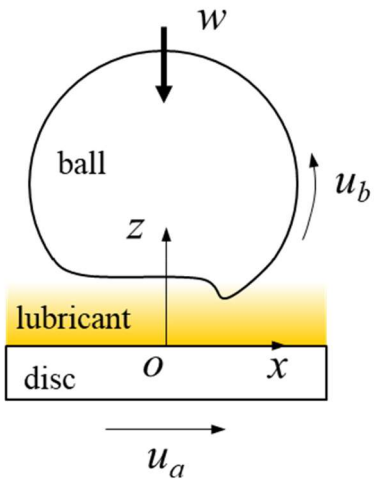

Figure 3-2 Schematic of pure rolling motion, $u_a = u_b$.

Table 3-2 lists the operation conditions used in this section. The ball radius is set as

12.7 mm, which is commonly used in the rolling bearings. Applied load is 30 N, and it kept constant during the whole simulation under pure rolling motion. The slide-roll ratio SRR is 0 under pure rolling motion ($u_a = u_b$). In order to investigate the influence of velocity slip on lubrication, the velocity slip length varies from 0 to 2 μm comparable to the film thickness in EHL, while the thermal slip length is set as 0. For the investigation of thermal slip effect, the velocity slip length is set as 0.

Table 3-2 Operation conditions.

Ambient temperature, T_0, K	313
Ball radius, R, m	0.0127
Load, w, N	30
Half width of Hertzian contact, a, μm	136
Entrainment velocity, $u_e = (u_a + u_b)/2$, m/s	0 ~ 10
Slide-roll ratio, SRR = $(u_a - u_b)/u_e$	0
Velocity slip length, l_s, μm	0 ~ 2
Thermal slip length, l_k, μm	0 ~ 1

3.2.2 Velocity slip effect

Furnishing boundary slip at one of the solid–lubricant interfaces in a bearing contact has significant effect on lubrication under pure rolling motion. The contour maps of the film thickness, pressure, and film thickness profiles are shown in Fig. 3-3. In this plot, $-1 \leq X = x/a \leq 1$ and $-1 \leq Y = y/a \leq 1$ correspond to the area of the Hertzian contact, and $X = Y = 0$ corresponds to the center of the contact area. The employed slip lengths are 0.2 μm, 0.5 μm, and 1.0 μm, where the thermal slip length $l_k = 0$. These values of the slip lengths are comparable to EHL film thickness (approximate 1.0 μm). The result of $l_s = 0$, which is a typical solution of the EHL point contact, is shown in Fig. 3-3(a). A central plateau and an outer constriction are evident in the contour maps. As the slip length increases, the central flat plateau is enlarged, while the minimum film thickness in the

constriction decreases. Fig. 3-3 also presents the pressure and film thickness profiles in the plane Y = 0 along the entrainment direction. As the slip length l_s increases, the second pressure peak near outlet shifts downward, while the film thickness decreases significantly over the entire contact region.

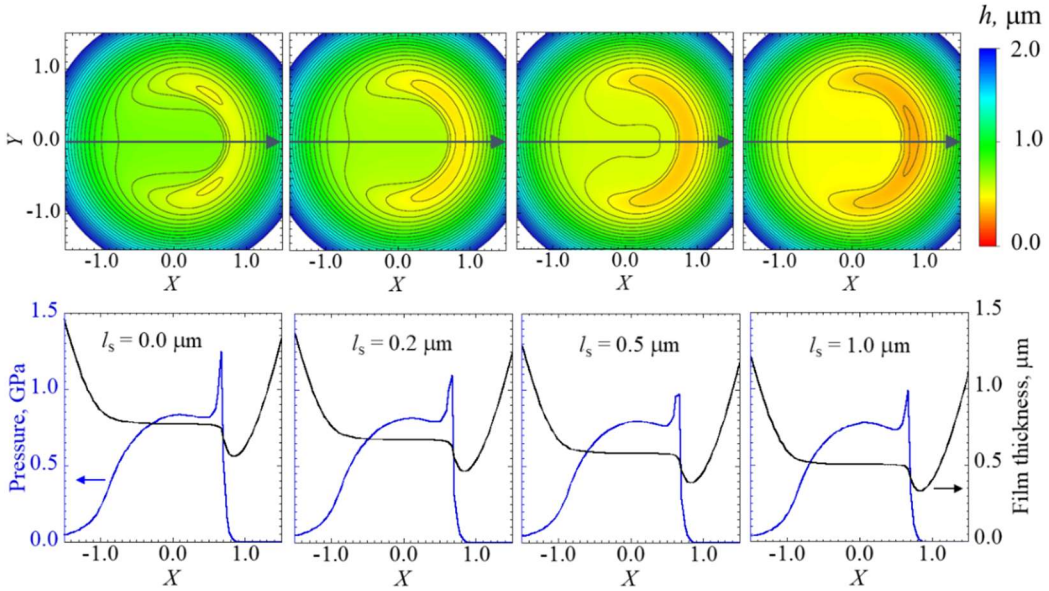

Figure 3-3 Contour maps of film thickness (top) and pressure, film thickness profiles on center plane Y = 0 (bottom) at u_e = 2 m/s under different boundary conditions: (a) no slip; (b) l_s = 0.2 μm; (c) l_s = 0.5 μm; (d) l_s = 1.0 μm. Velocity slip at disc surface.

The film thickness reduction induced by the velocity slip is attributed to the lower lubricant velocity, which entrains less lubricant into the contact area [186]. Fig. 3-4 shows the lubricant velocity profiles across the lubricant film and the slip velocity at locations *a* (X = -1.0, Y = 0.0), *b* (X = 0.0, Y = 0.0), and *c* (X = 1.0, Y = 0.0). Velocity slip occurs on surface *a* (Z = 0.0), while surface *b* (Z = 1.0) is under the continuum boundary condition. At the inlet location *a*, the velocity profiles across the lubricant film in the *z* direction are hindered by the occurrence of velocity slip shown in Fig. 3-4(a). As the slip length increases, the negative velocity gradient on the surface *a* (Z = 0.0) and the corresponding slip velocity u_s at location *a* increase monotonically, as shown in Fig. 3-4(d). However, at location *b*, the observed velocity profiles are linear and independent of the slip length.

Thus, the velocity gradient is almost zero along the z direction, resulting in zero slip velocity u_s, as shown in Fig. 3-4(d). At location c, the shape of the lubricant velocity profile varies with the slip length. For l_s = 0.5 μm and 1.0 μm, lubricant velocity is smaller than that no slip condition for the area of near surface b, while the reverse is true for the area of near surface a. The curve of u_s is quadratic at location c with a peak at l_s = 0.5 μm, as shown in Fig. 3-4(d). The existence of velocity slip on surface a decreases the entrainment velocity in the inlet region, which reduces the amount of lubricant entrained in the contact region. Consequently, the film thickness decreases.

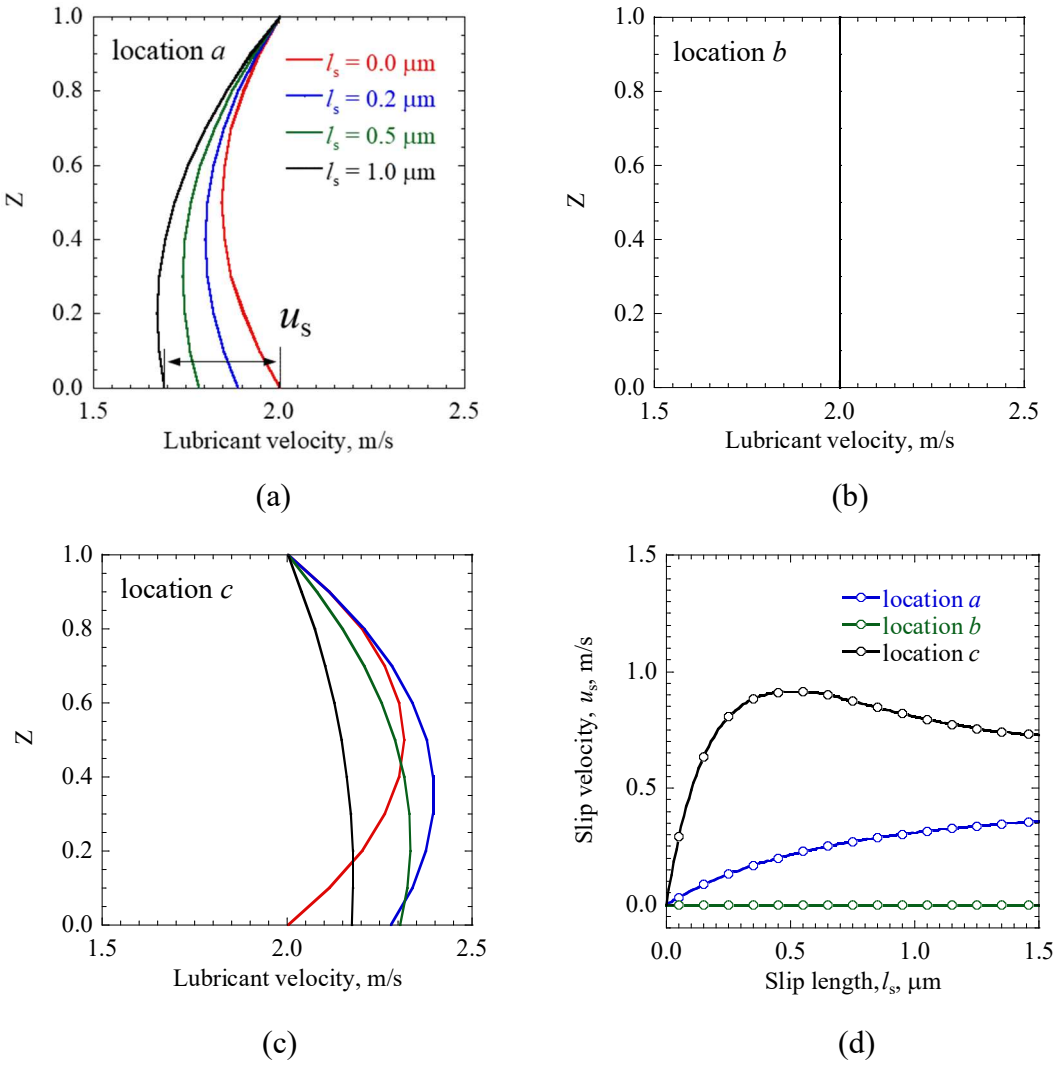

Figure 3-4 Effect of slip length on (a–c) lubricant velocity distributions across lubricant film and (d) slip velocity at location a (X = -1.0, Y = 0.0), location b (X = 0.0, Y = 0.0), and location c (X = 1.0, Y = 0.0). Velocity slip at disc surface.

Fig. 3-5 describes the variations in the film thickness ratios corresponding to the increases in entrainment velocity for different slip lengths. D_{cen} and D_{min} are the ratios of the center and minimum film thicknesses with velocity slip to those without velocity slip. Without the occurrence of velocity slip (l_s = 0.0 μm), D_{cen} and D_{min} are always 1.0. According to Fig. 3-5, D_{cen} and D_{min} increase asymptotically as the entrainment velocity increases, indicating that the influence of slip length on film thickness in the low-velocity region is more apparent than that in the high-velocity region. For the same entrainment velocity, both D_{cen} and D_{min} decrease as l_s increases, while the value of D_{min} remains greater than that of D_{cen}. This means that the film thickness at the center is more significantly affected by the slip length than that in the constriction.

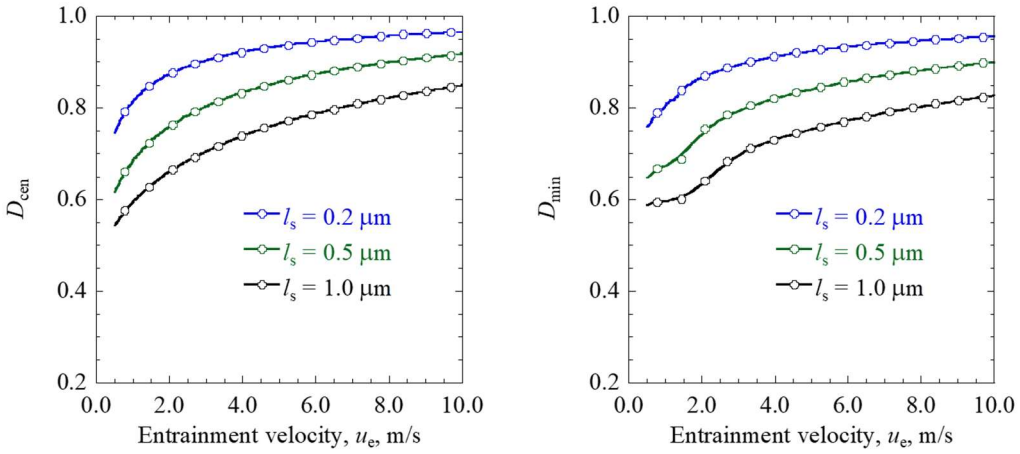

Figure 3-5 Effect of slip length on (a) central film thickness and (b) minimum film thickness with increasing entrainment velocity under pure rolling contact. Velocity slip at disc surface.

In practical applications, velocity slip may occur on both surfaces, which has more significant effect on lubrication performances under pure rolling motion. The contour maps of the film thickness, pressure, and film thickness profiles with velocity slip at both surfaces are plotted in Fig. 3-6, where velocity occurs at both surfaces. These values of the slip lengths employed in this figure are same to Fig. 3-3. As the slip length increases, the film thickness in center area and constriction gradually decreases, similar to the results with velocity slip at surface *a*. The second pressure peak shifts downward as the slip length l_s increases. When l_s = 1.0 μm as shown in Fig. 3-6(d), the second pressure peak

almost disappear.

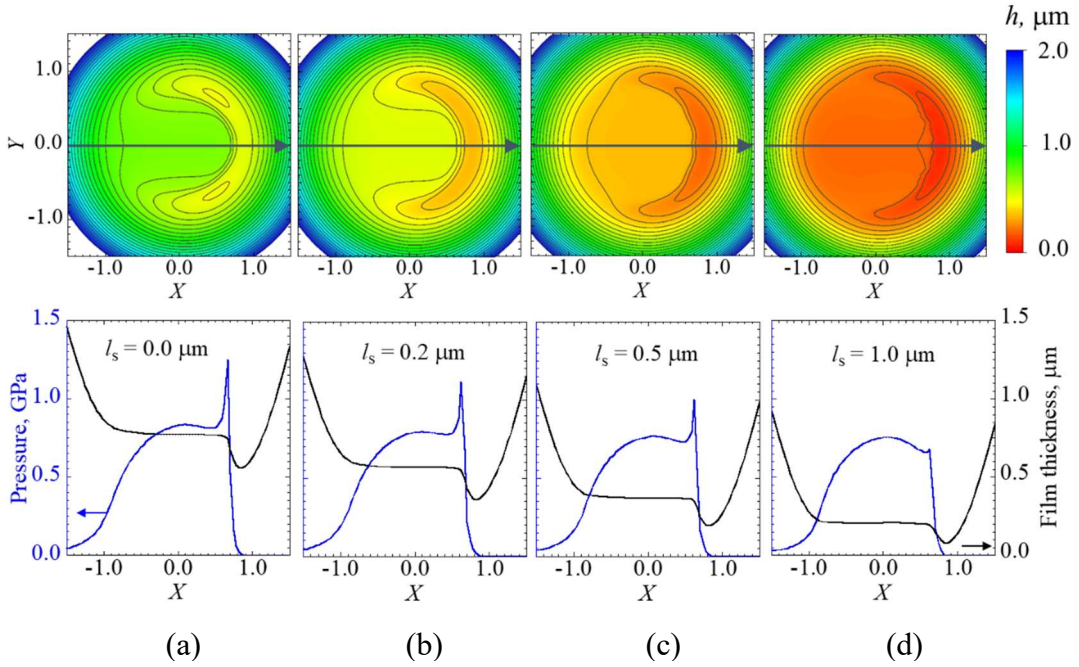

Figure 3-6 Contour maps of film thickness (top) and pressure, film thickness profiles on center plane Y = 0 (bottom) at u_e = 2 m/s under different boundary conditions: (a) no slip; (b) l_s = 0.2 μm; (c) l_s = 0.5 μm; (d) l_s = 1.0 μm. Velocity slip at both surfaces.

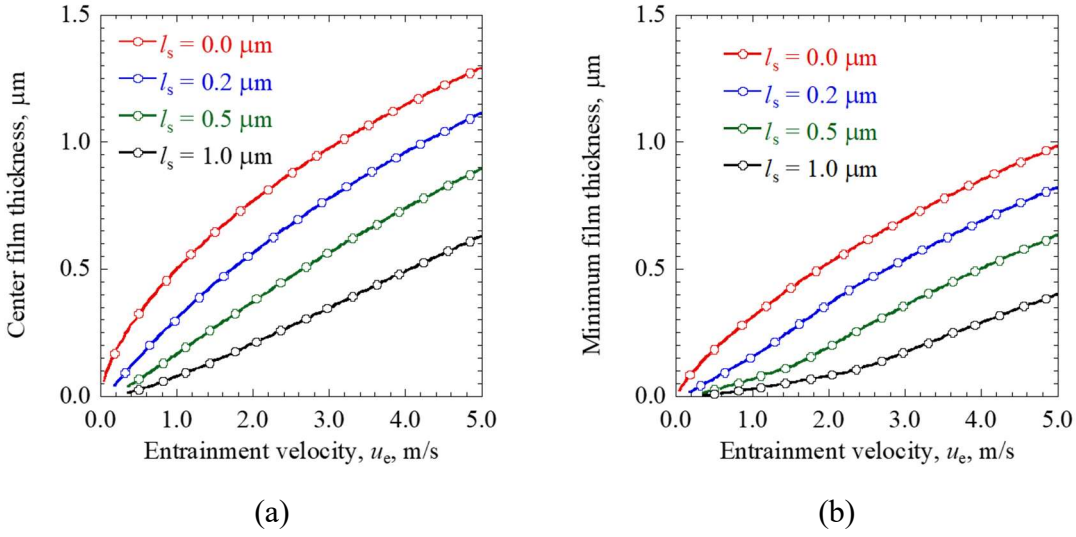

Figure 3-7 (a) Central film thickness and (b) minimum film thickness curves with velocity slips under pure rolling contact. Velocity slip at both surfaces.

The entrainment velocity under pure rolling motion is related to the amount and velocity of lubricant entrained into the contact area, affect the velocity slip effect on film thickness distribution. The central film thickness and minimum film thickness distributions with entrainment velocity are depicted Fig. 3-7. Significant film thickness reduction for l_s = 0.2 μm, 0.5 μm and 1.0 μm is observed because the velocity slip occurs at both contact surfaces. The larger slip length, the greater film thickness reduction. Furthermore, the value of film thickness reduction becomes larger with increasing entrainment velocity owing to the fact that the high velocity leads to great central and minimum film thickness.

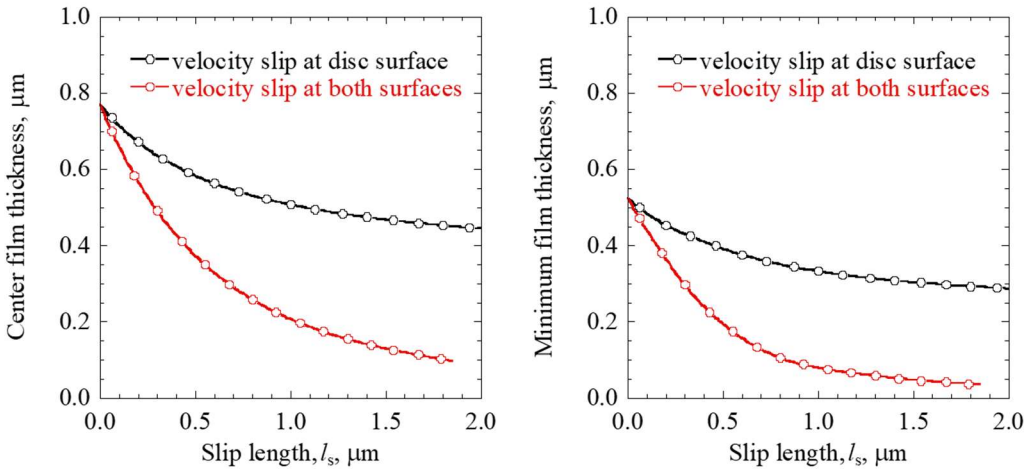

Figure 3-8 Comparison of (a) central film thickness and (b) minimum film thickness with increasing slip length for velocity slip at disc surface or both surfaces. u_e = 2 m/s.

In Fig. 3-8, the film thickness reduction results caused by velocity slip at disc surface (surface *a*) or both surfaces are presented to make comparison. For the case of velocity slip at both surfaces, the film thickness reductions of central and minimum film thickness are greater than the case of velocity slip at disc surface. The larger slip length, the more significant reduction between the two cases. That is because the existence of velocity slip on both surfaces caused the entrainment velocity in the inlet region is smaller than the case of velocity slip on disc surface, as shown in Fig. 3-4(a), limited the amount lubricant entrained in the contact region. Consequently, the film thickness reduction with velocity

slip on both surfaces is more remarkable.

3.2.3 Thermal slip effect

Thermal slip at the solid–lubricant interface, which is also called temperature jump phenomena, arises when the heat flows across the liquid–solid interface. Generally, the degree of thermal slip can be identified by thermal slip length, as schematized in Fig. 2-2. The thermal slip increases the thermal resistance at interface, making the heat conduction from lubricant to solid more difficult.

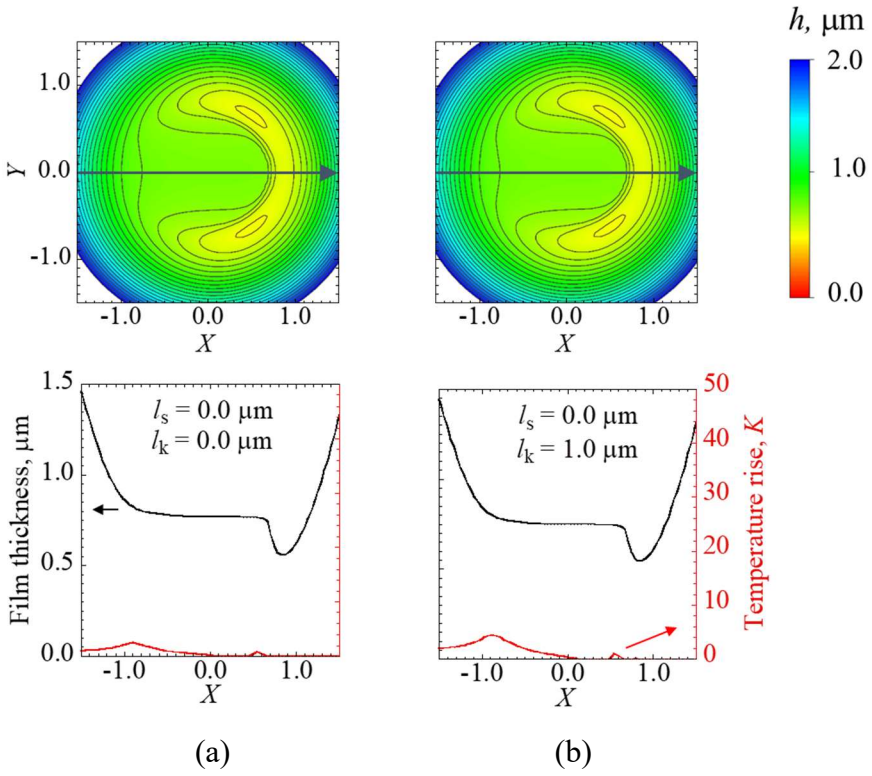

Figure 3-9 Contour maps of film thickness (top) and temperature, film thickness profiles on center plane Y = 0 (bottom) at u_e = 2 m/s under different thermal slip: (a) no slip; (b) l_s = 0.0 μm, l_k = 1.0 μm.

Fig. 3-9 shows the influence of thermal slip on contour maps (top), film thickness and temperature profiles (bottom) at center plane Y = 0 under pure rolling motion. Thermal slip occurs at the disc surface. The velocity slip length is set as 0 to avoid the velocity slip effects. By comparing the results in Figs. 3-9 (a) and (b), the contour maps and film

thickness distributions are almost identical with or without thermal slip. It is indicated that the influence of thermal slip on lubrication performance is negligible due to the insignificant temperature rise. Therefore, the thermal slip is not considered under pure rolling motion.

3.3 Opposite sliding motion

3.3.1 Simulation system

In contrast to the abovementioned pure rolling motion (slide-roll ratio S = 0) in which two surfaces move in the same direction, zero entrainment velocity (ZEV) contact involves two surfaces moving in opposite directions (for example, surface *a* moving from the left to the right, while surface *b* moving from the right to the left, as shown in Fig. 3-10) with the same speed (slide-roll ratio S =∞). Thus, under ZEV contact, the temperature rise is expected to be more significant than that under pure rolling motion in the same working conditions. This temperature increase is a dominant factor in maintaining a beneficial lubrication state, which is characterized by a surface dimple formed due to lubricant accumulation. Because the dimple is governed by the surface velocity and the subsequent temperature viscosity wedge effect [83,92], the slip boundary condition may significantly influence the shape of the dimpled film.

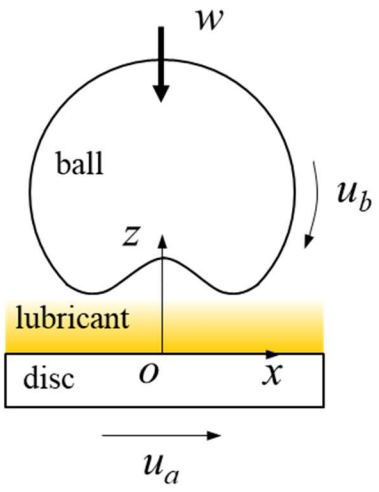

Figure 3-10 Schematic of opposite sliding motion, u_a =- u_b.

Here, the steel–steel ZEV contact shown in Fig. 3-10 is employed to investigate the effects of the slip boundary condition on the lubrication performance, where the velocity/thermal slips occur on disc surface (surface *a*). For the ZEV contact, semi-field calculation is adopted in *y* direction to achieve stable solutions with fast convergence. The semi-field calculation [70] solve the entire problem on half of the geometrical domain while the solution on the other half is deduced by symmetry. Four grid levels with 513 nodes along the *x* direction and 197 nodes along the *y* direction at the finest grid level were applied in the calculation domain $-3a \le x \le 3a$, $0 \le y \le 1.8a$. The calculation domain in the *z* direction is same to that of the pure rolling case.

Table 3-3 lists the operation conditions. Under ZEV motion, the slide-roll ratio is ∞ due to $u_a = -u_b$. Three cases of boundary slips, i.e., velocity slip, thermal slip, and coupled velocity/thermal slips, are employed at disc surface (surface *a*), where the ball surface (surface *b*) is under no slip boundary condition.

Table 3-3 Operation conditions.

Ambient temperature, T_0, K	313
Ball radius, R, m	0.025
Load, w, N	31.6
Half width of Hertzian contact, a, μm	173
Surface speed, $u_a = -u_b$, m/s	2.1 ~ 4.2
Slide-roll ratio, SRR = $(u_a - u_b)/u_e$	∞
Velocity slip length, l_s, nm	0 ~ 400
Thermal slip length, l_k, nm	0 ~ 400

3.3.2 Velocity slip effect

To simplify comparisons of the boundary slip effects, the thermal slip length is set to zero ($l_k = 0$) in this section. Fig. 3-11 shows the contour maps of the lubricant film (top), and the pressure and film thickness profiles (bottom) in the plane Y = 0 for l_s = 0, 25 and

50 nm with $u_a = -u_b = 2.1$ m/s. Under the no slip boundary condition ($l_s = 0$), a large surface dimple is formed in the contact area due to the temperature viscosity wedge effect. As the slip length increases, the constriction in the left contact area is enlarged; consequently, the dimple is pushed toward the right side of the contact region. In the pressure and film thickness profiles shown in the bottom of Fig. 3-11, the pressure peak close to center shifts toward the right side of the contact region, and its magnitude increases as the slip length increases. The film thickness in the left side of the dimple thereby decreases, which squeezes the dimple toward the right.

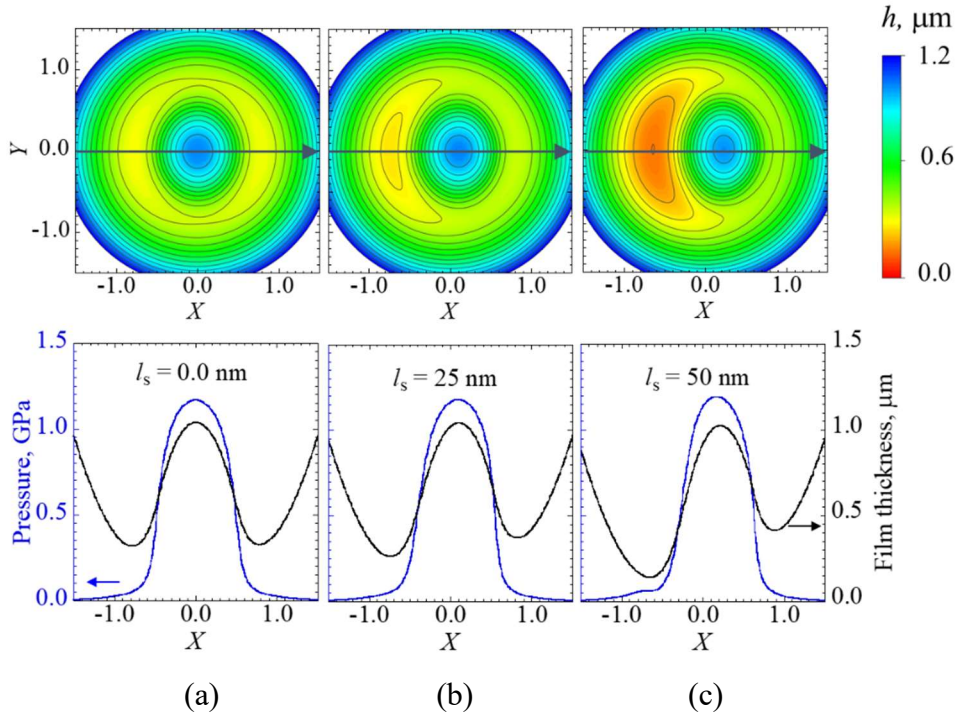

Figure 3-11 Contour maps of film thickness (top) and pressure, film thickness profiles on center plane Y = 0 (bottom) at $u_a = -u_b = 2.1$ m/s, $l_k = 0$ under different velocity slip: (a) $l_s = 0$; (b) $l_s = 25$ nm; (c) $l_s = 50$ nm.

Fig. 3-12 shows the variations in lubricant velocity for $l_s = 0$, 25 and 50 nm across the lubricant film and the slip velocity at the three locations. In this section. locations *a*, *b*, and *c* are denoted as the two sides and the center of the contact region, respectively (Location *a*: X = -1.0, Y = 0.0; Location *b*: X = 0.0, Y = 0.0; Location *c*: X = 1.0, Y = 0.0). Larger slip length results in larger slip velocities at locations *a* and *c*, and smaller lubricant velocity, as shown in Fig. 3-12(*a*) and (*c*). However, the slip velocity at location

b is almost zero, and thus, the effect of slip length on lubricant velocity can be neglected at the center of the contact region. Since the absolute lubricant velocity near surface *a* is smaller than that near surface *b*, surface *a* drags less lubricant into the contact region than surface *b*. Therefore, the area of lubricant accumulation shifts from the center toward the right side of the contact region. Correspondingly, the pressure peak and the surface dimple shift right.

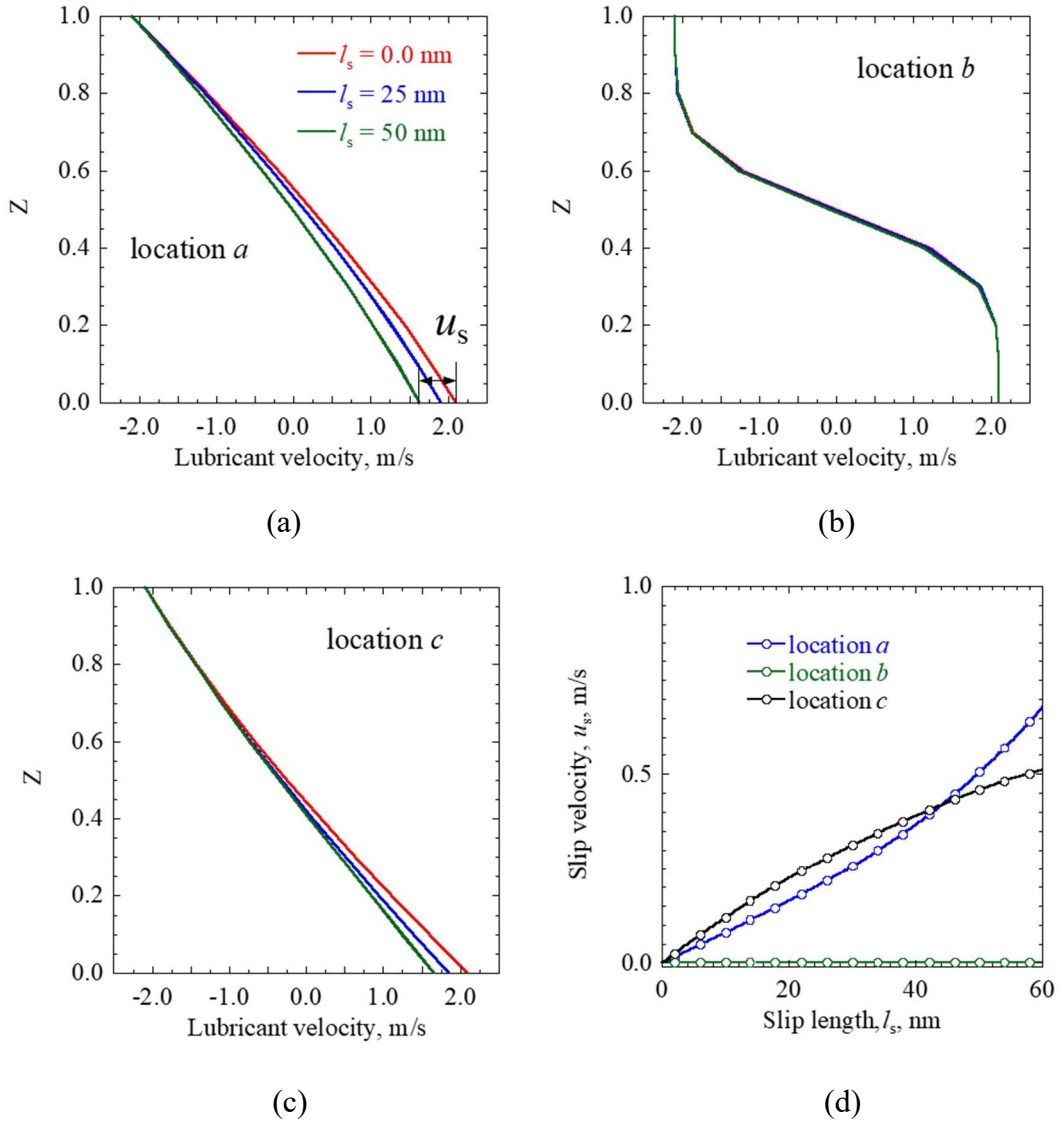

Figure 3-12 Effect of slip length on (a–c) lubricant velocity distributions across lubricant film and (d) slip velocity at location *a* (X = -1.0, Y = 0.0), location *b* (X = 0.0, Y = 0.0), and location *c* (X = 1.0, Y = 0.0). $u_a = -u_b = 2.1$ m/s, $l_k = 0$.

Fig. 3-13 shows the contour maps of the lubricant film (top), and the pressure and film thickness profiles (bottom) in the plane Y = 0 for extreme slip length condition: l_s = 100, 200 and 300 nm with $u_a = -u_b = 2.1$ m/s. In comparison with the Fig. 3-11, the locations of dimple and maximum pressure shift closer to right side with the reduction of dimple size. The large slip length results the lubricant velocity near surface *a* is smaller than that near surface *b*. Thus, the surface *b* (from right to left) plays more dominant role on the entrained lubricant, leads the great constriction at left side and small dimple at right side. The maximum pressure overlaps with the location of dimple.

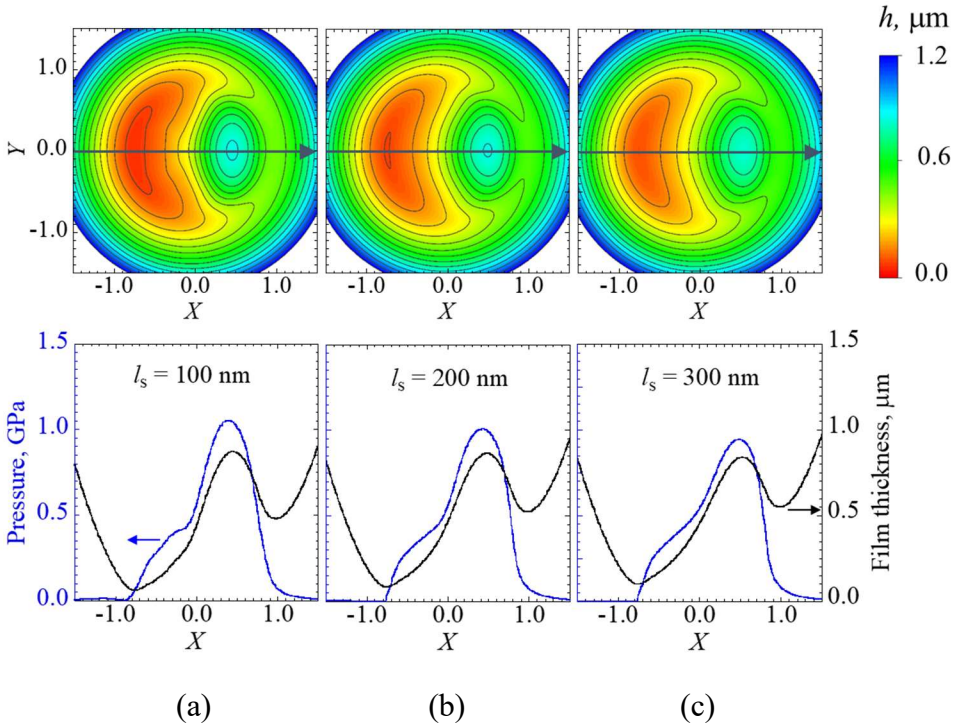

Figure 3-13 Contour maps of film thickness (top) and pressure, film thickness profiles on center plane Y = 0 (bottom) at $u_a = -u_b = 2.1$ m/s, $l_k = 0$ under extreme slip length: (a) $l_s = 100$ nm; (b) $l_s = 200$ nm; (c) $l_s = 300$ nm.

The contour maps of film thickness with velocity slips at high surface velocity are shown in Figure 3-14. Under no slip condition $l_s = 0$, the surface dimple is located in the center contact area due to the temperature viscosity wedge effect [92]. As the surface velocity increases, the size of dimple becomes smaller. Under velocity slips, the film thickness at left side contact area decreases, squeezing the dimple moves to right side. The smaller surface velocity, the more significant film thickness reduction in the left

constriction. That is, at high surface velocity, the lubrication region falls into the category of hydrodynamic lubrication and the surface dimple shrunk because the absence of elastic deformation. Thus, the influence of velocity slip on dimple shape film weakens as the surface velocity increases.

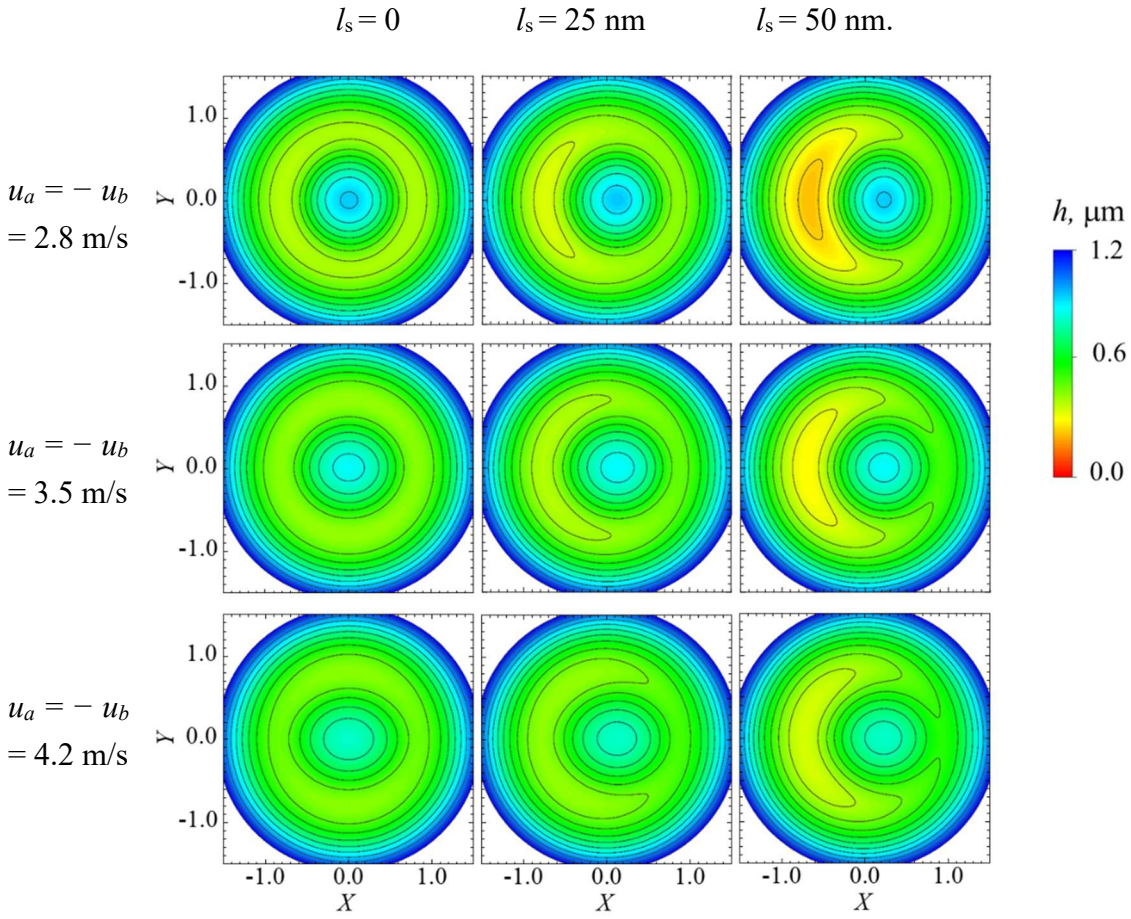

Figure 3-14 Contour maps of film thickness under different surface velocity: $u_a = -u_b$ = 2.8 m/s, 3.5 m/s, 4.2 m/s, and different velocity slip: l_s = 0, 25 nm, 50 nm.

Fig. 3-15 shows the pressure and film thickness profiles at the plane Y = 0 corresponding to Fig. 3-14. As the surface velocity increases, the depth of dimple and the minimum film thickness decrease under l_s = 0. As the slip length increases, the film thickness at the left side of the dimple decreases while the film thickness at the right side increases, squeezing the dimple to right side. The maximum pressure moves to the right side due to velocity slip, overlapping with the maximum film thickness.

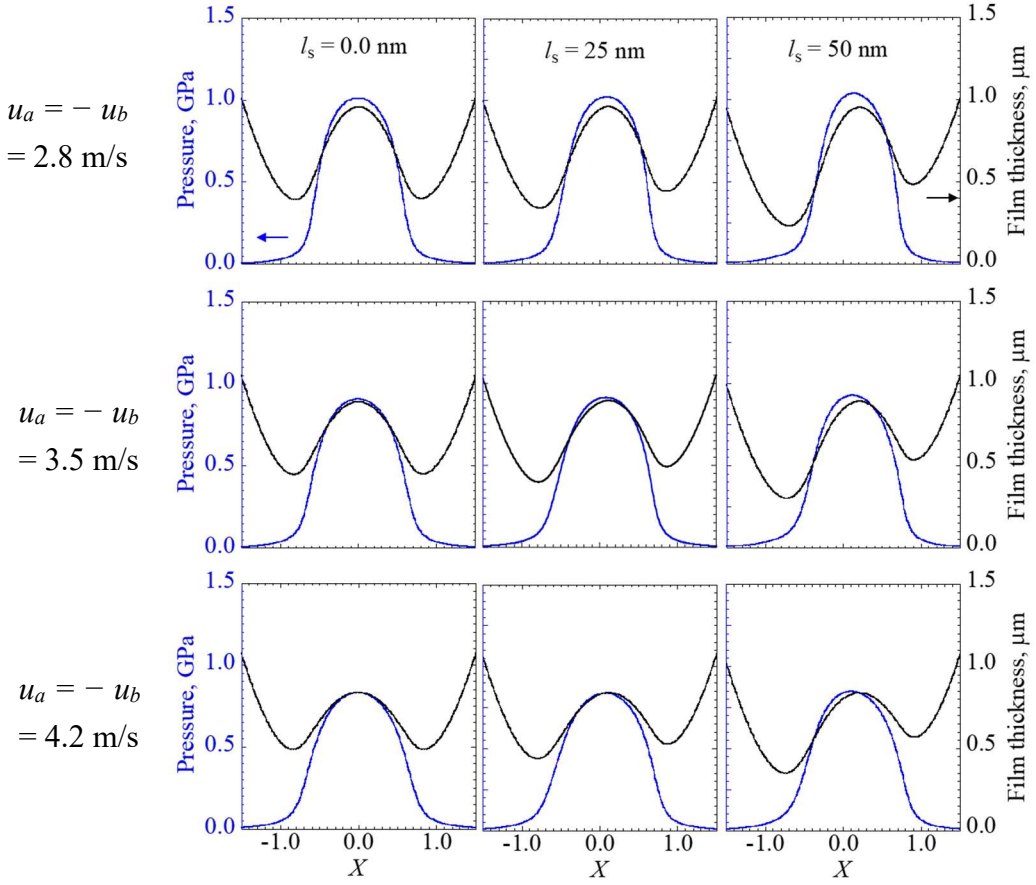

Figure 3-15 Film thickness and pressure profiles at the plane Y = 0 at different surface velocity: $u_a = -u_b$ = 2.8 m/s, 3.5 m/s, 4.2 m/s, and different velocity slip: l_s = 0, 25 nm, 50 nm.

3.3.3 Thermal slip effect

This section set the slip length of zero ($l_s = 0$) to focus on the thermal slip effect. The film thickness contour maps, and the corresponding pressure and film thickness profiles in the plane Y = 0 are illustrated in Fig. 3-16 for l_k = 0, 25 nm, and 50 nm with $u_a = -u_b$ = 2.1 m/s. In contrast to the results obtained under velocity slip, the surface dimple moves toward the opposite direction, that is, toward the left side of the contact region under the thermal slip. As the l_k increases, the film thickness at the left side decreases while the film thickness at right side increases, results in the pressure peak and the surface dimple move toward the left from the center area, which is consistent with the film thickness contour maps. Meanwhile, the dimple depth decreases significantly at l_k = 50 nm.

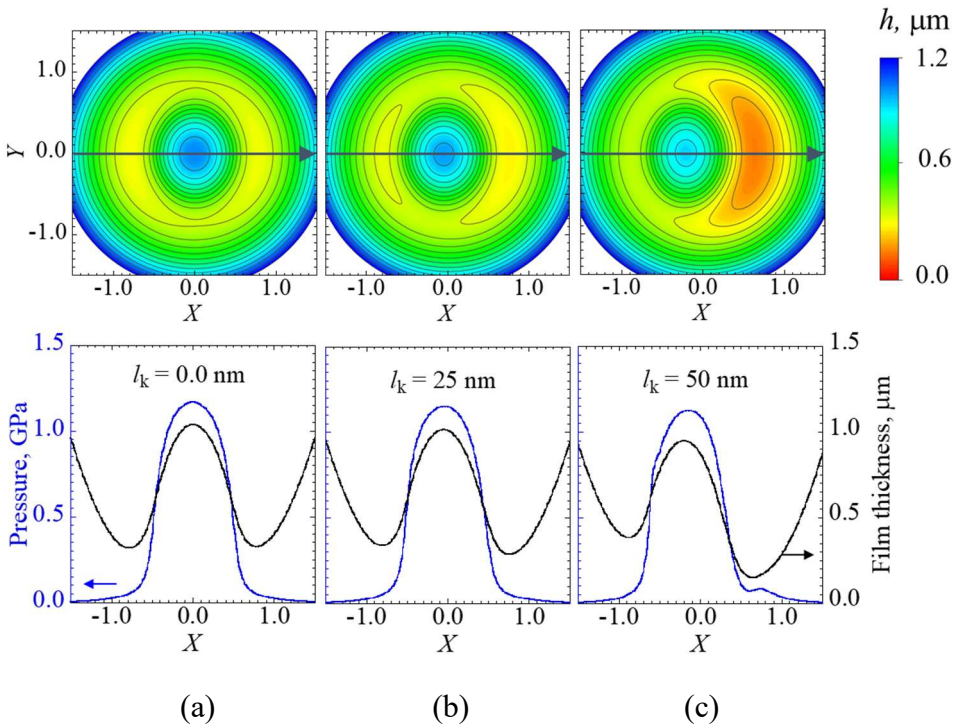

Figure 3-16 Contour maps of film thickness (top) and pressure, film thickness profiles on center plane Y = 0 (bottom) at $u_a = -u_b = 2.1$ m/s, $l_s = 0$ under different thermal slip: (a) $l_k = 0$; (b) $l_k = 25$ nm; (c) $l_k = 50$ nm.

Fig. 3-17 shows the temperature distributions along the x, y direction for $l_k = 0$, 25 nm, 50 nm on surfaces *a* and *b*. The temperature fields are non-uniform, and the temperature rise at $l_k = 50$ nm is the most prominent among the three simulation cases on surface *a*. while the temperature distributions on surface *b* is unremarkable because of the no slip conditions. The generated heat caused by shearing and compression of the lubricant is expected to dissipate through the lubricant and through surfaces *a* and *b*. However, the higher thermal resistance on surface *a* due to the increase in the thermal slip length limits heat dissipation from the lubricant to surface *a*. Thus, a significant temperature rise occurs, induces a reduction in the lubricant viscosity. Consequently, a greater amount of lubricant is retained on surface *a* (moving right) at $l_k = 50$ nm than that at $l_k = 0$, which causes the accumulated lubricant to be pushed toward the left side of the contact region. Therefore, the surface dimples in Fig. 3-16 move toward the left, which contradicts the dimple shift tendency in Fig. 3-11 caused by the velocity slip singularity.

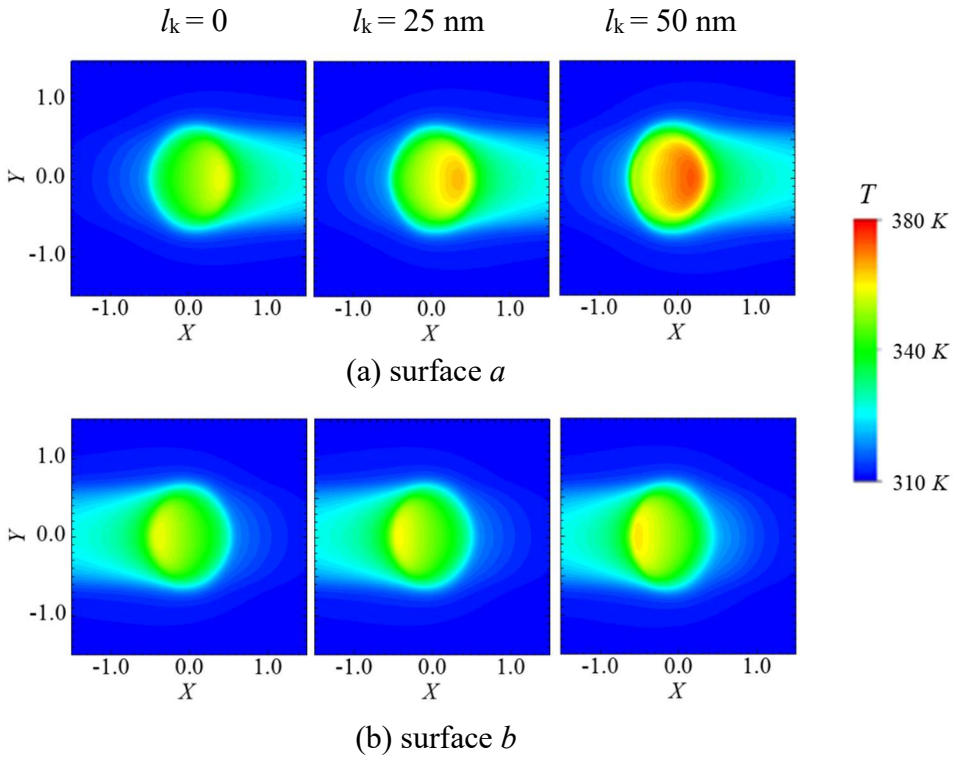

Figure 3-17 Effect of thermal slip length on lubricant temperature distributions on (a) surface *a* and (b) surface *b* under with $u_a = -u_b = 2.1$ m/s, $l_s = 0$.

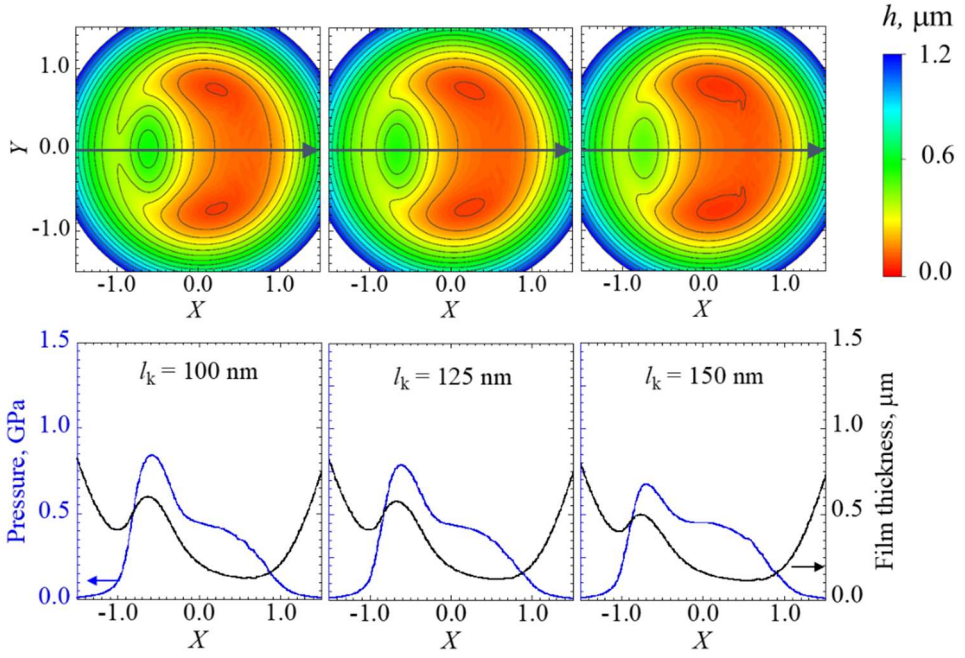

Figure 3-18 Contour maps of film thickness (top) and pressure, film thickness profiles on center plane Y = 0 (bottom) at $u_a = -u_b = 2.1$ m/s, $l_s = 0$.

Fig. 3-18 shows the contour maps of the lubricant film (top), and the pressure and film thickness profiles (bottom) in the plane Y = 0 for extreme thermal slip length condition: l_k = 100, 125 and 150 nm with $u_a = -u_b$ = 2.1 m/s. With the thermal slip length further increases, the film thickness at left constriction continues decreases, leads the dimple close to the location X = -1.0. Meanwhile, both the magnitude of the pressure peak and the dimple depth decrease significantly at large thermal slip length conditions.

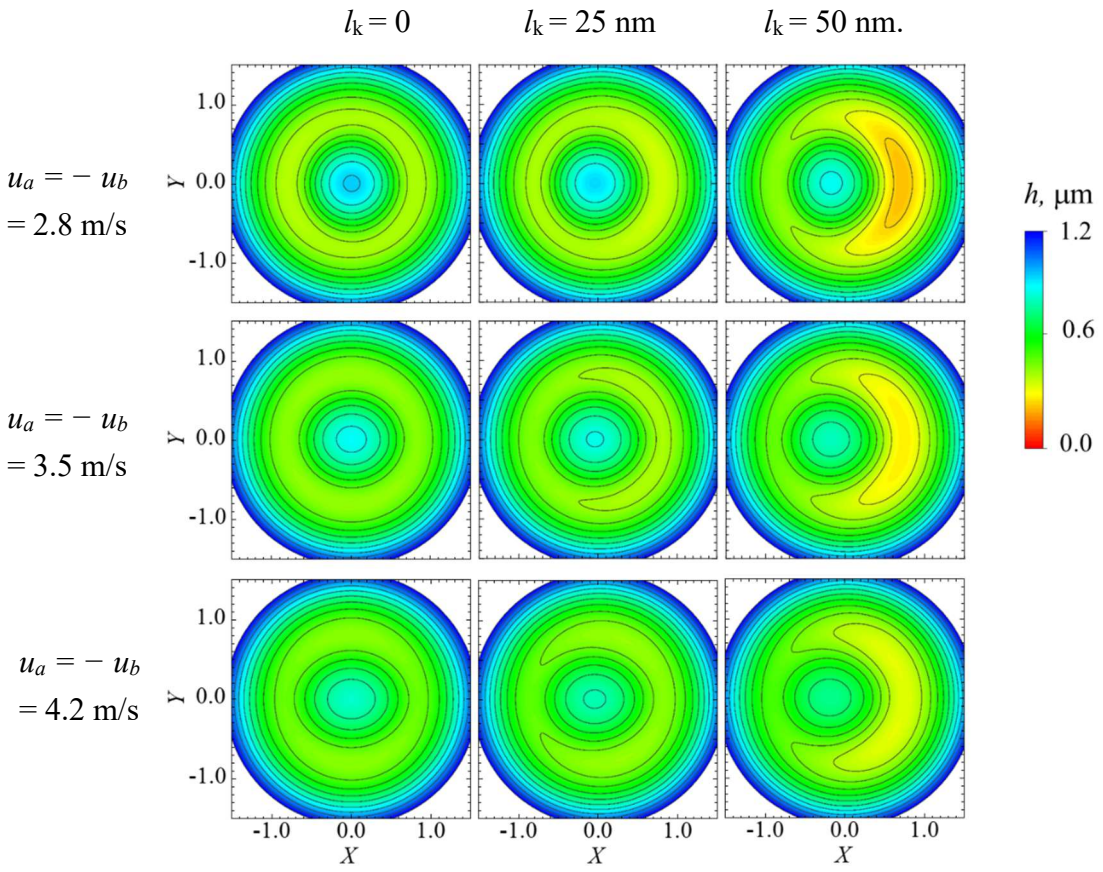

Figure 3-19 Contour maps of film thickness under different surface velocity: $u_a = -u_b$ = 2.8 m/s, 3.5 m/s, 4.2 m/s, and different thermal slip: l_k = 0, 25 nm, 50 nm.

Under high surface velocity, the lubrication region falls into the category of hydrodynamic lubrication and the surface dimple shrunk because the absence of elastic deformation. Figure 3-19 shows the contour maps of film thickness with different surface velocity: $u_a = -u_b$ = 2.8 m/s, 3.5 m/s, 4.2 m/s, and different thermal slip length: l_k = 0, 25 nm, 50 nm. With the increment of thermal slip length, the film thickness at the right side of dimple decreases and the dimple shifts to left side, opposite to velocity slip. At l_k = 50

nm, a significant constriction is observed. As the surface velocity or the thermal slip length increases, the size of dimple decreases due to the hydrodynamic lubrication. The larger surface velocity, the smaller influence of thermal slip length on surface dimple.

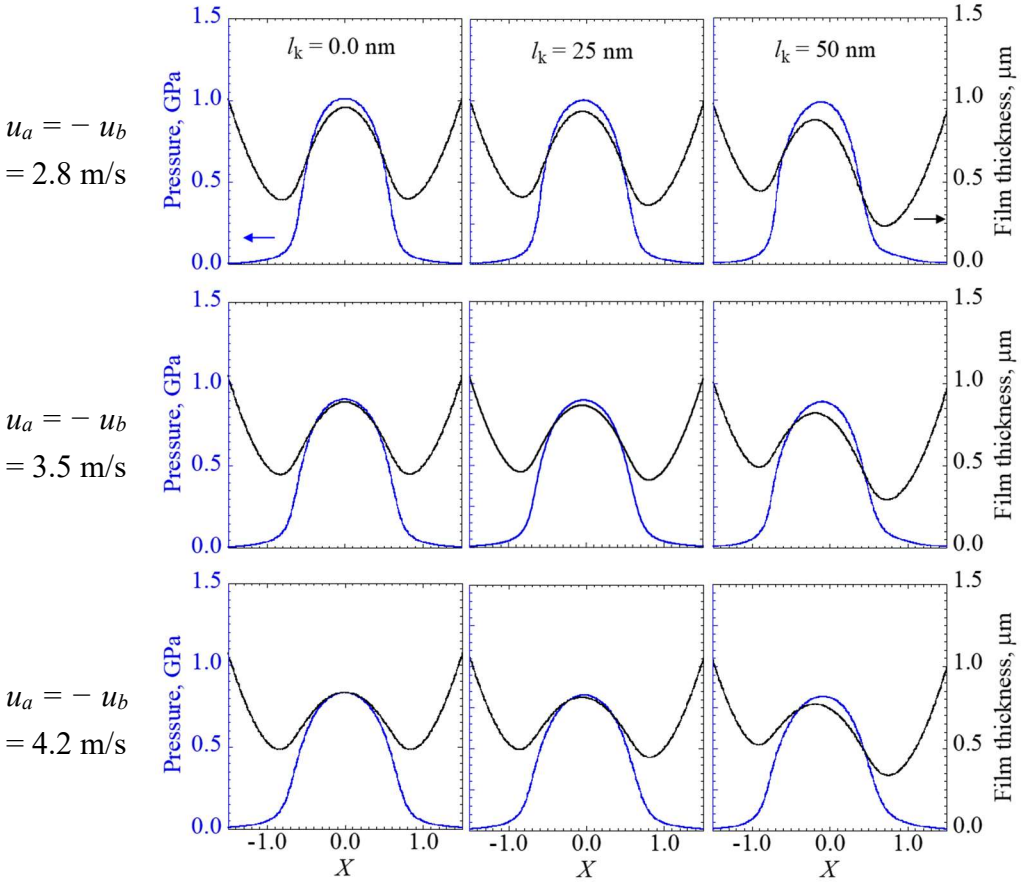

Figure 3-20 Film thickness and pressure profiles at the plane Y = 0 at different surface velocity: $u_a = -u_b$ = 2.8 m/s, 3.5 m/s, 4.2 m/s, and different thermal slip: l_k = 0, 25 nm, 50 nm.

The corresponding pressure and film thickness profiles at the plane Y = 0 are shown in Fig. 3-20. As the surface velocity increases, the pressure peak and maximum film thickness shift downward because of the hydrodynamic lubrication. With the increment of thermal slip length, the film thickness at the left side of the dimple increases while the film thickness at the right side of the dimple decreases, results in the location of the pressure peak and the dimple moves to left side of contact area, in contrast to the velocity slip results in Fig. 3-14.

3.3.4 Coupled velocity/thermal slips effect

In practice, the thermal slip and velocity slip could coexist in lubrication region when slip boundary occurs. The thermal slip and velocity slip may be related; however, there is no guarantee that the velocity and thermal slips depend on each other [144,150]. The coupled effect of velocity slip and thermal slip on the lubrication performance is discussed in this section based on the individual investigations described in previous sections.

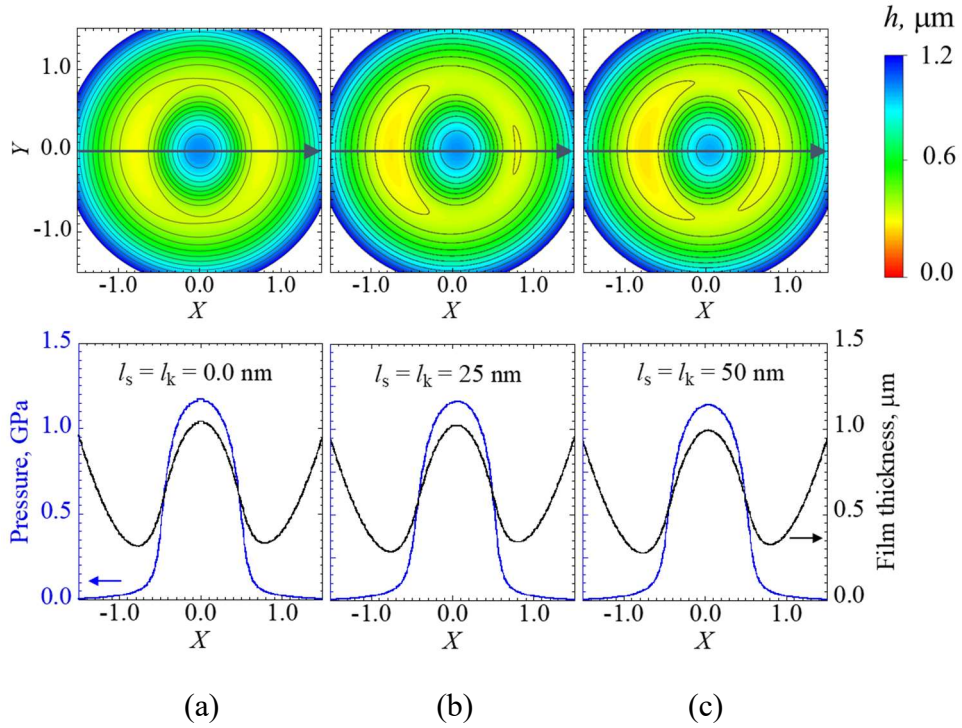

Figure 3-21 Contour maps of film thickness (top) and pressure, film thickness profiles on center plane Y = 0 (bottom) at $u_a = -u_b = 2.1$ m/s under different coupled velocity/thermal slips: (a) $l_s = l_k = 0$; (b) $l_s = l_k = 25$ nm; (c) $l_s = l_k = 50$ nm.

Fig. 3-21 shows the contour maps of film thickness (top) and pressure, film thickness profiles on center plane Y = 0 (bottom) at $u_a = -u_b = 2.1$ m/s under different coupled velocity/thermal slips. The velocity slip length is adopted equal to thermal slip length under the conditions of coupled velocity/thermal slips. In Figs. 3-21(b) and (c), a shallow constriction appears at the sides of dimple, the pressure and film thickness profiles have neglectable variation. That is, the coupled effects of velocity and thermal slips cancel out

one another when the slip length is comparable to the thermal slip length as $l_s = l_k = 25$ nm, and $l_s = l_k = 50$ nm.

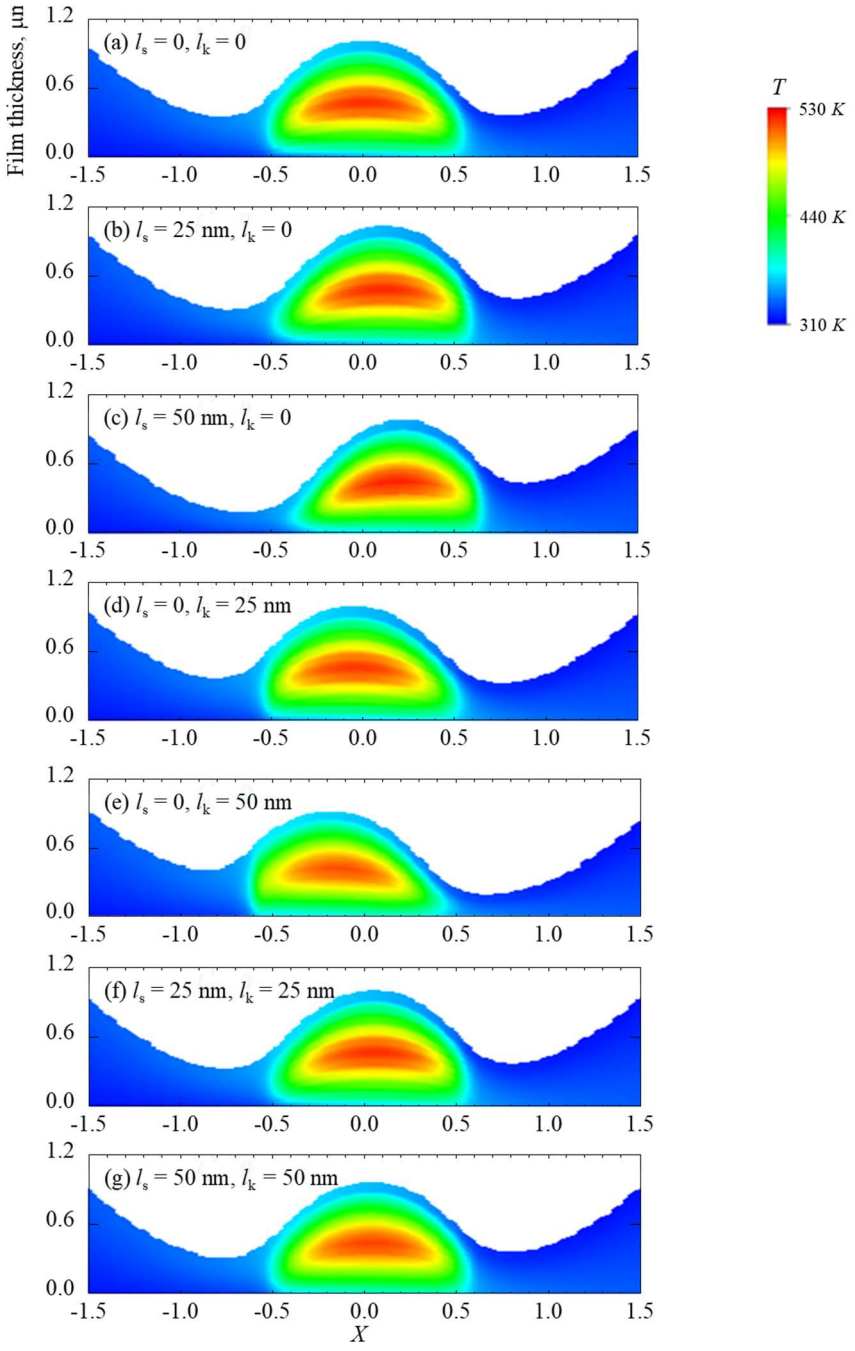

Figure 3-22 Temperature distributions inside the lubricant film on the plane Y = 0 at $u_a = -u_b = 2.1$ m/s under different boundary slips: (a) $l_s = l_k = 0$; (b) $l_s = 25$ nm, $l_k = 0$; (c) $l_s = 50$ nm, $l_k = 0$; (d) $l_s = 0$, $l_k = 25$ nm; (e) $l_s = 0$, $l_k = 50$ nm; (f) $l_s = l_k = 25$ nm; (g) $l_s = l_k = 50$ nm.

Fig. 3-22 shows the temperature distributions inside the lubricant film in the plane Y = 0 for (a) no slip, (b) and (c) only velocity slip, (d) and (e) only thermal slip, (f) and (g) coupled velocity and thermal slips. As shown in Fig. 3-22(a), the maximum lubricant temperature due to shearing and compression of the lubricant is at the center of the contact area, overlapping with the locations of the maximum pressure and surface dimple. A comparison among Figs. 3-22(a), (b), and (c) shows that the location of the maximum temperature moves from the center toward the right as the slip length increases. By contrast, the increase of the thermal slip length causes the temperature rise region to shift leftward, as shown in Figs. 3-22(d) and (e). Unexpectedly, the effects of the coupled velocity slip and thermal slip (l_s = l_k) on the temperature distributions cancel out one another, as shown in Figs. 3-22(f) and (g), resulting in a similar temperature map as that in Fig. 3-22(a).

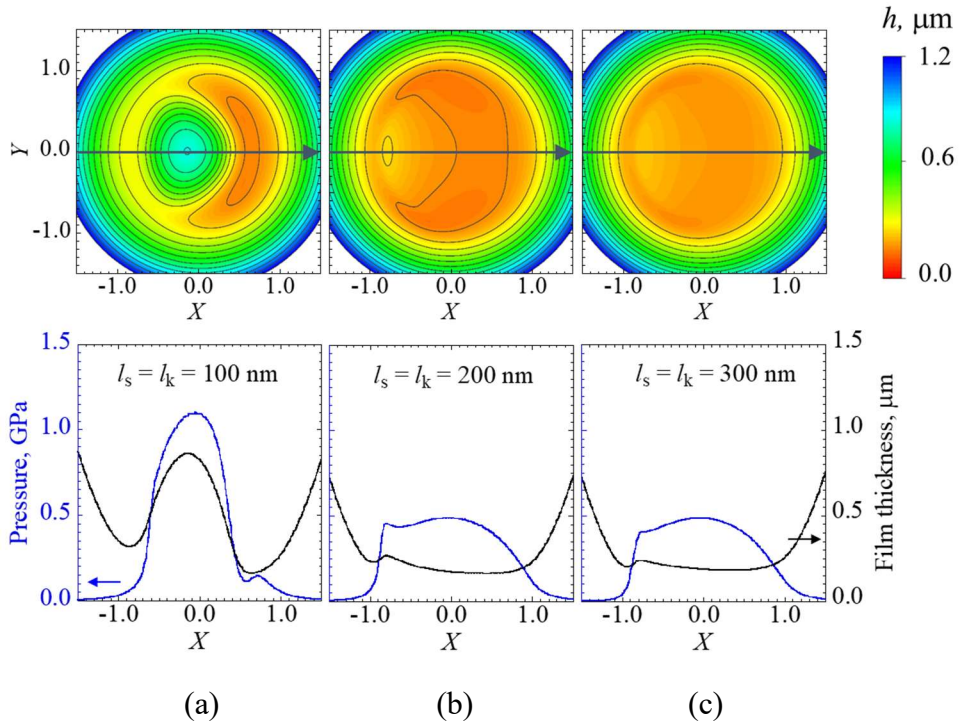

Figure 3-23 Contour maps of film thickness (top) and pressure, film thickness profiles on center plane Y = 0 (bottom) at $u_a = -u_b$ = 2.1 m/s under extreme coupled velocity/thermal slips: (a) $l_s = l_k$ = 100 nm; (b) $l_s = l_k$ = 200 nm; (c) $l_s = l_k$ = 300 nm.

Fig. 3-23 shows the contour maps of film thickness (top) and pressure, film thickness profiles on center plane Y = 0 (bottom) at $u_a = -u_b$ = 2.1 m/s under extreme coupled

velocity/thermal slips $l_s = l_k = 100$ nm, 200 nm, 300 nm. In Fig. 3-23(a), $l_s = l_k = 100$ nm, a significant constriction appears at right side of contact area, pushing the dimple and the pressure peak towards to left side. As the value of l_s and l_k further increases, the dimple becomes insignificant while the pressure peak decreases. When $l_s = l_k = 300$ nm, the dimple almost disappears and the film shape in contact turns into a plateau.

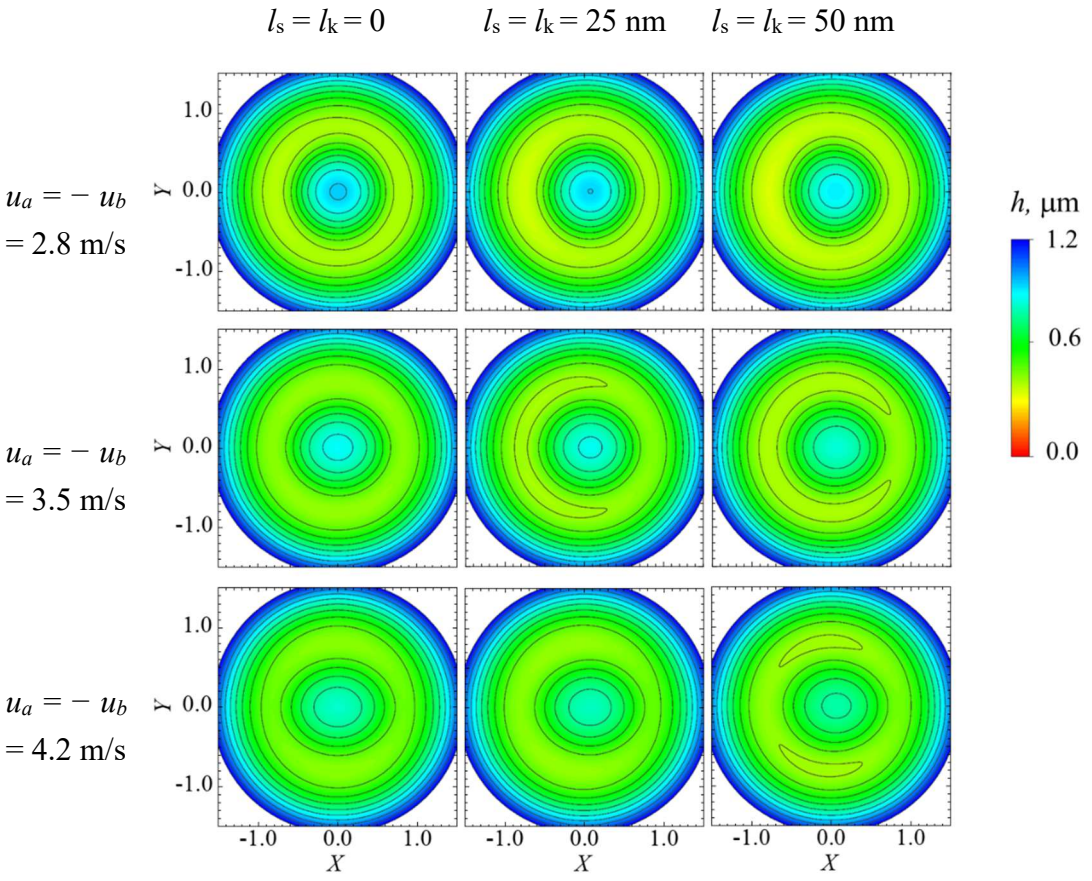

Figure 3-24 Contour maps of film thickness under different surface velocity: $u_a = -u_b = 2.8$ m/s, 3.5 m/s, 4.2 m/s, and different coupled velocity/thermal slips: $l_s = l_k = 0$, 25 nm, 50 nm.

The comparison results of different surface velocity and coupled velocity/thermal slips are presented by contour maps of film thickness shown in Fig. 3-24 and the corresponding pressure, film thickness profiles shown in Fig. 3-25. It is clearly evident that, at the case of $u_a = -u_b = 2.8$ m/s, the film thickness and pressure show a little variation with the increment of l_s and l_k. At the cases of high surface velocity $u_a = -u_b = 3.5$ m/s and 4.2 m/s, the film thickness at left side slightly decreases, results in a shallow constriction in

contour maps of film thickness. However, this variation is neglectable because the effects of velocity and thermal slips cancel out one another when $l_s = l_k = 25$ nm, 50 nm.

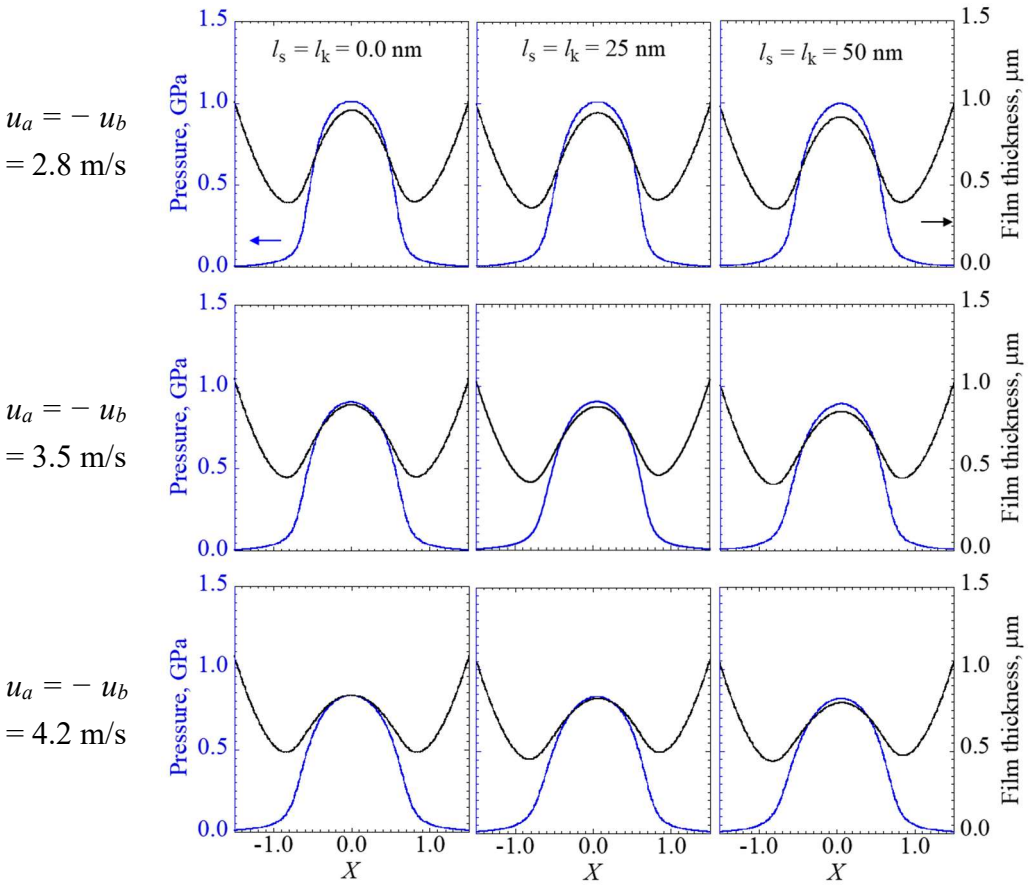

Figure 3-25 Film thickness and pressure profiles at the plane Y = 0 at different surface velocity: $u_a = -u_b$ = 2.8 m/s, 3.5 m/s, 4.2 m/s, and different coupled velocity/thermal slips: $l_s = l_k = 0$, 25 nm, 50 nm.

In summary, the film thickness under ZEV contact can be significantly influenced by both velocity slip and thermal slip at the solid–lubricant interface due to the comparable scale of the slip lengths to the film thickness. However, the coupled effects of velocity and thermal slips cancel out one another when the slip length is comparable to the thermal slip length. Although the shape of the dimple changes slightly under the boundary slips for ZEV contact, the locations of the dimple, pressure peak, and temperature rise change remarkably. Because there is no guarantee that the slip length and the thermal slip length are comparable at a practical solid–lubricant interface, the effects of the coupled slips on

the main factor (that is, either slip length or thermal slip length) should be carefully considered. When the slip length is the main factor, the lubrication features will follow the results presented in section 3.3.1. When the thermal slip length is the main factor, the lubrication features will follow the results presented in section 3.3.2.

3.4 Rolling/sliding motion

3.4.1 Simulation system

Under rolling/sliding motion, the contact surfaces move in same direction but with different velocities, in which the temperature rise and film thickness reduction are the most important factors to estimate the lubrication in EHL. From a fundamental perspective, the coupling of the velocity discontinuity [138,157] and temperature jump [144,158,159] at the solid–lubricant interface are of particular importance for ensuring the lubrication performance in EHL contacts to avoid lubrication breakdown.

Boundary slips at one sliding surface have been investigated in previous sections; however, temperature rise and film thickness reduction may become prominent when boundary slips occur at all moving surfaces. Therefore, we conducted a further thermal EHL analysis in this section by applying boundary slip conditions to two moving surfaces under rolling/sliding motion. Three cases of boundary slips, i.e., velocity, thermal, and coupled velocity/thermal slips, were investigated to clarify the temperature rise and film thickness reduction with the entrainment velocity or slide–roll ratio in EHL.

Table 3-4 Operation conditions.

Ball radius, R, m	0.0127
Load, w, N	30
Entrainment velocity, $u_e = (u_a + u_b)/2$, m/s	0 ~ 15
Slide-roll ratio, SRR = $(u_a - u_b)/u_e$	0 ~ 2
Velocity slip length, l_s, μm	0 ~ 50
Thermal slip length, l_k, μm	0 ~ 50

Table 3-4 shows the operation conditions used in this section. The entrainment velocity various from 0 to 15 m/s, and the slide-roll ratio changes from 0 to 2 to emphasizes the effect of temperature rise on lubrication performances. Both the values of the velocity slip length and thermal slip length in a range of 0 ~ 50 μm are selected by considering their effects on lubrication behaviors.

3.4.2 Boundary slip effect

To characterize the effects of boundary slip on lubrication, three cases of boundary slips were investigated in our numerical simulations: (1) velocity slip, (2) thermal slip, and (3) coupled velocity/thermal slips; subsequently, these cases were compared with the classical no slip solution.

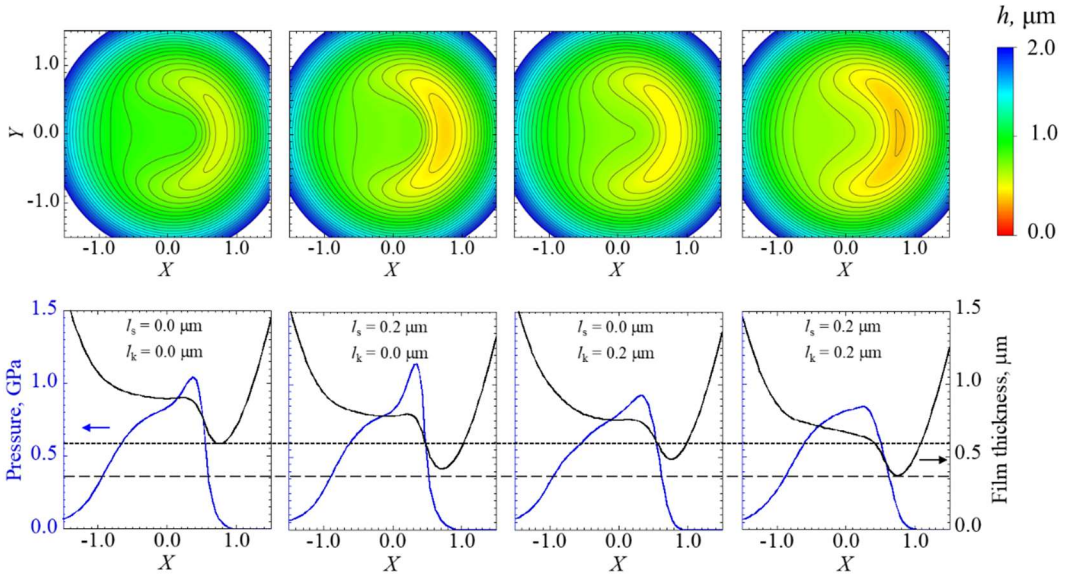

Figure 3-26 Contour maps of film thickness (top) and pressure, film thickness profiles on center plane Y = 0 (bottom) at u_e = 3.6 m/s, SRR = 1.5 under different boundary conditions: (a) no slip; (b) velocity slip; (c) thermal slip; (d) coupled velocity/thermal slips. Dotted line represents minimum film thickness of no-slip case; dashed line represents minimum film thickness for case of $l_s = l_k = 0.2$ μm.

The contour maps of the film thickness, pressure, and film thickness profiles are shown in Fig. 3-26. Here, the boundary slips length of 0.2 μm is comparable to the classical film

thickness of the EHL contact [84]. The result of $l_s = l_k = 0$, which is a typical solution of the EHL point contact, is shown in Fig. 3-26(a). A central plateau and an outer constriction are evident in the contour maps. Compared with Fig. 3-26(a), a greater pressure peak is shown in Fig. 3-26(b), whereas lower pressure peaks are shown in Figs. 3-26(c) and (d). Meanwhile, the film thickness at the outer constrictions decreases when $l_s = 0.2$ μm and $l_k = 0$, as shown in Fig. 3-26(b), whereas the central plateau film inclines slightly when $l_s = 0$ and $l_k = 0.2$ μm, as shown in Fig. 3-26(c). For the coupled velocity/thermal slips when $l_s = l_k = 0.2$ μm, as shown in Fig. 3-26(d), the film thickness at the outer constrictions decreases, accompanied by an inclined lubricant film. The film thickness shown in Fig. 3-26(d) is the thinnest among the cases, owing to the reduction in film thickness induced by the velocity slip and thermal slip. The film thickness reduction induced by the velocity slip is attributed to the lower lubricant velocity, which entrains less lubricant into the contact area [142,175]. On the other hand, the thermal slip-induced film thickness reduction is attributed to the lower viscosity of the lubricant due to the temperature rise in the contact area. Comparing the minimum film thickness with that of the no slip (dotted line) and $l_s = l_k = 0.2$ μm (dashed line) cases, it is clear that the film thickness reduction is primarily induced by the velocity slip.

Fig. 3-27 presents the temperature profiles on the center plane (Y = 0) in the EHL contact area. Fig. 3-27(a) shows the results of the no slip boundary condition ($l_s = l_k = 0$), where the temperature of the lubricant increases significantly at the center of the film thickness. This temperature rise is caused by the heat generated in the lubricant film due to the compression and shearing in the EHL contact area. Since the generated heat can be removed from the lubricant to the two moving solid walls, increasing the wall velocity can enhance heat dissipation. Consequently, both the surface temperature and the inner temperature of solid *a* are smaller than those of solid *b* because the velocity of solid *a* is seven times larger than that of solid *b* at SRR = 1.5. In the case of $l_s = 0.2$ μm, the temperature profile in Fig. 3-27(b) is similar to that in Fig. 3-27(a), but the maximum lubricant temperature is higher than that in Fig. 3-27(a) because of the increase in the maximum pressure under velocity slip. Comparing Figs. 3-27(c) and (d) to (a), the area of lubricant temperature exceeding 400 K (green) expands significantly at the left side of the contact area, whereas the maximum lubricant temperature decreases. In particular, the lubricant temperature near the solid walls increases significantly. The main reason for this

temperature rise is the limited heat dissipation from the lubricant to solids under thermal slip at the two moving solid boundaries.

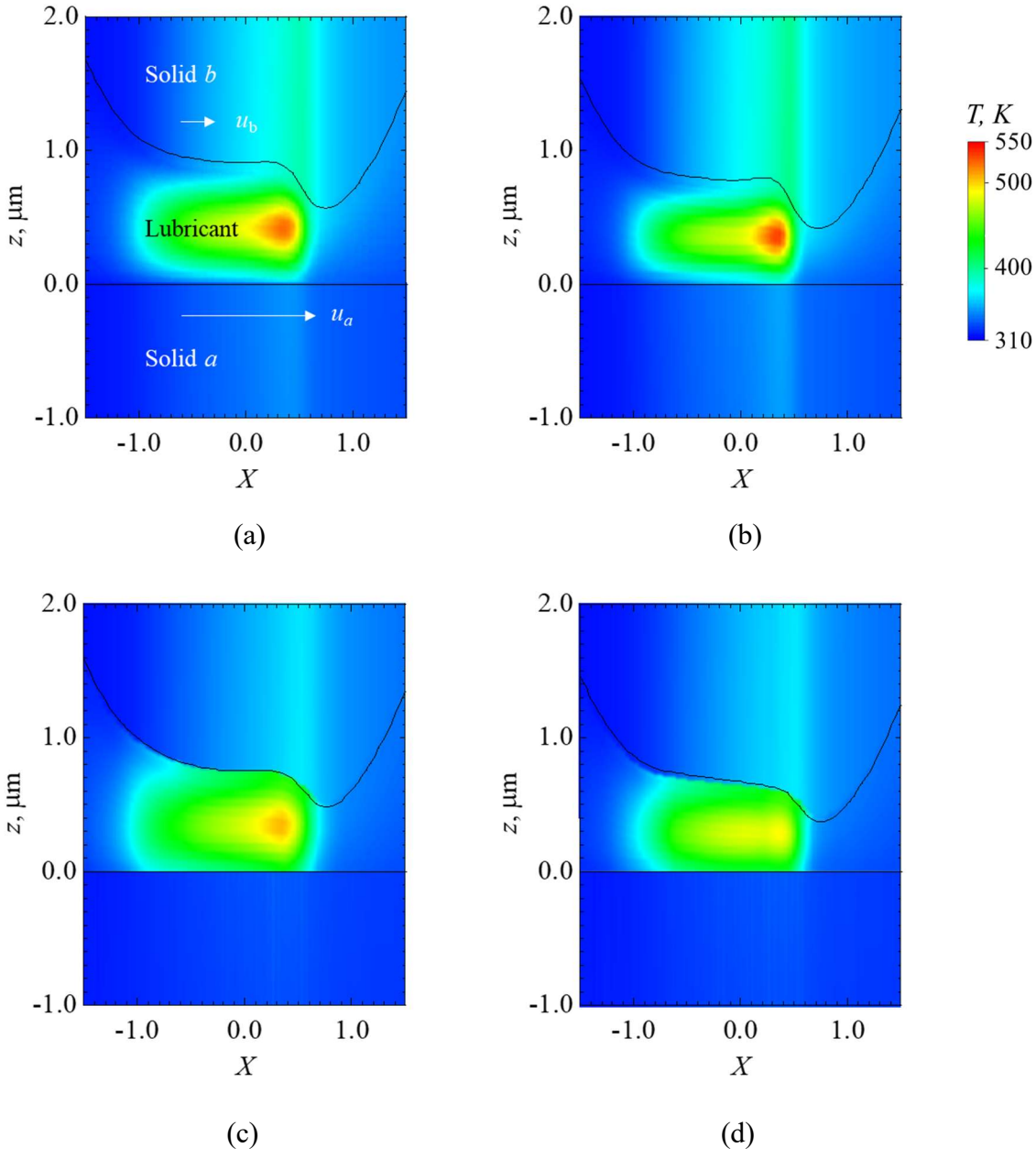

Figure 3-27 Temperature profiles on center plane (Y = 0) in EHL contact area at u_e = 3.6 m/s, SRR = 1.5 under different boundary conditions: (a) $l_s = l_k = 0$; (b) l_s = 0.2 μm, $l_k = 0$; (c) $l_s = 0$, l_k = 0.2 μm; (d) $l_s = l_k$ = 0.2 μm.

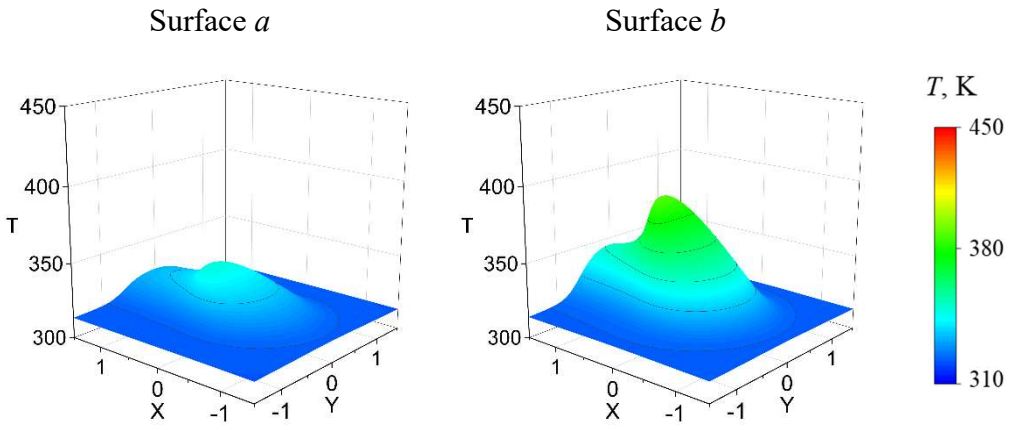

(a) $l_s = l_k = 0$

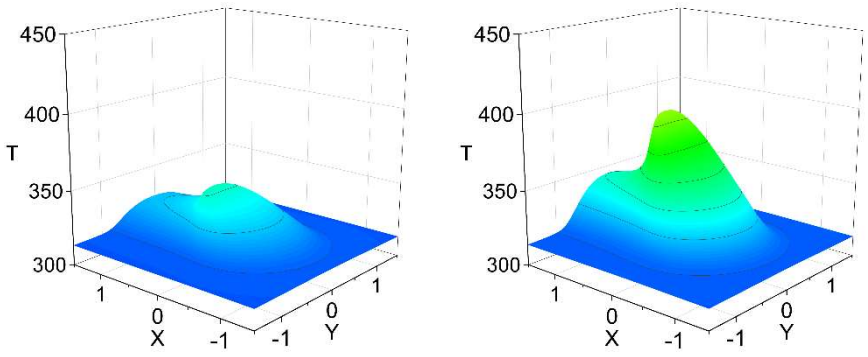

(b) $l_s = 0.2$ μm, $l_k = 0$

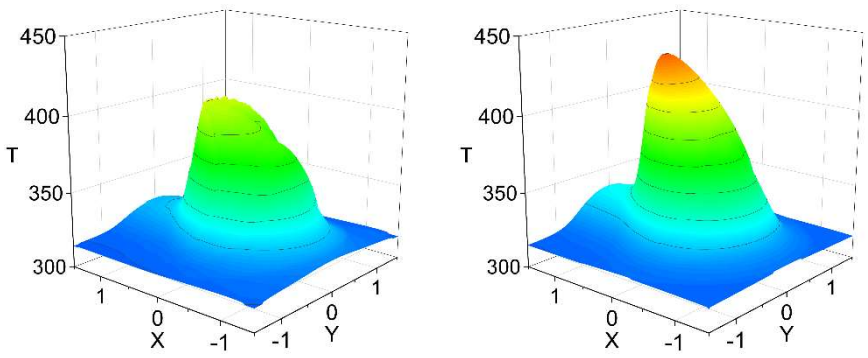

(c) $l_s = 0$, $l_k = 0.2$ μm

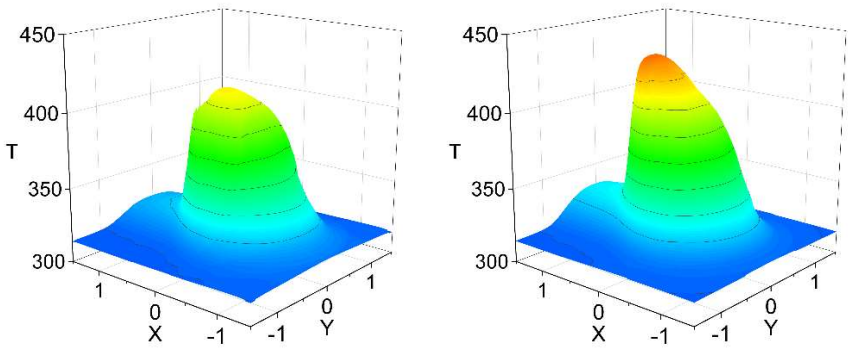

(d) $l_s = l_k = 0.2$ μm

Figure 3-28 Temperature profiles on surfaces *a* and *b* in EHL contact area at u_e = 3.6 m/s, SRR = 1.5 under different boundary conditions: (a) $l_s = l_k = 0$; (b) l_s = 0.2 μm, $l_k = 0$; (c) $l_s = 0$, l_k = 0.2 μm; (d) $l_s = l_k$ = 0.2 μm.

Fig. 3-28 shows the 3D temperature rise on surfaces *a* and *b* in EHL contact area under different boundary conditions, corresponding to Figs. 3-27 and 3-26. The maximum temperature is at the center of contact area owing to effect of the lubricant shearing, overlapping with the maximum temperature of lubricant in Fig. 3-27. It also can be clearly seen that the temperature rises in solids *a* and *b* are unsignificant with velocity slip shown in Figs. 3-28(a) and (b), while those shown in Figs. 3-28(c) and (d) are remarkable compared with those in Figs. 3-28(a) and (b) due to the restricted heat dissipation by thermal slip. Meanwhile, the temperature rise on surface *a* is smaller than that on surface *b*. That is, under SRR = 1.5, the velocity of solid *a* is seven times larger than that of solid *b*. The wall velocity can enhance heat dissipation from the lubricant to the two moving solids, consequently, the surface temperature distributions of solid *a* are smaller than those of solid *b*. In Figs. 3-28(c) and (d), due to the thermal slip effect, this difference decreases. Since a higher lubricant temperature result in a lower viscosity, thinner film thicknesses are formed in Figs. 3-28(c) and (d) compared with those shown in Fig. 3-28(a). However, the film thickness reduction induced by the thermal slip is smaller than that induced by the velocity slip. In other words, when the thermal slip length is the same as the slip length, the film thickness reduction is primarily induced by the velocity slip, as described previously.

The results presented in Fig. 3-26 show that the coupled velocity/thermal slips exhibit the worst tribological performance among the cases investigated. In particular, the effect of thermal slip on the temperature rise in the vicinity of the solid walls is dominant. Since the thermal slip length might not be of the same order as the slip length [149,150], further analysis was conducted to investigate the superiority of the boundary slips.

Figs. 3-29 show the results under the coupled velocity/thermal slips, where the cases of $l_s / l_k < 1$ indicate the superiority of thermal slip over velocity slip, and those of $l_s / l_k > 1$ indicate the superiority of velocity slip over thermal slip. As shown in the contour maps, the film thickness at the center plateau and outer constriction decreases with the increase in the thermal slip length (Figs. 3-29(a)–(c)) or velocity slip length (Figs. 3-29(d)–(f)). The film thickness reduction shown in Figs. 3-29(c) and (f) is more significant than that of the other cases, where a thin lubricant film of 20–60 nm covers the entire EHL contact area. Meanwhile, the pressure peak shown in Figs. 3-29(c) and (f) are less evident compared with those shown in Figs. 3-29(a) and (d). A further increase in the boundary slips might result in a transition from EHL to boundary lubrication, accompanied by lubrication failure. In the case of $l_s / l_k < 1$, the film thickness reductions are dominated by thermal slip, whereas those of $l_s / l_k > 1$ are due to the superiority of the velocity slip.

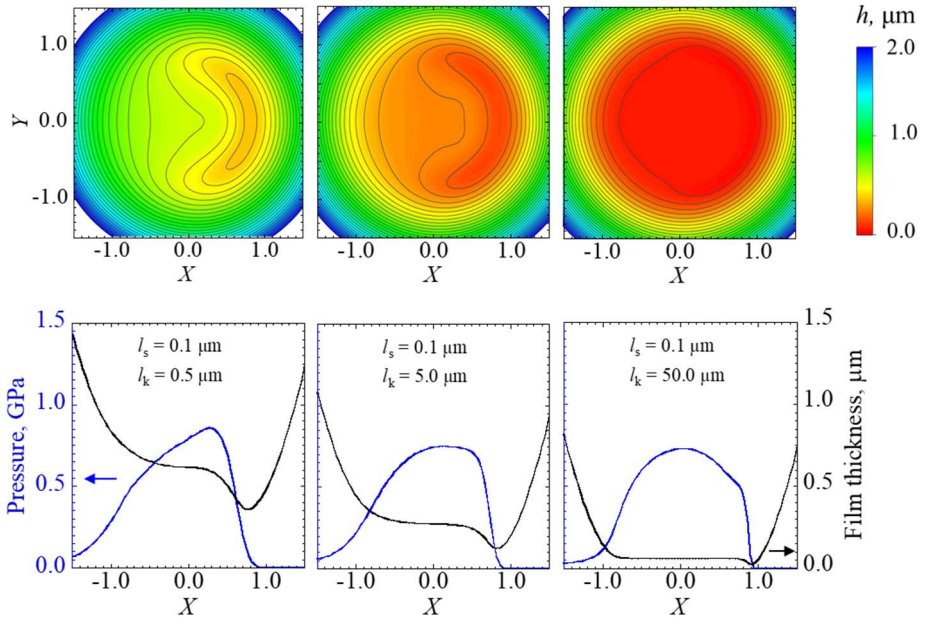

(a) (b) (c)

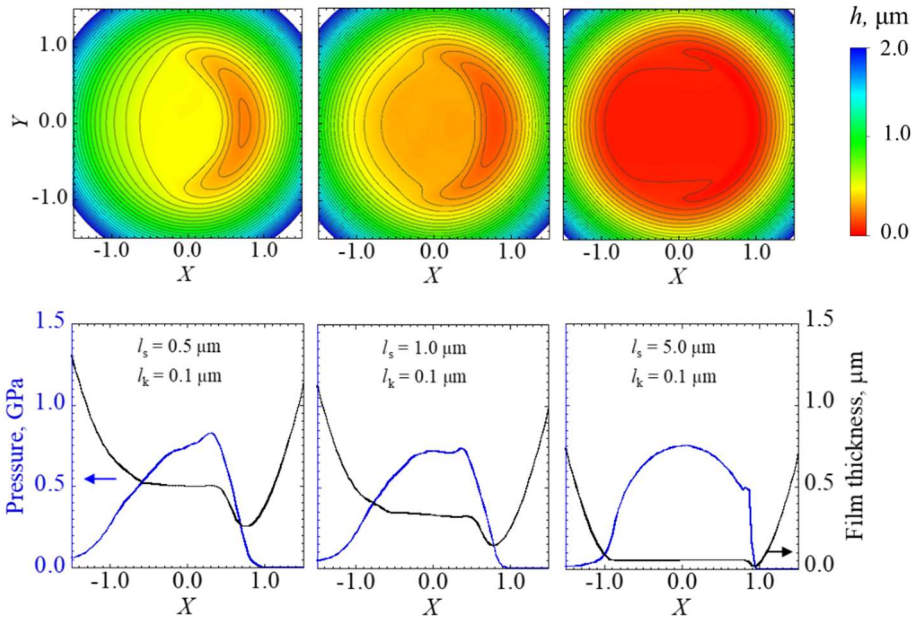

(d) (e) (f)

Figure 3-29 Contour maps of film thickness (top) and pressure, film thickness profiles on center plane Y = 0 (bottom) at u_e = 3.6 m/s, SRR = 1.5 under coupled velocity/thermal slips: (a) l_s / l_k = 0.1 μm/ 0.5 μm; (b) l_s / l_k = 0.1 μm/ 5.0 μm; (c) l_s / l_k = 0.1 μm/ 50.0 μm; (d) l_s / l_k = 0.5 μm/ 0.1 μm; (e) l_s / l_k = 1.0 μm/ 0.1 μm; (f) l_s / l_k = 5.0 μm/ 0.1 μm.

Similar to Fig. 3-27, Fig. 3-30 shows the temperature profiles under the coupled velocity/thermal slips; Figs. 3-30(a)–(c) show the cases of l_s / l_k < 1, whereas Figs. 3-30(d)–(f) show the cases of l_s / l_k > 1. As shown in Figs. 3-30(a)–(c), a larger l_k induces a more significant lubricant temperature rise in the entire contact area. The reason contributing to the l_k-induced temperature rise is the same as that for Fig. 3-30, i.e., the limited heat dissipation from the lubricant to the solids. The maximum lubricant temperature rise is approximately 300 K at l_k = 50.0 μm, as shown in Fig. 3-30(c), accompanied by a temperature rise in the entire contact area of the lubricant. Simultaneously, the lubricant film thickness decreases to a critical level owing to the reduced viscosity corresponding to the temperature rise. Meanwhile, the larger l_s induces a lower lubricant temperature rise, as shown in Figs. 3-30(d)–(f). Since the lubricant velocity decreases under the velocity slip, the amount of heat generation decreases and hence, a smaller temperature rise is induced in the contact area. Meanwhile, the lower

lubricant velocity limits the amount of lubricant entraining into the contact area and hence, reduces the film thickness.

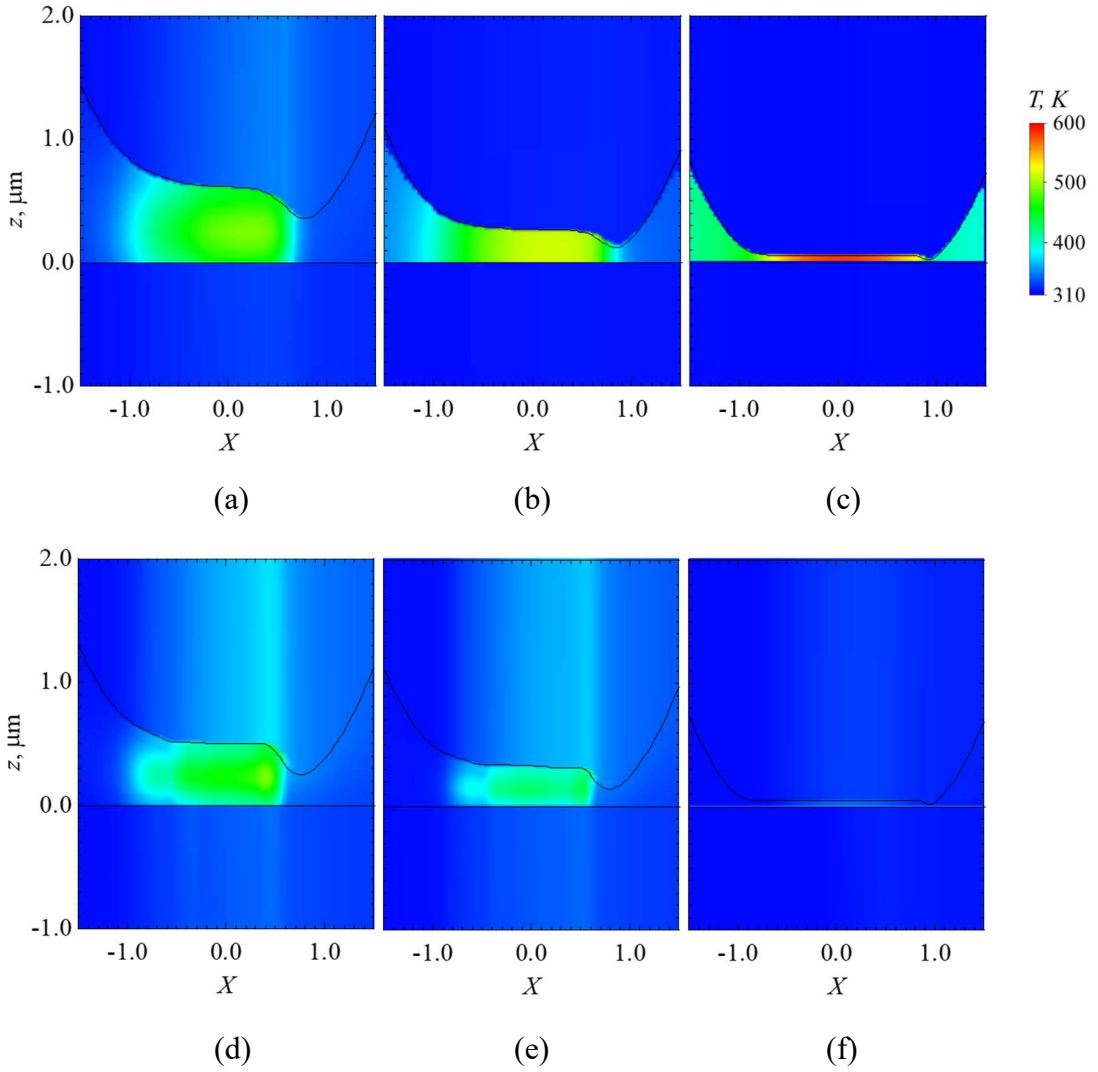

Figure 3-30 Temperature profiles on center plane (Y = 0) in EHL contact area at u_e = 3.6 m/s, SRR = 1.5 under different boundary conditions: (a) l_s / l_k = 0.1 μm/ 0.5 μm; (b) l_s / l_k = 0.1 μm/ 5.0 μm; (c) l_s / l_k = 0.1 μm/ 50.0 μm; (d) l_s / l_k = 0.5 μm/ 0.1 μm; (e) l_s / l_k = 1.0 μm/ 0.1 μm; (f) l_s / l_k = 5.0 μm/ 0.1 μm.

In summary, the velocity slip dominates the film thickness reduction when the slip length is comparable to the thermal slip length, whereas the thermal slip dominates the film thickness reduction when the slip length is negligible compared with the thermal slip length. In the coupled velocity/thermal slips case, the superior velocity slip might result

in a lower temperature in the lubricant and solids, whereas the superior thermal slip might result in a temperature rise in the entire contact area in the lubricant as the film thickness decreases simultaneously.

3.4.3 Entrainment velocity

The entrainment velocity is known as one of the key parameters in the lubrication of sliding/rolling contacts because the entrainment velocity can result in a variation in the amount of entrained lubricant and shear rate. Hence, the effects of the entrainment velocity on the lubrication characteristics with boundary slips at SRR = 1.5 are discussed in this section.

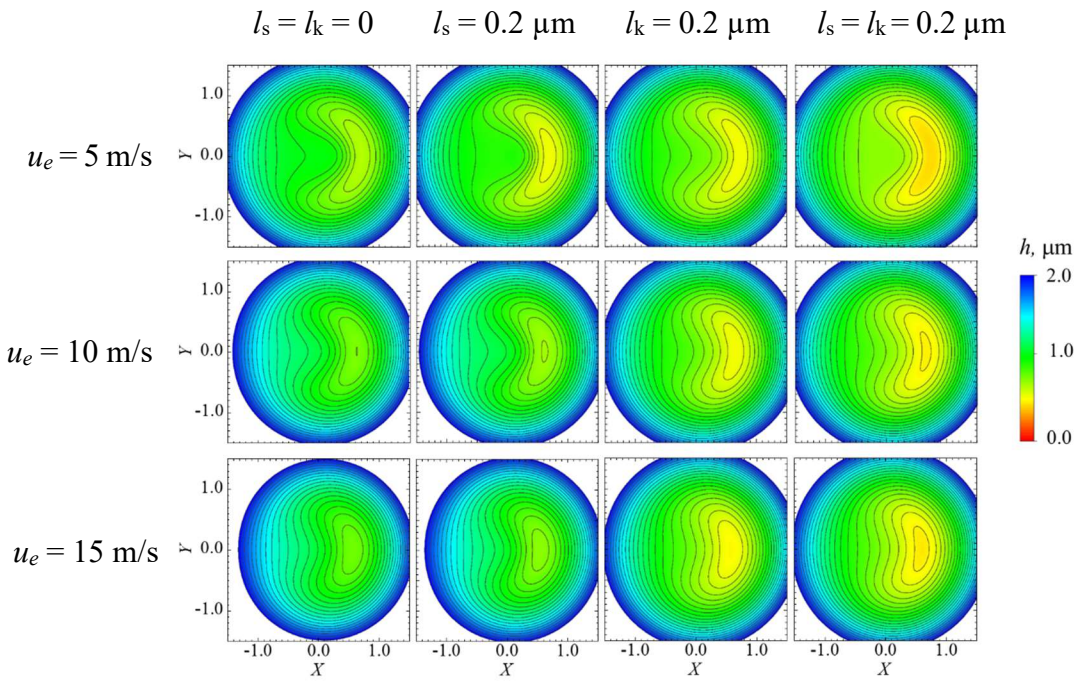

Figure 3-31 Contour maps of film thickness at different entrainment velocity: u_e = 5 m/s, 10 m/s, 15 m/s, and different boundary slips: no slip $l_s = l_k = 0$, velocity slip $l_s = 0.2$ μm, $l_k = 0$, thermal slip $l_k = 0.2$ μm, $l_s = 0$, coupled velocity/thermal slips $l_s = l_k = 0.2$ μm

Fig. 3-31 shows the comparison results of the film thickness contour maps at different entrainment velocities: u_e = 5 m/s, 10 m/s, 15 m/s, and different boundary slips: no slip, velocity slip, thermal slip, coupled velocity/thermal slips. The value of the boundary slips

length of 0.2 μm is adopted same to Fig. 3-26. Under no slip condition $l_s = l_k = 0$, the shape of film inclines more sharply as the entrainment velocity increases. At high entrainment velocity, the lubrication falls into the hydrodynamic lubrication, reduces the elastic deformation of surface. Thus, the classical center plateau disappears. Compared with no slip results, the velocity slip results in slightly smaller film thickness, while the reduction in film thickness caused by thermal slip is more significant as shown in Fig. 3-30. When $l_s = l_k = 0.2$ μm, the coupled velocity/thermal slips exhibit the thinnest film thickness among these cases. Furthermore, the value of film thickness reduction caused by velocity slip decreases at high entrainment velocity. Meanwhile, the film thickness reduction caused by thermal slip becomes remarkable. That is, increases entrainment velocity leads large film thickness and the temperature rise. The large film thickness reduces the influences of velocity slip while the high temperature rise promotes the thermal slip effect, leads greater film thickness than the case of velocity slip.

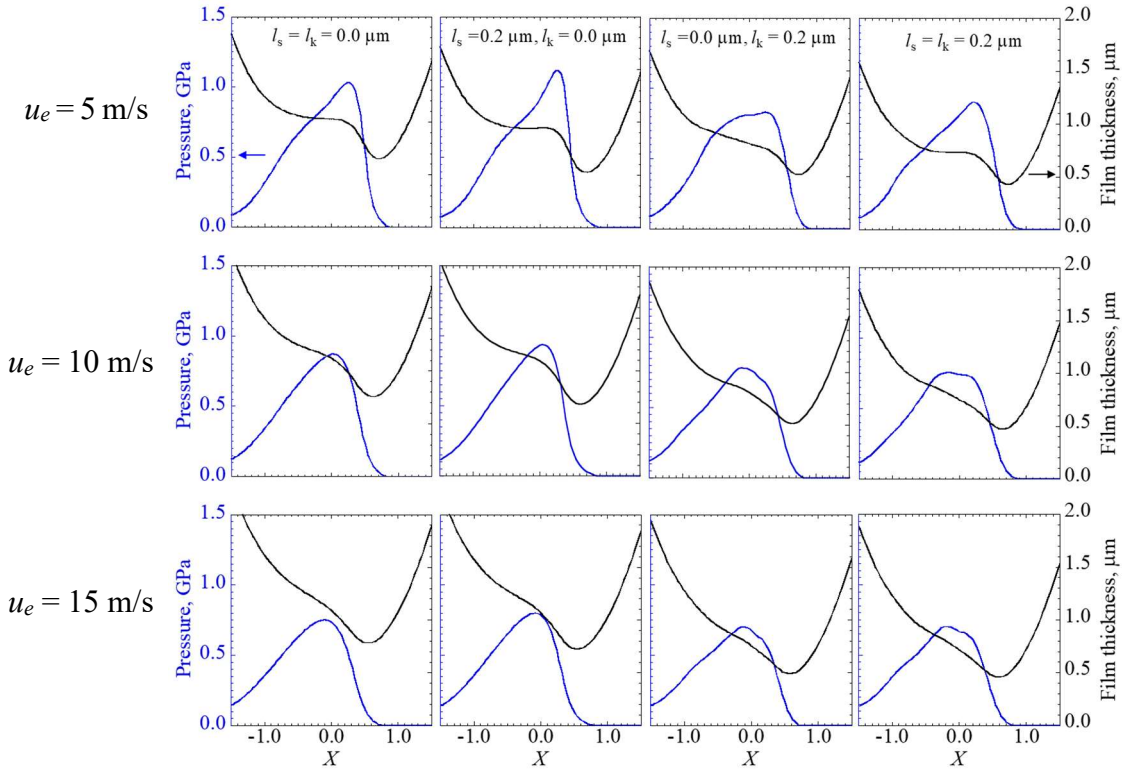

Figure 3-32 Pressure and film thickness profiles at the plane Y = 0 at different entrainment velocity: u_e = 5 m/s, 10 m/s, 15 m/s, and different boundary slips: no slip $l_s = l_k = 0$, velocity slip $l_s = 0.2$ μm, $l_k = 0$, thermal slip $l_k = 0.2$ μm, $l_s = 0$, coupled velocity/thermal slips $l_s = l_k = 0.2$ μm

The corresponding pressure, and film thickness profiles are shown in Fig. 3-32. At the case of 5 m/s, the velocity slip induces a center plateau while the thermal slip leads inclined film shape at contact area. The thinnest minimum film thickness is observed when $l_s = l_k = 0.2$ μm. With entrainment velocity further increases $u_e = 10$ m/s and 15 m/s, the film thickness reduction induced by velocity slip becomes indistinguishable, whereas the thermal slip causes more notable film reduction, and the pressure peak shifts downward. Under the case of coupled velocity/thermal slip, the pressure and film profiles are similar to the case of thermal slip. At high entrainment velocity, more lubricant is entrained into the contact area, generated large film thickness and significant temperature rise by shearing. The thermal slip at solid–lubricant interfaces restrict the heat dissipation, leads lower lubricant viscosity and thinner film thickness. Therefore, the influences of thermal slip on film thickness reduction becomes more prominent.

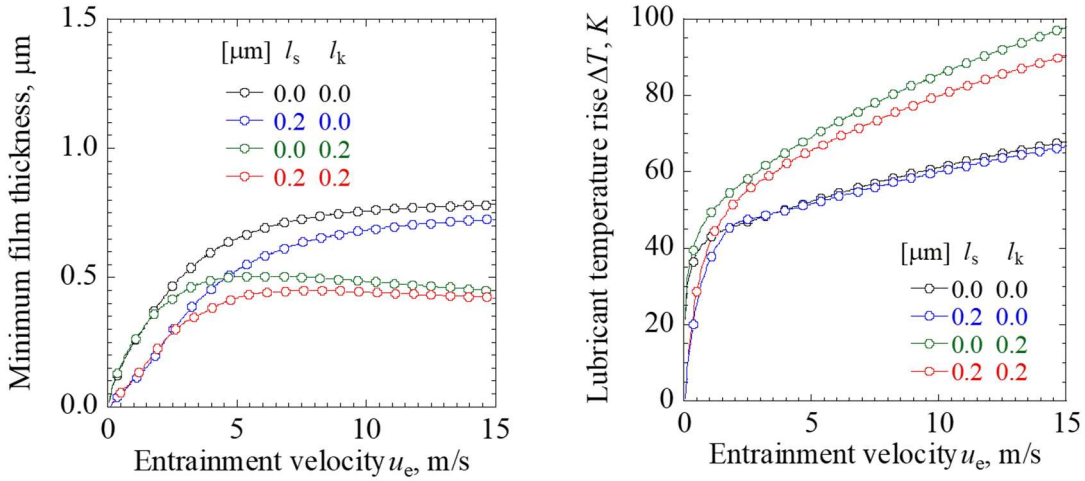

Figure 3-33 Effect of entrainment velocity on lubrication performance at SRR = 1.5: (a) minimum film thickness; (b) mean lubricant temperature rise in entire contact area.

Fig. 3-33 shows the minimum film thickness and mean lubricant temperature rise curves with the entrainment velocity under boundary slips, where ΔT is the average value of the lubricant temperature rise over the entire contact area. In the low entrainment velocity region of $u_e < 3$ m/s, the minimum film thickness of the no slip case (black) is consistent with that of the thermal slip case (green) because of the insignificant

temperature rise, whereas those of the cases with velocity slips (blue and red) are relatively smaller. Therefore, the minimum film thickness reduction is primarily caused by velocity slip. When the entrainment velocity increases, the minimum film thickness reduction caused by the velocity slip (blue) decreases; however, that caused by the thermal slip (green and red) increases. With an increase in the entrainment velocity, the amount of entrained lubricant in the contact area increases, which facilitates the increase in the film thickness. By contrast, heat generation increases owing to increased lubricant shearing, resulting in a reduction in the film thickness. The contributions of velocity and thermal slips to the minimum film thickness reduction are equal at u_e = 4.6 m/s. Meanwhile, an apparent discrepancy appears in the cases with and without thermal slip in the high entrainment velocity region. The reason is shown Fig. 3-30(b), where the temperature rise is significant in the cases with thermal slip, which results in the apparent discrepancy in the minimum film thicknesses in the high entrainment velocity region.

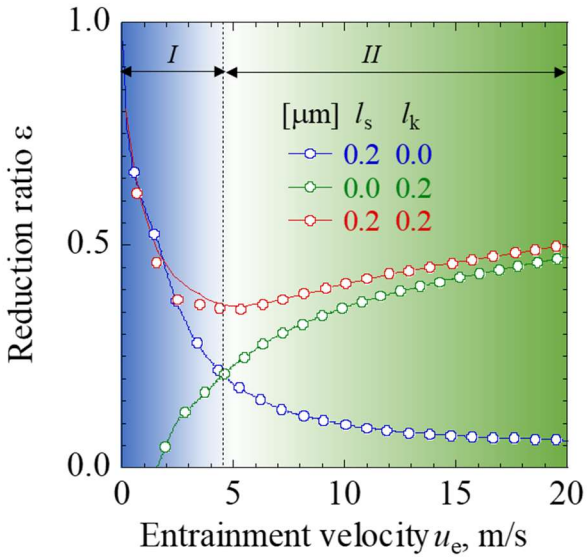

Figure 3-34 Reduction ratio of minimum film thickness ε vs. entrainment velocity curves at SRR = 1.5. Dashed line represents threshold between regions *I* and *II*.

To compare the effects of boundary slips on the minimum film thickness, the ratio of the minimum film thickness reduction is plotted as a function of the entrainment velocity, as show in Fig. 3-34. The ratio of the minimum film thickness reduction ε is defined as $\varepsilon = (h_{min0} - h_{min}) / h_{min0}$, where h_{min0} is the minimum film thickness under the no slip

boundary condition. As shown in Fig. 3-34, at u_e = 4.6 m/s, the ε of the velocity slip case (blue) is equal to that of the thermal slip case (green), whereas that of the coupled velocity/thermal slips case (red) shows the minimum value. This implies that in region *I* of u_e < 4.6 m/s, velocity slip dominates the minimum film thickness reduction. By contrast, in region *II* of u_e > 4.6 m/s, the effect of thermal slip on ε is more dominant than that of velocity slip.

3.4.4 Slide-roll ratio

Since the lubricant temperature rise is induced by the lubricant shearing with regard to the lubricant shear rate or the relative velocity between solids *a* and *b* in the EHL contact, the effects of SRR on the lubrication characteristics are discussed in this section.

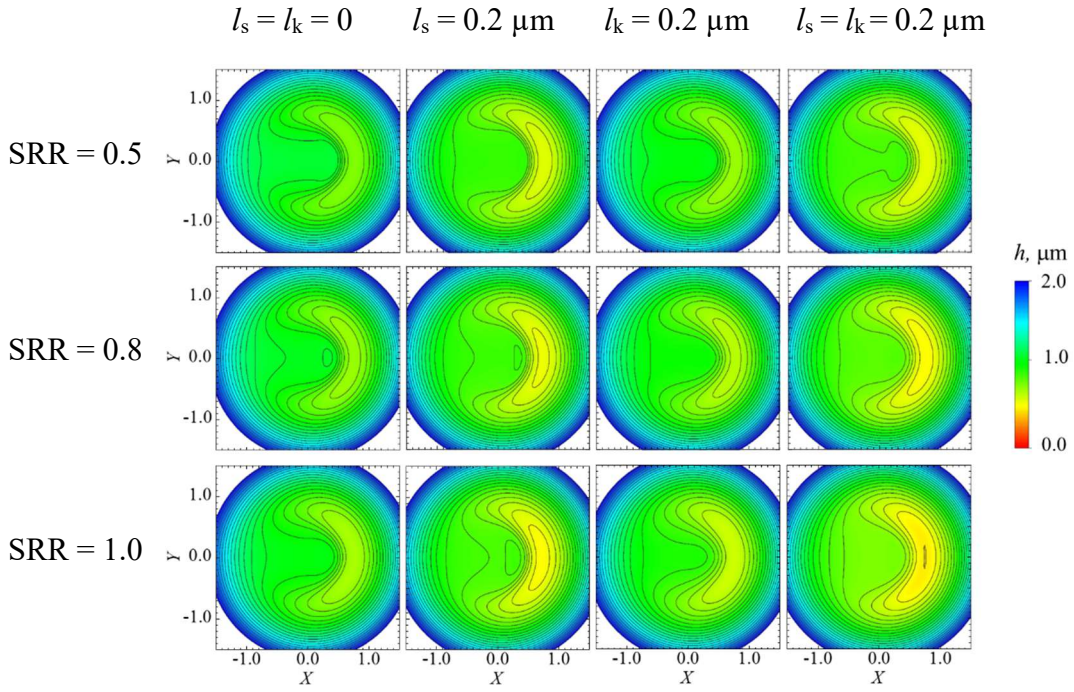

Figure 3-35 Contour maps of film thickness at different slide-roll ratios: SRR = 0.5, 0.8, 1.0, and different boundary slips: no slip $l_s = l_k = 0$, velocity slip l_s = 0.2 μm, l_k = 0, thermal slip l_k = 0.2 μm, l_s = 0, coupled velocity/thermal slips $l_s = l_k$ = 0.2 μm.

Fig. 3-35 shows the contour maps of the film thickness at different slide-roll ratios: SRR = 0.5, 0.8, 1.0, and different boundary slips: no slip, velocity slip, thermal slip,

coupled velocity/thermal slips. The contours maps are typical solution of the EHL point contact, with a central plateau and an outer constriction. Compared with the results of no slip condition, the velocity induced the deeper constriction than thermal slip, while the thinnest film thickness is observed when $l_s = l_k = 0.2$ μm, owing to the reduction in film thickness induced by the velocity slip and thermal slip. The larger SRR, the thinner film thickness is produced. Furthermore, the film thickness reduction induced by thermal slip becomes insignificant with the decreases of SRR due to the reduced thermal effect.

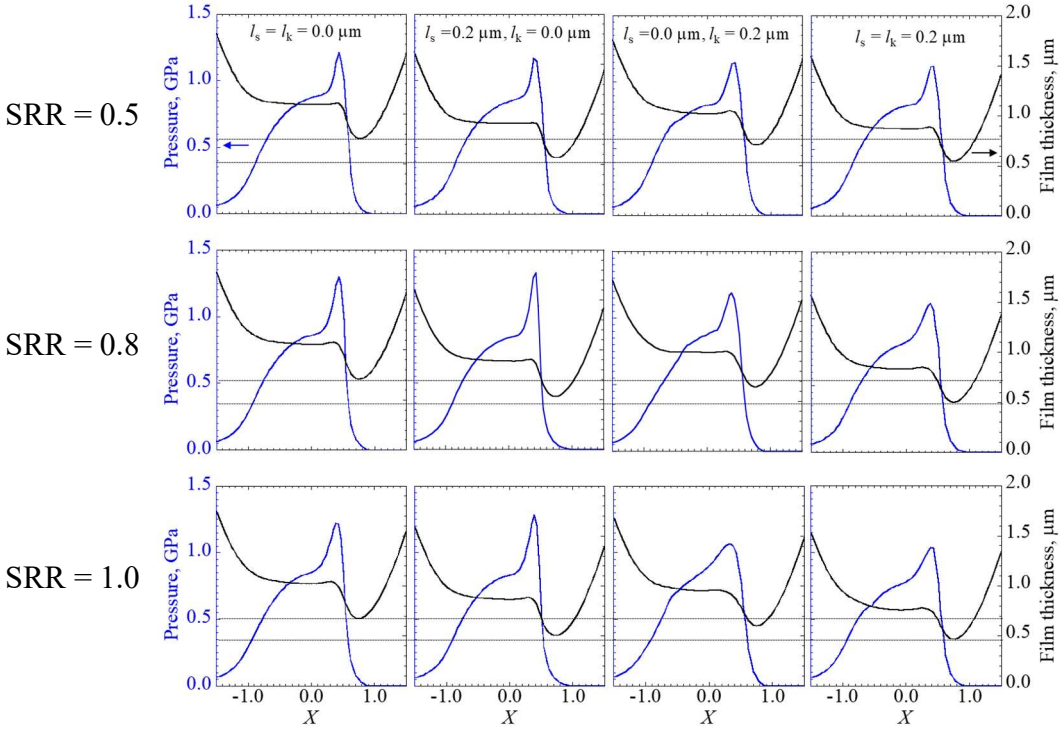

Figure 3-36 Pressure, and film thickness profiles on the plane Y = 0 at different slide-roll ratios: SRR = 0.5, 0.8, 1.0, and different boundary slips: no slip $l_s = l_k = 0$, velocity slip $l_s = 0.2$ μm, $l_k = 0$, thermal slip $l_k = 0.2$ μm, $l_s = 0$, coupled velocity/thermal slips $l_s = l_k = 0.2$ μm. Dotted line represents minimum film thickness of no-slip case; dashed line represents minimum film thickness for case of $l_s = l_k = 0.2$ μm.

Fig. 3-36 shows the pressure, and film thickness profiles on the plane Y = 0. Dotted line represents minimum film thickness of no slip case; dashed line represents minimum film thickness for case of $l_s = l_k = 0.2$ μm. The velocity slip caused the significant film thickness reduction, while the effect of thermal slip is small. Velocity slip induced film thickness reduction by lower lubricant velocity, which entrains less lubricant into the

contact area. The thermal slip-induced film thickness reduction is attributed to the lower viscosity of the lubricant due to the temperature rise in the contact area. As the SRR decreases, the generated heat by lubricant shearing shifts down, leads smaller temperature rise. Therefore, comparing the minimum film thickness with that of the no slip (dotted line) and $l_s = l_k = 0.2$ μm (dashed line) cases, the film thickness reduction is primarily induced by the velocity slip.

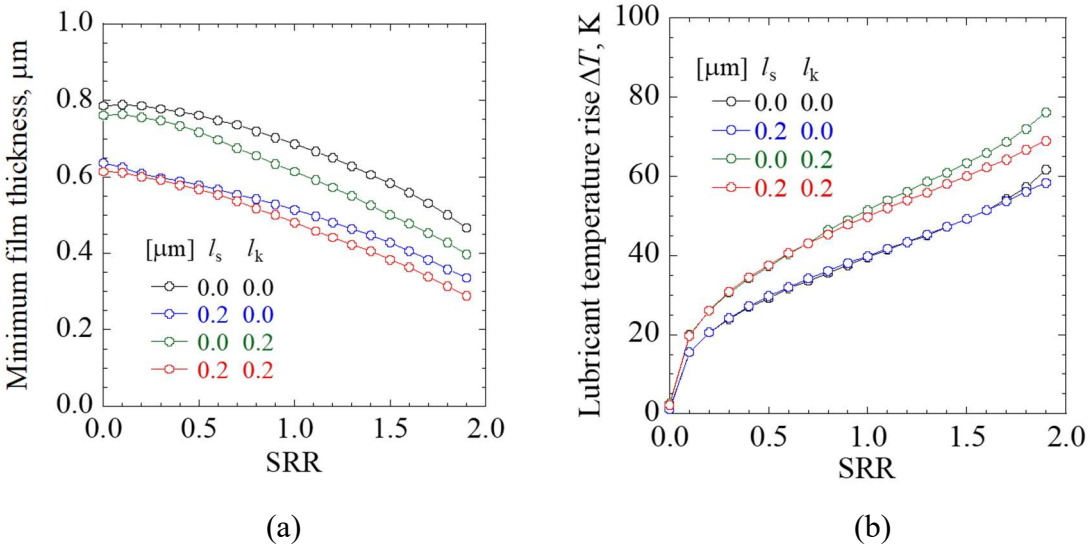

Figure 3-37 Effect of SRR on lubrication performance at $u_e = 3.6$ m/s: (a) minimum film thickness; (b) mean lubricant temperature rise in entire contact area.

Figs. 3-37(a) and (b) show the variations in the minimum film thickness and lubricant temperature rise with boundary slips. The entrainment velocity is given as $u_e = 3.6$ m/s. It is clear that increasing the SRR reduces the minimum film thickness but increases in the temperature rise. As shown in Fig. 3-37(a), the thermal slip has less significant effect than the velocity slip on the minimum film thickness reduction, whereas the velocity slip yields a significant minimum film thickness reduction of approximately 0.15 μm. Meanwhile, the film thickness reduction of the coupled velocity/thermal slips is dominated by the velocity slip in the low SRR region, whereas the effect of the thermal slip on the film thickness reduction become more prominent in the large SRR region. As discussed previously, the film thickness reduction is caused by two reasons: (1) the lower lubricant velocity induced by the velocity slip, and (2) the lower viscosity induced by the thermal slip. The latter coincides with the temperature rise in the entire contact area,

which increases with the SRR, as shown in Fig. 3-37 (b). Hence, the film thickness reduction in the case of coupled velocity/thermal slips is the largest among the cases investigated.

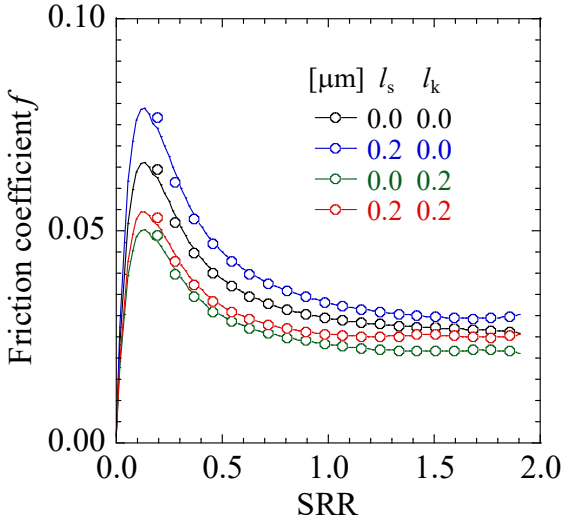

Figure 3-38 Friction coefficient vs. SRR curves at u_e = 3.6 m/s.

Fig. 3-38 shows the *f*-SRR curves at u_e = 3.6 m/s, where *f* is the friction coefficient. As shown, a greater velocity slip results in a higher *f*, whereas a greater thermal slip results in a lower *f*. The former is caused by the film thickness reduction subjected to a large velocity gradient, whereas the latter is caused by the reduction in lubricant viscosity due to a temperature rise.

3.5 Summary

In this chapter, the effect of boundary slips on lubrication behaviors of EHL under pure rolling motion, opposite sliding motion and rolling/sliding motion were characterized. Three cases of boundary slips, i.e., velocity slip, thermal slip, and coupled velocity/thermal slips, were investigated. Numerical simulations were conducted based on the modified Reynolds equation and the energy equation by considering the velocity slip and thermal slip simultaneously on contacting surfaces. The following conclusions were drawn:

1. Under the pure rolling motion, velocity slip induced a lubricant velocity distribution across the film, which led to a general reduction in film thickness. The influences of thermal slip on lubrication performance are negligible due to the insignificant temperature rise.

2. Under the opposite sliding motion, velocity slip caused the surface dimple to shift along the sliding direction, while thermal slip caused the surface dimple to shift in the opposite direction as the pressure peak shifted downward and the dimple depth decreased. The effects of velocity slip and thermal slip canceled out one another when the velocity slip length and thermal slip length were equal.

3. Under rolling/sliding motion, velocity slip dominates the film thickness reduction when the slip length is comparable to the thermal slip length, whereas the thermal slip dominates the film thickness reduction when the slip length is negligible compared with the thermal slip length. In the coupled velocity/thermal slips case, the superior velocity slip might result in a lower temperature in the lubricant and solids, whereas the superior thermal slip might cause a temperature rise in the entire contact area in the lubricant as the film thickness decreases simultaneously. Hence, the coupled velocity/thermal slips case leads the most significant temperature rise and film thickness reduction among the three cases.

4. The effect of thermal slip on lubrication is more dominant than that of velocity slip while increase entrainment velocity or SRR. At the critical entrainment velocity, the coupled velocity/thermal slips case has the minimum film thickness reduction ratio, which can improve the tribological performance.

This chapter, for the first time, revealed the effect of thermal slip at the solid–lubricant interface on lubrication behavior, which might be one of the key parameters in EHL contact. Further experimental investigations are necessary to verify the results obtained.

Chapter 4

4. Experimental study on lubrication with oleophobic coating

4.1 Introduction

In the elastohydrodynamic lubrication (EHL) regime, continuum boundary condition was widely accepted, which states that lubricant at each interface has a velocity and temperature equal to that of the adjacent solid surface [37,71]. Up until recent years, there were a few experimental papers receive great attention for the influences of boundary slips on lubrication [102,119,152,174]. The mechanisms of slip are often explored by measuring the hydrodynamic force generated as two surfaces approach each other [133,176]. It is also possible to directly study the flow of liquids close to a solid surface using total internal reflection combined with fluorescence recovery after photobleaching [97]. For the EHL regime, the film thickness and friction are usually determined to qualify the boundary slips at interfaces [128,177].

The understanding of boundary slips in EHL is focused on the application of kinds of coatings. Many studies have been performed which indicate the existence of slip and its effect on friction [178,179]. The hydrophobic/oleophobic coating with high contact angle is indicative of a weak interaction between liquid and solid, that can be more easily overcome, causing the lubricant molecules to slip across the solid. The potential use of coating to reduce friction in tribology is promising. To master this potential, it is necessary to directly correlate interfacial slip at coating surface with friction and lubricant film thickness, which is crucial to the protection of tribological surfaces.

The purpose of this chapter is to measure the film thickness and friction of EHL using the ball–disc contact with or without coating. To make a comparison, two kinds of

surfaces, hydrophobic/oleophobic coated surface, and uncoated surface, are employed to estimate the degree of boundary slips.

4.2 Experimental method

4.2.1 Experimental apparatus

The film thickness in the center of the contact was measured using an EHL rig PCS Instruments, in which a steel ball is loaded against a disc. Both ball and disc are rotated by independent motors so that a range of slide-roll ratios can be achieved, and the ball is in a lubricant bath to control the temperature of lubricant entrained into the contact area. The lower surface of disc, which is in contact with the ball, is coated with a spacer layer with thicknesses of approximately 500 nm. This enables central film thickness to be obtained by Ultra-Thin Film Interferometry, UTFI, whereby a spectrometer disperses light reflected from the contact into component wavelengths and film thickness is calculated based on those interfere.

Figure 4-1 Outline view of PCS Instruments

The PCS Instruments Ultra Thin Film Measurement System is a fully automated computer-controlled instrument for measuring the film thickness and traction coefficient (friction coefficient) of lubricants in the elastohydrodynamic lubricating regime. The

instrument can measure lubricant film thickness down to 1 nm with a precision of +/- 1 nm. The contact pressures and shear rates in this contact are similar to those found in, for example, gears, rolling element bearings and cams. In addition to film thickness measurements, traction coefficients can be measured at any slide/roll ratio from pure rolling up to 100%.

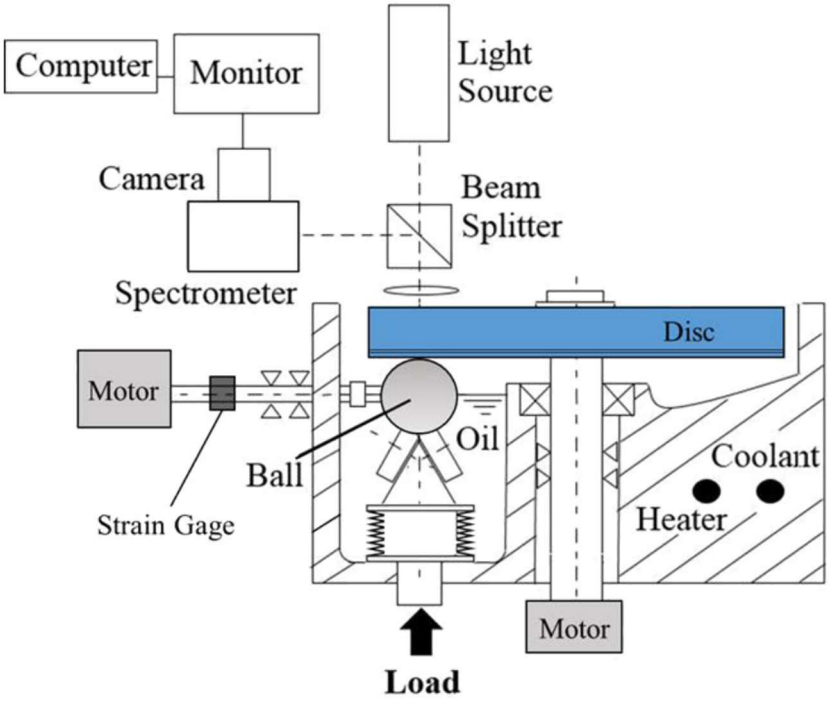

Figure 4-2 Schematic of PCS Instruments

Main parts:

1) Lubricant pot. It has an internal reservoir to accommodate the test lubricant. The heater and coolant are used to control the temperature of lubricant.
2) Disc and ball. The EHL contact is formed between the rolling ball and sliding disc. The ball is derived by ball drive motor via a strain gauge traction transducer, while the disc is derived by same type of motor, connected to the disc by a reduction pulley and gearbox. These motors drive an absolute encoder which provides the software with a continuous speed readout. To achieve boundary slips, the surfaces of the ball and disc are coated with hydrophobic/oleophobic coating for comparison with the uncoated surfaces.

3) Loading system. This is a stainless steel bellows which allows vertical movement of the ball whilst holding the ball accurately in position under the disc.
4) Light source. The monochromatic light is employed, which can provide excellent fringe visibility.
5) Spectrometer. The spectrometer is a scientific instrument used to separate and measure spectral components from the contact area.
6) PC and Monitor. It used to control the motion, collect and analysis the data.

The instrument measures the lubricant film thickness properties in the contact formed between a 19.05mm diameter steel ball and a rotating glass disc by optical interferometry. The contact between the ball and disc is illuminated by a white light source directed down a microscope through the disc on to the contact. Part of the light is reflected from the Cr layer and part travels through the SiO_2 layer and fluid film and is reflected back from the steel ball. Recombining the two light paths forms an interference image which is passed into a spectrometer and high-resolution monochrome CCD camera. The camera image is captured by a video frame grabber and analyzed by the control software to determine the film thickness.

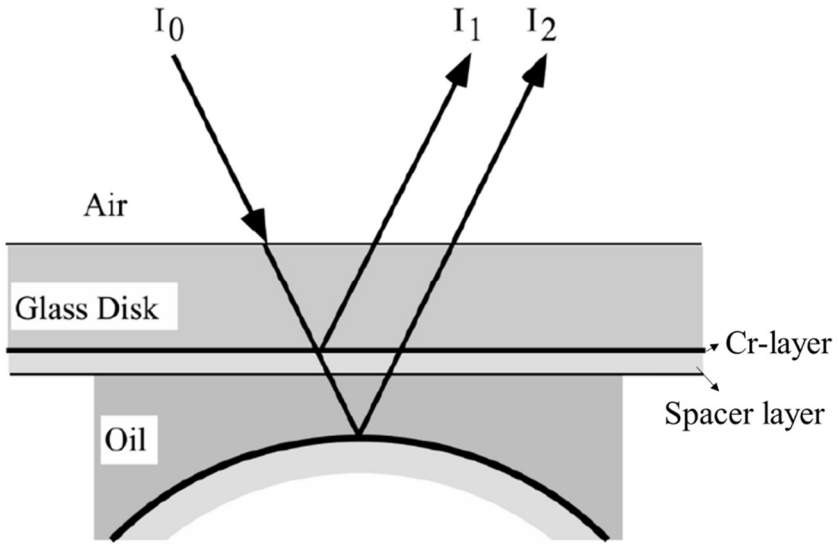

Figure 4-3 Schematic representation of spacer layer method

Compared to conventional interference approach, the ultra-thin film approach uses a

transparent, solid, spacer layer coating applied on top of the semi-reflecting film on the transparent flat. This coating consists of silicon dioxide and is around 500 nm thick, which enables interference fringes to be obtained even in the absence of an oil film.

The friction tests were carried out using a minitraction machine. In the PCS Instruments, the ball is loaded and rotated against the sliding disc in lubricant pot. The ball and disc are driven by independent motors to enable any combination of sliding and rolling. The drive motors, applied load, and temperature are all computer controlled. The friction is measured by force transducers mounted on the ball drive shaft.

PCS Instruments performance limits:

Film thickness	1 to approx. 250 nm
Speed	0 to 4 m/s
Slide to roll ratio	0 to 1
Load	0 to 50 N
Temperature	ambient to 150℃

Features and benefits:

- Fully automated, easy to calibrate and intuitive software programs, improves repeatability, and reduces training needs.
- Precision components enable accurate measurements down to 1nm.
- Two independently driven motors allow any slide to roll ratio to be entered, enabling many applications to be replicated.
- Temperature controlled test chamber further expands testing capabilities.
- Compact, ergonomic design minimizes the required lab space.
- Small sample volume, saving on cleaning time, sample wastage and running costs.

4.2.2 Experimental process

Before the measurement of the film thickness and friction, it is essential to thoroughly clean the instrument and materials.

For the cleaning of the instrument, the loading system, ball carriage and lubricant pot

were cleaned by using the suitable solvents. Using a wash bottle, fill the lubricant reservoir to the normal operating level with the light hydrocarbon solvent. Leave the filled solvent for 2–3 minutes then drain and refill. Clean around the inside of the pot and reservoir with paper wipes moistened with solvent. Drain the solvent then refill either with the same solvent or preferably with a more volatile solvent. Then, drain and allow to dry. Drying can be accelerated by using a filled air or nitrogen line to gently blow solvent out. For the cleaning of disc and ball, same solvent was used.

Film thickness measurement

1. Start the PC system and ULTRA software.
2. Clean the pot, lubricant reservoir, disc, ball, and other components.
3. Consult the track log for the selected disc and choose the desired track radius.
4. Locate the ball carriage on the top of the loading system bellows. Then, fill the reservoir with the test lubricant up to the level of the center of the ball drive shaft.
5. Place the disc, disc cover and the pot lid on the pot with the hole.
6. Attach the microscope assembly to the limb block so that the microscope objective lens passes through the hole in the pot lid. Inset the light source in the adapter at the top of the microscope tube and check that the microscope to spectrometer tube is correctly aligned at right angles to the face of the spectrometer.
7. Fill the required parameters into the dialogue box and set zero film thickness for the disc spacer layer thickness.
8. Set the test temperature at the load of 2 N and speed of 0.5 m/s.
9. Set the speed to the first speed in the sequence, then applied the desired load. Measure the film thickness at the center contact area.
10. At the end of the test, set the load to zero and stop the disc. Drain the lubricant whilst it is still hot. Shut the system down and save the data.

Friction measurement

1. Switch on the PC system and start the TRACTION software.
2. Clean the pot, lubricant reservoir, ball, disc and other components.
3. Consult the track log for the disc and choose the desired track radius.
4. Locate the ball carriage on the top of the loading system. Attach the cleaned ball

to the ball drive adapter and tighten the attachment screw.

5. Fill the reservoir with the test lubricant up to the level of the center of the ball drive shaft.
6. Place the disc, disc cover and the pot lid on the pot.
7. Fill the required details and parameters on the form.
8. Set the test temperature at the load of 2 N and speed of 0.5 m/s.
9. Set the speed to the first speed in the sequence, then applied the desired load. Measure the friction coefficient.
10. At the end of the test, set the load to zero and stop the disc. Shut the system down and save the data.

4.2.3 Surface treatment

In many engineering applications, coatings are commonly used in mechanical components to improve tribological performance, for instance, the enhancement of electrical and thermal conductivity and reduction of friction and wear. This improvement can be seen in a variety of applications, including the automotive, electronics, optical storage disk, and cutting tool industries. Under EHL regime, the usage of surface coating has recently come to the forefront, especially in terms of the boundary slips. In this work, the hydrophobic/oleophobic coating is applied on the moving surfaces to investigate the influences of boundary slips on lubrication performances.

Hydrophobic/oleophobic coating

The hydrophobic coating is coated on both disc and ball surfaces by the company of DAIKIN. The coating material is Optool UD509 with following characteristics:

- Fluorosolvent-borne modified PFPE.
- Forms a durable bond with glass surfaces.
- Effective on surfaces coated with SiO_2 but also applicable to other surfaces.
- Highly transparent in the visible spectrum.
- Can be applied by wet methods, such as spray, dip, spin or flow coating.
- Significantly reduces static and kinetic coefficients of friction of bare glass.

As a modified PFPE (perfluoropolyether) nanocoating, Optool UD applied to a surface is transparent and yet produces smudge resistance, easy-to-clean, and anti-fingerprint properties. In addition, Optool coated surfaces have a pleasantly smooth or slippery feeling to them.

The thickness of coating is around 7nm, and the coating method is physical vapor deposition (PVD). PVD is characterized by a process in which the material goes from a condensed phase to a vapor phase and then back to a thin film condensed phase. The most common PVD processes are sputtering and evaporation. Comparing to other deposition methods, the advantages of PVD are sometimes harder and more corrosion resistant than coatings applied by the electroplating process. Most coatings have high temperature and good impact strength, excellent abrasion resistance and are so durable that protective topcoats are rarely necessary.

Water contact angle on coating surfaces

The evolution of surface wettability is based on the measurement of water contact angle (WCA) in a room under constant temperature and pressure. The WCA measurement system and the outline of measurement method are shown in Fig.4-4.

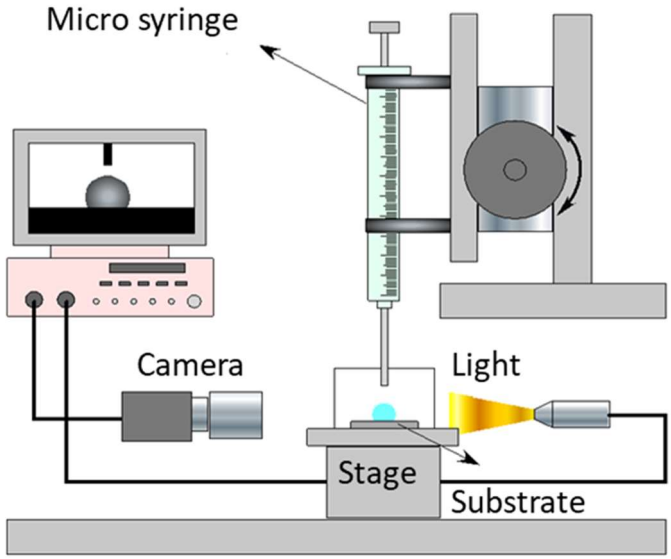

Figure 4-4 Schematic view of the contact angle measurement device

The wetting behavior was investigated at ambient conditions (25℃, 40% RH). Four-

microliter (4 μL) pure water (Wako, LC/MS 214-01301) droplets were dropped carefully onto the surface. The side views of droplets were obtained using a digital microscope (Keyence VHX-200). Fig. 4-5 shows the microscope images of droplets on the coating surfaces. Each surface was measured five times to ensure the accuracy of contact angle. In comparison with the uncoated surface (26.97° ± 2.62°), the hydrophobic/oleophobic coating surface has a higher contact angle (93.94° ± 1.10).

(a) hydrophobic/oleophobic coated surface

(b) uncoated surface

Figure 4-5 Microscope images of a droplet upon the surfaces

Table 4-1 Measured water contact angles

Surfaces	WCA (deg.)		
	left	right	average
Uncoated surface	26.40	26.24	26.97 ± 2.62
	26.98	25.21	
	32.51	30.49	
	26.84	26.41	
	24.42	24.18	
Hydrophobic/oleophobic coated surface	93.33	95.66	93.94 ± 1.10
	94.19	93.93	
	92.38	92.32	

	95.05	94.55	
	93.33	94.67	

The roughness and structures of surfaces with or without coating are measured by White interference microscope (NPFLEX). The NPFLEX 3D Metrology System offers the most flexible, noncontact, 3D areal surface characterization for such large samples as orthopedic medical implants and the larger parts in aerospace, automotive and precision machining industries. It provides data density, resolution, and repeatability beyond what is possible with contact instrumentation, making it ideal as both a complementary technology and as a stand-alone metrology solution. The details information of NPFLEX are shown in Fig. 4-6 and Table 4-2.

Figure 4-6 White interference microscope (NPFLEX)

Table 4-2 NPFLEX information

Name	3D white interference microscope
Measurement principle	White vertical scanning interference method (VSI) Phase shift interference method (PSI) Phase shift + vertical scanning interference method (VXI)
Vertical resolution	0.01 nm

Level measurement accuracy	0.75 %
Light sources	High-intensity LED (white, green)
Maximum measurement velocity	73 μm/s
Maximum measurement range	10 mm
Measurement method	Vision64. Software
Measurement lens	Objective lens: …10, 50 x Inside lens: …0.55, 1.0, 2.0 x

Fig. 4-7 and Fig. 4-8 shows the surface and line roughness profiles of steel ball surfaces, respectively. The arithmetical mean height S_a is the extension of R_a (arithmetical mean height of a line) to a surface. It expresses, as an absolute value, the difference in height of each point compared to the arithmetical mean of the surface. This parameter is used generally to evaluate surface roughness. The maximum height S_z is defined as the sum of the largest peak height value and the largest pit depth value within the defined area. S_q represents the root mean square value of ordinate values within the definition area. It is equivalent to the standard deviation of heights.

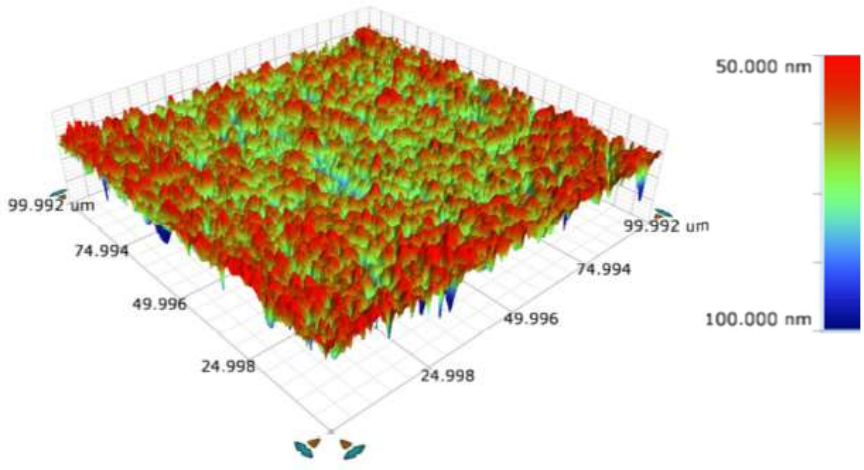

(a) uncoated steel ball surface

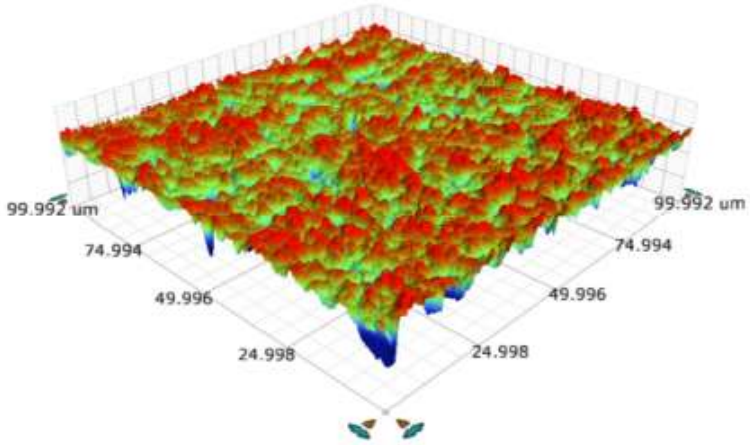

(b) hydrophobic coated steel ball surface

Figure 4-7 3D profiles of steel ball surfaces roughness

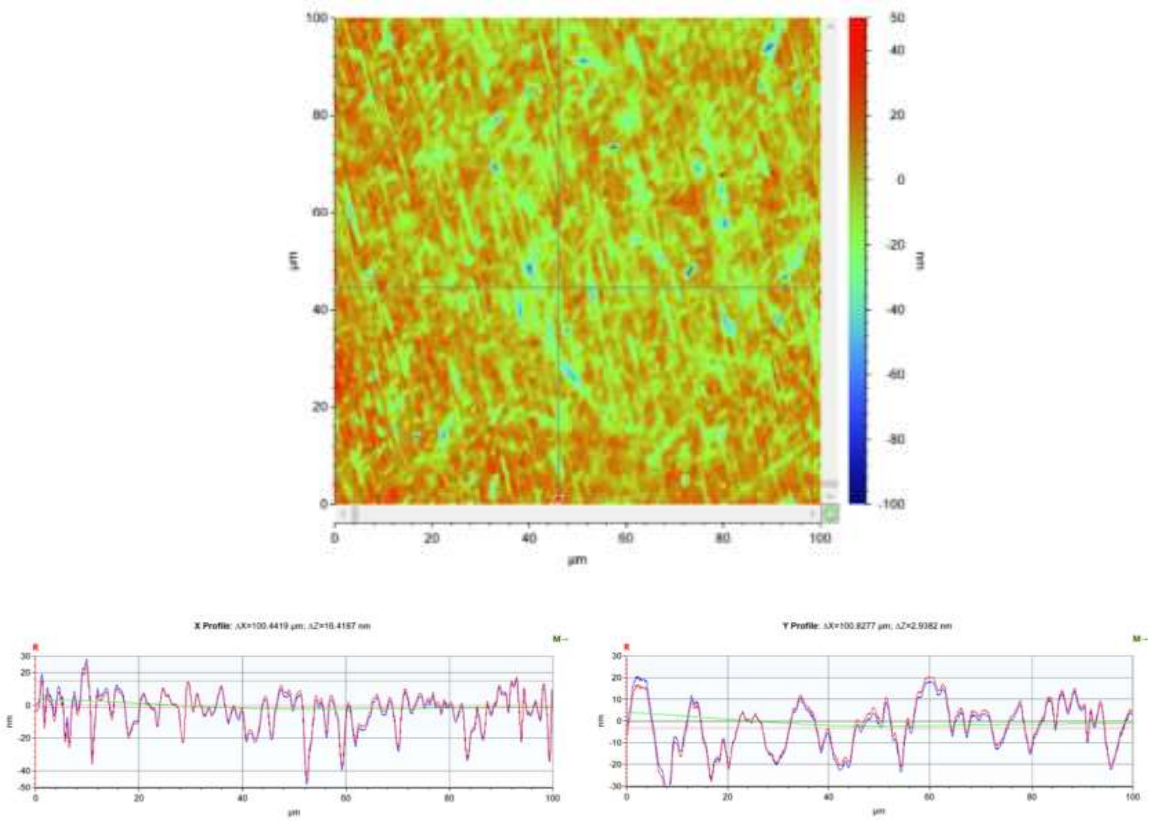

(a) uncoated steel ball surface

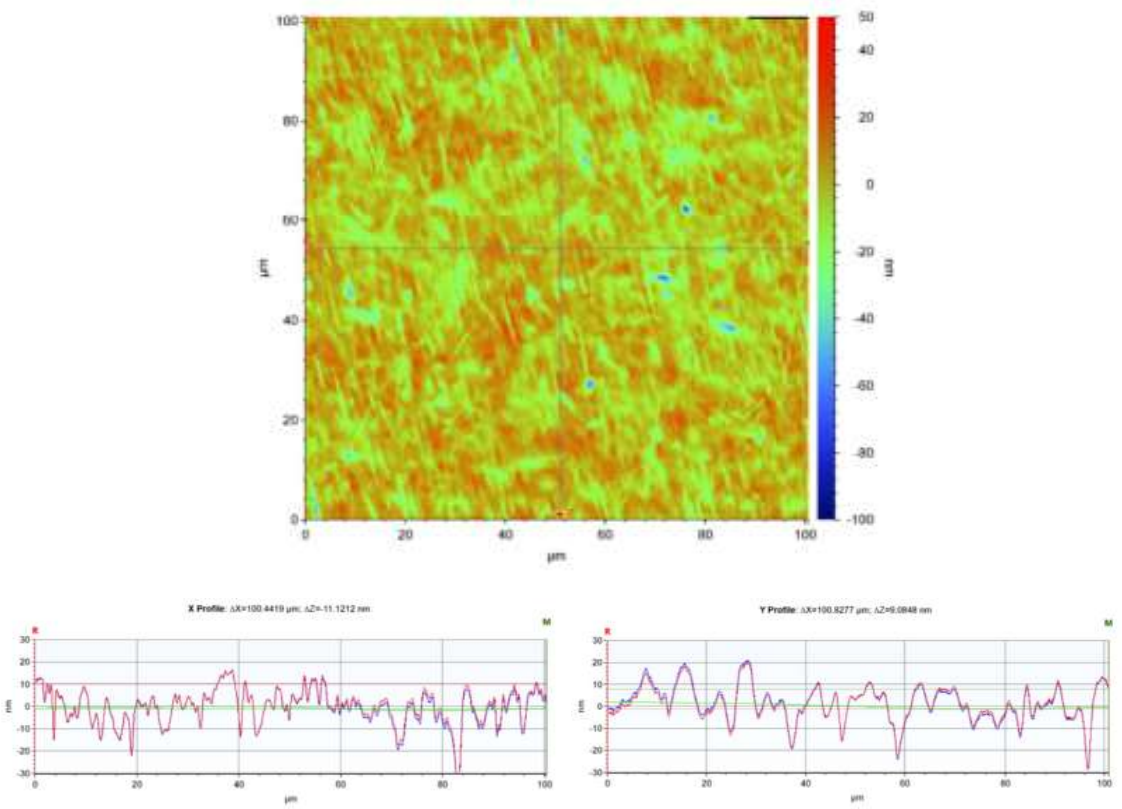

(b) coated steel ball surface

Figure 4-8 Line roughness of steel ball surfaces.

Table 4-3 Roughness of surfaces

	Uncoated steel ball, nm	Coated steel ball, nm
S_a	8.20	6.49
S_q	10.82	8.59
S_z	149	113
$R_{a,x}$	8.21	5.96
$R_{q,x}$	10.55	7.11
$R_{z,x}$	70.99	38.16
$R_{a,y}$	9.19	6.12

$R_{q,y}$	11.71	7.81
$R_{z,y}$	56.66	43.25

4.3 Results and discussion

The lubricant used in this work is continuously variable transmission fluid (CVTF), which is a premium-quality, full-synthetic transmission fluid specifically designed for use in passenger cars with belt driven continuously variable transmissions. It has been specifically engineered to have the unique frictional properties required for use in this type of transmission. Table 4-4 shows the properties of CVTF.

Table 4-4 Properties of lubricant (CVTF).

Density, ρ, kg/m^3, @25℃	842
Density, ρ, kg/m^3, @80℃	809
Viscosity, η, Pa·s, @25℃	0.038
Viscosity, η, Pa·s, @80℃	0.00728
Viscosity-pressure coefficient, GPa^{-1}, @25℃	18
Viscosity-pressure coefficient, GPa^{-1}, @80℃	10

The features and benefits of lubricant CVTF are showed as follows:

- Meets performance requirements for nearly all vehicles with belt-type continuously variable transmissions.
- High steel on steel friction to prevent belt slippage, which can result in high or even catastrophic wear.
- Low steel on paper friction to prevent torque converter clutch slippage, which can result in shudder.
- Excellent oxidation resistance and thermal stability for long fluid life.
- Protects against sludge and varnish formation.

- Protects against wear.
- Protects against rust and corrosion.
- Excellent low temperature properties for easier shifting in cold weather.
- Good seal compatibility.
- Good foam resistance.

The elastic contact is formed between a glass disc and steel ball. And the properties of contact materials are shown in Table 4-5.

Table 4-5 Properties of contact surfaces.

Density of steel, ρ, kg/m^3	7850
Specific heat of steel, c, J/(kg·K)	470
Thermal conductivity of steel, k, W/(m·K)	46
Poisson's ratio of steel, v, -	0.3
Young's modulus of steel, GPa	206
Density of glass, ρ, kg/m^3	2500
Specific heat of glass, c, J/(kg·K)	840
Thermal conductivity of glass, k, W/(m·K)	0.78
Poisson's ratio of glass, v, -	0.2
Young's modulus of glass, GPa	60

4.3.1 Friction

Since the EHL friction is determined by the material properties (i.e., lubricant viscosity, surface thermal conductivity and wettability etc.) and operating parameters (i.e., entrainment velocity, load and SRR etc.), the friction coefficient can be measured as a function of entrainment velocity, load and ambient temperature while the SRR kept constant during the measurement process.

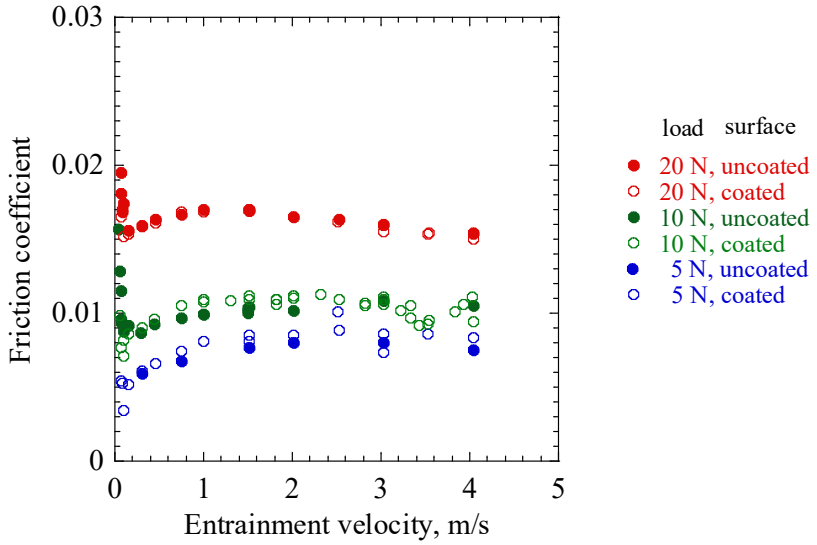

Figure 4-9 Friction coefficient curves for different loads and surfaces at the conditions of T_0 = 40 ℃, SRR = -1.0.

Fig. 4-9 compares the friction coefficient curves for the three loads: 20 N, 10 N, 5 N, and two types of contact surfaces: uncoated surfaces, hydrophobic/oleophobic coated surfaces. The SRR is -1.0, which means the ball surface moves faster than disc surface (SRR = $2(u_d-u_b)/(u_d+u_b)$). In comparison with the uncoated surfaces, both the disc and ball surfaces are dealt with hydrophobic/oleophobic coating, and the properties of the coating are shown in Fig. 4-5. In the beginning, the friction coefficient decreases sharply when the entrainment velocity $u_e \leq 0.1$ m/s due to the mixed lubrication. In the regime of EHL, the value of friction coefficient firstly increases with u_e because of the increases in sliding velocity, and thus the increase in shear rate as well as for the local stress. After reach the maximum value, the friction coefficient decreases with u_e due to the thermal effect. The increment of sliding velocity results in significant temperature rise of contact area, and thus the decreases in lubricant viscosity and shear stress. Note that the larger load, the higher friction coefficient value. Another feature in Fig. 4-9 to note is that the uncoated and coated surfaces curves coincide with each other and there is only a small difference between them. The effect of hydrophobic/oleophobic coating on friction coefficient is invisible at the ambient temperature T_0 = 40 ℃.

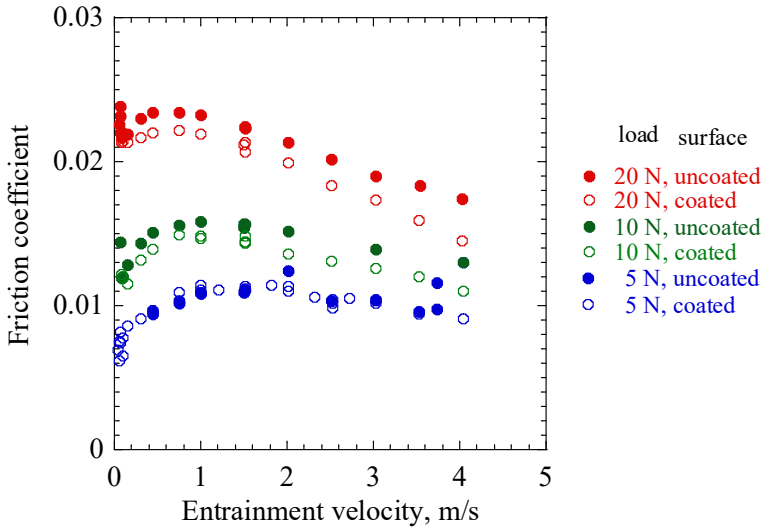

Figure 4-10 Friction coefficient curves for different loads and surfaces at the conditions of T_0 = 26 ℃, SRR = -1.0.

Fig. 4-10 shows the friction coefficient curves at lower ambient temperature of 26 ℃. Except for the change of the temperature, the other working parameters are kept the same as the high temperature case in Fig. 4-9. The curves between the uncoated and hydrophobic/oleophobic coated surfaces coincide with each other only for the case at the lowest applied load 5 N. Other than that, the uncoated surface friction curves are always higher than the coated ones. It can be seen that the difference between the uncoated and the hydrophobic/oleophobic coated curves is becoming larger with increasing load or entrainment velocity. The possible reasons are the boundary slips. At cases of the large load and high entrainment velocity, lubricant viscosity is affected obviously by the temperature rise, while the boundary slips occurring at the hydrophobic/oleophobic coated surface, especially the thermal slip at solid–lubricant interfaces, limited the heat dissipation form lubricant to solids. The temperature rise in lubricant results in the viscosity decreases, thus the friction coefficient.

By comparing Fig. 4-9 and Fig. 4-10, it is revealed that the influences of coating on friction coefficient becomes great at the cases of low ambient temperature and high load. Therefore, the friction curves at T_0 = 26 ℃, w = 50 N between uncoated surfaces and hydrophobic/oleophobic coated surfaces are examined next to clear the friction coefficient reduction, as shown in Fig. 4-11.

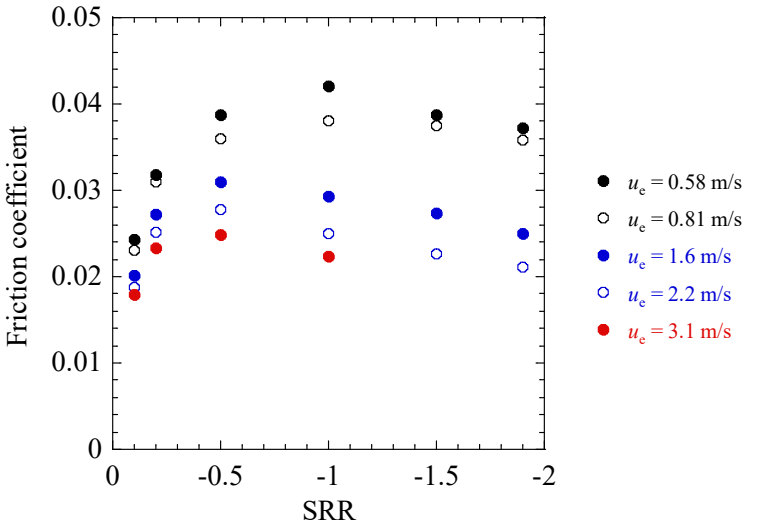

(a) uncoated surfaces

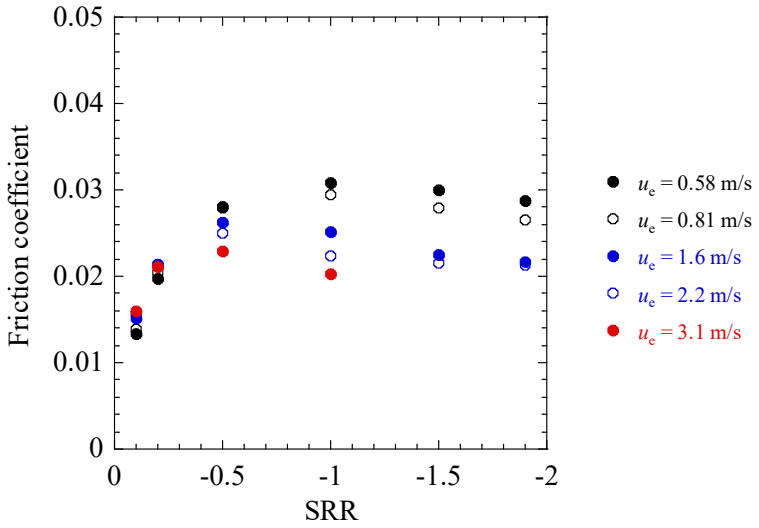

(b) hydrophobic/oleophobic coated surfaces

Figure 4-11 Friction coefficient curves for different entrainment velocities at the conditions of T_0 = 26 °C, w = 50 N: (a) uncoated glass disc – uncoated steel ball contact; (b) coated glass disc –coated steel ball contact.

In Fig. 4-11, the results show how the friction coefficient is changing with the SRR at five different entrainment velocities: 0.58 m/s, 0.81 m/s, 1.6 m/s, 2.2 m/s and 3.1 m/s. The measurements conducted with hydrophobic coated surfaces in Fig. 4-11(a) shows significantly lower coefficients of friction compared with the uncoated surface in Fig. 4-11(b). It is clearly that the relative reduction in friction is greatest at the lowest entrainment velocity and reduced when the entrainment velocity increases.

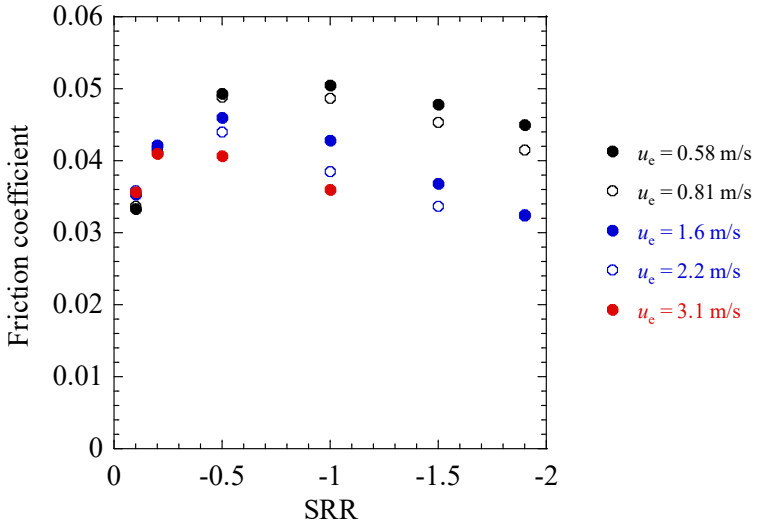

(a) uncoated surfaces

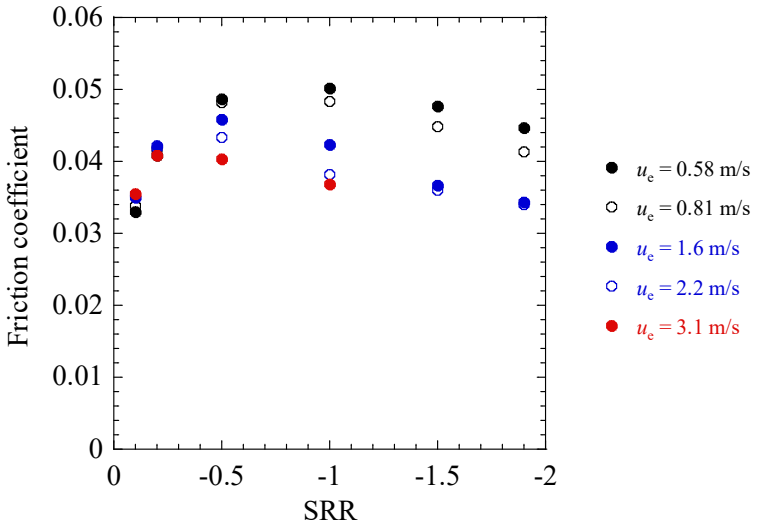

(b) hydrophobic/oleophobic coated surfaces

Figure 4-12 Friction coefficient curves for different entrainment velocities at the conditions of $T_0 = 26$ °C, $w = 50$ N: (a) uncoated steel disc – uncoated steel ball contact; (b) uncoated steel disc –coated steel ball contact.

Different form the glass disc – steel ball contact in Fig. 4-11, the steel disc – steel ball contact is employed in Fig. 4-12. Except for the contact material, other operating parameters are same to Fig. 4-11. Although the friction coefficient under steel–steel contact is larger than that under glass–steel contact in absolute value, the shape and trend of the friction coefficient curves are qualitatively similar for both coated and uncoated

cases. It also can be noted that the deviation in friction between uncoated surface and uncoated surfaces is invisible, which can be attributed to thermal effects. As known, the steel disc has a much larger thermal conductivity (46 W/(m·K)) and Young's modulus (206 GPa) than that of glass disc (0.78 W/(m·K), 60 GPa), leading small temperature rise in lubricant and elastic deformation in contact surfaces. Therefore, the friction coefficient under steel–steel contact is larger than that under glass–steel contact while the influence of hydrophobic/oleophobic coating on friction is negligible due to the insignificant thermal effect.

4.3.2 Film thickness

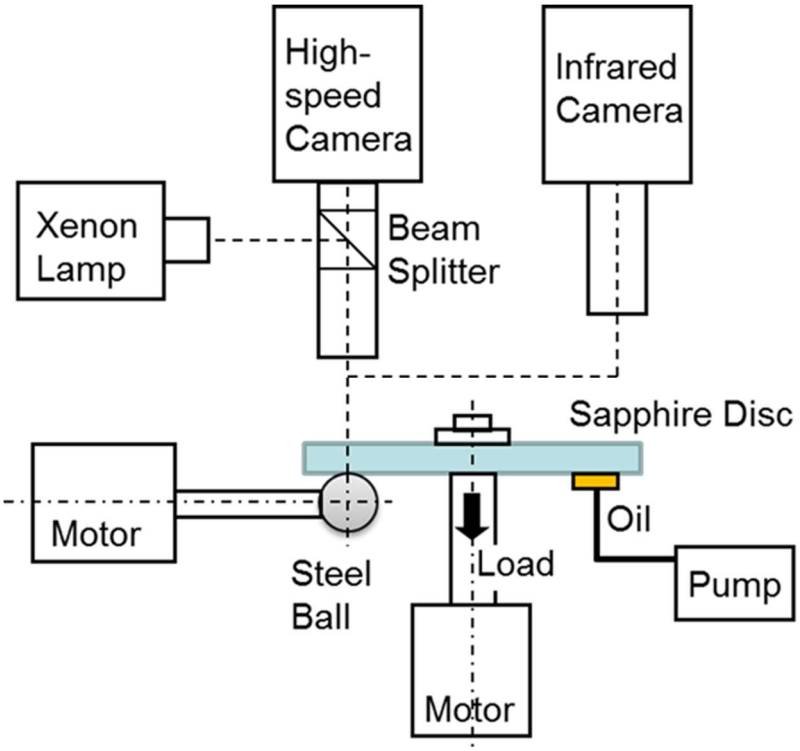

Figure 4-13 Experimental apparatus.

Fig. 4-13 shows a representation of the experimental apparatus WAM tribology test platform (Wedeven Associates Machine) used in this study. The device consists of following main parts: Xenon lamp, Infrared camera, Beam splitter, Motor, Ball, Disc and Oil pump. The elastohydrodynamic film thickness and contour map were measured in a

ball on disc optical rig whose basic parts are a disc and a ball of 25.4 mm in diameter. Both the ball and disc are independently driven by two motors. The whole contact area together with the lubricant KTF-1 is enclosed in a lubricant chamber that is to keep the constant temperature 25 ℃. The contact area is illuminated with a light source built in the microscope illuminator. The chromatic interferograms produced by the contact are captured by the Canon camera mounted on an eyepiece port of the microscope. The used lubricant is KTF-1, one type of the CVTF, which is superior in oxidation stability, resistant to heat and temperature change, and has stable frictional properties. In addition, it prevents foaming, which causes power transmission to become inefficient, and reduces vibration at low speed. Also, it can be used as power-steering fluid.

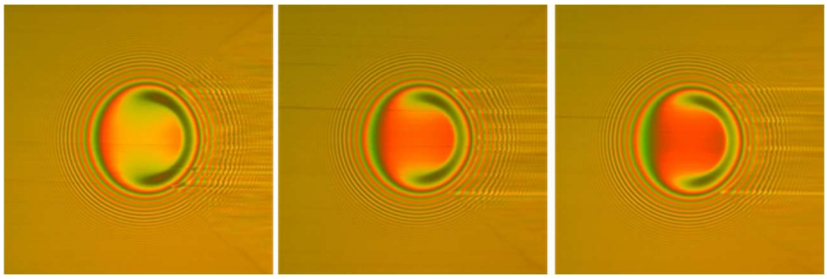

(a) SRR = -1.5 (b) SRR = -1.2 (c) SRR = -1.0

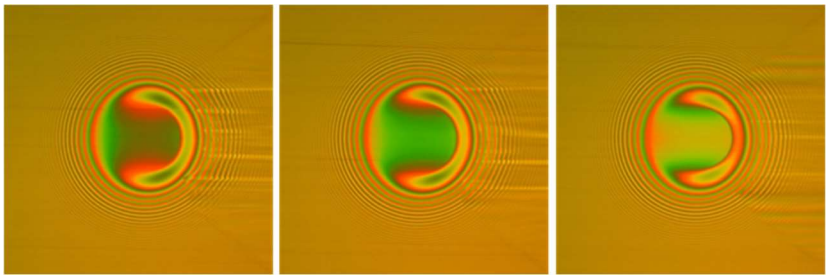

(d) SRR = -0.7 (e) SRR = -0.5 (f) SRR = -0.2

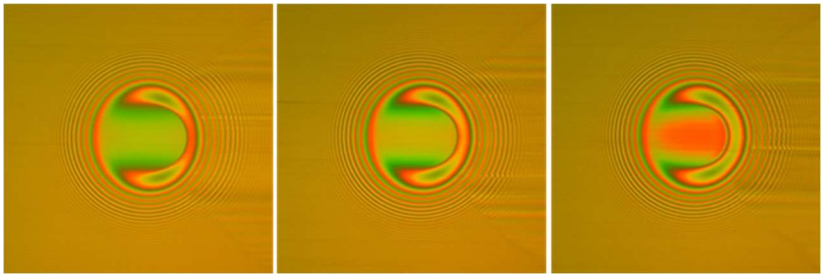

(g) SRR = 0.0 (h) SRR = 0.2 (i) SRR = 0.5

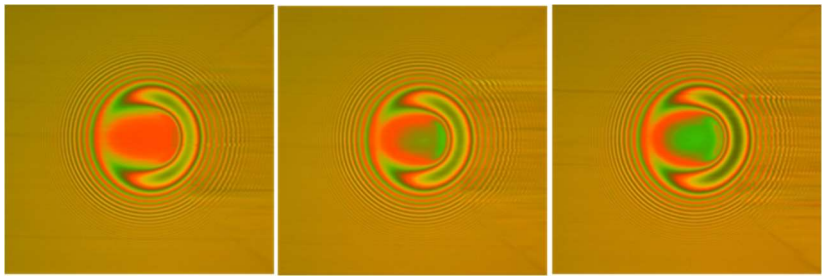

(j) SRR = 0.7 (k) SRR = 1.0 (l) SRR = 1.2

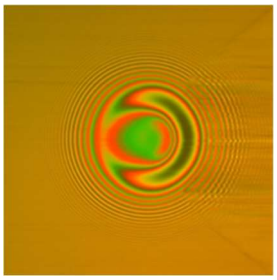

(m) SRR = 1.5

Figure 4-14 Contour maps of film thickness at the SRR range of -1.5 to 1.5 for glass–steel contact. u_e = 1 m/s, T_0 = 25 ℃, w = 20 N.

Fig. 4-14 shows interferograms of EHL contact under glass disc–steel ball contact in the SRR range from -1.5 to 1.5 with the conditions of u_e = 1 m/s, T_0 = 25 ℃, w = 20 N. A classical horseshoe film shape, i.e., a flat plateau bounded by a horseshoe shaped constriction and the minimum film thickness located at the two side lobes, is observed in the negative SRR from -1.5 to 0, which means the ball speed is larger than disc speed (SRR = $2(u_d-u_b)/(u_d+u_b)$). In the SRR range from 0 to 1.5 shown in Figs. 4-14(g)–(m), a slight dimple appears near the constriction area. The larger SRR, the deeper dimple is. Since the thermal conductivity of ball (46 W/(m·K)) is much larger than that of disc (0.78 W/(m·K)), the heat generated inside lubricant is easy dissipated to the ball. In addition, the surface velocity affects the heat dissipation rate. The higher surface velocity, the larger heat dissipation rate. For the negative SRR (from -1.5 to 0) where ball velocity is larger than disc, the heat is mostly dissipated from lubricant to ball surface, results in the horseshoe shape film in contact area shown in Figs. 4-14(a)–(g). When the disc surface velocity becomes larger than the ball surface velocity SRR ≥ 0, the played role of disc on

heat dissipation increases. The lubricant heat part to disc surface, part to ball surface through the conduction, resulting in the significant temperature viscosity wedge effect. Thus, the dimple is observed at the SRR range of 0 to 1.5.

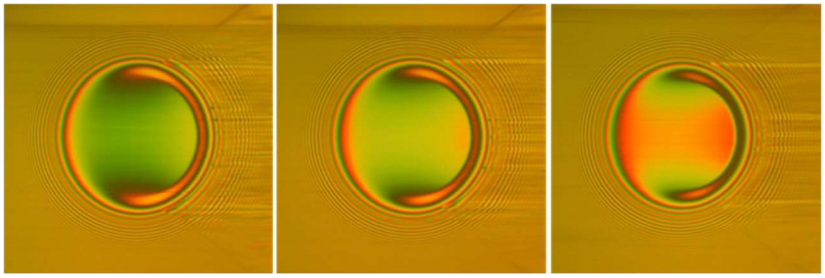

(a) SRR = -1.5 (b) SRR = -1.2 (c) SRR = -1.0

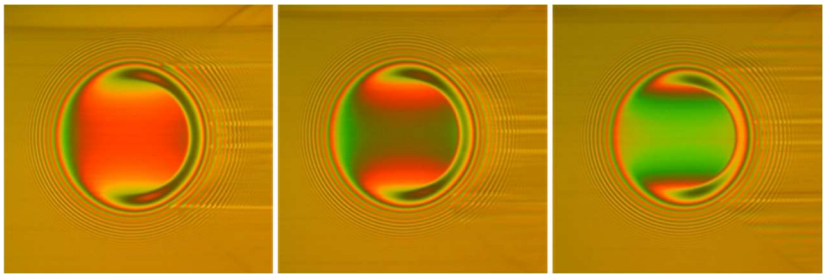

(d) SRR = -0.7 (e) SRR = -0.5 (f) SRR = -0.2

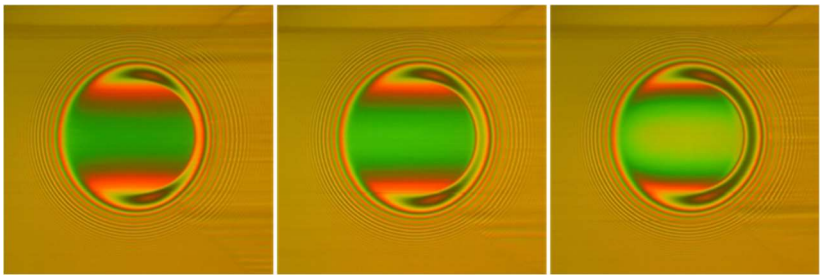

(g) SRR = 0.0 (h) SRR = 0.2 (i) SRR = 0.5

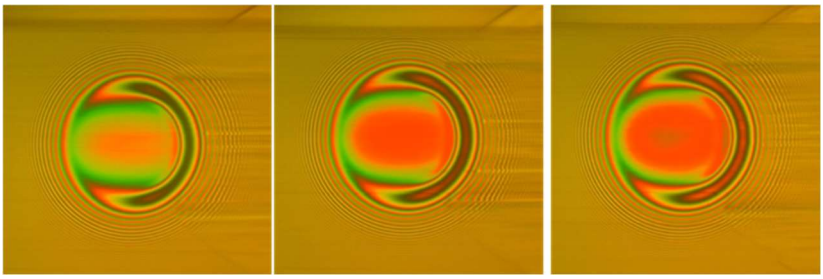

(j) SRR = 0.7 (k) SRR = 1.0 (l) SRR = 1.2

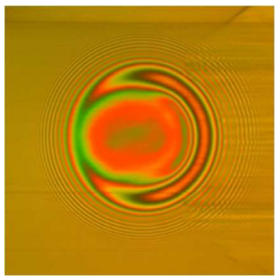

(m) SRR = 1.5

Figure 4-15 Contour maps of film thickness at the SRR range of -1.5 to 1.5 for glass–steel contact. u_e = 1 m/s, T_0 = 25 ℃, w = 50 N.

The effects of load on the interferograms with different SRR are illustrated in Fig. 4-15. The other operation parameters are same to Fig. 4-14. As the load is increased to 50 N, the size of the contact area increases due to the large elastic deformation of surfaces. However, the classical horseshoe shape film in Figs. 4-15(a)–(g), and dimple phenomenon in Figs. 4-15(h)–(m) are still observed. The trends of film shape variation are similar to Fig. 4-14.

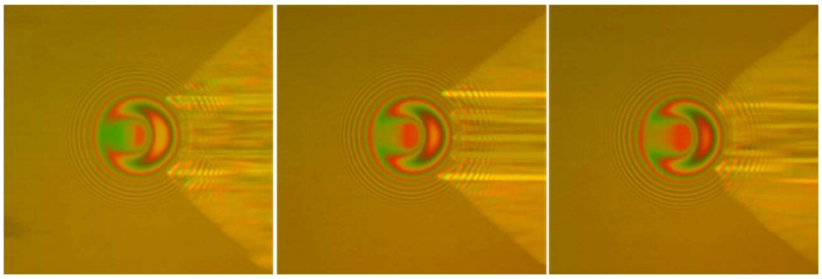

(a) SRR = -1.5 (b) SRR = -1.2 (c) SRR = -1.0

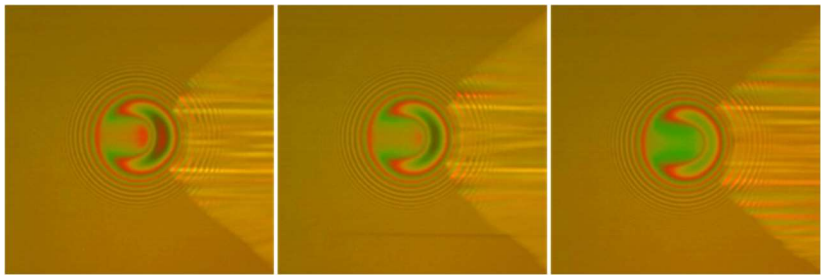

(d) SRR = -0.7 (e) SRR = -0.5 (f) SRR = -0.2

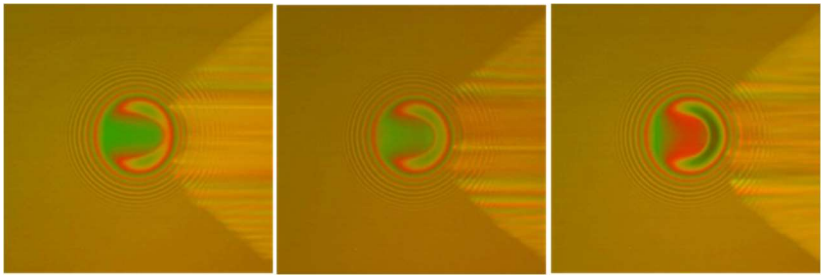

(g) SRR = 0.0 (h) SRR = 0.2 (i) SRR = 0.5

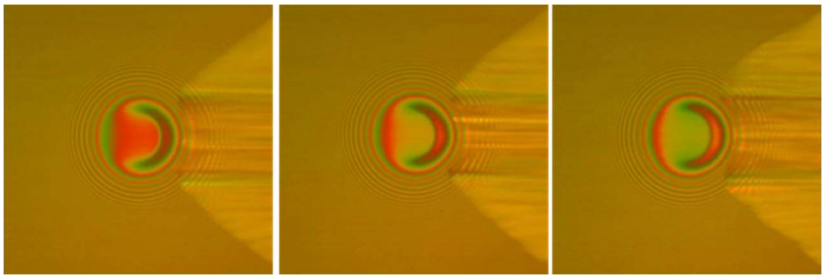

(j) SRR = 0.7 (k) SRR = 1.0 (l) SRR = 1.2

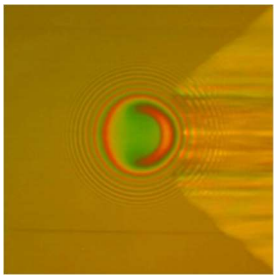

(m) SRR = 1.5

Figure 4-16 Contour maps of film thickness at the SRR range of -1.5 ~ 1.5 for sapphire–zirconia contact. u_e = 1 m/s, T_0 = 25 ℃, w = 20 N.

In Figs. 4-14 and 4-15, the dimple appeared at the conditions of SRR > 0, where disc velocity is larger than ball velocity, is attributed to temperature viscosity wedge effect. When the high thermal conductivity surface (steel ball) has a smaller velocity than that of low thermal conductivity surface (glass disc), the generated temperature viscosity wedge effect leads a dimple in contact area. To verify this phenomenon, a sapphire disc–zirconia ball contact is employed in Fig. 4-16. The thermal conductivity of sapphire disc

40 W/(m·K) is similar to steel ball, while the thermal conductivity of zirconia ball 3 W/(m·K) is close to glass disc. Other operation conditions are same to Fig. 4-14. In contrast to glass–steel contact, the dimple can be seen in the conditions of SRR < 0. At SRR > 0, a unique film distribution resembling a horseshoe is observed. Thorough the comparison with Figs. 4-14 and 4-15, it allows the conclusion that the dimple phenomenon mainly depends on the thermal conductivity of contact materials. Furthermore, the size of contact area under sapphire–zirconia contact is smaller than under glass–steel contact because of the Young's modulus. The Young's modulus of sapphire (360 GPa) and zirconia (100 GPa) are larger than steel (206 GPa) and glass (81 GPa), results in less deformation of surfaces and thus the size of contact area.

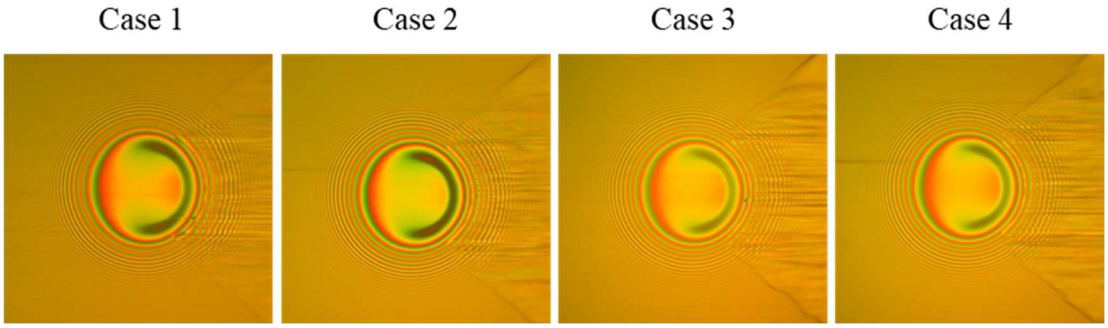

(a) SRR = -1.5

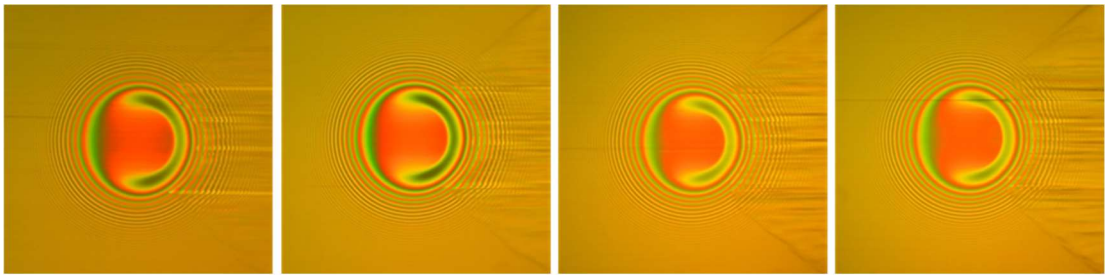

(b) SRR = -1.0

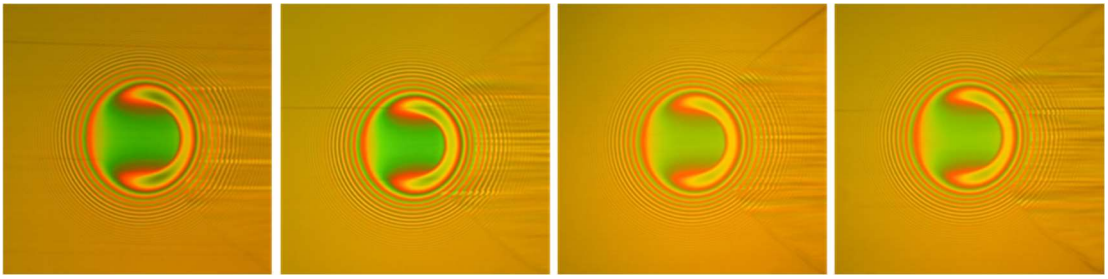

(c) SRR = -0.5

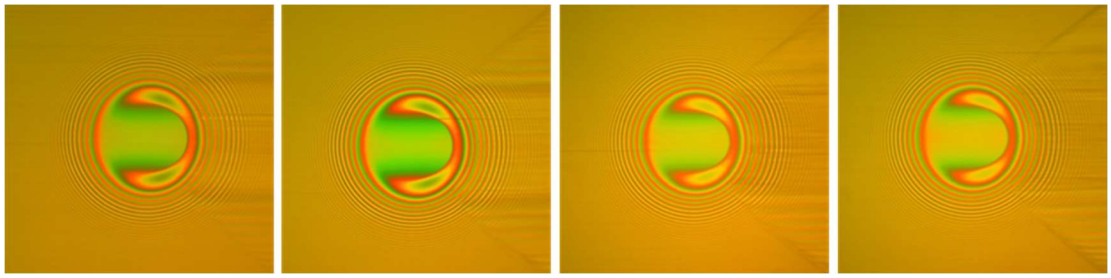

(d) SRR = 0.0

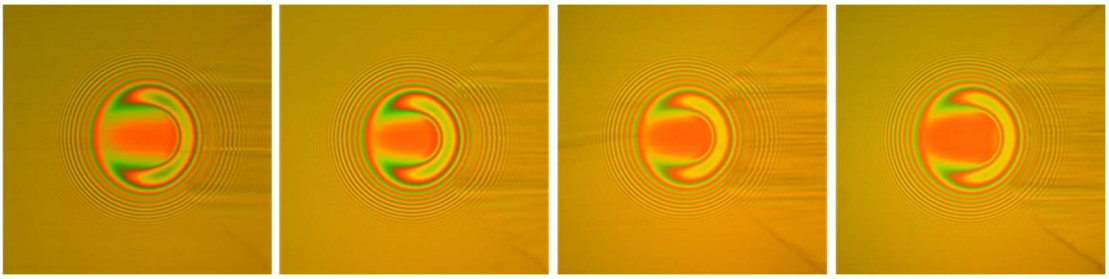

(e) SRR = 0.5

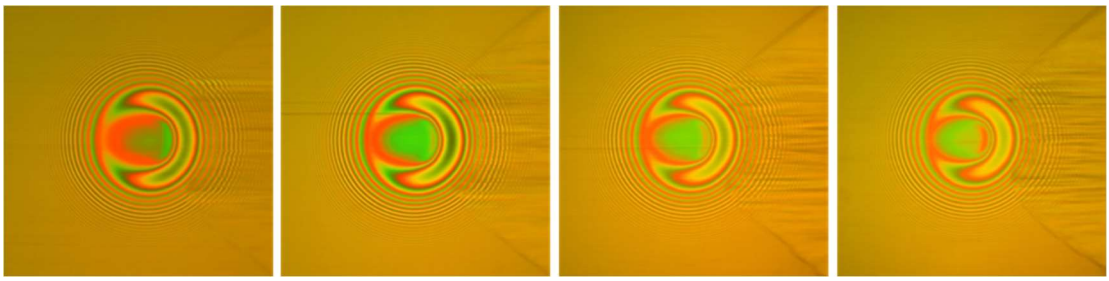

(f) SRR = 1.0

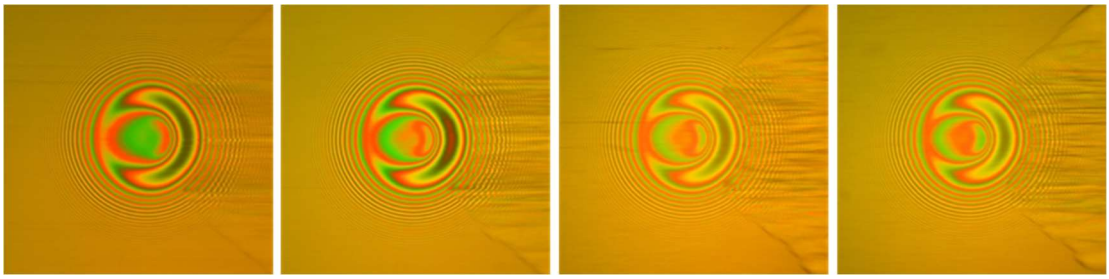

(g) SRR = 1.5

Figure 4-17 Contour maps of film thickness at the SRR range of -1.5 ~ 1.5 under steel–glass contact. u_e = 1 m/s, T_0 = 25 °C, w = 20 N. Case 1: Uncoated steel ball + Uncoated glass disc; Case 2: Hydrophobic coated steel ball + Uncoated glass disc; Case 3: Uncoated steel ball + Hydrophobic coated glass disc; Case 4: Hydrophobic steel ball + Hydrophobic glass disc.

Fig. 4-17 presents the interferograms of EHL contact with or without

hydrophobic/oleophobic coating. The working conditions are u_e = 1 m/s, T_0 = 25 °C, w = 20 N. To study the effects of boundary slips on film shape, the hydrophobic coated steel ball–uncoated glass disc contact, uncoated steel ball–hydrophobic coated glass disc contact and hydrophobic coated steel ball–hydrophobic coated glass disc contact are employed in comparison with the uncoated steel ball– uncoated glass disc contact. When the steel ball moves faster than the glass disc, SRR < 0, the interferograms of film shows classical horseshoe shape, while the effect hydrophobic coating on film thickness is invisible shown in Figs. 4-17(a)–(c). When the SRR > 0, Figs. 4-17(e)–(g) shows a dimple film shape. Furthermore, the hydrophobic/oleophobic coating leads a more significant dimple than the uncoated surface contact. The lager SRR, the greater effect of hydrophobic/oleophobic coating on dimple film shape.

4.3.3 Comparison with simulation

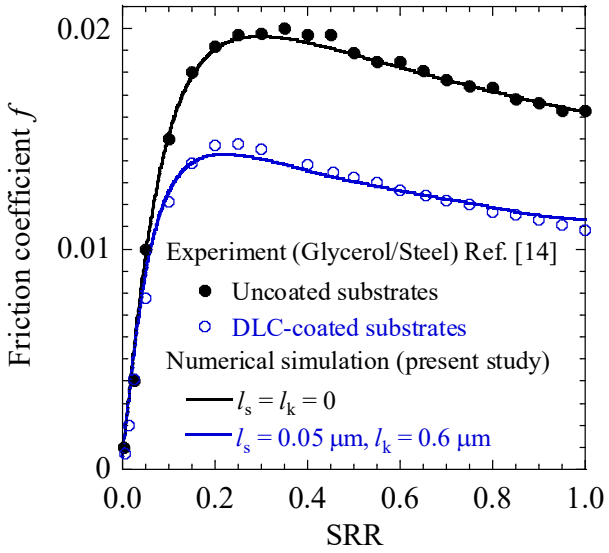

Figure 4-18 Comparisons of f-SRR curve between experiments [14] and numerical simulations at u_e = 1.6 m/s and w = 300 N

To date, only a few experimental results reported are comparable to simulation results or theoretical predictions. In Fig. 4-18, for illustrative purposes, the experimental results [14] are compared with the simulation results using the operating conditions reported in Ref. [14]. The simulation results under the no slip condition of $l_s = l_k = 0$ are consistent

with the experimental results for the uncoated substrates, whereas those under the coupled slips of l_s = 0.05 μm and l_k = 0.6 μm are consistent with the experiments of DLC-coated substrates. Here, the thermal slip length for the DLC-coated surface [14] is estimated to 0.6 μm, including both the effects of the DLC coating and the interfacial thermal resistance. Since the DLC coating is 2.8 μm in thickness and its thermal conductivity is 2 W/(m·K), the thermal resistant of the coating layer is 1.4×10^{-6} K/W. This is 2 orders of magnitude smaller than that of equivalent interfacial thermal resistance (approximately 1.2×10^{-4} K/W), Therefore, the estimated thermal slip length l_k = 0.6 μm principally attributes to the interfacial thermal resistance. Accordingly, the deviations of the experimental results between the uncoated and DLC-coated substrates are significant, which imply that the boundary slips are of great importance to the superlubricity.

The comparison between the simulation and experimental results of Fig. 4-11 are shown in Fig. 4-19. At low entrainment velocity u_e = 0.58 m/s, the boundary slip lengths at coated surfaces are estimated as l_s = 0.1 μm and l_k = 0.8 μm, while at u_e = 2.2 m/s, the boundary slip lengths are l_s = 0.07 μm and l_k = 0.15 μm. It is noticeable from Fig. 4-19 that the estimated thermal slip length l_k at hydrophobic/oleophobic coated surfaces is much larger than the slip length l_s. As the entrainment velocity u_e increases, the boundary slip lengths decrease, especially the thermal slip length l_k decreases form 0.8 μm to 0.15 μm when the u_e increases to 2.2 m/s.

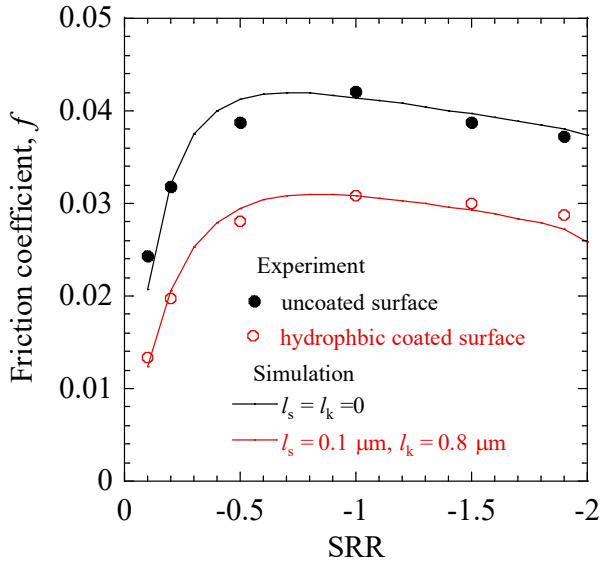

(a) u_e = 0.58 m/s

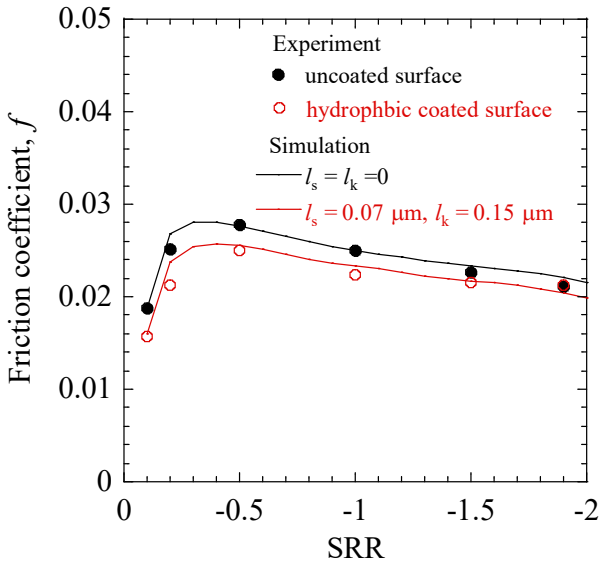

(b) u_e = 2.2 m/s

Figure 4-19 Comparisons of *f*-SRR curve between experiments and numerical simulations at u_e = 0.58 m/s, 2.2 m/s and w = 50 N.

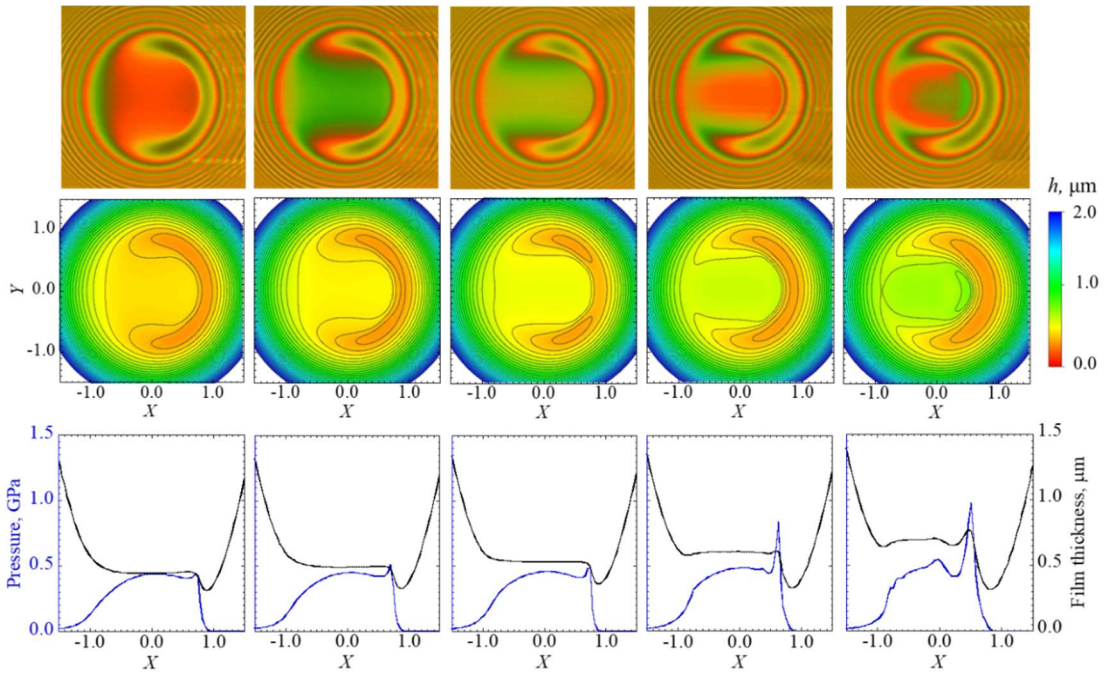

Figure 4-20 Comparisons of film contour maps between experiments and numerical simulations under steel–glass contact at u_e = 0.58 m/s, 2.2 m/s and w = 50 N. (a) SRR = -1.0; (b) SRR = -0.5; (c) SRR = 0.0; (d) SRR = 0.5; (e) SRR = 1.0.

Fig. 4-20 shows the comparison between experimental and simulation results under steel ball–glass disc contact. Top is the experimental interferograms while bottom is the contour maps of film and its corresponding pressure, film thickness profiles. The SRR range is from -1.0 to 1.0 (SRR = $2(u_d-u_b)/(u_d+u_b)$). From the figure it is evident that the shape of film from simulation agrees well with the experimental results. By examining the pressure and film thickness profiles provided in bottom, it is clear that the maximum pressure and film thickness gradually increases with SRR. When SRR = 1.0, the glass disc surface moves faster than the steel ball ($u_d = 3u_b$), a second slight dimple and pressure peak appears at the center contact area.

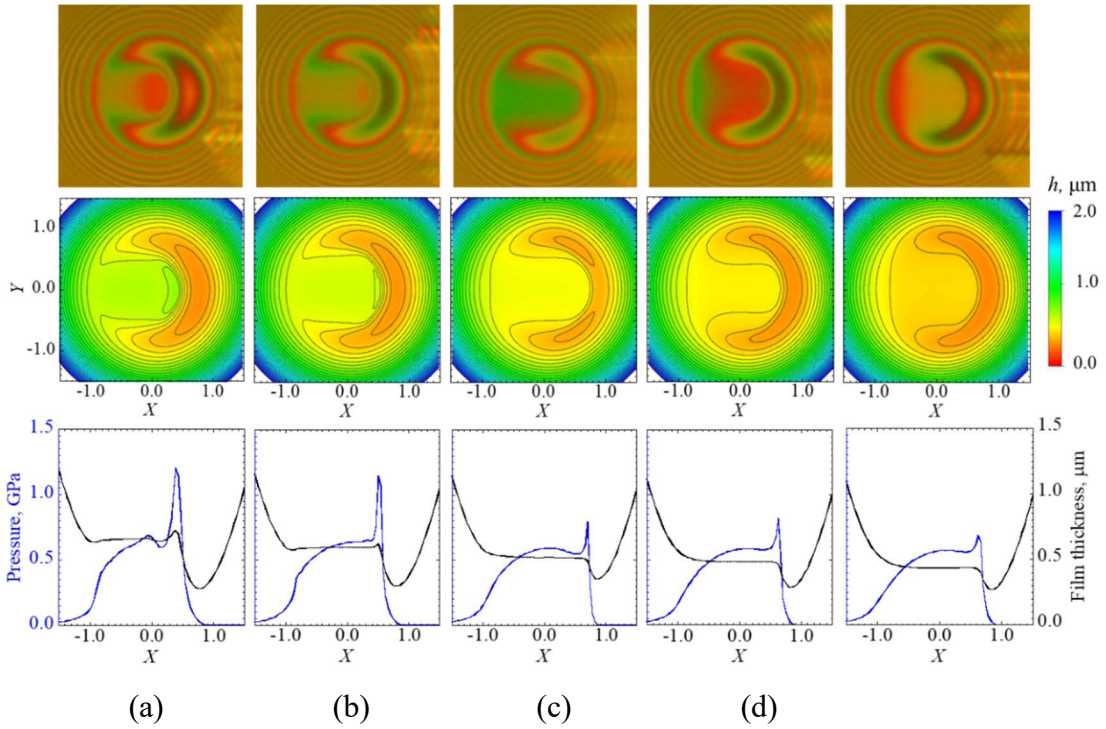

Figure 4-21 Comparisons of film contour maps between experiments and numerical simulations under zirconia–sapphire contact at u_e = 0.58 m/s, 2.2 m/s and w = 50 N. (a) SRR = -1.0; (b) SRR = -0.5; (c) SRR = 0.0; (d) SRR = 0.5; (e) SRR = 1.0.

Differ from the steel ball–glass disc contact, Fig. 4-21 shows the comparison results under zirconia ball–sapphire disc contact. Other working conditions are same to Fig. 4-20. The thermal conductivity of sapphire disc 40 W/(m·K) is similar to steel ball, while the thermal conductivity of zirconia ball 3 W/(m·K) is close to glass disc. In the SRR

range from -1.0 to 1.0, the maximum pressure and film thickness decreases with SRR. The dimple shape film appeared at the negative SRR cases (Figs. 4-21(a)–(b)) vanished, became a horseshoe shape film at the positive SRR cases (Figs. 4-21(d)–(e)), which is contrast to the results under steel ball–glass disc contact. In conclusion, the thermal conductivity of contact surfaces influences the pressure and film thickness distribution in EHL regime. When the low thermal conductivity surface moves faster than the high thermal conductivity surface, the dimple phenomenon appears, corresponding with the high film thickness and pressure distribution. On the contrary, the dimple disappears.

4.4 Summary

In this chapter, it has been shown experimentally that friction coefficient with different contact surfaces show different results of friction at comparable conditions, i.e. at entrainment velocity, SRR, load and materials. The friction reduction induced by hydrophobic/oleophobic coating can be predicated qualitatively by boundary slips at sloid–lubricant interfaces. The main conclusions are:

1. As the entrainment velocity or SRR increases, the friction coefficient firstly increases, then decreases due to the thermal effect.

2. The hydrophobic/oleophobic coated surface results in low friction. As the lubricant temperature increases or load decreases, the effect of coating surface on friction decreases. Through the comparison between the simulation and experimental results, the estimated thermal slip length l_k at hydrophobic/oleophobic coated surfaces is much larger than the slip length l_s.

3. Though the comparison of interferograms under steel–glass contact and zirconia–sapphire contact, the dimple phenomenon occurs when the low thermal conductivity surface moves faster than the high thermal conductivity surface.

The proposed method for estimating the slip length and thermal slip length quantitatively is challenging but beneficial for gaining a fundamental understanding of superlubrication. Further experimental investigations are necessary to verify the results obtained.

Chapter 5

5. Conclusions and outlook

5.1 Conclusions

This thesis is mainly concentrated on the solid–lubricant interfacial resistance, i.e., velocity slip and thermal slip, for thermal EHL problem. Although the velocity slip of EHL contact has been studied extensively, the thermal slip has been rarely coupled with velocity slip in EHL. Therefore, this thesis described a thermal EHL theory, experiments, as well as the comparison between theoretical and experimental results considering boundary slips at solid–lubricant interface. The most important results are summarized as following.

A thermal EHL theory was developed to understand the lubrication performances with boundary slips for point contact problem. The modified Reynolds equation, coupled with load balance equation, film thickness equation and energy equations, were solved to obtain the pressure, film thickness and temperature in contact area. Based on this theory, the effects of velocity and thermal slips on lubrication performances under different working conditions, entrainment velocity and slide-roll ratio etc. were qualified.

Numerical simulations were conducted to characterize the effect of boundary slips on lubrication behaviors of EHL under pure rolling motion, opposite sliding motion and rolling/sliding motion. Three cases of boundary slips, i.e., velocity slip, thermal slip, and coupled velocity/thermal slips, were investigated. Under the pure rolling motion, velocity slip induced a lubricant velocity distribution across the film, which led to a general reduction in film thickness. Under the opposite sliding motion, velocity slip caused the surface dimple to shift along the sliding direction, while thermal slip caused the surface dimple to shift in the opposite direction as the pressure peak shifted downward and the dimple depth decreased. The effects of velocity slip and thermal slip canceled out one

another when the velocity slip length and thermal slip length were equal. Under rolling/sliding motion, velocity slip dominates the film thickness reduction when the slip length is comparable to the thermal slip length, whereas the thermal slip dominates the film thickness reduction when the slip length is negligible compared with the thermal slip length. The coupled velocity/thermal slips case leads the most significant temperature rise and film thickness reduction among the three cases.

In the experimental study of boundary slips, the hydrophobic/oleophobic coating was fabricated on contact surfaces by physical vapor deposition method. The friction coefficient was measured on a ball on disc rig. Comparing with the uncoated surfaces, a significant friction reduction was induced by the hydrophobic/oleophobic coated surfaces. This friction reduction gradually decreases while increase entrainment velocity or ambient temperature. Through the comparison between the numerical simulation and experiment results, the occurrence of boundary slips on hydrophobic/oleophobic coated surface is verified. And the estimated thermal slip length at coated surfaces is much larger than the slip length. The proposed method for estimating the slip length and thermal slip length quantitatively is challenging but beneficial for gaining a fundamental understanding of superlubrication.

Through the numerical and experimental study, this thesis, for the first time, revealed the effect of thermal slip at the solid–lubricant interface on lubrication behavior, which might be one of the key parameters in EHL contact. This work will also provide useful insights into the understanding of the boundary slips at solid–lubricant interface and design guidelines for various applications.

5.2 Outlook

There are several future work directions should be addressed based on this thesis, which can be summarized below.

For the numerical simulation, as the influence of interfacial resistance on lubrication is very complex, the present model makes some hypotheses for simplification, such as Newtonian fluid, constant thermal conductivity of materials. Therefore, future models will consider the lubricant rheology and the varication of materials thermal conductivity, which will play a vital role on heat dissipation. Furthermore, it is interesting to see scale

and contact geometrical effects exist in the analysis of interfacial resistance. Much work needs to be carried out for a better understanding of the effect of interfacial resistance on lubrication performance in EHL or mixed lubrication regime.

For the experimental study, while the friction coefficient and interferograms of EHL contact are measured in this thesis, the temperature distributions are still not clear. To better understand the effects of boundary slips on lubrication, the temperature distribution in contact area will be investigated by infrared and optical interferometry techniques. Besides the full film lubrication and smooth contact surfaces used in this study, further work will also be focused on considering the starvation and roughness EHL contact, then extended to mixed lubrication or boundary lubrication in the Stribeck curve.

References

[1] Britain G. Lubrication (Tribology), education and research; a report on the present position and industry's needs. London: **1966**.

[2] Dašić P, Franek F, Assenova E, Radovanović M. International standardization and organizations in the field of tribology. *Industrial Lubrication and Tribology*, **2003**, 55:287–91.

[3] Hamrock BJ. Fundamentals of fluid film lubrication. *Nasa Publication 1255*, **1991**:301–18.

[4] Tower B. First report on friction experiments. *Proceedings of the Institution of Mechanical Engineers*, **1883**, 34:632–59.

[5] Smith FW. Lubricant behavior in concentrated contact—some rheological problems. *ASLE Transactions*, **1960**, 3:18–25.

[6] Crook AW. The lubrication of rollers IV. Measurements of friction and effective viscosity. *Philosophical Transactions of the Royal Society of London Series A, Mathematical and Physical Sciences*, **1963**, 255:281–312.

[7] Johnson KL, Cameron R. Fourth Paper: Shear behaviour of Elastohydrodynamic oil films at high rolling contact pressures. *Proceedings of the Institution of Mechanical Engineers*, **1967**, 182:307–30.

[8] Lu J, Reddyhoff T, Dini D. A study of thermal effects in EHL rheology and friction using infrared microscopy. *Tribology International*, **2020**, 146:106179.

[9] Zhang J, Spikes H. Measurement of EHD friction at very high contact pressures. *Tribology Letters*, **2020**, 68:1–12.

[10] Chhowalla M, Amaratunga GAJ. Thin films of fullerene-like MoS2 nanoparticles with ultra-low friction and wear. *Nature*, **2000**, 407:164–7.

[11] Meng F, Han H, Gao X, Yang C, Zheng Z. Experiment study on tribological performances of GNPs/MoS2 coating. *Tribology International*, **2018**, 118:400–7.

[12] Moskalewicz T, Zimowski S, Wendler B, Nolbrzak P, Czyrska-Filemonowicz A. Microstructure and tribological properties of low-friction composite MoS2(Ti,W)

coating on the oxygen hardened Ti-6Al-4V alloy. *Metals and Materials International*, **2014**, 20:269–76.

[13] He Y, Wang SC, Walsh FC, Chiu YL, Reed PAS. Self-lubricating Ni-P-MoS2 composite coatings. *Surface and Coatings Technology*, **2016**, 307:926–34.

[14] Björling M, Shi Y. DLC and glycerol: Superlubricity in rolling/sliding elastohydrodynamic lubrication. *Tribology Letters*, **2019**, 67:23.

[15] Evans RD, Cogdell JD, Richter GA. Traction of lubricated rolling contacts between thin-film coatings and steel. *Tribology Transactions*, **2009**, 52:106–13.

[16] Kalin M, Polajnar M. The correlation between the surface energy, the contact angle and the spreading parameter, and their relevance for the wetting behaviour of DLC with lubricating oils. *Tribology International*, **2013**, 66:225–33.

[17] Kalin M, Velkavrh I, Vižintin J. The Stribeck curve and lubrication design for non-fully wetted surfaces. *Wear*, **2009**, 267:1232–40.

[18] Beilicke R, Bobach L, Bartel D. Transient thermal elastohydrodynamic simulation of a DLC coated helical gear pair considering limiting shear stress behavior of the lubricant. *Tribology International*, **2016**, 97:136–50.

[19] Habchi W. Thermal analysis of friction in coated elastohydrodynamic circular contacts. *Tribology International*, **2016**, 93:530–8.

[20] Björling M, Habchi W, Bair S, Larsson R, Marklund P. Friction Reduction in Elastohydrodynamic Contacts by Thin-Layer Thermal Insulation. *Tribology Letters*, **2014**, 53:477–86.

[21] Yu X, Meng Y, Tian Y, Zhang J, Liang W. Measurement of lubricant viscosity and detection of boundary slip at high shear rates. *Tribology International*, **2016**, 94:20–5.

[22] Berman D, Deshmukh SA, Sankaranarayanan SKRS, Erdemir A, Sumant A V. Extraordinary macroscale wear resistance of one atom thick graphene layer. *Advanced Functional Materials*, **2014**, 24:6640–6.

[23] Berman D, Erdemir A, Sumant A V. Graphene as a protective coating and superior lubricant for electrical contacts. *Applied Physics Letters*, **2014**, 105:231907.

[24] Li S, Li Q, Carpick RW, Gumbsch P, Liu XZ, Ding X, et al. The evolving quality of frictional contact with graphene. *Nature*, **2016**, 539:541–5.

[25] Yakubov GE, McColl J, Bongaerts JHH, Ramsden JJ. Viscous boundary

lubrication of hydrophobic surfaces by mucin. *Langmuir*, **2009**, 25:2313–21.

[26] Ma Q, He T, Khan AM, Wang Q, Chung YW. Achieving macroscale liquid superlubricity using glycerol aqueous solutions. *Tribology International*, **2021**, 160:107006.

[27] Crook AW. Elastohydrodynamic lubrication of rollers. *Nature*, **1961**, 190:1182–3.

[28] Wedeven LD. Optical measurements of elastohydrodynamics in rolling contact bearings. University of London, **1970**.

[29] Kaneta M, Nishikawa H, Kameishi K. Observation of wall slip in elastohydrodynamic lubrication. *Journal of Tribology*, **1990**, 112:447–52.

[30] Kaneta M, Nishikawa H, Kanada T, Matsuda K. Abnormal phenomena appearing in EHL contacts. *Journal of Tribology*, **1996**:886–92.

[31] Yagi K, Kyogoku K, Nakahara T. Relationship between temperature distribution in EHL film and dimple formation. *Journal of Tribology*, **2005**, 127:658–65.

[32] Cameron A. Hydrodynamic lubrication of rotating disks in pure sliding. A new type of oil film formation. *Journal of the Institute of Petroleum*, **1951**, 37:471–86.

[33] Cameron A. The viscosity wedge. *A S L E Transactions*, **1958**, 1:248–53.

[34] Yagi K, Vergne P, Nakahara T. In situ pressure measurements in dimpled elastohydrodynamic sliding contacts by Raman microspectroscopy. *Tribology International*, **2009**, 42:724–30.

[35] Hartl M. Differential colorimetry: tool for evaluation of chromatic interference patterns. *Optical Engineering*, **1997**, 36:2384–91.

[36] Hartl M, Křupka I, Poliščuk R, Liška M. An automatic system for real-time evaluation of EHD film thickness and shape based on the colorimetric interferometry. *Tribology Transactions*, **1999**, 42:303–9.

[37] Krupka I, Bair S, Kumar P, Khonsari MM, Hartl M. An experimental validation of the recently discovered scale effect in generalized newtonian EHL. *Tribology Letters*, **2009**, 33:127–35.

[38] Hili J, Olver A V., Edwards S, Jacobs L. Experimental investigation of elastohydrodynamic (EHD) film thickness behavior at high speeds. *Tribology Transactions*, **2010**, 53:658–66.

[39] Menga X, Zhanga B, Wanga J, Zou Q. Experimental observation on the surface

dimple variations in starved EHL of sliding steel–glass point contacts. *Tribology International*, **2017**, 105:166–74.

[40] Zhang Y, Wang W, Zhang S, Zhao Z. Experimental study of EHL film thickness behaviour at high speed in ball-on-ring contacts. *Tribology International*, **2017**, 113:216–23.

[41] Turchina V, Sanborn DM, Winer WO. Temperature measurements in sliding elastohydrodynamic point contacts. *American Society of Mechanical Engineers (Paper)*, **1973**:464–9.

[42] Ausherman VK, Nagaraj HS, Sanborn DM, Winer WO. Infrared temperature mapping in elastohydrodynamic lubrication. *J Lubr Technol Trans ASME*, **1976**, 98:236–43.

[43] Yagi K, Kyogoku K, Nakahara T. Experimental investigation of effects of slip ratio on elastohydrodynamic lubrication film related to temperature distribution in oil films. *Proceedings of the Institution of Mechanical Engineers, Part J: Journal of Engineering Tribology*, **2006**, 220:353–63.

[44] Yagi K, Kyogoku K, Nakahara T. Mechanism of dimple formation under elastohydrodynamic conditions. *Tribology Series*, **2003**, 41:111–20.

[45] Spikes HA, Anghel V, Glovnea R. Measurement of the rheology of lubricant films within elastohydrodynamic contacts. *Tribology Letters*, **2004**, 17:593–605.

[46] Lu J, Reddyhoff T, Dini D. 3D measurements of lubricant and surface temperatures within an elastohydrodynamic contact. *Tribology Letters*, **2018**, 66:1–16.

[47] Nishikawa H, Shimada T, Tsuda S, Kaneta M. Effect of surface ridges on oil film temperature in EHL contacts. *5th World Tribology Congress, WTC 2013*, **2013**, 2:1683–5.

[48] Omasta M, Adam J, Sperka P, Krupka I, Hartl M. On the temperature and lubricant film thickness distribution in EHL contacts with arbitrary entrainment. *Lubricants*, **2018**, 6:101.

[49] Petrusevich AI. Fundamental conclusions from the contact hydrodynamic theory of lubrication. *Izvestiya Akademii Nauk SSSR (OTN)*, **1951**, 3:209–23.

[50] Dowson D, Higginson GR. A numerical solution to the elasto-Hydrodynamic problem. *Journal of Mechanical Engineering Science*, **1959**, 1:6–15.

[51] Gohar R. Elastohydrodynamics. Imperial College Press; **2001**.

[52] Houpert LG, Hamrock BJ. Fast approach for calculating film thicknesses and pressures in elastohydrodynamically lubricated contacts at high loads. *Journal of Tribology*, **1986**, 108:411–9.

[53] Okanura H. A contribution to the numerical analysis of isothermal elastohydrodynamic lubrication. *Proc 9th Leeds-Lyon Symp, 1982*, **1982**.

[54] Venner CH. Multilevel solution of the EHL line and point contact problems. **1991**.

[55] Brandt A. Multi-level adaptive solutions to boundary value problems **1977**:333–90.

[56] Cheng HS. A refined solution to the thermal-elastohydrodynamic lubrication of rolling and sliding cylinders. *ASLE Transactions*, **1965**, 8:397–410.

[57] Cheng HS, Sternlicht B. A numerical solution for the pressure, temperature, and film thickness between two infinitely long, lubricated rolling and sliding cylinders, under heavy loads. *Journal of Fluids Engineering, Transactions of the ASME*, **1965**, 87:695–704.

[58] Sadeghi F, Dow T, Johnson RR. Thermal effects in rolling/sliding contacts: part 3-approximate method for prediction of mid-film temperature and sliding traction. *Journal of Tribology-Transactions of The Asme*, **1987**, 109:519–23.

[59] Büiggemann H, Kollmann FG. A numerical solution of the thermal elastohydrodynamic lubrication in an elliptical contact. *Journal of Tribology*, **1982**, 104:392–400.

[60] Dowson D, Whitaker A V. Paper 4: A numerical procedure for the solution of the elastohydrodynamic problem of rolling and sliding contacts lubricated by a Newtonian fluid. *Proceedings of the Institution of Mechanical Engineers, Conference Proceedings*, **1965**, 180:57–71.

[61] Liu HC, Zhang BB, Bader N, Poll G, Venner CH. Influences of solid and lubricant thermal conductivity on traction in an EHL circular contact. *Tribology International*, **2020**, 146:106059.

[62] Liu HC, Zhang BB, Badera N, Venner CH, Poll G. Scale and contact geometry effects on friction in thermal EHL: twin-disc versus ball-on-disc. *Tribology International*, **2020**, 154:106694.

[63] Habchi W, Bair S. The role of the thermal conductivity of steel in quantitative elastohydrodynamic friction. *Tribology International*, **2020**, 142:105970.

[64] Liu HC, Zhang BB, Bader N, Guo F, Poll G, Yang P. Crucial role of solid body temperature on elastohydrodynamic film thickness and traction. *Tribology International*, **2019**, 131:386–97.

[65] Kim KH, Sadeghi F. Three-dimensional temperature distribution in ehd lubrication: Part II-Point contact and numerical formulation. *Journal of Tribology*, **1993**, 115:36–45.

[66] Guo F, Yang P. Influence of a ring flat zone in the point contact surface on thermal elastohydrodynamic lubrication. *Tribology International*, **1999**, 32:167–75.

[67] Dong Z, Shi-Zhu W. A full numerical solution for the thermoelastohydrodynamic problem in elliptical contacts. *Journal of Tribology*, **1984**, 106:246–54.

[68] Hsiao HSS, Hamrock BJ. Temperature distribution and thermal degradation of the lubricant in ehl line contact conjunctions. *Journal of Tribology*, **1994**, 116:794–803.

[69] Wang J, Yang P. A numerical analysis for TEHL of eccentric-tappet pair subjected to transient load. *Journal of Tribology*, **2003**, 125:770–9.

[70] Wang X, Liu Y, Zhu D. Numerical solution of mixed thermal elastohydrodynamic lubrication in point contacts with three-dimensional surface roughness. *Journal of Tribology*, **2017**, 139:011501.

[71] Ebner M, Ziegltrum A, Lohner T, Michaelis K, Stahl K. Measurement of EHL temperature by thin film sensors – Thermal insulation effects. *Tribology International*, **2018**:105515.

[72] Liu Y, Wang QJ, Bair S, Vergne P. A quantitative solution for the full shear-thinning EHL point contact problem including traction. *Tribology Letters*, **2007**, 28:171–81.

[73] Bair SS, Winer WO. Surface temperatures and glassy state investigations in tribology, part 3. *GEORGIA INST OF TECH ATLANTA*, **1980**.

[74] Bair S. The viscosity at the glass transition of a liquid lubricant. *Friction*, **2019**, 7:86–91.

[75] Almqvist T, Larsson R. The Navier-Stokes approach for thermal EHL line contact solutions. *Tribology International*, **2002**, 35:163–70.

[76] Guo F, Yang P, Qu S. On the theory of thermal elastohydrodynamic lubrication at high slide-roll ratios - Circular glass–steel contact solution at opposite sliding. *Journal of Tribology*, **2001**, 123:816–21.

[77] Wang Y, Li H, Tong J, Yang P. Transient thermoelastohydrodynamic lubrication analysis of an involute spur gear. *Tribology International*, **2004**, 37:773–82.

[78] Yang P, Wen S. The behavior of non-newtonian thermal EHL film in line contacts at dynamic loads. *Journal of Tribology*, **1992**, 114:81–5.

[79] Liu X, Jiang M, Yang P, Kaneta M. Non-Newtonian thermal analyses of point EHL contacts using the Eyring model. *Journal of Tribology*, **2005**, 127:70–81.

[80] Yang P, Liu X. Effects of solid body temperature on the non-Newtonian thermal elastohydrodynamic lubrication behaviour in point contacts. Proceedings of the Institution of Mechanical Engineers, Part J: Journal of Engineering Tribology, vol. 223, **2009**, p. 959–69.

[81] Liu X, Yang P. Influence of solid body temperature on the thermal EHL behavior in circular contacts. *Journal of Tribology*, **2008**, 130:014501.

[82] de la Guerra Ochoa E, Echávarri Otero J, Sánchez López A, Chacón Tanarro E, del Río López B. Film thickness formula for thermal EHL line contact considering a new Reynolds–Carreau equation. *Tribology Letters*, **2018**, 66:1–12.

[83] Zhang B, Wang J, Omasta M, Kaneta M. Effect of fluid rheology on the thermal EHL under ZEV in line contact. *Tribology International*, **2015**, 87:40–9.

[84] Hamrock BJ, Dowson D. Ball bearing lubrication (the elastohydrodynamics of elliptical contacts). **1982**:279–81.

[85] Kaneta M, Yang P. Formation mechanism of steady multi-dimples in thermal EHL point contacts. *Journal of Tribology*, **2003**, 125:241–51.

[86] Yang P, Qu S, Kaneta M, Nishikawa H. Formation of steady dimples in point TEHL contacts. *Journal of Tribology*, **2001**, 123:42–9.

[87] Yagi K, Kyogoku K, Nakahara T. Temperature measurements of oil film and surface in point contact EHL under high slip ratio conditions. *Japanese Journal of Tribology*, **2001**, 46:290–1.

[88] Wang S, Wang J, Han Y, Li W. Variation of zero entraining velocity dimple in grease-lubricated reciprocating motion. *Proceedings of the Institution of Mechanical Engineers, Part J: Journal of Engineering Tribology*, **2019**, 233:1661–87.

[89] Dyson, A., Naylor, H., Wilson A. The measurement of oil-film thickness in elastohydrodynamic contacts. *Proc Inst Mech Engrs*, **1965**, 180:119–34.

[90] Guo F, Wong PL, Yang P, Yagi K. Film formation in EHL point contacts under zero entraining velocity conditions. *Tribology Transactions*, **2002**, 45:521–30.

[91] Guo F, Yang P, Wong PL. On the thermal elastohydrodynamic lubrication in opposite sliding circular contacts. *Tribology International*, **2001**, 34:443–52.

[92] Zhang B, Wang J, Omasta M, Kaneta M. Variation of surface dimple in point contact thermal EHL under ZEV condition. *Tribology International*, **2016**, 94:383–94.

[93] Navier CL. Memorie sur les lois du lois du mouvement des fluides. *Mem Acad Sci Inst France*, **1827**, 6:298–440.

[94] Lee C, Kim CJ. Maximizing the giant liquid slip on superhydrophobic microstructures by nanostructuring their sidewalls. *Langmuir*, **2009**, 25:12812–8.

[95] Lee C, Kim CJ. Influence of surface hierarchy of superhydrophobic surfaces on liquid slip. *Langmuir*, **2011**, 27:4243–8.

[96] Pit R, Hervet H, Léger L. Friction and slip of a simple liquid at a solid surface. *Tribology Letters*, **1999**, 7:147–52.

[97] Pit R, Hervet H, Léger L. Direct experimental evidence of slip in hexadecane: solid interfaces. *Physical Review Letters*, **2000**, 85:980–3.

[98] Schäffel D, Koynov K, Vollmer D, Butt HJ, Schönecker C. Local flow field and slip length of superhydrophobic surfaces. *Physical Review Letters*, **2016**, 116:134501.

[99] Bonaccurso E, Butt HJ, Craig VSJ. Surface roughness and hydrodynamic boundary slip of a Newtonian fluid in a completely wetting system. *Physical Review Letters*, **2003**, 90:4.

[100] Maali A, Pan Y, Bhushan B, Charlaix E. Hydrodynamic drag-force measurement and slip length on microstructured surfaces. *Physical Review E - Statistical, Nonlinear, and Soft Matter Physics*, **2012**, 85:066310.

[101] Guo F, Wong PL, Geng M, Kaneta M. Occurrence of wall slip in elastohydrodynamic lubrication contacts. *Tribology Letters*, **2009**, 34:103–11.

[102] Wong PL, Li XM, Guo F. Evidence of lubricant slip on steel surface in EHL contact. *Tribology International*, **2013**, 61:116–9.

[103] Li XM, Guo F, Wong PL. Study of boundary slippage using movement of a post-impact EHL dimple under conditions of pure sliding and zero entrainment velocity.

Tribology Letters, **2011**, 44:159–65.

[104] Zhu L, Attard P, Neto C. Reliable measurements of interfacial slip by colloid probe atomic force microscopy. II. hydrodynamic force measurements. *Langmuir*, **2011**, 27:6712–9.

[105] Zhu L, Neto C, Attard P. Reliable measurements of interfacial slip by colloid probe atomic force microscopy. III. Shear-rate-dependent slip. *Langmuir*, **2012**, 28:3465–73.

[106] Zhu L, Attard P, Neto C. Reliable measurements of interfacial slip by colloid probe atomic force microscopy. I. Mathematical modeling. *Langmuir*, **2011**, 27:6701–11.

[107] Zhu L, Attard P, Neto C. Reconciling slip measurements in symmetric and asymmetric systems. *Langmuir*, **2012**, 28:7768–74.

[108] Ehret P, Bauget F. Observation of Kaneta's dimples in elastohydrodynamic lubrication contacts. *Proceedings of the Institution of Mechanical Engineers, Part J: Journal of Engineering Tribology*, **2001**, 215:289–300.

[109] Ehret P, Dowson D, Taylor CM. On lubricant transport conditions in elastohydrodynamic conjunctions. *Proceedings of the Royal Society A: Mathematical, Physical and Engineering Sciences*, **1998**, 454:763–87.

[110] Spikes H, Granick S. Equation for slip of simple liquids at smooth solid surfaces. *Langmuir*, **2003**, 19:5065–71.

[111] Zhang Y, Wen S. An analysis of elastohydrodynamic lubrication with limiting shear stress: part ii — load influence. *Tribology Transactions*, **2002**, 45:211–6.

[112] Ståhl J, Jacobson BO. A lubricant model considering wall-slip in EHL line contacts. *Journal of Tribology*, **2003**, 125:523–32.

[113] Zhang Y, Wen S. An analysis of elastohydrodynamic lubrication with limiting shear stress: Part i—theory and solutions. *Tribology Transactions*, **2002**, 45:135–44.

[114] Zhao Y, Wong PL, Guo L. Linear complementarity solution of 2D boundary slip EHL contact. *Tribology International*, **2020**, 145:106178.

[115] Zhang Y, Wang W, Liang H, Zhao Z. Layered oil slip model for investigation of film thickness behaviours at high speed conditions. *Tribology International*, **2019**, 131:137–47.

[116] Zhang Y, Wang W, Liang H, Zhao Z. Slip status in lubricated point-contact based on layered oil slip lubrication model. *Tribology International*, **2020**, 144:106104.

[117] Chu LM, Lin JR, Li WL, Lu JM. A model for line-contact EHL problems-consideration of effects of navier-slip and lubricant rheology. *Journal of Tribology*, **2012**, 134:031502.

[118] Chen Q Da, Jao HC, Chu LM, Li WL. Effects of anisotropic slip on the elastohydrodynamic lubrication of circular contacts. *Journal of Tribology*, **2016**, 138:1–48.

[119] Wang P, Reddyhoff T. Wall slip in an EHL contact lubricated with 1-dodecanol. *Tribology International*, **2017**, 113:197–205.

[120] Zhao Y, Wong PL, Mao JH. Solving coupled boundary slip and heat transfer EHL problem under large slide–roll ratio conditions. *Tribology International*, **2019**, 133:73–87.

[121] Zhao Y, Wong PL. Thermal-EHL analysis of slip/no-slip contact at high slide-to-roll ratio. *Tribology International*, **2021**, 153:106617.

[122] Spikes HA. The half-wetted bearing. Part 1: Extended Reynolds equation. *Proceedings of the Institution of Mechanical Engineers, Part J: Journal of Engineering Tribology*, **2003**, 217:1–14.

[123] Spikes HA. The half-wetted bearing. Part 2: Potential application in low load contacts. *Proceedings of the Institution of Mechanical Engineers, Part J: Journal of Engineering Tribology*, **2003**, 217:15–26.

[124] Choo JH, Forrest AK, Spikes HA. Influence of organic friction modifier on liquid slip: A new mechanism of organic friction modifier action. *Tribology Letters*, **2007**.

[125] Choo JH, Glovnea RP, Forrest AK, Spikes HA. A low friction bearing based on liquid slip at the wall. *Journal of Tribology*, **2007**, 129:611–20.

[126] Kalin M, Polajnar M. The effect of wetting and surface energy on the friction and slip in oil-lubricated contacts. *Tribology Letters*, **2013**, 52:185–94.

[127] Zhao Y, Wong PL, Mao JH. EHL film formation under zero entrainment velocity condition. *Tribology International*, **2018**, 124:1–9.

[128] Wong PL, Zhao Y, Mao J. Facilitating effective hydrodynamic lubrication for zero-entrainment-velocity contacts based on boundary slip mechanism. *Tribology International*, **2018**, 128:89–95.

[129] Migler KB, Hervet H, Leger L. Slip transition of a polymer melt under shear stress. *Physical Review Letters*, **1993**, 70:287–90.

[130] Tretheway DC, Meinhart CD. Apparent fluid slip at hydrophobic microchannel walls. *Physics of Fluids*, **2002**, 14:L9–12.

[131] Jao HC, Chang KM, Chu LM, Li WL. A modified average Reynolds equation for rough bearings with anisotropic slip. *Journal of Tribology*, **2016**, 138:011702.

[132] Zhu Y, Granick S. Rate-Dependent Slip of Newtonian Liquid at Smooth Surfaces. *Physical Review Letters*, **2001**, 87:1–4.

[133] Zhu Y, Granick S. Limits of the hydrodynamic no-slip boundary condition. *Physical Review Letters*, **2002**, 88:4.

[134] Münch A, Wagner B, Witelski TP. Lubrication models with small to large slip lengths. *Journal of Engineering Mathematics*, **2005**, 53:359–83.

[135] Wang LL, Lu CH, Wang M, Fu WX. The numerical analysis of the radial sleeve bearing with combined surface slip. *Tribology International*, **2012**, 47:100–4.

[136] Cheng F, Ji W. A velocity-slip model for analysis of the fluid film in the cavitation region of a journal bearing. *Tribology International*, **2016**, 97:163–72.

[137] Thompson PA, Robbins MO. Shear flow near solids: Epitaxial order and flow boundary conditions. *Physical Review A*, **1990**, 41:6830–7.

[138] Thompson PA, Troian SM. A general boundary condition for liquid flow at solid surfaces. *Nature*, **1997**, 389:360–2.

[139] Priezjev N V., Troian SM. Molecular origin and dynamic behavior of slip in sheared polymer films. *Physical Review Letters*, **2004**, 92:4.

[140] Asproulis N, Drikakis D. Boundary slip dependency on surface stiffness. *Physical Review E - Statistical, Nonlinear, and Soft Matter Physics*, **2010**, 81:061503.

[141] Savio D, Fillot N, Vergne P, Zaccheddu M. A model for wall slip prediction of confined n-alkanes: effect of wall-fluid interaction versus fluid resistance. *Tribology Letters*, **2012**, 46:11–22.

[142] Savio D, Fillot N, Vergne P, Hetzler H, Seemann W, Morales Espejel GE. A multiscale study on the wall slip effect in a ceramic-steel contact with nanometer-thick lubricant film by a nano-to-elastohydrodynamic lubrication approach. *Journal of Tribology*, **2015**, 137:031502.

[143] Barrat J, Chiaruttini F. Kapitza resistance at the liquid—solid interface. *Molecular Physics*, **2003**, 101:1605–10.

[144] Nagayama G. Boundary conditions and microscale heat transfer at solid–liquid interface. *Journal of the Heat Transfer Society of Japan*, **2011**, 50:29–36.

[145] Kim BH, Beskok A, Cagin T. Thermal interactions in nanoscale fluid flow: Molecular dynamics simulations with solid–liquid interfaces. *Microfluidics and Nanofluidics*, **2008**, 5:551–9.

[146] Kim BH, Beskok A, Cagin T. Molecular dynamics simulations of thermal resistance at the liquid–solid interface. *Journal of Chemical Physics*, **2008**, 129:174701.

[147] Voeltzel N, Giuliani A, Fillot N, Vergne P, Joly L. Nanolubrication by ionic liquids: Molecular dynamics simulations reveal an anomalous effective rheology. *Physical Chemistry Chemical Physics*, **2015**, 17:23226–35.

[148] Shenogina N, Godawat R, Keblinski P, Garde S. How wetting and adhesion affect thermal conductance of a range of hydrophobic to hydrophilic aqueous interfaces. *Physical Review Letters*, **2009**, 102:156101.

[149] Nagayama G, Cheng P. Effects of interface wettability on microscale flow by molecular dynamics simulation. *International Journal of Heat and Mass Transfer*, **2004**, 47:501–13.

[150] Nagayama G, Matsumoto T, Fukushima K, Tsuruta T. Scale effect of slip boundary condition at solid–liquid interface. *Scientific Reports*, **2017**, 7:1–8.

[151] Fu Z, Guo F, Wong PL. Non-classical elastohydrodynamic lubricating film shape under large slide-roll ratios. *Tribology Letters*, **2007**, 27:211–9.

[152] Ponjavic A, Wong JSS. The effect of boundary slip on elastohydrodynamic lubrication. *RSC Advances*, **2014**, 4:20821–9.

[153] Ponjavic A, Chennaoui M, Wong JSS. Through-thickness velocity profile measurements in an elastohydrodynamic contact. *Tribology Letters*, **2013**, 50:261–77.

[154] Wen S, Zhang Y. EHL Performance of the Lubricant With Shear Strength: Part I — Boundary Slippage and Film Failure. *Tribology Transactions*, **2000**, 43:700–10.

[155] Kamisli F. Analysis of Herchel-Bulkley fluid flows in planar and circular microducts with constant heat flux and slip boundary condition. *International Communications in Heat and Mass Transfer*, **2020**, 119:104947.

[156] Echeverri Restrepo S, van Eijk MCP, Ewen JP. Behaviour of n-alkanes confined

between iron oxide surfaces at high pressure and shear rate: a nonequilibrium molecular dynamics study. *Tribology International*, **2019**, 137:420–32.

[157] Neto C, Evans DR, Bonaccurso E, Butt HJ, Craig VSJ. Boundary slip in Newtonian liquids: A review of experimental studies. *Reports on Progress in Physics*, **2005**, 68:2859–97.

[158] Kapitza PL. The study of heat transfer in Helium II. Helium 4, **1971**, p. 114–53.

[159] Pollack GL. Kapitza Resistance. *Reviews of Modern Physics*, **1969**, 41:48–81.

[160] Kaneta M, Cui J, Yang P, Krupka I, Hartl M. Influence of thermal conductivity of contact bodies on perturbed film caused by a ridge and groove in point EHL contacts. *Tribology International*, **2016**, 100:84–98.

[161] Wang J, Kaneta M, Yang P. Numerical analysis of TEHL line contact problem under reciprocating motion. *Tribology International*, **2005**, 38:165–78.

[162] Wang J, Yang P, Kaneta M, Nishikawa H. On the surface dimple phenomena in elliptical TEHL contacts with arbitrary entrainment. *Journal of Tribology*, **2003**, 125:102–9.

[163] Baudry J, Charlaix E, Tonck A, Mazuyer D. Experimental evidence for a large slip effect at a nonwetting fluid-solid interface. *Langmuir*, **2001**, 17:5232–6.

[164] Peiran Y, Shizhu W. A generalized Reynolds equation based on non-Newtonian flow in lubrication mechanics. *Acta Mechanica Sinica*, **1990**, 6:289–95.

[165] Dowson D, Higginson GR. Elasto-hydrodynamic theory. New York: Elsevier Ltd.; **1977**.

[166] Roelands CJA, Winer WO, Wright WA. Correlational aspects of the viscosity-temperature-pressure relationship of lubricating oils. *Journal of Lubrication Technology*, **1971**:209–10.

[167] Yang P. Numerical analysis of fluid lubrication. Beijing: National Defense Industry Press; **1998**.

[168] Venner CH, Lubrecht AA. Multilevel methods in lubrication. New York: Elsevier B.V.; **2000**.

[169] Venner CH. Multilevel solution of the EHL line and point contact problems. Twente University, **1991**.

[170] Yang P, Rodkiewicz CM. On the numerical analysis to the

thermoelastohydrodynamic lubrication of a tilting pad inclusive of side leakage. *Tribology Transactions*, **1997**, 40:259–66.

[171] Qu S, Yang P, Guo F. Theoretical investigation on the dimple occurrence in the thermal EHL of simple sliding steel–glass circular contacts. *Tribology International*, **2000**, 33:59–65.

[172] Yang P, Qu S, Chang Q, Guo F. On the theory of thermal elastohydrodynamic lubrication at high slide-roll ratios - Line contact solution. *Journal of Tribology*, **2001**, 123:36–41.

[173] Reddyhoff T, Schmidt A, Spikes H. Thermal conductivity and flash temperature. *Tribology Letters*, **2019**, 67:22.

[174] Guo F, Li XM, Wong PL. A novel approach to measures slip-length of thin lubricant films under high pressures. *Tribology International*, **2012**, 46:22–9.

[175] Meng X, Wang J, Nishikawa H, Nagayama G. Effects of boundary slips on thermal elastohydrodynamic lubrication under pure rolling and opposite sliding contacts. *Tribology International*, **2021**, 155:106801.

[176] Bonaccurso E, Kappl M, Butt HJ. Hydrodynamic Force Measurements: Boundary Slip of Water on Hydrophilic Surfaces and Electrokinetic Effects. *Physical Review Letters*, **2002**, 88:4.

[177] Guo F, Wong PL. Variations of an EHL film under boundary slippage. *Solid Mechanics and Its Applications*, **2006**, 134:285–96.

[178] Ronen S, Goltsberg R, Etsion I. A comparison of stick and slip contact conditions for a coated sphere compressed by a rigid flat. *Friction*, **2017**, 5:326–38.

[179] Jamari J, Muchammad M, Hilmy F, Tauviqirrahman M. Effect of inertia on the cavitation phenomena of hydrodynamic textured bearings considering slip. *Journal of the Brazilian Society of Mechanical Sciences and Engineering*, **2019**, 41:1–14.

Acknowledgements

I have taken efforts in my Ph.D. program. However, it would not have been possible without the kind support and help of many individuals. I would like to extend my sincere thanks to all of them.

Firstly, I am highly indebted to my supervisor, Professor Gyoko Nagayama for her patience, guidance, and continuous support of my Ph.D. program. It has been a great privilege and joy to study under her supervision. I am also grateful of her advice on my life to allow me to have a comfortable and easy life in the foreign environment.

Besides my supervisor, I would like to thank Professor Jing Wang for her encouragement and useful instruction on my study. I also want to thank Hiroshi Nishikawa sensei who gave me much support on my experimental study. Thanks to Professor Takaharu Tsuruta and Professor Masato Yamamura for their kind advice and patient teachings.

Sincere gratitude should also go to all my colleagues of the Heat Transfer group for their daily support and the nice working atmosphere. They have greatly helped me in my study as well as the living in Japan.

Many thanks go to the Kyushu Institute of Technology and the Ministry of Education, Culture, Sports, Science and Technology, Japan for providing the Monbusho Scholarship during October 2017–March 2022.

Finally, my cordial thanks go to my parents for their love and encouragement.

Xianghua Meng

December 2021

Appendix

Publication lists

1. Effects of boundary slips on thermal elastohydrodynamic lubrication under pure rolling and opposite sliding contacts,
   Tribology International, Volume 155, 106801, 2021,
   Xianghua Meng, Jing Wang, Hiroshi Nishikawa, Gyoko Nagayama.

2. Boundary slips induced temperature rise and film thickness reduction under sliding/rolling contact in thermal elastohydrodynamic lubrication,
   ASME Journal of Tribology. Volume 144, 071602-1, July 2022,
   Xianghua Meng, Jing Wang, Gyoko Nagayama.

Tribology International
Volume 155, March 2021, 106801
https://doi.org/10.1016/j.triboint.2020.106801

Effects of boundary slips on thermal elastohydrodynamic lubrication under pure rolling and opposite sliding contacts

Xianghua Meng [a], Jing Wang [b], Hiroshi Nishikawa [c], Gyoko Nagayama [c, *]

[a] Graduate School of Engineering, Kyushu Institute of Technology, 8048550, Fukuoka, Japan

[b] College of Mechanical Engineering, Donghua University, 201620, Shanghai, China

[c] Department of Mechanical Engineering, Kyushu Institute of Technology, 8048550, Fukuoka, Japan

Abstract: In elastohydrodynamic lubrication (EHL) contact, the film thickness strongly depends on boundary slips, including velocity slip and thermal slip at the solid–lubricant interface. In the EHL studies published thus far, velocity slip at the solid–lubricant interface has been investigated individually without considering thermal slip. In this study, the effects of both types of boundary slip on film thickness were investigated simultaneously in rolling/sliding contact. Numerical simulations were conducted based on the modified Reynolds equation and energy equation by considering boundary slips on the sliding surface. The results indicate that the velocity slip causes a reduction in film thickness under pure rolling contact, while a shifted surface dimple is formed along the sliding direction due to both velocity slip and thermal slip under zero entrainment velocity (ZEV) contact.

Keywords:
Slip length, Thermal slip length, Slip boundary condition, Thermal elastohydrodynamic lubrication.

1 Introduction

In the elastohydrodynamic lubrication (EHL) regime, the no-slip boundary condition has been commonly accepted for many years. However, with the recent technical advances in interface sciences, the slip boundary condition has attracted the attention of EHL researchers. According to the no-slip boundary hypothesis, both the velocity and temperature of the lubricant adjacent to the solid surface are the same as those of the solid surface [1–3], while the slip boundary includes a velocity discontinuity and a temperature jump at the solid–lubricant interface [4–8] The slip boundary condition plays a vital role in lubrication analyses, especially in the two typical rolling/sliding contacts of (a) pure rolling and (b) zero entrainment velocity (ZEV), as shown in Fig. 1. The velocity discontinuity shown in Fig. 1 (c) can be described in terms of slip length, which is defined as the distance between the solid–lubricant interface and the position at which the lubricant velocity and solid velocity are equal [4,6]. Analogously, the temperature jump shown in Fig. 1 (c) can be determined using the thermal slip length, which is the distance from the interface to the position at which the temperature difference

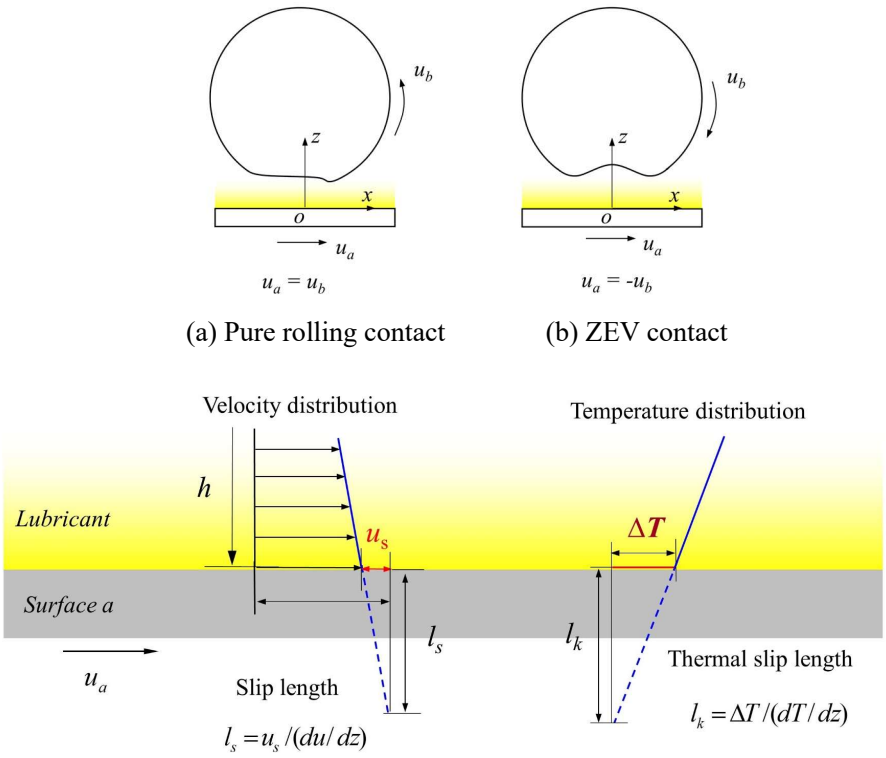

(a) Pure rolling contact (b) ZEV contact

(c) Slip boundary condition on surface *a*

Fig. 1 Schematic of (a) pure rolling contact, (b) ZEV contact, and (c) slip boundary condition at surface *a*.

between the lubricant and solid is zero [7–10].

Velocity discontinuity at the interface is one of the most important features considered in EHL analyses. Kaneta et al. [11] reported that a lubricant film behaved like a solid and slipped at the interface in EHL contact. Wong et al. [12] performed a series of optical interferometry experiments to gather evidence of the velocity slip based on the relative movement of the lubricant entrapped in the contact area. Ponjavic and Wong [13] used the photobleached-fluorescence imaging velocimetry technique to measure slip under steady conditions and found that friction and film thickness decreased due to the velocity slip in EHL contact. In the experiments of Wang and Reddyhoff [14], an anomalous EHL film shape was obtained by using the lubricant 1-dodecanol. They hypothesized that the velocity slip that occurred at the interface caused an increase in film thickness to maintain flow continuity. Moreover, theoretical models with the velocity slip assumption have been developed for EHL contacts. Ehret et al. [15] proposed a plug flow model for the EHL regime with an interfacial slip assumption and demonstrated the formation of a surface dimple under the sliding condition. The results of a molecular dynamics simulation performed by Nagayama et al. [16,17] indicated that the solid–liquid boundary condition depends on the interface wettability and the driving force for liquid flow in a nanochannel. Wen and Zhang [18], as well as Chu et al. [19], proposed an ideal viscoplastic

rheological model for isothermal EHL line contact with velocity boundary slippage, and this model yielded considerably thinner films than those obtained using the no-slip theory. Chen et al. [20] investigated the effect of anisotropic velocity slip on pressure and film distributions under point EHL contacts. Furthermore, Zhao et al. [21] conducted a thermal point EHL analysis to investigate the coupled effects of velocity slip and heat transfer. They found that the velocity slip at the interface constrained temperature rise and increased film thickness under large slide-roll ratio conditions.

In addition to the aforementioned boundary slips, the surface sliding direction can influence the lubrication performance in the EHL regime. When two bounding surfaces have equal but opposite velocities (known as ZEV contact), the working condition may be the most severe for ball screws or roller bearings without a cage. Cameron [22,23] first described film formation under ZEV contact and proposed the viscosity wedge theory to demonstrate the viscosity variations induced by the temperature gradient across the lubricant film. Yang et al. [24] renamed Cameron's viscosity wedge theory as the "temperature-viscosity wedge" mechanism to highlight the importance of temperature rise. The complete numerical solutions obtained by Guo et al. [25,26] indicated that the film shape in the contact area was characterized by a deep central dimple, which was mainly ascribed to the temperature-viscosity wedge effect. Yagi et al. [27] measured the temperature distribution in the dimple zone, and their results indicated that the maximum temperature occasionally reached 400 K. In addition, Meziane et al. [28] found the results of numerical simulations, including thermal effects, agreed with the experimental results, thus allowing for tentative prediction of the minimum film thickness in wide-point EHL contact. Zhang et al. [29,30] theoretically investigated surface dimple variations and found that the existence of the surface dimple was related to the temperature rise under ZEV contact. Considering the reasonable doubts about the no-slip boundary conditions applied in previous studies, Wong et al. [31,32] fabricated oleophobic/oleophilic surfaces under ZEV contact with extremely low surface velocity, where a considerable velocity slip might occur at the solid–lubricant interface.

Although the velocity slip of EHL contact has been studied extensively, few comparisons have been made between experimental and simulation data. Moreover, thermal slip has been rarely coupled with velocity slip in the existing studies, especially under ZEV contact. Hence, in this study, the effects of velocity slip and thermal slip on lubrication were investigated simultaneously under the pure rolling and ZEV contacts. Numerical simulations were conducted based on a modified Reynolds equation and the energy equation by considering the two types of boundary slips on a sliding surface.

2 Governing equations

Considering the pure rolling contact and ZEV contact shown in Fig. 1, the slip boundary conditions shown in Fig. 1 (c) were applied to surface a, on which both velocity slip and thermal slip occur, and the continuum boundary condition was applied to surface b. According to the linear Navier boundary condition [4–6] the slip velocity

at an interface is proportional to the slip length:

$$u_s = l_s \left.\frac{\partial u}{\partial z}\right|_{z=0}. \quad (1)$$

The thermal slip accompanying the velocity slip can be expressed as follows [7]:

$$\Delta T = l_k \left.\frac{\partial T}{\partial z}\right|_{z=0}. \quad (2)$$

For the thermal point EHL contact, the modified Reynolds equation accounting for boundary slips on one surface is derived based on the generalized Reynolds equation [33]:

$$\frac{\partial}{\partial x}\left[\left(\frac{\rho}{\eta}\right)_{es} h^3 \frac{\partial p}{\partial x}\right] + \frac{\partial}{\partial x}\left[\left(\frac{\rho}{\eta}\right)_{e} h^3 \frac{\partial p}{\partial x}\right] + \frac{\partial}{\partial y}\left[\left(\frac{\rho}{\eta}\right)_{e} h^3 \frac{\partial p}{\partial y}\right] = 6(u_a+u_b)\frac{\partial \rho^* h}{\partial x}$$

where $\left(\frac{\rho}{\eta}\right)_{es} = 12\left(l_s \frac{\rho_e}{A}\frac{\eta_e}{\eta_e'} + \left(\frac{h}{A}\eta_{z=0}\text{-}1\right)\frac{\eta_e}{\eta_e'}\rho_e'\right)$,

$\left(\frac{\rho}{\eta}\right)_{e} = 12\left(\frac{\eta_e}{\eta_e'}\rho_e'\text{-}\rho_e''\right)$, $A = h\eta_{z=0} + l_s\eta_e$, $\eta_e = h \Big/ \int_0^h \frac{1}{\eta} dz$,

$\eta_e' = h^2 \Big/ \int_0^h \frac{z}{\eta} dz$, $\rho_e = \frac{1}{h}\int_0^h \rho dz$, $\rho_e' = \frac{1}{h^2}\int_0^h \rho \int_0^z \frac{1}{\eta} dz' dz$,

$\rho_e'' = \frac{1}{h^3}\int_0^h \rho \int_0^z \frac{z'}{\eta} dz' dz$, $\rho^* = \frac{2}{u_a+u_b}\left[u_a\rho_e\text{-}(u_a\text{-}\right.$

$\left. u_b)\eta_e\rho_e'\rho_{es}\right]$, and $\rho_{es} = \frac{1}{A}\left(l_s\frac{\rho_e}{\rho_e'} + h\eta_{z=0}\right)$.

Here, $(\rho/\eta)_{es}$ and ρ_{es} are the slip parameters. When $l_s = 0$, $(\rho/\eta)_{es} = 0$, and $\rho_{es} = 1$, surface *a* is under the continuum boundary condition, and Eq. (3) turns into the generalized Reynolds equation [33].

The pressure boundary conditions for the Reynolds equation are:

$$\begin{cases} p = 0, \text{ at } x=x_{in}=x_{out},\ y=y_{out} \\ p \geq 0, \text{ at } x_{in}<x<x_{out},\ -y_{out}<y<y_{out} \end{cases} \quad (4)$$

where x_{in}, and x_{out}, y_{out} represent the start and end of the calculation domain, respectively.

Considering the surface deformation and geometry, the film thickness for point contact is given as:

$$h(x,y) = h_{00} + \frac{x^2}{2R_x} + \frac{y^2}{2R_y} + \frac{2}{\pi E'}\frac{p(x',y')}{\sqrt{(x\text{-}x')^2+(y\text{-}y')^2}}dx'dy'.$$

The load balance equation can be written as follows:

$$\iint p(x,y)dxdy = w. \quad (6)$$

Because the lubricant density and viscosity vary with the local pressure and local temperature, the Dowson and Higginson model [34] is used to express the density-pressure-temperature relationship, and the viscosity-pressure-temperature relationship is determined using the Roelands equation [35]:

$$\rho = \rho_0\left\{1+\frac{0.6\times10^{-9}p}{1+1.7\times10^{-9}p}\text{-}0.00065(T\text{-}T_0)\right\}$$

$$\eta = \eta_0\left\{(\ln\eta_0+9.67)\left\{\text{-}1+(1+5.1\times10^{-9}p)^{Z_0}\left(\frac{T\text{-}138}{T_0\text{-}138}\right)^{S_0}\right\}\right\}$$

where $Z_0 = \frac{\alpha}{5.1\times10^{-9}[\ln(\eta_0)+9.67]}$, $S_0 = \frac{\beta(T_0\text{-}138)}{\ln(\eta_0)+9.67}$.

The evolution of the temperature field is composed of the lubricant film and two bounding solids [36]. The energy equation of the lubricant film is:

$$c\left\{\rho u\frac{\partial T}{\partial x} + \rho v\frac{\partial T}{\partial y} - \left(\frac{\partial}{\partial x}\int_0^z \rho u dz' + \frac{\partial}{\partial y}\int_0^z \rho v dz'\right)\frac{\partial T}{\partial z}\right\} - k\frac{\partial^2 T}{\partial z^2}$$

$$= -\frac{T}{\rho}\frac{\partial \rho}{\partial T}\left(u\frac{\partial p}{\partial x} + v\frac{\partial p}{\partial y}\right) + \eta\left[\left(\frac{\partial u}{\partial z}\right)^2 + \left(\frac{\partial v}{\partial z}\right)^2\right]$$

The temperature boundary conditions for Eq. (8) are as follows.

$$\begin{cases} T(x = x_{in}) = T_0, \ (u \geq 0) \\ T(x = x_{out}) = T_0, \ (u \leq 0) \end{cases} \quad (9)$$

The energy equations of the two bounding solids can be written as:

$$\begin{cases} c_a\rho_a u_a \dfrac{\partial T}{\partial x} = k_a \dfrac{\partial^2 T}{\partial z_a^2} \\ c_b\rho_b u_b \dfrac{\partial T}{\partial x} = k_b \dfrac{\partial^2 T}{\partial z_b^2} \end{cases}. \quad (10)$$

The boundary conditions for Eq. (10) are as follows.

$$\begin{cases} T(x = x_{in}) = T_0 \\ T(z_a = -d) = T_0 \\ T(z_b = d) = T_0 \end{cases} \quad (11)$$

At the solid–lubricant interface, the following continuity equations of heat flux, are applied to satisfy the no-slip boundary condition on surface *b*, and the temperature jump ΔT on surface *a* is taken as the thermal slip boundary condition.

3 **Numerical methods**

To facilitate programing and calculation, all of the governing equations were used in non-dimensionalized form. The dimensionless parameters have the following forms: $W=\frac{w}{E'R_x^2}$, $U_0=\frac{u_0\eta_0}{E'R_x}$, $X=\frac{x}{a}$, $Y=\frac{y}{a}$, $Z=\frac{z}{h}$, $Z_{a,b}=\frac{z_{a,b}}{a}$, $\overline{d}=\frac{d}{a}$, $h_0=\frac{a^2}{R_x}$, $H=\frac{h}{h_0}$, $P=\frac{p}{p_H}$, $\overline{T}=\frac{T}{T_0}$, $U=\frac{u}{u_0}$, $U_{a,b}=\frac{u_{a,b}}{u_0}$, $\overline{\eta}=\frac{\eta}{\eta_0}$, $\overline{\rho}=\frac{\rho}{\rho_0}$, $l_s^*=\frac{l_s}{h_0}$, and $l_k^*=\frac{l_k}{h_0}$.

In the EHL calculation based on the Reynolds equation in Eq. (3), the pressure distribution and elastic deformation were solved using the multigrid method and the multi-level multi-integration technique, respectively [37]. To obtain the temperature distribution, a sequential column sweeping method [38] was employed to solve the energy equations of both the solids and the lubricant film. Considering the boundary conditions in the inlet and outlet regions, forward and backward marching processes were repeatedly executed under ZEV contact. An initial pressure field was applied to calculate the temperature field. Then, the pressure field was renewed based on the calculated temperature field, and the temperature field was updated using the renewed pressure field. By repeating the above two steps, convergence was achieved when the relative errors of the pressure, load, and temperature values were smaller than 1×10^{-5}, 1×10^{-4}, and 1×10^{-6}, respectively. All errors were checked at the finest grid level.

For the pure rolling contact, five grid levels with 256 nodes along the *x*- and *y*-directions at the finest grid level were applied in the calculation domain $-4.5a \le x \le 1.5a$, $-3a \le y \le 3a$. Therefore, the pressure boundary condition is adopted as $p = 0$ at $x = -4.5a = 1.5a$, $y = -3a = 3a$, and $p \ge 0$ at $-4.5a \le x \le 1.5a$, $-3a \le y \le 3a$. In the *z*-direction, eleven nodes were used in the film, and six non-equidistant nodes were adopted in each solid in each solid of d=3.15a in thickness. The calculation domain is $-3.15a \le z_a \le 0$ for solid *a*, $0 \le z_b \le 3.15a$ for solid *b*, and $0 \le z \le h$ for lubricant. The main input data are given in Table 1.

For the ZEV contact, semi-field calculation is adopted in *y*-direction. Four grid levels with 513 nodes along the *x*-direction and 197 nodes along the *y*-direction at the finest grid level were applied in the calculation domain $-3a \le x \le 3a$, $0 \le y \le 1.8a$. Therefore, the pressure boundary condition is $p = 0$ at $x = -3a = 3a$, $y = 1.8a$, and $p \ge 0$ at $-3a \le x \le 3a$, $0 \le y \le 1.8a$. The calculation domain in the *z*-direction is same to that of the pure rolling case. The calculation parameters are listed in Table 2.

Table 1 Input data for pure rolling contact.

Density of glass, ρ_a, kg/m^{-3}	2500
Specific heat of glass, c_a, J/(kg·K)	840
Thermal conductivity of glass, k_a, W/(m·K)	0.78
Density of steel, ρ_b, kg/m^{-3}	7850
Specific heat of steel, c_b, J/(kg·K)	470
Thermal conductivity of glass, k_b, W/(m·K)	46
Density of lubricant, ρ_0, kg/m^{-3}	877
Specific heat of lubricant, c, J/(kg·K)	2000
Thermal conductivity of lubricant, k, W/(m·K)	0.14
Pressure viscosity coefficient, α, Pa^{-1}	2.4*10^{-8}
Viscosity of lubricant, η_0, Pa·s	1.365
Reduced elastic modules, E', Pa	1.17*10^{11}
Equivalent radius, Rx, m	0.0127
Applied load, w, N	50

Table 2 Input data for ZEV contact.

Density of steel, $\rho_{a,b}$, kg/m^{-3}	7850
Specific heat of steel, $c_{a,b}$, J/(kg·K)	470
Thermal conductivity of steel, $k_{a,b}$, W/(m·K)	46
Ambient density of lubricant, ρ_0, kg/m^{-3}	875
Specific heat of lubricant, c, J/(kg·K)	2000
Thermal conductivity of lubricant, k, W/(m·K)	0.14
Pressure viscosity coefficient, α, Pa^{-1}	2.2*10^{-8}
Ambient viscosity of lubricant, η_0, Pa·s	0.08
Thermal viscosity coefficient pf lubricant, β, K^{-1}	0.042
Reduced elastic modules, E', Pa	2.26*10^{11}
Ambient temperature, T_0, K	313
Equivalent radius, R_x, m	0.025
Applied load, w, N	31.6

4 Results and discussions

4.1 Pure rolling contact

To discuss the effects of velocity slip on the variations in the EHL lubricant film, a glass–steel contact was considered under the pure rolling contact, where velocity slip occurred on the glass surface. Since the two bounding surfaces moved with the same velocity under the pure rolling contact (Fig. 1 (a)), the temperature of the lubricant film increased negligibly. Therefore, the thermal slip at the solid–lubricant interface was neglectable in the thermal analysis. Notably, the modified Reynolds equation (Eq. (3)) without thermal slip was found to be consistent with the equation in Ref. [21].

Fig. 2 shows the contour maps of the lubricant film thickness for $U_0 = 3.0 \times 10^{-10}$ with $l_s^* = 0, 0.063, 0.157, 0.314$. Here, l_s^* denotes the velocity slip according to the linear Navier slip condition. The employed slip length are in dimensionless forms, corresponding to 0.2 μm ($l_s^* = 0.063$), 0.5 μm ($l_s^* = 0.157$), and 1.0 μm ($l_s^* = 0.314$), respectively. These values of the slip lengths are comparable to EHL film thickness (approximate 1 μm). All of the contour maps exhibit a horseshoe shape of EHL contact, that is, a flat center plateau with two side lobes. In Fig. 2 (b), the small slip length of 0.063 does not induce an obvious difference in the film shape. As the slip length increases further, the central flat plateau is enlarged, while the minimum film thickness in the side lobes decreases. Fig. 3 presents the pressure and film thickness profiles in the plane $Y = 0$ along the entrainment direction. The three locations *a, b,* and *c* are denoted as the inlet, center, and outlet of

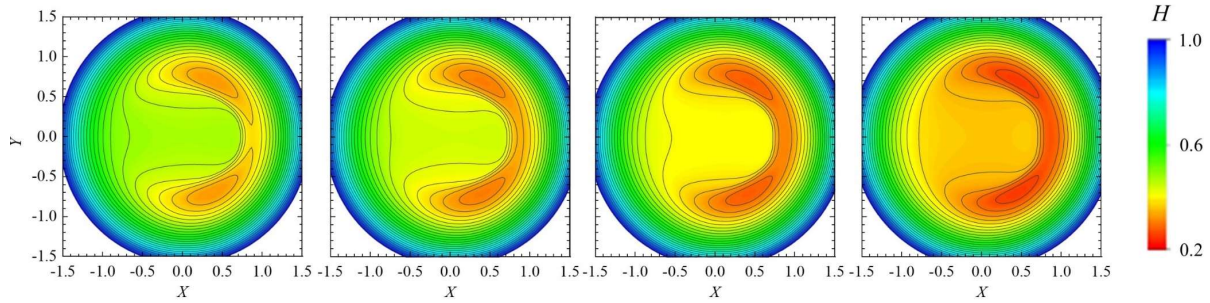

(a) $l_s^* = 0.0$ (b) $l_s^* = 0.063$ (c) $l_s^* = 0.157$ (d) $l_s^* = 0.314$

Fig. 2 Contour maps of lubricant film thickness under pure rolling contact at slip lengths of (a) $l_s^* = 0$, (b) $l_s^* = 0.063$, (c) $l_s^* = 0.157$, and (d) $l_s^* = 0.314$.

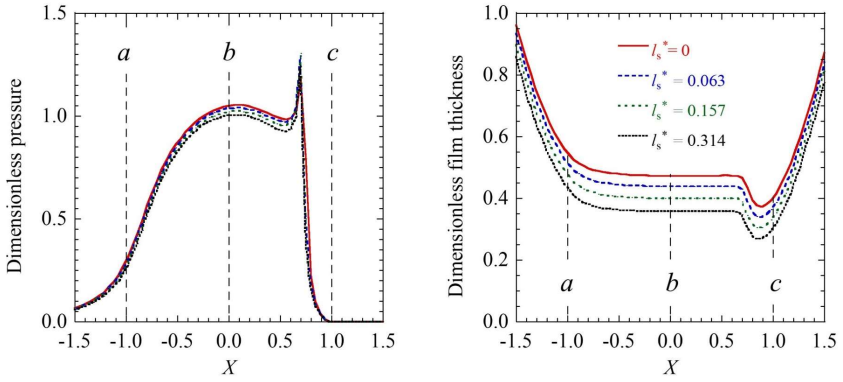

(a) Pressure (b) Film thickness

Fig. 3 Effect of slip length on (a) pressure and (b) film thickness at the plane $Y = 0$ under pure rolling contact.

the contact region, respectively. As the slip length l_s^* increases, the pressure peak near location *b* shifts downward, and the second pressure peak close to location *c* shifts marginally upward, while the film thickness decreases significantly over the entire contact region.

Fig. 4 shows the lubricant velocity profiles across the lubricant film and the slip velocity at locations *a, b,* and *c*. As described in Fig. 1, velocity slip occurs on surface *a* (Z = 0), while surface *b* (Z = 1) is under the continuum boundary condition. At the inlet location *a* (X = -1, Y = 0), the velocity profiles across the lubricant film in the *z*-direction are hindered by the occurrence of velocity slip shown in Fig. 4 (a). As the slip length increases, the negative velocity gradient on the surface *a* (Z = 0) and the corresponding slip velocity U_s at location *a* increase monotonically, as shown in Fig. 4 (d). However, at location *b* (X = 0, Y = 0), the observed velocity profiles are linear and independent of the slip length. Thus, the velocity gradient is almost zero along the *z*-direction, resulting in zero slip velocity U_s, as shown in Fig. 4 (d). At location *c* (X = 1, Y = 0), the shape of the lubricant velocity profile varies with the slip length.

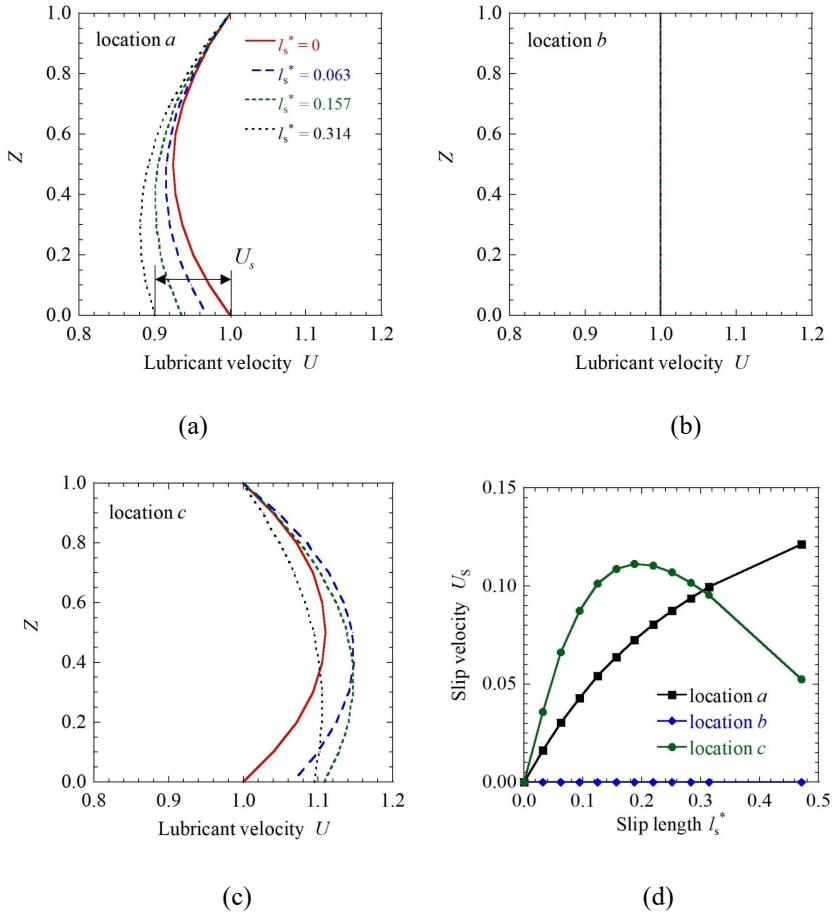

Fig. 4 Effect of slip length on (a–c) lubricant velocity distributions across lubricant film and (d) slip velocity at location *a* ($X = -1$, $Y = 0$), location *b* ($X = 0$, $Y = 0$), and location *c* ($X = 1$, $Y = 0$).

For $l_s^* = 0.314$, $U_{l_s^*=0.314} > U_{l_s^*=0}$ for $0 < Z \leq 0.4$, while the reverse is true for $0.4 < Z \leq 1.0$. The curve of U_s is quadratic at location *c* with a peak at $l_s^* \approx 0.2$, as shown in Fig. 4 (d). The existence of velocity slip on surface *a* decreases the entrainment velocity in the inlet region, which reduces the amount of lubricant entrained in the contact region. Consequently, the film thickness decreases, as shown in Fig. 3.

Fig. 5 describes the variations in the film thickness ratios corresponding to the increases in entrainment velocity for different slip lengths. D_{cen} and D_{min} are the ratios of the center and minimum film thicknesses with velocity slip to those without velocity slip. Without the occurrence of velocity slip ($l_s^* = 0.0$), D_{cen} and D_{min} are always 1.0. According to Fig. 5, D_{cen} and D_{min} increase asymptotically as the entrainment velocity increases, indicating that the influence of slip length on film thickness in the low-velocity region is more apparent than that in the high-velocity region. For the same entrainment velocity, both D_{cen} and D_{min} decrease as l_s^* increases, while the value of D_{min} remains greater than that of D_{cen}. This means that the film thickness at the center is

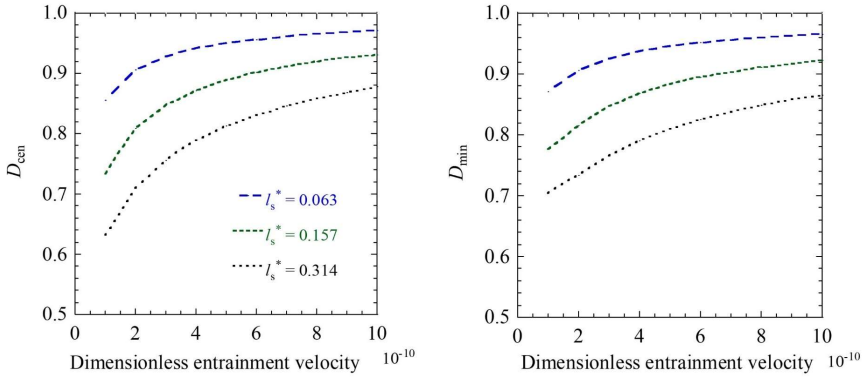

(a) Central film thickness (b) Minimum film thickness

Fig. 5 Effect of slip length on (a) central film thickness and (b) minimum film thickness with increasing entrainment velocity under pure rolling contact.

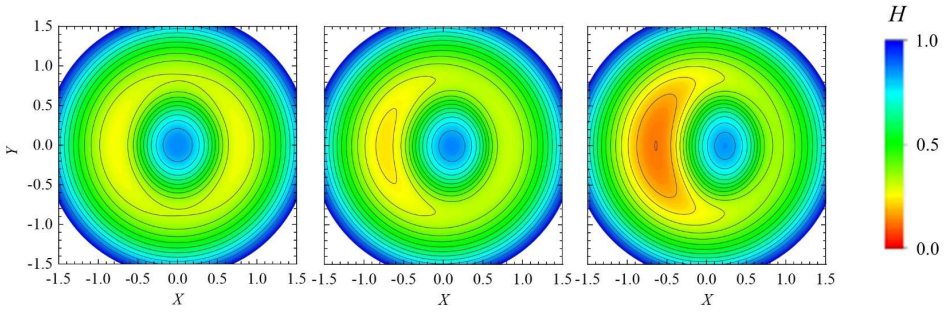

(a) $l_s^* = 0.0$ (b) $l_s^* = 0.02$ (c) $l_s^* = 0.04$

Fig. 6 Contour maps of lubricant film thickness under ZEV contact with U_a = $-U_b$= 1.5 and l_k^*= 0.

more significantly affected by the slip length than that in the side lobes.

4.2 ZEV contact

In contrast to the abovementioned pure rolling contact (slide-roll ratio S = 0) in which two surfaces move in the same direction, ZEV contact involves two surfaces moving in opposite directions (for example, surface *a* moving from the left to the right, while surface *b* moving from the right to the left, as shown in Fig. 1 (b)) with the same speed (slide-roll ratio S = ∞). Thus, under ZEV contact, the temperature rise is expected to be more significant than that under pure rolling contact in the same working conditions. On the other hand, the temperature rise also can be caused by reducing thermal conductivity. Habchi et al. [39], Reddyhoff et al.[40] and Liu et al. [41]. discussed the effects of the thermal conductivity on the EHL performance. To simplify the problem, the thermal conductivity of steel in its annealed/soft state is given as 46 W/(m·K), which is commonly used in literatures [24, 25, 29, 30].

This temperature increase is a dominant factor in maintaining a beneficial lubrication state, which is characterized by a surface dimple formed due to

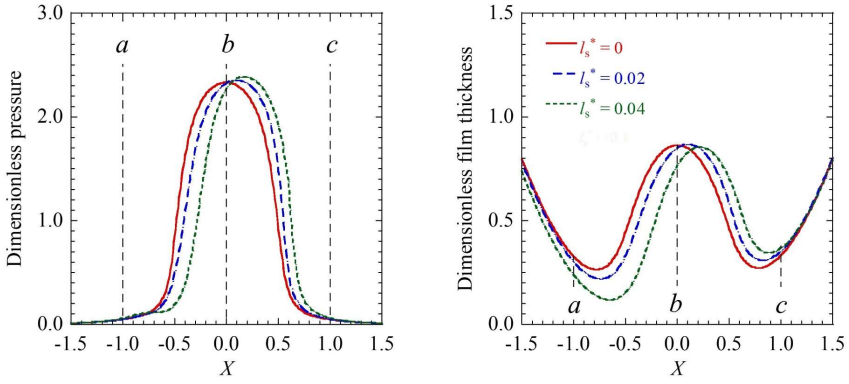

(a) Pressure (b) Film thickness

Fig. 7 Effect of slip length on (a) pressure and (b) film thickness in the plane $Y = 0$ under ZEV contact with $U_a = -U_b = 1.5$ and $l_k^* = 0$.

lubricant accumulation. Because the dimple is governed by the surface velocity and the subsequent temperature-viscosity wedge effect [29,30], the slip boundary condition may significantly influence the shape of the dimpled film. Here, the steel–steel ZEV contact shown in Fig. 1 (b) is employed to investigate the effects of the slip boundary condition on the lubrication performance, where the velocity/thermal slips occur on surface *a*.

4.2.1 Velocity slip effect

To simplify comparisons of the slip effects, the thermal slip length was set to zero ($l_k^* = 0$) in Figs. 6–9. Fig. 6 shows the contour maps of the lubricant film for $l_s^* = 0$, 0.02 and 0.04 with $U_a = -U_b = 1.5$. Under the no-slip boundary condition ($l_s^* = 0$), a large surface dimple is formed in the contact area due to the temperature-viscosity wedge effect. As the slip length increases, the constriction in the left contact area is enlarged; consequently, the dimple is pushed toward the right side of the contact region. Fig. 7 shows the pressure and film thickness profiles in the plane $Y = 0$. Locations *a, b,* and *c* are denoted as the two sides and the center of the contact region, respectively. The pressure peak close to location *b* shifts toward the right side of the contact region (location *c*), and its magnitude increases as the slip length increases. The film thickness in the left side of the dimple thereby decreases, which squeezes the dimple toward the right.

Fig. 8 shows the variations in lubricant velocity for $l_s^* = 0$, 0.02 and 0.04 across the lubricant film and the slip velocity at the three locations (indicated in Fig. 7). Larger slip length results in larger slip velocities at locations *a* and *c*, and smaller lubricant velocity, as shown in Figs. 8 (a) and (c). However, the slip velocity at location *b* is almost zero, and thus, the effect of slip length on lubricant velocity can be neglected at the center of the contact region. Since the absolute lubricant velocity near surface *a* is smaller than that near surface *b*, surface *a* drags less lubricant into the contact region than surface *b*. Therefore, the area of lubricant accumulation shifts from the center toward the right side of the contact region.

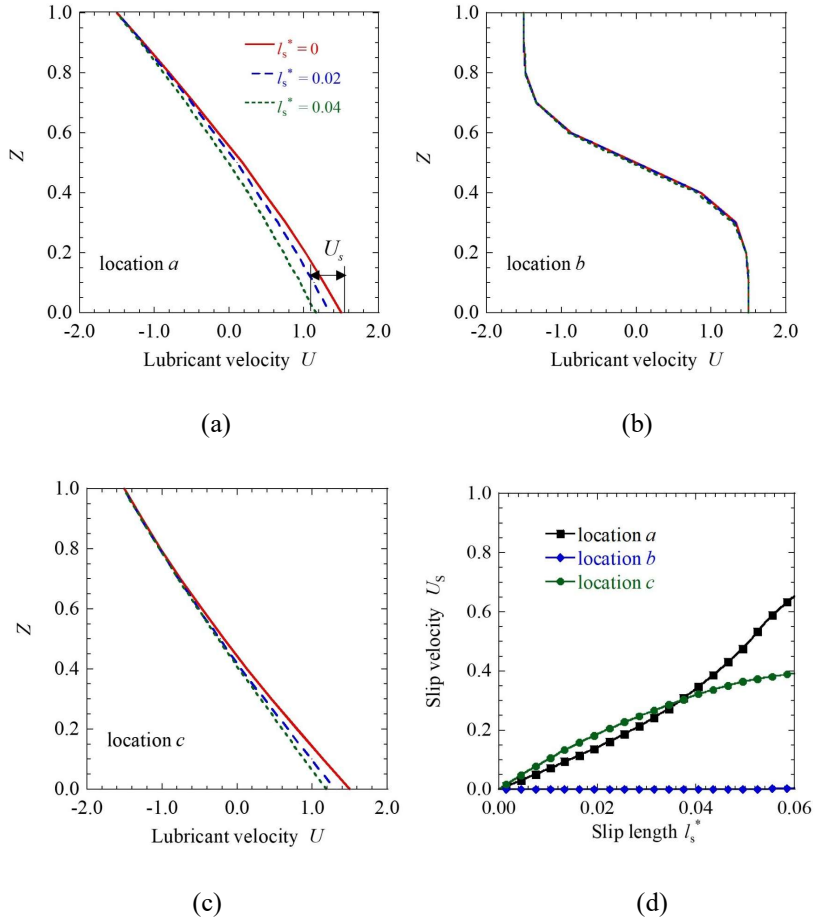

Fig. 8 Effect of slip length on (a–c) lubricant velocity distributions across the oil film and (d) slip velocity at location *a* ($X = -1$, $Y = 0$), location *b* ($X = 0$, $Y = 0$), and location *c* ($X = 1$, $Y = 0$).

Correspondingly, the pressure peak and the surface dimple shift right.

Fig. 9 summarizes the maximum and minimum film thicknesses versus the slip length for three cases: $U_a = -U_b = 0.778$, 1.5, and 2.0. It is shown that both the maximum and minimum film thicknesses decrease as the slip length increases. Since hydrodynamic lubrication is accompanied with the EHL as the surface velocities U_a and U_b increase, the surface dimple is insignificant due to a reduction in elastic deformation [26]. Thus, in the case of $U_a = -U_b = 0.778$, the maximum film thicknesses are the largest while the minimum film thicknesses are the smallest among the three cases. In Fig. 9 (b), the minimum film thicknesses decrease to a constant value of 0.06 when the slip length is larger than a critical value in all of the three cases. The critical slip lengths are 0.03 for $U_a = -U_b = 0.778$, 0.05 for $U_a = -U_b = 1.5$, and 0.07 for $U_a = -U_b = 2.0$.

An increase in temperature was found in the contact region due to the shearing and compression of the lubricant, consistent with previous studies [24–30]. The degree of the temperature rise is affected by the reduced lubricant velocity at

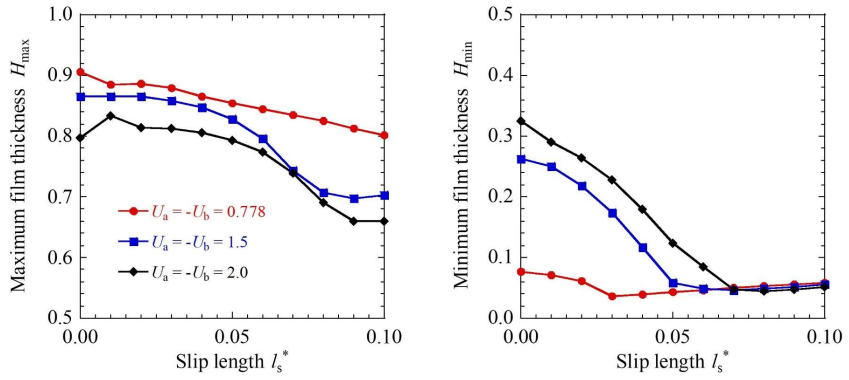

(a) Maximum film thickness (b) Minimum film thickness

Fig. 9 Film thickness variation with increase in slip length at l_k^*= 0.

surface a. The details of the shifted temperature profiles will be discussed in section 4.2.3.

4.2.2 Thermal slip effect

This section uses a slip length of zero (l_s^* = 0) to focus on the thermal slip effect. The film thickness contour maps are illustrated in Fig. 10 for l_k^* = 0, 0.02, and 0.04 with l_s^* = 0, U_a = -U_b = 1.5. In contrast to the results obtained in the previous section, the surface dimple moves toward the opposite direction, that is, toward the left side of the contact region under the thermal slip. Fig. 11 shows the pressure and film thickness profiles in the plane Y = 0 corresponding to Fig. 10. As the thermal slip length increases, the pressure peak and the surface dimple move toward the left from the center area, which is consistent with the film thickness contour maps shown in Fig. 10. Meanwhile, both the magnitude of the pressure peak and the dimple depth decrease significantly at l_k^* = 0.04.

Fig. 12 shows the temperature distributions along the x-y direction for l_k^* = 0, 0.02, and 0.04 on surface a. The temperature fields are non-uniform, and the temperature rise at l_k^* = 0.04 is

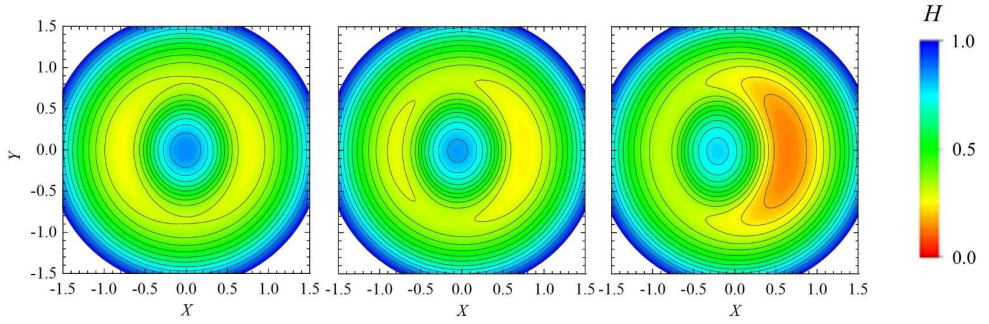

(a) l_k^* = 0.0 (b) l_k^* = 0.02 (c) l_k^* = 0.04

Fig. 10 Contour maps of lubricant film thickness under ZEV contact with U_a = -U_b= 1.5 and l_s^*= 0.

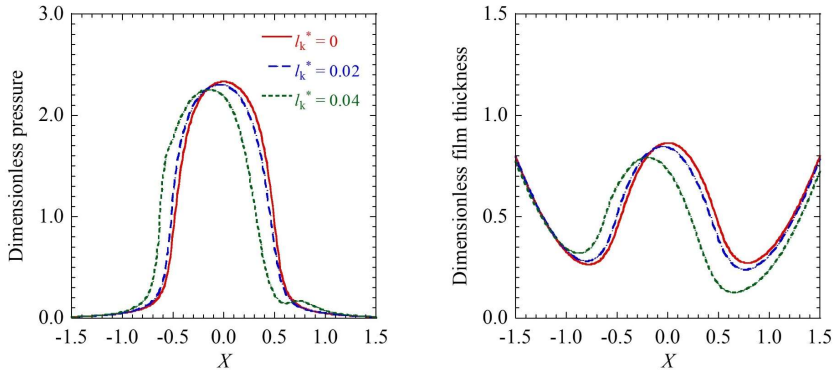

(a) Pressure (b) Film thickness

Fig. 11 Effect of thermal slip length on (a) pressure and (b) film thickness in the plane $Y = 0$ under ZEV contact with $U_a = -U_b = 1.5$ and $l_s^* = 0$.

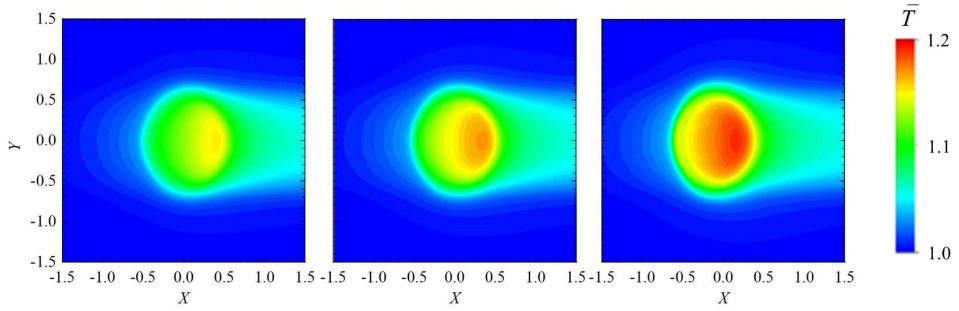

(a) $l_k^* = 0.0$ (b) $l_k^* = 0.02$ (c) $l_k^* = 0.04$

Fig. 12 Effects of thermal slip length on the temperature distributions on surface *a* under ZEV contact with $U_a = -U_b = 1.5$ and $l_s^* = 0$.

the most prominent among the three simulation cases. The generated heat caused by shearing and compression of the lubricant is expected to dissipate through the lubricant and through surfaces *a* and *b*. However, the higher thermal resistance on surface *a* due to the increase in the thermal slip length limits heat dissipation from the lubricant to surface *a*. Thus, a significant temperature rise occurs, induces a reduction in the lubricant viscosity. Consequently, a greater amount of lubricant is retained on surface *a* (moving right) at $l_k^* = 0.04$ than that at $l_k^* = 0$, which causes the accumulated lubricant to be pushed toward the left side of the contact region. Therefore, the surface dimples in Figs. 10 (b) and (c) move toward the left, which contradicts the dimple shift tendency in Fig. 7 caused by the velocity slip singularity.

The variations in the maximum and minimum film thicknesses with the thermal slip length for $U_a = -U_b = 0.778$, 1.5, and 2.0 are shown in Fig. 13. Greater thermal slip length results in lower maximum and minimum film thicknesses. Notably, at $U_a = -U_b = 0.778$, the maximum film thickness decreases rapidly, while the minimum film thickness remains constant. In contrast, at $U_a = -U_b = 1.5$ and 2.0, the two extreme film

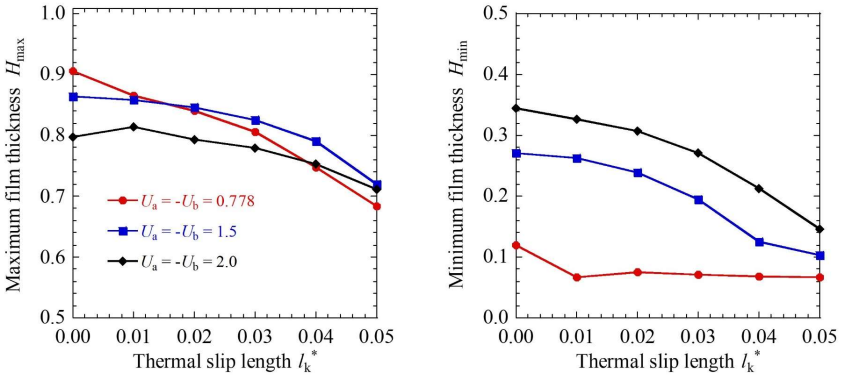

(a) Maximum film thickness (b) Minimum film thickness

Fig. 13 Film thickness variation with increase in thermal slip length under ZEV contact at $l_s^* = 0$.

thicknesses decrease in almost the same manner as the thermal slip length increases.

4.2.3 Coupling thermal slip with velocity slip

In practice, the thermal slip and velocity slip could co-exist in lubrication region when slip boundary occurs. The thermal slip and velocity slip may be related; however, there is no guarantee that the velocity and thermal slips depend on each other [9, 10, 16, 17, 42]. The coupled effect of velocity slip and thermal slip on the lubrication performance is discussed in this section based on the individual investigations described in sections 4.2.1 and 4.2.2. Fig. 14 shows the temperature distributions inside the lubricant film in the plane $Y = 0$ for (a) no slip, (b) and (c) only velocity slip, (d) and (e) only thermal slip, (f) and (g) coupled velocity and thermal slips. As shown in Fig. 14 (a), the maximum lubricant temperature due to shearing and compression of the lubricant is at the center of the contact area, overlapping with the locations of the maximum pressure and surface dimple. A comparison among Figs. 14 (a), (b), and (c) shows that the location of the maximum temperature moves from the center toward the right as the slip length increases. By contrast, the increase of the thermal slip length causes the temperature-rise region to shift leftward, as shown in Figs. 14 (d) and (e). Unexpectedly, the effects of the coupled velocity slip and thermal slip ($l_s^* = l_k^*$) on the temperature distributions cancel out one another, as shown in Figs. 14 (f) and (g), resulting in a similar temperature map as that in Fig. 14 (a).

In summary, the film thickness under ZEV contact can be significantly influenced by both velocity slip and thermal slip at the solid–lubricant interface due to the comparable scale of the slip lengths to the film thickness. However, the coupled effects of velocity and thermal slips cancel out one another when the slip length is comparable to the thermal slip length. Although the shape of the dimple changes slightly under the boundary slips for ZEV contact, the locations of the dimple, pressure peak, and temperature rise change remarkably. Because there is no guarantee that the slip length and the thermal slip length are comparable at a practical solid–lubricant interface, the effects of the coupled slips on the main factor

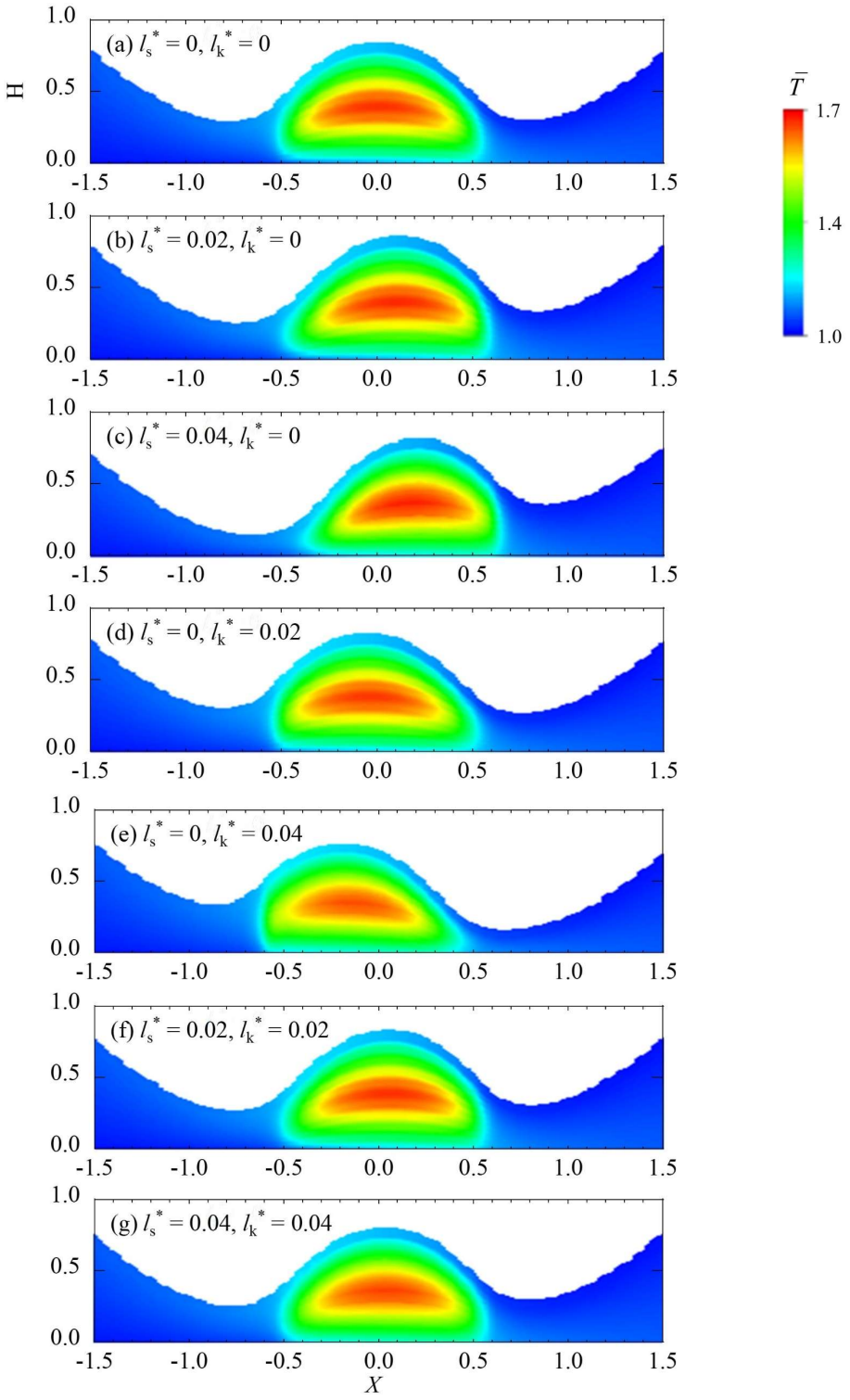

Fig. 14 Temperature distributions inside the lubricant film in the plane $Y = 0$ under ZEV contact with $U_a = -U_b = 1.5$.

(that is, either slip length or thermal slip length) should be carefully considered. When the slip length is the main factor, the lubrication features will follow the results presented in section 4.2.1.

When the thermal slip length is the main factor, the lubrication features will follow the results presented in section 4.2.2.

In this study, the slip boundary condition was applied only on the sliding surface a. However, the slip boundary condition may occur on surface b or on surfaces *a* and *b*. Future works on boundary slips in EHL should be conducted with the aim of explaining the existing gap between the experimental results and the theoretical results.

5 Conclusions

The effects of boundary slip on the film thickness in point contact under pure rolling and opposite sliding contacts were investigated. Numerical simulations were conducted based on the modified Reynolds equation and the energy equation by considering the velocity slip and thermal slip simultaneously on a sliding surface. The following conclusions were drawn:

Under the pure rolling contact, velocity slip induced a lubricant velocity distribution across the film, which led to a general reduction in film thickness. The influence of velocity slip on film thickness weakened as the entrainment velocity increased.

Under the ZEV contact, velocity slip caused the surface dimple to shift along the sliding direction, while thermal slip caused the surface dimple to shift in the opposite direction as the pressure peak shifted downward and the dimple depth decreased. The effects of velocity slip and thermal slip canceled out one another when the velocity slip length and thermal slip length were equal.

This study, for the first time, revealed the effect of thermal slip at the solid–lubricant interface on lubrication behavior, which might be one of the key parameters in EHL contact.

References

[1] Hamrock BJ, Dowson D. Ball bearing lubrication. The elastohydrodynamics of elliptical contacts. 1981.

[2] Gohar R, Cameron A. Optical Measurement of Oil Film Thickness under Elasto-hydrodynamic Lubrication. Nature 1963;200:458–9.

[3] Wedeven LD. Optical measurements of elastohydrodynamics in rolling-contact bearings. University of London, 1970.

[4] Lamb H. Hydrodynamics. 6th edition. C.U.P; 1932.

[5] Neto C, Evans DR, Bonaccurso E, Butt HJ, Craig VSJ. Boundary slip in Newtonian liquids: A review of experimental studies. Reports on Progress in Physics 2005.

[6] Thompson PA, Troian SM. A general boundary condition for liquid flow at solid surfaces. Nature 1997;389:360–2.

[7] Kapitza PL. The study of heat transfer in Helium II. Helium 4, 1971, p. 114–53.

[8] Pollack GL. Kapitza Resistance. Reviews of Modern Physics 1969;41:48–81.

[9] Nagayama G. Boundary conditions and microscale heat transfer at solid–liquid interface. Journal of the Heat Transfer Society of Japan 2011;50:29–36.

[10] Nagayama G, Matsumoto T, Fukushima K, Tsuruta T. Scale effect of slip boundary condition at solid–liquid interface. Scientific Reports 2017;7:1–8.

[11] Kaneta M, Nishikawa H, Kameishi K. Observation of wall slip in elastohydrodynamic lubrication. Journal of Tribology 1990;112:447–52.

[12] Wong PL, Li XM, Guo F. Evidence of lubricant slip on steel surface in EHL contact. Tribology International 2013;61:116–9.

[13] Ponjavic A, Wong JSS. The effect of boundary slip on elastohydrodynamic lubrication. RSC Advances 2014;4:20821–9.

[14] Wang P, Reddyhoff T. Wall slip in an EHL contact lubricated with 1-dodecanol. Tribology International 2017;113:197–205.

[15] Ehret P, Dowson D, Taylor CM. On

lubricant transport conditions in elastohydrodynamic conjunctions. Proceedings of the Royal Society A: Mathematical, Physical and Engineering Sciences 1998;454:763–87.

[16] Nagayama G, Cheng P. Effects of interface wettability on microscale flow by molecular dynamics simulation. International Journal of Heat and Mass Transfer 2004;47:501–13.

[17] Nagayama G, Tsuruta T, Cheng P. Molecular dynamics simulation on bubble formation in a nanochannel. International Journal of Heat and Mass Transfer 2006;49:4437–43.

[18] Wen S, Zhang Y. EHL performance of the lubricant with shear strength: Part i — boundary slippage and film failure. Tribology Transactions 2000.

[19] Chu LM, Lin JR, Li WL, Lu JM. A model for line-contact EHL problems-consideration of effects of navier-slip and lubricant rheology. Journal of Tribology 2012;134.

[20] Chen Q Da, Jao HC, Chu LM, Li WL. Effects of Anisotropic Slip on the Elastohydrodynamic Lubrication of Circular Contacts. Journal of Tribology 2016.

[21] Zhao Y, Wong PL, Mao JH. Solving coupled boundary slip and heat transfer EHL problem under large slide–roll ratio conditions. Tribology International 2019;133:73–87.

[22] Cameron A. Hydrodynamic Lubrication of Rotating Disks in Pure Sliding. A new Type of Oil Film Formation. Journal of the Institute of Petroleum 1951;37:471–86.

[23] Cameron A. The Viscosity Wedge. A S L E Transactions 1958;1:248–53.

[24] Yang P, Qu S, Chang Q, Guo F. On the theory of thermal elastohydrodynamic lubrication at high slide-roll ratios - Line contact solution. Journal of Tribology 2001;123:36–41.

[25] Guo F, Yang P, Wong PL. On the thermal elastohydrodynamic lubrication in opposite sliding circular contacts. Tribology International 2001.

[26] Guo F, Wong PL, Yang P, Yagi K. Film formation in EHL point contacts under zero entraining velocity conditions. Tribology Transactions 2002.

[27] Yagi K, Kyogoku K, Nakahara T. Relationship between temperature distribution in EHL film and dimple formation. Journal of Tribology 2005;127:658–65.

[28] Meziane B, Vergne P, Devaux N, Lafarge L, Morales-Espejel GE, Fillot N. Film thickness build-up in zero entrainment velocity wide point contacts. Tribology International 2020;141:105897.

[29] Zhang B, Wang J, Omasta M, Kaneta M. Effect of fluid rheology on the thermal EHL under ZEV in line contact. Tribology International 2015;87:40–9.

[30] Zhang B, Wang J, Omasta M, Kaneta M. Variation of surface dimple in point contact thermal EHL under ZEV condition. Tribology International 2016;94:383–94.

[31] Wong PL, Zhao Y, Mao J. Facilitating effective hydrodynamic lubrication for zero-entrainment-velocity contacts based on boundary slip mechanism. Tribology International 2018;128:89–95.

[32] Zhao Y, Wong PL, Mao JH. EHL film formation under zero entrainment velocity condition. Tribology International 2018;124:1–9.

[33] Peiran Y, Shizhu W. A generalized Reynolds equation based on non-Newtonian flow in lubrication mechanics. Acta Mechanica Sinica 1990;6:289–95.

[34] Dowson D, Higginson GR. Elasto-hydrodynamic theory. 1977.

[35] Roelands C. Correlational Aspects of the Viscosity-Temperature Pressure Relationship of Lubricating Oils. PhD Thesis 1966:495.

[36] Yang P. Numerical analysis of fluid lubrication. National Defense Industry Press; 1998.

[37] Venner CH, Lubrecht AA. Multilevel methods in lubrication. Tribology Series 2000.

[38] Yang P, Rodkiewicz CM. On the numerical analysis to the thermoelastohydrodynamic lubrication of a tilting pad inclusive of side leakage. Tribology Transactions 1997.

[39] Habchi W, Bair S. The role of the thermal conductivity of steel in quantitative elastohydrodynamic friction. Tribology International 2020;142:105970.

[40] Reddyhoff T, Schmidt A, Spikes H. Thermal conductivity and flash temperature. Tribology Letters 2019;67:0.

[41] Liu HC, Zhang BB, Bader N, Poll G,

Venner CH. Influences of solid and lubricant thermal conductivity on traction in an EHL circular contact. Tribology International 2020;146, 106059.

[42] Nagayama G, Kawagoe M, Tokunaga A, Tsuruta T. On the evaporation rate of ultra-thin liquid film at the nanostructured surface: A molecular dynamics study. International Journal of Thermal Sciences 2010;49:59–66.

Journal of Tribology
Volume 144, 071602-1, July 2022
https://doi.org/10.1115/1.4053180

Boundary slips induced temperature rise and film thickness reduction under sliding/rolling contact in thermal elastohydrodynamic lubrication

Xianghua Meng [a], Jing Wang [b], Gyoko Nagayama [c, *]

[a] Graduate School of Engineering, Kyushu Institute of Technology, 8048550, Fukuoka, Japan

[b] College of Mechanical Engineering, Donghua University, 201620, Shanghai, China

[c] Department of Mechanical Engineering, Kyushu Institute of Technology, 8048550, Fukuoka, Japan

Abstract: Temperature rise and film thickness reduction are the most important factors in elastohydrodynamic lubrication (EHL). In the EHL contact area, interfacial resistances (velocity/thermal slips) induced by the molecular interaction between lubricant and solid become significant due to the large surface/volume ratio. Although the velocity slip has been investigated extensively, less attention has been paid on the thermal slip in the EHL regime. In this study, numerical simulations were conducted by applying three cases of boundary slips to surfaces under sliding/rolling contacts moving in the same direction for the Newtonian thermal EHL. We found that the coupled velocity/thermal slips lead the most significant temperature rise and film thickness reduction among the three cases. The velocity slip results in a lower temperature in the lubricant and solids, whereas the thermal slip causes a temperature rise in the entire contact area in the lubricant as the film thickness decreases simultaneously. Furthermore, the effect of thermal slip on lubrication is more dominant than that of velocity slip while increases the entrainment velocity or slide–roll ratio.

Keywords:

bearings, elastohydrodynamic lubrication, films, friction, interface, sliding, thermal elastohydrodynamic lubrication

1 Introduction

Superlubricity-induced ultralow friction has garnered significant attention owing to its promising prospects of energy saving, environmentally friendly lubrication, and long-life machine operation in industrial applications [1]. To reduce friction in elastohydrodynamic lubrication (EHL) contacts, significant efforts have been expended [2–5]; however, friction reduction caused by the boundary slips between a lubricant and a solid surface is typically accompanied by a significant temperature rise and film thickness reduction in the contact area [6]. From a fundamental perspective, the coupling of the velocity discontinuity [7,8] and temperature jump [9–11] at the solid–lubricant interface are of particular importance for ensuring the lubrication performance in EHL contacts to avoid lubrication breakdown or surface failure.

Over the past decades, boundary slips in EHL have been investigated extensively. The major

studies are summarized in Table 1. The lubricant slip effect near the contact surfaces was first reported by Kaneta et al. [12] in 1990. Subsequently, Ehret et al. [13] verified Kanetas' results under different sliding conditions. Fu et al. [14] experimentally demonstrated that an inlet dimple was generated in an EHL film, which was attributed to a velocity slip. Kalin et al. [15] reported that the slip on diamond-like carbon (DLC) coating surfaces resulted in a 20% reduction in the friction coefficient under DLC/DLC contacts compared with that under steel/steel contacts. Guo and Wong et al. [16–18] measured the slip length at a solid surface from the relative movement between an entrapped lubricant and a contact surface. Ponjavic et al. [19,20] performed photobleached imaging to evaluate the effect of interfacial slip on the friction and film thickness in an EHL contact. The velocity slip presented by Wang et al. [21] occurred at a disc surface (that moved faster than the ball surface), which resulted in an anomalous EHL film shape. Under zero

Table 1 Review of EHL studies on velocity slip.

Year	Authors	Method/findings	Ref.
Experimental studies			
1990	Kaneta et al.	Ball–disc under pure rolling and sliding contact / velocity slip at or near contact surfaces	[12]
2007	Fu et al.	Ball–disc under pure sliding contact with high viscosity polymeric lubricant / velocity slip induced inlet dimple in contact region	[14]
2009	Kalin et al.	DLC–DLC contacts / 20% friction reduction compared to steel–steel contact	[15]
2012	Guo et al.	Entrapped lubricant in ball–disc contact / slip length of 0–12 μm at steel–lubricant (PB900/PB1300)–glass surfaces	[16]
2014	Ponjavic et al.	Glass–Fusso contact in PCS Instruments / central film thickness reduction of 50% due to velocity slip at Fusso coating surface	[19,20]
2017	Wang et al.	Ball–disc contact lubricated by 1-dodecanol / anomalous EHL film caused by velocity slip	[21]
2018	Wong et al.	ZEV contact with oleophobic coating / hydrodynamic lubrication film due to velocity slip at oleophobic surface	[22,23]
Theoretical analysis			
2000	Wen et al.	Isothermal line contact, viscoplastic rheological model / velocity slip occurred at the inlet zone	[24]
2003	Ståhl et al.	Line contact, limiting shear stress / central film thickness variations due to velocity slip	[25]
2012	Chu et al.	Line contact, Navier-slip and flow rheology / correlation between slip length and film thickness	[26]
2016	Chen et al.	Circular contact, anisotropic slip / film thickness reduction due to slip length in sliding direction	[27]
2019	Zhao et al.	Point contact, SRR = 44, velocity slips at two surfaces / variations of temperature rise and film thickness	[32]
2020	Zhang et al.	Point contact, layered oil slip model / reduction of film thickness due to velocity slip and thermal effect	[33,34]
2021	Meng et al.	Point contact, boundary slips at one of moving surfaces / film thickness reduction and temperature rise in contact region	[6]

Table 2 Recent studies on thermal slip at solid–liquid interface.

Year	Authors	Method/findings	Ref.
Experimental studies			
2006	Ge et al.	Time-domain thermoreflectance / water–Au interface, l_k = 3–6 nm at hydrophilic interfaces, l_k = 10–12 nm at hydrophobic interfaces	[35]
2010	Timofeeva et al.	Transient hot wire method / water–α-SiC interface, $l_k \approx 4.2 \pm 0.3$ nm	[36]
2017	Nagayama et al.	Forced convection in fully developed microchannel flow / water–Si interface, l_k = 50–150 μm	[37]
Molecular dynamics studies			
2010	Nagayama et al.	Nonequilibrium molecular dynamics simulations / Pt–Ar nanostructured interface, l_k = 3.4 – 9.8 nm at hydrophilic surface, l_k = 16.4 – 51.6 nm at hydrophobic surface	[38]
2012	Hu et al.	Molecular dynamics simulations using LAMMPS / water–gold interface, $l_k \approx 2 – 5$ nm	[39]
2012	Shi et al.	Molecular dynamics simulations using LAMMPS / l_k = 0 – 1.2 nm at Ar–silver interface, l_k = 3.1 – 3.5 nm at Ar–graphite interface	[40]
2014	Barisik et al.	Molecular dynamics simulations using LAMMPS / water–Si interface, $l_k \approx 8.5 – 9$ nm	[41]
2016	Pham et al.	Molecular dynamics simulations using LAMMPS / water and graphene–coated–Cu (111) interface, l_k = 10 – 50 nm	[42]
2021	Song et al.	Molecular dynamics simulations using LAMMPS / Ar–Cu interface, l_k = 0–14 nm in rough nanochannels	[43]

entrainment velocity (ZEV) bearing contacts, Wong et al. [22,23] reported a hydrodynamic lubrication film generated by a velocity slip on an oleophobic coating.

In addition to the experimental studies, theoretical models were established to consider the effect of boundary slip on lubrication performance in EHL [24–27, 32–34]. Wen et al. [24] proposed a lubricant ideal viscoplastic rheological model incorporating velocity slip into the line contact without thermal effect. Ståhl et al. [25] and Chu et al. [26] developed slip models for isothermal line contacts. Chen et al. [27] applied an anisotropic velocity slip to a point contact model and discovered a reduction in film thickness in a circular contact. In addition to the friction reduction induced by the boundary slips, the temperature rise induced via heat generation from the lubricant can lower friction owing to the reduction in the lubricant viscosity in the EHL contact. Consequently, temperature rise in the contact regime is an indispensable factor in tribology [28–31]. Zhao et al. [32] found that the velocity slip reduced temperature rise and increased the film thickness owing to the positive effect of lubricant entrainment under large slide–roll ratios (SRRs). Zhang et al. [33,34] proposed a layered oil slip lubrication model that included the thermal effect of the EHL point contact under various operation conditions.

Although the effect of velocity slip on lubrication performance has been investigated extensively, the thermal slip and the coupled velocity/thermal slips have rarely been considered in the EHL regime. Related studies on the thermal slip were summarized in Table 2. Due to the difficulties in measurement of thermal slip, various advanced techniques have been applied to the experimental systems including the solid–liquid interface. Despite the fact that great efforts have

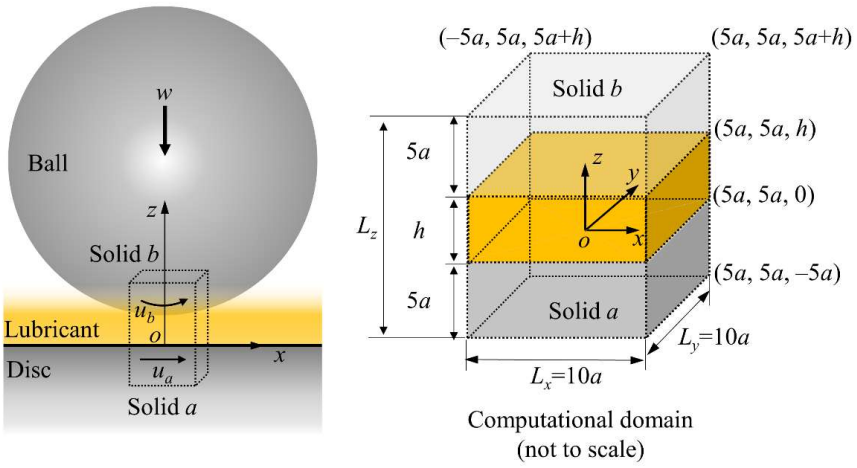

(a) (b)

Fig. 1 Schematic illustrations of (a) sliding/rolling contact, and (b) computational domain (not to scale).

been devoted to the measurement, it is still a challenging work to evaluate the thermal slip at the solid–liquid interface experimentally. On the other hand, with the aid of molecular dynamics simulation, the thermal slip at the solid–liquid interface has been extensively investigated. The thermal slip length (i.e., Kapitza length) at the hydrophilic solid–liquid interface is qualitatively smaller than that at the hydrophobic solid–liquid interface.

In the EHL contact area, interfacial resistances (velocity/thermal slips) induced by the molecular interaction between lubricant and solid become significant due to the large surface/volume ratio. That is, the boundary slips can no longer be ignored when the slip length or thermal slip length is comparable to the characteristic film thickness. In our previous study, we applied velocity and thermal slips to one of the sliding/rolling surfaces in ZEV contact; however, less attention has been paid on the temperature rise and the film thickness reduction [6]. Since boundary slips may occur at all moving surfaces in practical EHL, we conducted a further thermal EHL analysis in this study by applying boundary slip conditions to two moving surfaces under sliding/rolling contacts in the same direction. Three cases of boundary slips, i.e., velocity, thermal, and coupled velocity/thermal slips, were investigated to clarify the phenomena of temperature rise and film thickness reduction in thermal EHL. The adopted boundary slips length is comparable to the typical film thickness of the EHL contact.

2 Method

A steel–steel configuration comprising a disc (solid *a*) and a ball (solid *b*) was employed as a stationary EHL point contact subjected to an external load w, as shown in Fig. 1(a). The velocities of the disc and ball are u_a and u_b in the x-direction, respectively. Fig. 1(b) shows the corresponding computational domain $-5a \leq x \leq 5a$, $-5a \leq y \leq 5a$, $-5a \leq z \leq 5a + h$,

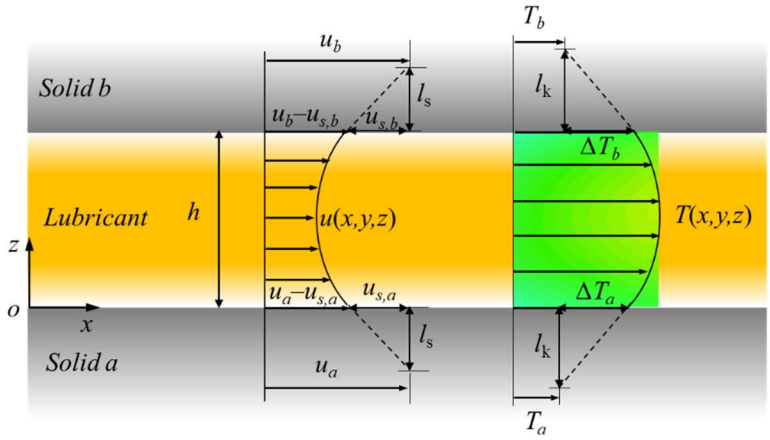

Fig. 2 Boundary slips at surfaces of moving solids: velocity slip (left) and thermal slip (right).

where a is the half Hertzian contact width, and h is the lubricant film thickness. The origin of coordinate system o is located at the center of the contact area. Five grid levels were employed in the computational domain. In the x- and y-directions, 256 equidistant nodes were adopted at the finest level, whereas in the z-direction, 11 equidistant nodes were adopted in the lubricant film and 12 non-equidistant nodes in the solids. Table 3 lists the operating conditions used in this study.

Table 3 Operating conditions

Ambient temperature, T_0, K	313
Ball radius, R, m	0.0127
Load, w, N	30
Half width of *Hertzian* contact, a, μm	136
Entrainment velocity, $u_e = (u_a + u_b)/2$, m/s	0 – 30
Slide-roll ratio, SRR = $(u_a - u_b)/u_e$	0 – 2

The lubrication performances were investigated by solving the Reynolds equation and energy equations under the boundary slips condition shown in Fig. 2. Since the lubricant is assumed to be the isotropic Newtonian fluid in this study, the linear relation between the shear strain rate and shear stress is considered. In contrast to our previous study [6], both the surfaces of solids a and b were assumed to be subjected to the same boundary slips. The linear Navier slip condition [7,8] and Kapitza resistance [9,10] were adopted for the slip velocity and temperature jump, as illustrated in Fig. 2, where l_s is the slip length and l_k is the thermal slip length. Hence, the lubricant velocity and temperature at the solid–lubricant interfaces are applied as follows:

$$\begin{cases} u_{z=0} = u_a - l_s \left.\dfrac{\partial u}{\partial z}\right|_{z=0} \\ u_{z=h} = u_b + l_s \left.\dfrac{\partial u}{\partial z}\right|_{z=h} \end{cases} \tag{1}$$

$$\begin{cases} T_{z=0} = T_a + l_k \left.\dfrac{\partial T}{\partial z}\right|_{z=0} \\ T_{z=h} = T_b - l_k \left.\dfrac{\partial T}{\partial z}\right|_{z=h} \end{cases} \tag{2}$$

By applying the lubricant velocity at the interfaces (specified in Eq. (1)) to the Reynolds equation, a modified Reynolds equation is obtained.

$$\frac{\partial}{\partial x}\left[\left(\frac{\rho}{\eta}\right)_{es} h^3 \frac{\partial p}{\partial x}\right] + \frac{\partial}{\partial x}\left[\left(\frac{\rho}{\eta}\right)_{e} h^3 \frac{\partial p}{\partial x}\right] + \frac{\partial}{\partial y}\left[\left(\frac{\rho}{\eta}\right)_{e} h^3 \frac{\partial p}{\partial y}\right] = 6(u_a + u_b)\frac{\partial \rho^* h}{\partial x} \tag{3}$$

where $\left(\frac{\rho}{\eta}\right)_{es}=12\left[l_s\frac{B}{A}\frac{\rho_e}{h^2}+\left(\frac{B}{A}\frac{\eta_{z=0}}{h}-\frac{\eta_e}{\eta_e'}\right)\rho_e'\right]$,

$\left(\frac{\rho}{\eta}\right)_e=12\left(\frac{\eta_e}{\eta_e'}\rho_e'-\rho_e''\right)$,

$A=h\eta_{z=0}\eta_{z=h}+l_s\eta_e\left(\eta_{z=h}-\eta_{z=0}\right)$,

$B=h^2\left(\frac{\eta_e}{\eta_e'}\right)\eta_{z=h}-l_s\eta_e h$, $\eta_e=h\Big/\int_0^h\frac{1}{\eta}dz$,

$\eta_e'=h^2\Big/\int_0^h\frac{z}{\eta}dz$, $\rho_e=h^{-1}\int_0^h\rho dz$,

$\rho_e'=h^{-2}\int_0^h\rho\int_0^z\frac{1}{\eta}dz'dz$, $\rho_e''=h^{-3}\int_0^h\rho\int_0^z\frac{z'}{\eta}dz'dz$,

$\rho^*=\frac{2}{u_a+u_b}\left[u_a\rho_e-\left(u_a-u_b\right)\eta_e\rho_e'\rho_{es}\right]$,

$\rho_{es}=\frac{\eta_{z=h}}{A}\left(l_s\frac{\rho_e}{\rho_e'}+h\eta_{z=0}\right)$.

Eq. (3) coincides with the Reynolds equation [44] under the no-slip boundary condition, where the slip parameters are $(\rho/\eta)_{es}$ = 0 and ρ_{es} = 1. To obtain the temperature profiles of the system, the full energy equations in the lubricant film and contacting solids were solved by considering the heat generated by the shearing and compression of the lubricant.

To resolve the local temperature filed, the full energy equations within the lubricant film and solids are described. Within the lubricant film, the energy equation [45] is expressed as

$$c\left(\rho u\frac{\partial T}{\partial x}+\rho v\frac{\partial T}{\partial y}-q\frac{\partial T}{\partial z}\right)-k\frac{\partial^2 T}{\partial z^2}=-\frac{T}{\rho}\frac{\partial\rho}{\partial T}\left(u\frac{\partial p}{\partial x}+v\frac{\partial p}{\partial y}\right)+\eta\left[\left(\frac{\partial u}{\partial z}\right)^2+\left(\frac{\partial v}{\partial z}\right)^2\right] \quad (4)$$

Within the solids, no compression and shearing are present, the energy equation for solids are written as:

$$\begin{cases}c_a\rho_a u_a\dfrac{\partial T}{\partial x}=k_a\left(\dfrac{\partial^2 T}{\partial z_a^2}+\dfrac{\partial^2 T}{\partial x^2}+\dfrac{\partial^2 T}{\partial y^2}\right)\\ c_b\rho_b u_b\dfrac{\partial T}{\partial x}=k_b\left(\dfrac{\partial^2 T}{\partial z_a^2}+\dfrac{\partial^2 T}{\partial x^2}+\dfrac{\partial^2 T}{\partial y^2}\right)\end{cases} \quad (5)$$

The relevant properties of the lubricant and steel are listed in Table 4. The Dowson and Higginson model [46] and the Roelands equation [47] were applied to estimate the density and viscosity of the lubricant as functions of pressure and temperature, as follows:

$$\rho=\rho_0\left[1+\frac{0.6\times10^{-9}p}{1+1.7\times10^{-9}p}-0.00065\left(T-T_0\right)\right]$$

$$\eta=\eta_0\exp\left\{\left(\ln\eta_0+9.67\right)\left[-1+\left(1+5.1\times10^{-9}p\right)^{Z_0}\left(\frac{T-138}{T_0-138}\right)^{-S_0}\right]\right\}$$

Here, ρ_0 is the density, η_0 is the viscosity of the lubricant at $p=0$ and $T=T_0$, Z_0 is the pressure–viscosity index, and S_0 is the temperature–viscosity index. Although the low thermal conductivity of steel would cause a temperature rise in the EHL contact [48–50], for simplicity, the steel thermal conductivity is set to 46 W/(m·K) in this study.

The simulation involved two procedures: (1) solving Eq. (3) under the fixed temperature field by applying the multilevel, multi-integration technique and multigrid method [51]; (2) solving the energy equations under the fixed pressure field (obtained from step (1)) by employing the sequential column sweeping method [52]. These procedures were repeated until the relative errors of pressure, load, and temperature were less than 1×10^{-3}, 1×10^{-3}, and 1×10^{-4}, respectively [6].

3. Results and discussion

3.1 Lubrication with boundary slips

Table 4 Properties of lubricant and steel

Density of steel, $\rho_{a,b}$, kg/m^3	7850
Specific heat of steel, $c_{a,b}$, J/(kg·K)	470
Thermal conductivity of steel, $k_{a,b}$, W/(m·K)	46
Ambient density of lubricant, ρ_0, kg/m^3	875
Specific heat of lubricant, c, J/(kg·K)	2000
Thermal conductivity of lubricant, k, W/(m·K)	0.14
Pressure viscosity coefficient, α, 1/Pa	2.4×10^{-8}
Ambient viscosity of lubricant, η_0, Pa·s	0.08
Thermal viscosity coefficient of lubricant, β,	0.042
Reduced elastic modules, E', Pa	2.26×10^{11}

To characterize the effects of boundary slip on lubrication, three cases of boundary slips were investigated in our numerical simulations: (1) velocity slip, (2) thermal slip, and (3) coupled velocity/thermal slips; subsequently, these cases were compared with the classical no-slip solution. Figs. 3–6 show the typical results obtained under u_e = 3.6 m/s and SRR = 1.5. In the current study, $-1 \le X = x/a \le 1$ and $-1 \le Y = y/a \le 1$ correspond to the area of the Hertzian contact, and $X = Y = 0$ corresponds to the center of the contact area.

The contour maps of the film thickness, pressure, and film thickness profiles are shown in Fig. 3. Here, the boundary slips length of 0.2 μm is adopted in this section, which is comparable to the typical film thickness of the EHL contact [53] The result of $l_s = l_k = 0$, which is a typical solution of the EHL point contact, is shown in Fig. 3(a). A central plateau and an outer constriction are evident in the contour maps. Compared with Fig. 3(a), a greater pressure peak is shown in Fig. 3(b), whereas lower pressure peaks are shown in Figs. 3(c) and 3(d). Meanwhile, the film thickness at the outer constrictions decreases when l_s = 0.2 μm and l_k = 0, as shown in Fig. 3(b), whereas the central plateau film inclines slightly when l_s = 0 and l_k = 0.2 μm, as shown in Fig. 3(c). For the coupled velocity/thermal slips when $l_s = l_k$ = 0.2 μm, as shown in Fig. 3(d), the film thickness at the outer constrictions decreases, accompanied by an inclined lubricant film. The film thickness shown in Fig. 3(d) is the thinnest among the cases, owing to the reduction in film thickness induced by the velocity slip and thermal slip. The film thickness reduction induced by the velocity slip is attributed to the lower lubricant velocity, which entrains less lubricant into the contact area [6,54] On the other hand, the thermal slip-induced film thickness reduction is attributed to the lower viscosity of the lubricant due to the temperature rise in the contact area. Comparing the minimum film thickness with that of the no-slip (dotted line) and $l_s = l_k$ = 0.2 μm (dashed line) cases, it is clear that the film thickness reduction is primarily induced by the velocity slip.

Fig. 4 presents the temperature profiles on the center plane (Y = 0) in the EHL contact area. Fig. 4(a) shows the results of the no-slip boundary condition ($l_s = l_k = 0$), where the temperature of the lubricant increases significantly at the center of the film thickness. This temperature rise is caused by the heat generated in the lubricant film due to the compression and shearing in the EHL contact area. Since the generated heat can be removed from the lubricant to the two moving solid walls, increasing the wall velocity can enhance heat dissipation. Consequently, both the surface temperature and the inner temperature of solid *a* are smaller than those of solid *b* because the velocity of solid *a* is seven

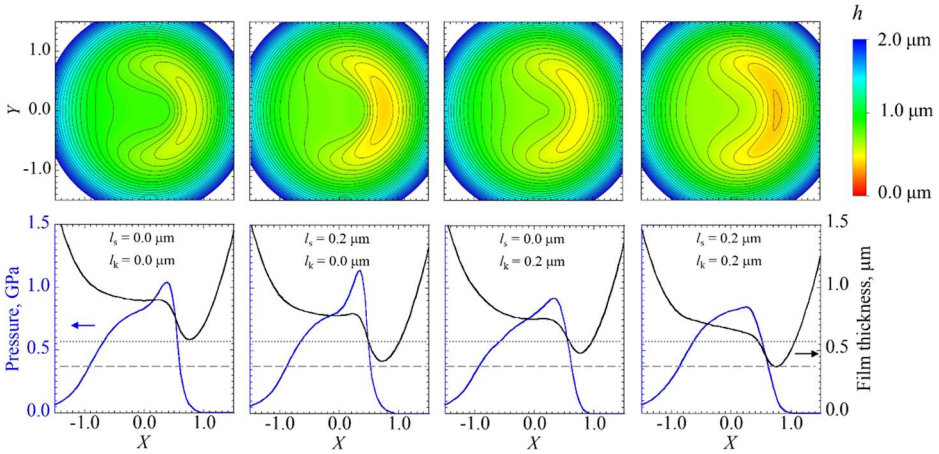

Fig. 3 Contour maps of film thickness (top) and pressure, film thickness profiles on center plane $Y = 0$ (bottom) at u_e = 3.6 m/s, SRR = 1.5 under different boundary conditions: (a) no slip; (b) velocity slip; (c) thermal slip; (d) coupled velocity/thermal slips. Dotted line represents minimum film thickness of no-slip case; dashed line represents minimum film thickness for case of $l_s = l_k$ = 0.2 μm.

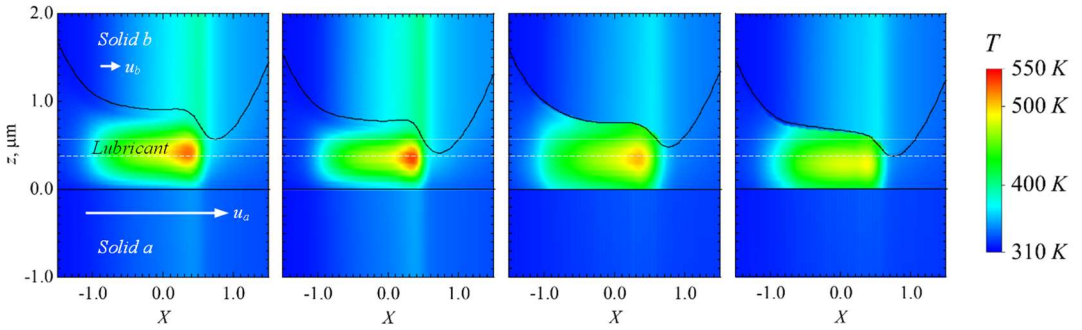

Fig. 4 Temperature profiles on center plane ($Y = 0$) in EHL contact area at u_e = 3.6 m/s, SRR = 1.5 under different boundary conditions: (a) $l_s = l_k = 0$; (b) l_s = 0.2 μm, $l_k = 0$; (c) $l_s = 0$, l_k = 0.2 μm; (d) $l_s = l_k$ = 0.2 μm. Dotted line represents minimum film thickness of (a); dashed line represents minimum film thickness of (d).

times larger than that of solid *b* at SRR = 1.5. In the case of l_s = 0.2 μm, the temperature profile in Fig. 4(b) is similar to that in Fig. 4(a), but the maximum lubricant temperature is higher than that in Fig. 4(a) because of the increase in the maximum pressure under velocity slip. Comparing Figs. 4(c) and 4(d) to 4(a), the area of lubricant temperature exceeding 400 K (green) expands significantly at the left side of the contact area, whereas the maximum lubricant temperature decreases. In particular, the lubricant temperature near the solid walls increases significantly. The main reason for

this temperature rise is the limited heat dissipation from the lubricant to solids under thermal slip at the two moving solid boundaries. Therefore, the temperature rises in solids *a* and *b* shown in Figs. 4(c) and 4(d) are undistinguishable compared with those in Figs. 4(a) and 4(b). Meanwhile, since a higher lubricant temperature results in a lower viscosity, thinner film thicknesses are formed in Figs. 4(c) and 4(d) compared with those shown in Fig. 4(a). However, the film thickness reduction induced by the thermal slip is smaller than that induced by the velocity slip. In other words, when the thermal slip length is the same as the slip length, the film thickness reduction is primarily induced by the velocity slip, as described previously.

The results presented in Figs. 3 and 4 show that the coupled velocity/thermal slips exhibit the worst tribological performance among the cases investigated. In particular, the effect of thermal slip on the temperature rise in the vicinity of the solid walls is dominant. Since the thermal slip length might not be of the same order as the slip length [37, 55], further analysis was conducted to investigate the superiority of the boundary slips.

Figs. 5–6 show the results under the coupled velocity/thermal slips, where the cases of $l_s / l_k < 1$ indicate the superiority of thermal slip over velocity slip, and those of $l_s / l_k > 1$ indicate the superiority of velocity slip over thermal slip. Similar to Fig. 3, the contour maps of the lubricant film thickness (top), centerline profiles of film thickness, and pressure (bottom) are shown in Fig. 5. As shown in the contour maps, the film thickness at the center plateau and outer constriction decreases with the increase in the thermal slip length (Figs. 5(a)–5(c)) or velocity slip length (Figs. 5(d), 5(e)). The film thickness reduction shown in Figs. 5(c) and 5(e) is more significant than that of the other cases, where a thin lubricant film of 20–60 nm covers the entire EHL contact area. Meanwhile, the pressure peak shown in Figs. 5(c) and 5(e) are less evident compared with those shown in Figs. 5(a) and 5(d). A further increase in the boundary slips might result in a transition from EHL to boundary lubrication, accompanied by lubrication failure at the contact area. In the case of $l_s / l_k < 1$, the film thickness reductions are dominated by thermal slip, whereas those of $l_s / l_k > 1$ are due to the superiority of the velocity slip.

Similar to Fig. 4, Fig. 6 shows the temperature profiles under the coupled velocity/thermal slips; Figs. 6(a)–6(c) show the cases of $l_s / l_k < 1$, whereas Figs. 6(d) and 6(e) show the cases of $l_s / l_k > 1$. As shown in Figs. 6(a)–6(c), a larger l_k induces a more significant lubricant temperature rise in the entire contact area. The reason contributing to the l_k-induced temperature rise is the same as that for Fig. 4, i.e., the limited heat dissipation from the lubricant to the solids. The maximum lubricant temperature rise is approximately 300 K at $l_k = 50.0$ μm, as shown in Fig. 6(c), accompanied by a temperature rise in the entire contact area of the lubricant. Simultaneously, the lubricant film thickness decreases to a critical level owing to the reduced viscosity corresponding to the temperature rise. Meanwhile, the larger l_s induces a lower lubricant temperature rise, as shown in Figs. 6(d) and 6(e). Since the lubricant velocity decreases under the velocity slip, the amount of heat generation decreases and hence, a smaller temperature rise is induced in the contact area. Meanwhile, the lower lubricant velocity limits the

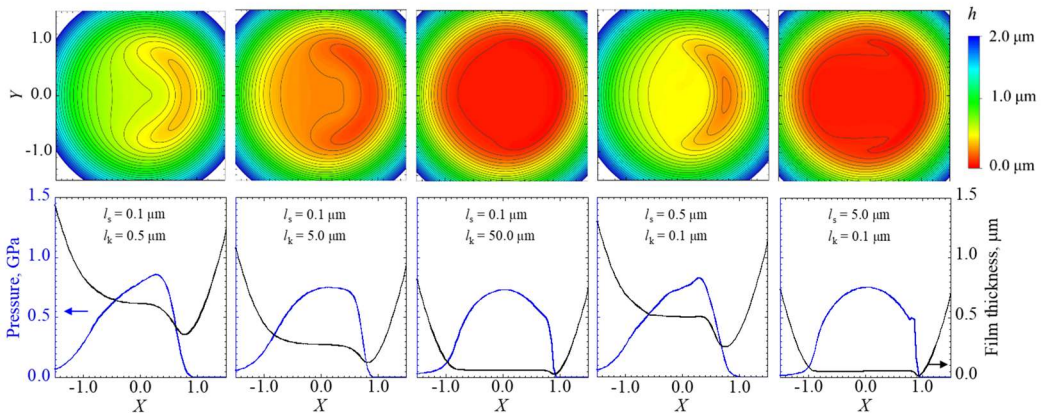

Fig. 5 Contour maps of film thickness (top) and pressure. Film profiles on center plane $Y = 0$ (bottom) at u_e = 3.6 m/s, SRR = 1.5 under coupled velocity/thermal slips: (a) l_s / l_k = 0.1 μm/ 0.5 μm; (b) l_s / l_k = 0.1 μm/ 5.0 μm; (c) l_s / l_k = 0.1 μm/ 50.0 μm; (d) l_s / l_k = 0.5 μm/ 0.1 μm; (e) l_s / l_k = 5.0 μm/ 0.1 μm.

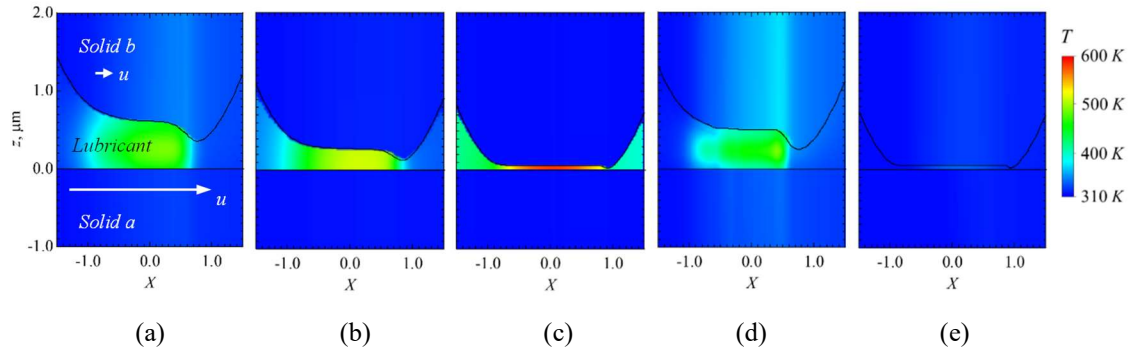

Fig. 6 Temperature profiles in EHL contact area on center plane $Y = 0$ at u_e = 3.6 m/s and SRR = 1.5 under coupled velocity/thermal slips: (a) l_s / l_k = 0.1 μm/ 0.5 μm; (b) l_s / l_k = 0.1 μm/ 5.0 μm; (c) l_s / l_k = 0.1 μm/ 50.0 μm; (d) l_s / l_k = 0.5 μm/ 0.1 μm; (e) l_s / l_k = 5.0 μm/ 0.1 μm.

amount of lubricant entraining into the contact area and hence, reduces the film thickness.

In summary, the velocity slip dominates the film thickness reduction when the slip length is comparable to the thermal slip length, whereas the thermal slip dominates the film thickness reduction when the slip length is negligible compared with the thermal slip length. In the coupled velocity/thermal slips case, the superior velocity slip might result in a lower temperature in the lubricant and solids, whereas the superior thermal slip might result in a temperature rise in the entire contact area in the lubricant as the film thickness decreases simultaneously.

3.2 Effects of entrainment velocity on lubrication with boundary slips at a specified SRR

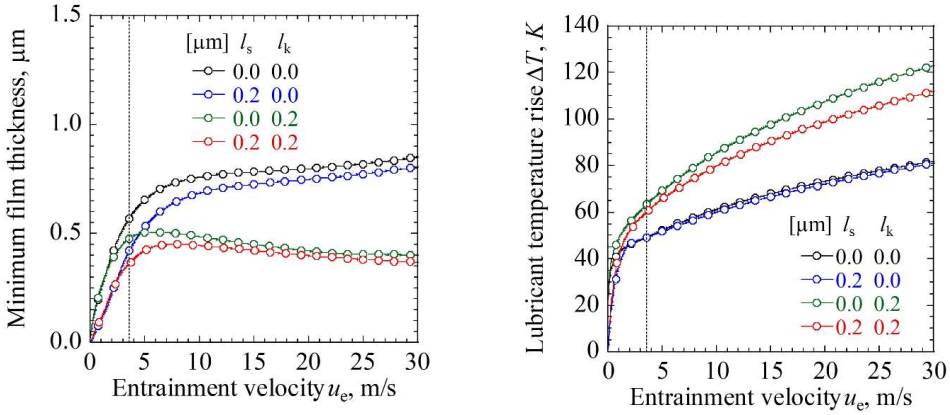

(a) (b)

Fig. 7 Effect of entrainment velocity on lubrication performance at SRR = 1.5: (a) minimum film thickness; (b) mean lubricant temperature rise in entire contact area. Dashed line corresponds to u_e = 3.6 m/s applied in Figs. 3–4.

The entrainment velocity is known as one of the key parameters in the lubrication of sliding/rolling contacts because the entrainment velocity can result in a variation in the amount of entrained lubricant and shear rate. Hence, the effects of the entrainment velocity on the lubrication characteristics with boundary slips at SRR = 1.5 are discussed in this section.

Fig. 7 shows the minimum film thickness and mean lubricant temperature rise curves with the entrainment velocity under boundary slips, where ΔT is the average value of the lubricant temperature rise over the entire contact area. The dashed line corresponds to u_e = 3.6 m/s applied in Figs. 3 and 4. In the low entrainment velocity region of u_e < 3 m/s, the minimum film thickness of the no-slip case (black) is consistent with that of the thermal slip case (green) because of the insignificant temperature rise, whereas those of the cases with velocity slips (blue and red) are relatively smaller. Therefore, the minimum film thickness reduction is primarily caused by velocity slip. When the entrainment velocity increases, the minimum film thickness reduction caused by the velocity slip (blue) decreases; however, that caused by the thermal slip (green and red) increases. With an increase in the entrainment velocity, the amount of entrained lubricant in the contact area increases, which facilitates the increase in the film thickness. By contrast, heat generation increases owing to increased lubricant shearing, resulting in a reduction in the film thickness. The contributions of velocity and thermal slips to the minimum film thickness reduction are equal at u_e = 4.6 m/s. Meanwhile, an apparent discrepancy appears in the cases with and without thermal slip in the high entrainment velocity region. The reason is shown Fig. 7(b), where the temperature rise is significant in the cases with thermal slip, which results in the apparent discrepancy in the minimum film thicknesses in the high entrainment velocity region.

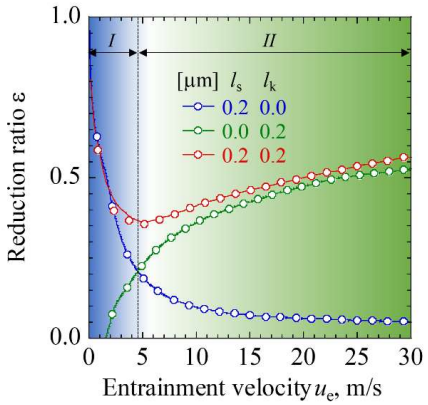

Fig. 8 Reduction ratio of minimum film thickness ε vs. entrainment velocity curves at SRR = 1.5. Dashed line represents threshold between regions *I* and *II*.

To compare the effects of boundary slips on the minimum film thickness, the ratio of the minimum film thickness reduction is plotted as a function of the entrainment velocity, as show in Fig. 8. The ratio of the minimum film thickness reduction ε is defined as $\varepsilon = (h_{min0} - h_{min}) / h_{min0}$, where h_{min0} is the minimum film thickness under the no-slip boundary condition. As shown in Fig. 8, at $u_e = 4.6$ m/s, the ε of the velocity slip case (blue) is equal to that of the thermal slip case (green), whereas that of the coupled velocity/thermal slips case (red) shows the minimum value. This implies that in region *I* of $u_e < 4.6$ m/s, velocity slip dominates the minimum film thickness reduction. By contrast, in region *II* of $u_e > 4.6$ m/s, the effect of thermal slip on ε is more dominant than that of velocity slip.

3.3 Effects of SRR on lubrication with boundary slips at specified entrainment velocity

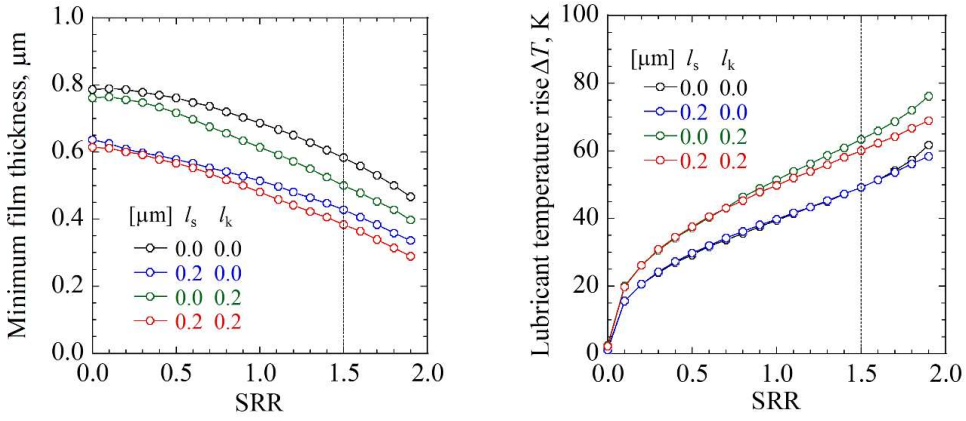

Fig. 9 Effect of SRR on lubrication performance at $u_e = 3.6$ m/s: (a) minimum film thickness; (b) mean lubricant temperature rise in entire contact area.

Since the lubricant temperature rise is induced by the lubricant shearing with regard to the lubricant shear rate or the relative velocity between solids *a* and *b* in the EHL contact, the effects of SRR on the lubrication characteristics are discussed in this section.

Figs. 9(a) and 9(b) show the variations in the minimum film thickness and lubricant temperature rise with boundary slips. The entrainment velocity is given as u_e = 3.6 m/s. The dashed line denotes SRR = 1.5, corresponding to the results shown in Figs. 3 and 4. It is clear that increasing the SRR reduces the minimum film thickness but increases in the temperature rise. As shown in Fig. 9(a), the thermal slip has less significant effect than the velocity slip on the minimum film thickness reduction, whereas the velocity slip yields a significant minimum film thickness reduction of approximately 0.15 μm. Meanwhile, the film thickness reduction of the coupled velocity/thermal slips is dominated by the velocity slip in the low SRR region, whereas the effect of the thermal slip on the film thickness reduction become more prominent in the large SRR region. As discussed previously in Section 3.1, the film thickness reduction is caused by two reasons: (1) the lower lubricant velocity induced by the velocity slip, and (2) the lower viscosity induced by the thermal slip. The latter coincides with the temperature rise in the entire contact area, which increases with the SRR, as shown in Fig. 9(b). Hence, the film thickness reduction in the case of coupled velocity/thermal slips is the largest among the cases investigated.

Fig. 10 shows the *f*-SRR curves at u_e = 3.6 m/s, where *f* is the friction coefficient. As shown, a greater velocity slip results in a higher *f*, whereas a greater thermal slip results in a lower *f*. The former is caused by the film thickness reduction subjected to a large velocity gradient, whereas the latter is caused by the reduction in lubricant viscosity due to a temperature rise.

Although the trend of the f-SRR curves is consistent with the experiments presented in [1,56], the operating conditions for those experiments are not comparable to those used in the present study. To date, only a few experimental results reported are comparable to simulation results or theoretical predictions. In Fig. 11, for illustrative purposes, the experimental results of glycerol/steel contact [1] are compared with the simulation results using the same operating conditions reported in [1]. The

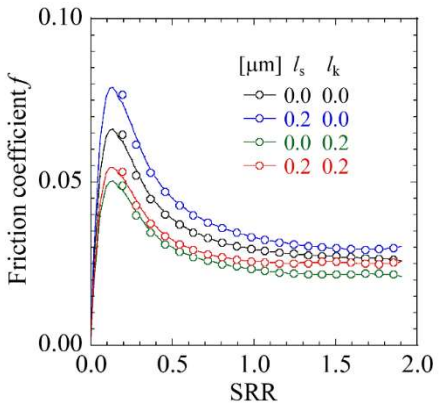

Fig. 10 Friction coefficient vs. SRR curves at u_e = 3.6 m/s.

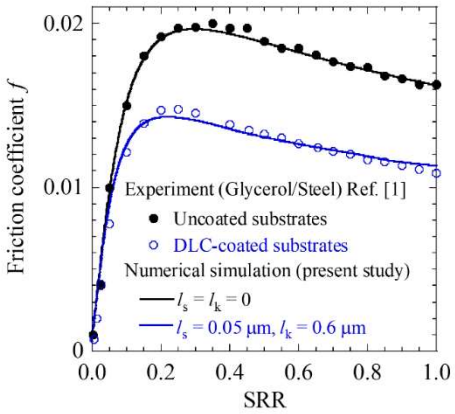

Fig. 11 Comparisons of f-SRR curve between experiments [1] and numerical simulations at u_e = 1.6 m/s and w = 300 N.

simulation results under the no-slip condition of $l_s = l_k = 0$ are consistent with the experimental results for the uncoated substrates, whereas those under the coupled slips of l_s = 0.05 μm and l_k = 0.6 μm are consistent with the experiments of DLC-coated substrates. Here, the thermal slip length for the DLC-coated surface [1] is estimated to 0.6 μm, including both the effects of the DLC coating and the interfacial thermal resistance. Since the DLC coating is 2.8 μm in thickness and its thermal conductivity is 2 W/(m·K), the thermal resistant of the coating layer is 1.4×10-6 K/W. This is 2 orders of magnitude smaller than that of equivalent interfacial thermal resistance (approximately 1.2×10^{-4} K/W), Therefore, the estimated thermal slip length l_k = 0.6 μm principally attributes to the interfacial thermal resistance. Accordingly, the deviations of the experimental results between the uncoated and DLC-coated substrates are significant, which imply that the boundary slips are of great importance to the superlubricity.

The quantitative estimation of the slip length and thermal slip length is crucial for providing a fundamental understanding of solid–lubricant interfaces for applications in superlubricity, albeit challenging. The method proposed herein facilitates the design and innovation of next-generation tribological technology.

Conclusion

Temperature rise and film thickness reduction were investigated via numerical simulations of thermal EHL under slip boundary conditions. Three cases of boundary slips, velocity, thermal, and coupled velocity/thermal slips, were applied to surfaces under sliding/rolling contacts moving in the same direction, and the following conclusions were obtained:

The velocity slip dominates the film thickness reduction when the slip length is comparable to the thermal slip length, whereas the thermal slip dominates the film thickness reduction when the slip length is negligible compared with the thermal slip length. In the coupled velocity/thermal slips case, the superior velocity slip might result in a lower temperature in the lubricant and solids, whereas the superior thermal slip might cause a temperature rise in the entire contact area in the

lubricant as the film thickness decreases simultaneously. Hence, the coupled velocity/thermal slips case leads the most significant temperature rise and film thickness reduction among the three cases.

The effect of thermal slip on lubrication is more dominant than that of velocity slip while increase entrainment velocity or SRR. At the critical entrainment velocity, the coupled velocity/thermal slips case has the minimum film thickness reduction ratio, which can improve the tribological performance.

The slip length and thermal slip length are estimated to be l_s = 0.05 μm and l_k = 0.6 μm on the DLC-coated surface based on the experimental data in [1].

The proposed method for estimating the slip length and thermal slip length quantitatively is challenging but beneficial for gaining a fundamental understanding of superlubrication. Further experimental investigations are necessary to verify the results obtained.

References

[1] Björling, M., and Shi, Y., 2019, "DLC and Glycerol: Superlubricity in Rolling/Sliding Elastohydrodynamic Lubrication," Tribology Letters, 67(1), p. 23.

[2] Sheeja, D., Tay, B. K., Krishnan, S. M., and Nung, L. N., 2003, "Tribological Characterization of Diamond-like Carbon (DLC) Coatings Sliding against DLC Coatings," Diamond and Related Materials, 12(8), pp. 1389–1395.

[3] Evans, R. D., Cogdell, J. D., and Richter, G. A., 2009, "Traction of Lubricated Rolling Contacts between Thin-Film Coatings and Steel," Tribology Transactions, 52(1), pp. 106–113.

[4] Katsaros, K., Bompos, D. A., Nikolakopoulos, P. G., and Theodossiades, S., 2018, "Thermal-Hydrodynamic Behaviour of Coated Pivoted Pad Thrust Bearings: Comparison between Babbitt, PTFE and DLC," Lubricants, 6(2), pp. 0–18.

[5] Wu, L. Y. L., Ngian, S. K., Chen, Z., and Xuan, D. T. T., 2011, "Quantitative Test Method for Evaluation of Anti-Fingerprint Property of Coated Surfaces," Applied Surface Science, 257(7), pp. 2965–2969.

[6] Meng, X., Wang, J., Nishikawa, H., and Nagayama, G., 2021, "Effects of Boundary Slips on Thermal Elastohydrodynamic Lubrication under Pure Rolling and Opposite Sliding Contacts," Tribology International, 155, p. 106801.

[7] Thompson, P. A., and Troian, S. M., 1997, "A General Boundary Condition for Liquid Flow at Solid Surfaces," Nature, 389(6649), pp. 360–362.

[8] Neto, C., Evans, D. R., Bonaccurso, E., Butt, H. J., and Craig, V. S. J., 2005, "Boundary Slip in Newtonian Liquids: A Review of Experimental Studies," Reports on Progress in Physics, 68(12), pp. 2859–2897.

[9] Kapitza, P. L., 1971, "The Study of Heat Transfer in Helium II," Helium 4, pp. 114–153.

[10] Pollack, G. L., 1969, "Kapitza Resistance," Reviews of Modern Physics, 41(1), pp. 48–81.

[11] Nagayama, G., 2011, "Boundary Conditions and Microscale Heat Transfer at Solid-Liquid Interface," Journal of the Heat Transfer Society of Japan, 50(211), pp. 29–36.

[12] Kaneta, M., Nishikawa, H., and Kameishi, K., 1990, "Observation of Wall Slip in Elastohydrodynamic Lubrication," Journal of Tribology, 112(3), pp. 447–452.

[13] Ehret, P., and Bauget, F., 2001, "Observation of Kaneta's Dimples in Elastohydrodynamic Lubrication Contacts," Proceedings of the Institution of Mechanical Engineers, Part J: Journal of Engineering Tribology, 215(3), pp. 289–300.

[14] Fu, Z., Guo, F., and Wong, P. L., 2007, "Non-Classical Elastohydrodynamic Lubricating Film Shape under Large Slide-Roll Ratios," Tribology Letters, 27(2), pp. 211–219.

[15] Kalin, M., Velkavrh, I., and Vižintin, J.,

2009, “The Stribeck Curve and Lubrication Design for Non-Fully Wetted Surfaces,” Wear, 267(5), pp. 1232–1240.

[16] Guo, F., Li, X. M., and Wong, P. L., 2012, “A Novel Approach to Measures Slip-Length of Thin Lubricant Films under High Pressures,” Tribology International, 46(1), pp. 22–29.

[17] Guo, F., and Wong, P. L., 2016, “An Anomalous Elastohydrodynamic Lubrication Film: Inlet Dimple,” Journal of Tribology, 127(2), pp. 425–434.

[18] Guo, F., and Wong, P. L., 2004, “Experimental Observation of a Dimple-Wedge Elastohydrodynamic Lubricating Film,” Tribology International, 37(2), pp. 119–127.

[19] Ponjavic, A., Chennaoui, M., and Wong, J. S. S., 2013, “Through-Thickness Velocity Profile Measurements in an Elastohydrodynamic Contact,” Tribology Letters, 50(2), pp. 261–277.

[20] Ponjavic, A., and Wong, J. S. S., 2014, “The Effect of Boundary Slip on Elastohydrodynamic Lubrication,” RSC Advances, 4(40), pp. 20821–20829.

[21] Wang, P., and Reddyhoff, T., 2017, “Wall Slip in an EHL Contact Lubricated with 1-Dodecanol,” Tribology International, 113, pp. 197–205.

[22] Zhao, Y., Wong, P. L., and Mao, J. H., 2018, “EHL Film Formation under Zero Entrainment Velocity Condition,” Tribology International, 124, pp. 1–9.

[23] Wong, P. L., Zhao, Y., and Mao, J., 2018, “Facilitating Effective Hydrodynamic Lubrication for Zero-Entrainment-Velocity Contacts Based on Boundary Slip Mechanism,” Tribology International, 128, pp. 89–95.

[24] Wen, S., and Zhang, Y., 2000, “EHL Performance of the Lubricant With Shear Strength: Part I — Boundary Slippage and Film Failure,” Tribology Transactions, 43(4), pp. 700–710.

[25] Ståhl, J., and Jacobson, B. O., 2003, “A Lubricant Model Considering Wall-Slip in EHL Line Contacts,” Journal of Tribology, 125(3), pp. 523–532.

[26] Chu, L. M., Lin, J. R., Li, W. L., and Lu, J. M., 2012, “A Model for Line-Contact EHL Problems-Consideration of Effects of Navier-Slip and Lubricant Rheology,” Journal of Tribology, 134(3), p. 031502.

[27] Chen, Q. Da, Jao, H. C., Chu, L. M., and Li, W. L., 2016, “Effects of Anisotropic Slip on the Elastohydrodynamic Lubrication of Circular Contacts,” Journal of Tribology, 138(3), pp. 1–48.

[28] Cheng, H. S., 1965, “A Refined Solution to the Thermal-Elastohydrodynamic Lubrication of Rolling and Sliding Cylinders,” ASLE Transactions, 8(4), pp. 397–410.

[29] Guo, F., Yang, P., and Qu, S., 2001, “On the Theory of Thermal Elastohydrodynamic Lubrication at High Slide-Roll Ratios - Circular Glass-Steel Contact Solution at Opposite Sliding,” Journal of Tribology, 123(4), pp. 816–821.

[30] Yagi, K., Kyogoku, K., and Nakahara, T., 2006, “Experimental Investigation of Effects of Slip Ratio on Elastohydrodynamic Lubrication Film Related to Temperature Distribution in Oil Films,” Proceedings of the Institution of Mechanical Engineers, Part J: Journal of Engineering Tribology, 220(4), pp. 353–363.

[31] Wang, J., and Yang, P., 2003, “A Numerical Analysis for TEHL of Eccentric-Tappet Pair Subjected to Transient Load,” Journal of Tribology, 125(4), pp. 770–779.

[32] Zhao, Y., Wong, P. L., and Mao, J. H., 2019, “Solving Coupled Boundary Slip and Heat Transfer EHL Problem under Large Slide–Roll Ratio Conditions,” Tribology International, 133, pp. 73–87.

[33] Zhang, Y., Wang, W., Liang, H., and Zhao, Z., 2020, “Slip Status in Lubricated Point-Contact Based on Layered Oil Slip Lubrication Model,” Tribology International, 144(September 2019), p. 106104.

[34] Zhang, Y., Wang, W., Liang, H., and Zhao, Z., 2019, “Layered Oil Slip Model for Investigation of Film Thickness Behaviours at High Speed Conditions,” Tribology International, 131(August 2018), pp. 137–147.

[35] Ge, Z., Cahill, D. G., and Braun, P. V., 2006, “Thermal Conductance of Hydrophilic and Hydrophobic Interfaces,” Physical Review Letters, 96(18), pp. 1–4.

[36] Timofeeva, E. V., Smith, D. S., Yu, W., France, D. M., Singh, D., and Routbort, J. L., 2010, “Particle Size and Interfacial Effects on Thermo-Physical and Heat

Transfer Characteristics of Water-Based α-SiC Nanofluids," Nanotechnology, 21, p. 215703.

[37] Nagayama, G., Matsumoto, T., Fukushima, K., and Tsuruta, T., 2017, "Scale Effect of Slip Boundary Condition at Solid-Liquid Interface," Scientific Reports, 7, pp. 1–8.

[38] Nagayama, G., Kawagoe, M., Tokunaga, A., and Tsuruta, T., 2010, "On the Evaporation Rate of Ultra-Thin Liquid Film at the Nanostructured Surface: A Molecular Dynamics Study," International Journal of Thermal Sciences, 49(1), pp. 59–66.

[39] Hu, H., and Sun, Y., 2012, "Effect of Nanopatterns on Kapitza Resistance at a Water-Gold Interface during Boiling: A Molecular Dynamics Study," Journal of Applied Physics, 112(5), p. 053508.

[40] Shi, Z., Barisik, M., and Beskok, A., 2012, "Molecular Dynamics Modeling of Thermal Resistance at Argon-Graphite and Argon-Silver Interfaces," International Journal of Thermal Sciences, 59, pp. 29–37.

[41] Barisik, M., and Beskok, A., 2014, "Temperature Dependence of Thermal Resistance at the Water/Silicon Interface," International Journal of Thermal Sciences, 77, pp. 47–54.

[42] Pham, A. T., Barisik, M., and Kim, B. H., 2016, "Interfacial Thermal Resistance between the Graphene-Coated Copper and Liquid Water," International Journal of Heat and Mass Transfer, 97, pp. 422–431.

[43] Song, Z., Cui, Z., Cao, Q., Liu, Y., and Li, J., 2021, "Molecular Dynamics Study of Convective Heat Transfer in Ordered Rough Nanochannels," Journal of Molecular Liquids, 337, p. 116052.

[44] Yang, P., and Wen, S., 1990, "A Generalized Reynolds Equation Based on Non-Newtonian Flow in Lubrication Mechanics," Acta Mechanica Sinica, 6(4), pp. 289–295.

[45] Yang, P., 1998, Numerical Analysis of Fluid Lubrication, National Defense Industry Press, Beijing.

[46] Dowson, D., and Higginson, G. R., 1977, Elasto-hydrodynamic Theory, Elsevier Ltd., New York.

[47] Roelands, C. J. A., Winer, W. O., and Wright, W. A., 1971, "Correlational Aspects of the Viscosity-Temperature-Pressure Relationship of Lubricating Oils," Journal of Lubrication Technology, pp. 209–210.

[48] Habchi, W., and Bair, S., 2020, "The Role of the Thermal Conductivity of Steel in Quantitative Elastohydrodynamic Friction," Tribology International, 142, p. 105970.

[49] Reddyhoff, T., Schmidt, A., and Spikes, H., 2019, "Thermal Conductivity and Flash Temperature," Tribology Letters, 67(1), p. 22.

[50] Liu, H. C., Zhang, B. B., Bader, N., Poll, G., and Venner, C. H., 2020, "Influences of Solid and Lubricant Thermal Conductivity on Traction in an EHL Circular Contact," Tribology International, 146(2), p. 106059.

[51] Venner, C. H., and Lubrecht, A. A., 2000, Multilevel Methods in Lubrication, Elsevier B.V., New York.

[52] Yang, P., and Rodkiewicz, C. M., 1997, "On the Numerical Analysis to the Thermoelastohydrodynamic Lubrication of a Tilting Pad Inclusive of Side Leakage," Tribology Transactions, 40(2), pp. 259–266.

[53] Hamrock, B. J., and Dowson, D., 1982, "Ball Bearing Lubrication (the Elastohydrodynamics of Elliptical Contacts).," pp. 279–281.

[54] Savio, D., Fillot, N., Vergne, P., Hetzler, H., Seemann, W., and Morales Espejel, G. E., 2015, "A Multiscale Study on the Wall Slip Effect in a Ceramic-Steel Contact with Nanometer-Thick Lubricant Film by a Nano-to-Elastohydrodynamic Lubrication Approach," Journal of Tribology, 137(3), p. 031502.

[55] Nagayama, G., and Cheng, P., 2004, "Effects of Interface Wettability on Microscale Flow by Molecular Dynamics Simulation," International Journal of Heat and Mass Transfer, 47(3), pp. 501–513.

[56] Björling, M., Habchi, W., Bair, S., Larsson, R., and Marklund, P., 2014, "Friction Reduction in Elastohydrodynamic Contacts by Thin-Layer Thermal Insulation," Tribology Letters, 53(2), pp. 477–486